Data-Driven and Machine Learning Frameworks for Condition Assessment of Plate Structure using Elastic Waves

A thesis submitted in the partial fulfillment of the requirements for the degree of

DOCTOR OF PHILOSOPHY

by

NUR MAHAMMAD MUSSA KALIMULLAH

(186104113)

Department of Civil Engineering

INDIAN INSTITUTE OF TECHNOLOGY, GUWAHATI

August 2024

Declaration

I hereby certify that the work compiled in this thesis is the outcome of the research work performed by myself, else stated, under the guidance of Dr. Amit Shelke.

Any part of this work has not been submitted for the award of any degree, diploma, associate fellowship, fellowship or its equivalent to any university or institution.

Nur Mahammad Mussa Kalimullah
Registration No.: 186104113
Department of Civil Engineering
Indian Institute of Technology Guwahati

Certificate

It is certified that the work contained in this dissertation entitled "**Data-Driven and Machine Learning Frameworks for Condition Assessment of Plate Structure using Elastic Waves**" by Mr. Nur Mahammad Mussa Kalimullah, a student in the department of Civil Engineering, Indian Institute of Technology Guwahati, India, for the award of the degree of the Doctor of Philosophy, has been carried out under my supervision and, that this work has not been submitted elsewhere for the degree.

Date: 14th Aug, 2024

Dr. Amit Shelke
Associate Professor
Department of Civil Engineering
Indian Institute of Technology Guwahati
Guwahati-781039, Assam, India

Acknowledgement

I stand at the culmination of a remarkable journey, one that has been shaped and enriched by the invaluable contributions and unwavering support of numerous individuals and institutions. As I take a moment to express my deepest gratitude, I am acutely aware that my words can scarcely convey the depth of my appreciation.

Foremost, I would like to express my sincere gratitude to my Dissertation Advisor, Dr. Amit Shelke, your guidance, mentorship, and unflagging belief in the significance of this research have been the cornerstones of my academic journey. Your unwavering dedication to excellence has not only elevated the quality of this dissertation but has also enriched my scholarly endeavours immeasurably. I shall remain always be grateful to him.

Besides my supervisor, I extend my heartfelt appreciation to the members of Doctoral Committee, Prof. Arbind K. Singh, Dr. Budhaditya Hazra and Prof. Vinayak Kulkarni for their constructive feedback, intellectual insights, and commitment to academic rigor. Your collective wisdom has been instrumental in shaping this dissertation into a meaningful contribution to our field.

Moreover, I would like to thank my project collaborators Dr. Anowarul Habib of UiT, The Arctic University of Norway and Dr. Maciej Radzieński of Institute of Fluid Flow Machinery, Poland for providing the experimental data reported in this research and their help, advice and motivating me throughout the course of my research. I gained invaluable knowledge through our interaction that helped significantly in my professional development.

I owe a debt of gratitude to the Indian Institute of Technology (IIT) Guwahati, whose resources, academic environment, and research facilities have provided the fertile ground upon which this work has grown. The financial support provided by the Indian Space Research Organisation (ISRO) (Grant No. ISRO/RES/STC/IITG/

2021-22) and grant from the publication fund of UiT The Arctic University of Norway was pivotal in facilitating my research activities, and for that, I am deeply thankful.

Special appreciation for the scientific officer, technical superintendents and support staffs of the Department of Civil Engineering namely, Dr. Arun Ch. Borsaikia, Mr. Biswajit Debnath, Mr. Pranab Hazarika, Mr. Saurabh Mudoi, Mr. Suresh Boro and Mr. Bipul Boniya. My fellow graduate students: Dr. Anupoju Rajeev, Dr. Lavish Pamwani and colleagues cum friends: Mr. Shivam Ojha, Mr. Ayush Thakur, Mr. Naveen Jangid, Mr. Satyam Panda, Mr. Ankush Gogoi and Ms. Anushka Vashistha at Department of Civil Engineering, IIT Guwahati have been a source of inspiration and camaraderie throughout this journey. Your discussions, shared challenges, and collaborative efforts have made the academic voyage a deeply enriching experience.

To my parents Mr. Ibrahim Ali and Mrs. Sultana F. Khanam, brother Nur Md. O. Faruque, sister Sultana A. Siddiqua, brother-in-law Harun A. Rashid, sister-in-law Bilkes Choudhury, and adorable Shakira, Armaan and Fareeha, all of your unwavering love and support have been my anchor during the turbulent seas of doctoral research. Your sacrifices, encouragement, and belief in my capabilities have sustained me through moments of doubt and exhaustion. I dedicate this accomplishment to you.

Lastly, to my friends back home Wadikur, Shahjahan, Rashidul, Nazeem, Junaid, Najmul, Sadik, Zishan, Washim and loved ones who provided moments of respite, laughter, and solace during this rigorous pursuit, I express my gratitude. Your presence in my life has reminded me of the importance of balance, joy, and the pursuit of dreams.

This dissertation stands as a testament to the collective effort of a multitude of individuals and institutions who have illuminated my path. I am deeply humbled and profoundly grateful for their contributions to this work and my personal and academic growth.

Thank you.

Nur Mahammad Mussa Kalimullah

August, 2024

Abstract

The evolving domain of structural health monitoring (SHM) is crucial for ensuring the integrity and extending the service life of engineering structures. This thesis presents a suite of data-driven and machine learning frameworks developed to enhance the condition assessment of plate structures, particularly focusing on the complexities of piezoelectric materials and anisotropic composites. In a comprehensive exploration of data-driven and machine learning frameworks for assessing the condition of plate structures, this dissertation presents a series of interconnected studies, each contributing to the advanced insights and application in SHM, particularly focusing on piezoelectric materials and anisotropic composites.

The effectiveness of piezoelectric sensors is deteriorated by the presence of defects, delamination, and corrosion, which must be identified and addressed to ensure the successful application of the SHM framework. The research begins by addressing anomaly detection in piezoelectric Lead Zirconate Titanate (PZT) substrates through the development of a novel multiresolution dynamic mode decomposition (mrDMD) algorithm. This method, effective at diagnosing and localizing surface defects, utilizes the interaction of ultrasonic waves with microscale defects. It leverages sophisticated image registration techniques and Kullback Leibler divergence to enhance the precision and effectiveness of defect localization in complex material systems.

Building on these foundational insights, the work progresses to the application of a deep autoencoder neural network, specifically tailored for anomaly detection in PZT sensors. This approach is beneficial at processing complex waveform data, identifies surface defects and delamination with high accuracy. The integration of image registration and peak signal-to-noise ratio metrics further refines the anomaly quantification, demonstrating a robust solution for handling the nonlinear interaction of waves with surface anomalies.

The development of a probabilistic approach using the unscented Kalman filter, aimed at estimating the stiffness matrix of an anisotropic piezoelectric material, in particular, Lithium Niobate substrate. This segment of research presents a groundbreaking integration of experimental measurements with a physics-based mathematical model. The implementation demonstrates the utility of Bayesian filtering in material characterization, especially under measurement uncertainties.

In an extension of these methodologies, the exploration turns to an anisotropic carbon fibre composites plate structure. Here, a probabilistic ML based on multi-output Gaussian process regression (moGPR) is employed to estimate the elastic constants of woven fabric reinforced composites. This study marks a notable advancement in interconnecting numerical simulations with experimental observations, specifically through the analysis of Lamb wave dispersion curves. The ML model correlates between theoretical predictions and practical measurements in composite laminates. Being a probabilistic framework, the implementation considers the measurement uncertainties.

The culmination of these methodologies is demonstrated in the final study, which introduces a multi-fidelity physics-informed neural network (mfPINN) for acoustic emission source localization in anisotropic composites. This innovative framework combines the strengths of data-driven and physics-informed learning. Further, this framework innovatively applies transfer learning to fuse low-fidelity physical models with sparse high-fidelity experimental data for acoustic emission source localization in composite panels. This implementation considers the uncertainties inherent in sensor measurements. This study showcasing the harmonious integration and advancement of the previously developed techniques. In other words, one can conduct this study after the diagnosis of piezoelectric transducer and characterising the composite laminates by using previous developed methods.

Collectively, these research works represent significant efforts towards the requirement of efficient, accurate, and robust SHM frameworks. Overall, this dissertation presents a holistic and sophisticated approach to structural health monitoring, setting new standards in the use of data-driven and machine learning methodologies for the detailed assessment and diagnosis of intricate systems.

Contents

List of Figures

List of Tables

Common Symbols, and Acronyms

Common Symbols

$\mathcal{D}_H$	High-fidelity data
$\mathcal{D}_L$	Low-fidelity data
$\mathfrak{D}_{noise}$	Dispersion data perturbed with noise
$\mathfrak{D}_{SMM}$	Dispersion data generated using SMM
$\mathbb{E}[\cdot]$	Expectation operator
$\mathbf{F}$	Matrix representation of discrete-time linear dynamics
$\widetilde{\mathbf{F}}$	Reduced dynamics on POD subspace
$\mathcal{F}$	Matrix representation of continuous-time linear dynamics
$\mathbf{H}$	Vector-valued observable functions on $\mathbf{x}$
$\mathbf{I}$	Identity matrix
$\mathbf{K}$	Kalman-gain matrix
L	Number of levels in mrDMD
l	Current level in mrDMD
M	Number of data snapshots
N	Dimension of the state, $\mathbf{x} \in \mathbb{R}^N$
$\mathcal{N}(\mu, \sigma)$	Normal random variable parameterized by μ and σ
$\mathbf{P}$	Covariance matrix of the state $\mathbf{x}$
p	Height of a snapshot
$\mathbf{Q}$	Covariance matrix of process noise
q	Width of a snapshot

$\mathbf{R}$	Covariance matrix of measurement noise
$\mathbb{R}$	Set of real numbers
$\mathbb{R}^N$	N-dimensional Euclidian space
$\mathbb{R}^{N\times M}$	$N \times M$ matrices with real numbers
r	Rank of truncated SVD
$\mathbf{S}$	Snapshot matrix, $\mathbf{S} \in \mathbb{R}^{(p\times q)\times M}$
t	Time
t_k	kth discrete time step
Δt	Time step
$\mathbf{U}$	Left singular vectors (POD modes) of $\mathbf{X}$
$\mathbf{V}$	Right singular vectors (POD modes) of $\mathbf{X}$
var[·]	Symbol for variance of a random variable
$\mathbf{W}$	Eigenvectors of $\widetilde{\mathbf{F}}$
$\mathbf{X}$	Data matrix, $\mathbf{X} \in \mathbb{R}^{N\times M}$
$\mathbf{x}$	State of system at time t
$\mathbf{y}$	Vector of measurements
δ_{ij}	Kronecker delta, equal to unity if $i = j$ and zero otherwise
$\mathbf{\Lambda}$	Diagonal matrix of DMD eigenvalues
λ	DMD eigenvalue
ν	Noise magnitude
ξ	Spatial variable
ρ	Radius of eigenvalue threshold for fast/slow separation in mrDMD
$\mathbf{\Sigma}$	Matrix of singular values
σ_k	kth singular value
σ_X^2, σ_X	Variance and standard deviation of random variable X
$\mathbf{\Phi}$	Matrix of DMD modes
$\phi_k^{(l,j)}$	kth DMD mode at level l and time bin j
ω	Continuous-time DMD eigenvalue, $\omega \triangleq \log(\lambda)/\Delta t$

Norms

$\|\mathbf{x}\|_2$	ℓ_2-norm of a vector $\mathbf{x}$ given by $\|\mathbf{x}\|_2 = \sqrt{\sum_{i=1}^{n}(x_i^2)}$
$\|\mathbf{X}\|_2$	2-norm of a matrix $\mathbf{X}$ given by $\|\mathbf{X}\|_2 = \max_{\mathbf{v}\neq\mathbf{0}} \|\mathbf{X}\mathbf{v}\|_2/\|\mathbf{v}\|_2$
$\|\cdot\|_F$	Frobenius norm of a matrix $\mathbf{X}$ given by $\|\mathbf{X}\|_F = \sqrt{\sum_{i=1}^{n}\sum_{j=1}^{m}\|X_{ij}\|^2}$

Acronyms

2D	Two dimensional
3D	Three dimensional
AE	Acoustic emission
ANN	Artificial neural network
CART	Classification and regression tree
CFRP	Carbon fibered reinforced polymer
CNN	Convolutional neural network
DL	Deep learning
DMD	Dynamic mode decomposition
EKF	Extended Kalman filter
EnEKF	Ensemble extended Kalman filter
FEM	Finite element method
FFT	Fast Fourier transform
GAN	Generative adversarial network
GMM	Gaussian Mixture Model
GloMM	Global matrix method
GP	Gaussian process
GPR	Gaussian process regression
HEKF	Hybrid extended Kalman filter
KL	Kullback Leibler

KF	Kalman filter
$LiNbO_3$	Lithium Niobate
LSTM	Long short-term memory
MAE	Mean absolute error
ML	Machine learning
MLE	Maximum likelihood estimation
MLP	Multilayer perceptron
moGPR	Multi-output Gaussian process regression
mrDMD	Multi-resolution dynamic mode decomposition
mfPINN	Multi-fidelity physics-informed neural network
NDE	Non-destructive evaluation
NDT	Non-destructive testing
NDT&E	Non-destructive testing and evaluation
NLP	Natural language processing
ODE	Ordinary differential equation
PCA	Principal component analysis
PDE	Partial differential equations
pdf	Probability density function
PINN	Physics-informed neural network
POD	Proper orthogonal decomposition
PSNR	Peak signal-to-noise ratio
PZT	Lead Zirconate Titanate
ReLU	Rectified linear unit
RNN	Recurrent neural network
SH	Shear horizontal
SLDV	Scanning laser Doppler vibrometer
SMM	Stiffness matrix method
SVD	Singular value decomposition

SVM	Support vector machine
SHM	Structural health monitoring
TDOA	Time difference of arrival
TOF	Time of flight
UKF	Unscented Kalman filter

Chapter 1
Introduction

In the modern era, machinery, equipment, and various structures, particularly lifelines such as roads, bridges, and powerlines, are of utmost importance and integral to our daily lives. Any potential threats of utility lifelines, regardless the extent, have the potential to cause a breakdown of any part of the system can eventually disrupt entire cities or countries. Predicting and detecting failures in these critical systems holds the promise of reducing both direct and indirect economic costs and human fatalities. The key to achieving this goal lies in the early identification of damage in these structures. Figure 1.1 shows the damage in composite structures due to bird strike and ice impact. Damage is broadly defined as any alteration to the material composition or geometry of a structure, including changes in boundary conditions, which can change the dynamic properties and response of the system [1, 2]. Traditionally, damage identification relied on periodic inspections, either through non-destructive testing and evaluation (NDT&E) or visual observation. However, visual observation is effective for straightforward applications, is prone to subjectivity, human errors, prolonged inspection times, and safety concerns when dealing with complex systems. Moreover, these traditional techniques often require prior knowledge of the specific areas where damage is suspected, makes the technique impractical for inaccessible regions without extensive dismantling. Additionally, these methods are localized and focus on specific areas, making them unable to capture the overall behaviour or response of the entire system.

The limitations of visual inspections for large and complex mechanical/civil infrastructure and infrequent inspection schedules have motivated the adoption of condition-based assessment methods. Structural health monitoring (SHM) has

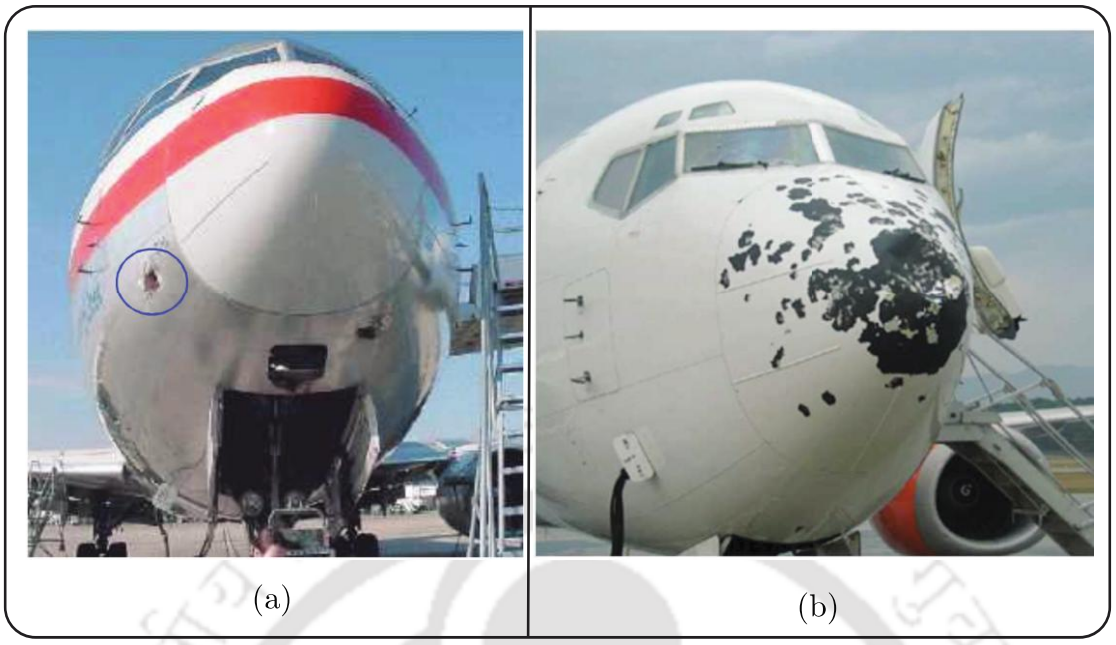

Figure 1.1 Damage in aircraft composite structure due to (a) bird strike, and (b) ice impact. (Source: Sandia National Laboratories, Albuquerque, NM, USA)

emerged as a solution for transitioning from periodic damage identification to nearly real-time and continuous damage assessment. In simple terms, SHM involves the use of continuous measurement devices to observe structures over extended periods. By analysing sensitive features extracted from this continuous data and employing statistical analysis, SHM can assess the current condition and performance of structures. An SHM system typically includes sensors strategically placed on the structure, data collection and transmission systems, and data analysis through various techniques and algorithms. Finally, decisions regarding inspections and maintenance are made based on the identified damage's location and severity as well as its potential future impact. Figure 1.2 illustrates the overall benefits of applying SHM in various structures.

1.1 Model-Driven and Data-Driven SHM

To detect damage in a structure, it is crucial to have a clear understanding of its undamaged condition. Without this baseline, assessing the extent of damage is difficult. Detecting damage relies on recognizing patterns of change compared to the previously recorded undamaged state. In some cases, SHM uses a prior model like a finite element (FE) model as a baseline, and model updating replaces initial assumptions with real measured values, establishing the original undamaged state.

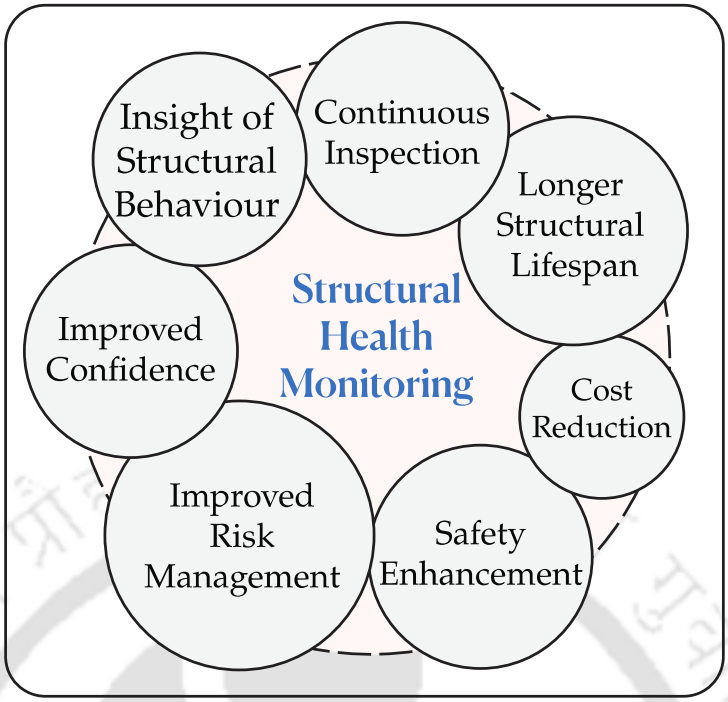

Figure 1.2 Benefits of SHM.

Further model updates can then identify damage by considering structural changes over time. This approach is known as a model-driven method and requires an accurate analytical/FE model of the structure [3].

Model-driven SHM has been a focus in various research works. For instance, Cao, *et al.* (2018) used piezoelectric impedance measurements in an inverse analysis for structural damage identification, while Moore, *et al.* (2012) employed model updating to detect cracks in thin plates [4, 5]. However, creating an accurate model can be challenging, especially for complex structures, where uncertainties about joints and bonds exist. This can lead to ill-posed inverse problems, necessitating regularization and simplification [6, 7]. An alternative approach to model-driven SHM is data-driven modelling, where the construction of the model relies on statistical pattern recognition, typically through machine learning (ML) algorithms, rather than a physical model of the structure.

In between these two approaches lies the hybrid method, which combines elements of both model-driven and data-driven techniques. Hybrid SHM leverages the strengths of physical models while incorporating data-driven methods to handle uncertainties and improve accuracy. For example, a hybrid approach might use an FE model to provide initial predictions and then apply ML algorithms to refine these predictions

based on real-time data. This method benefits from the interpretability and theoretical foundation of physical models, along with the adaptability and predictive power of ML algorithms, creating a more robust and flexible SHM strategy [8-10].

In contrast to the approach of initially having a FE model and later updating it, data-driven SHM systems make more convenient use of sensor data from structures in undamaged state, with fewer instances in the damaged state. In situations where there is a lack of labelled data, a data-driven approach can be adopted in an unsupervised manner, or a hybrid model can be used to generate additional data [11]. Augmenting data-driven SHM with FE model can create labelled datasets for training and validation. However, it is important to note that physical models can be computationally intensive and require validation with experimental results [9]. It is worth highlighting that not all ML algorithms are capable of damage prognosis, so data-driven approaches may not always serve as predictive models. Damage prognosis refers to the prediction of the remaining useful life and future condition of a structure based on current and historical data, allowing for proactive maintenance and management [12]. The choice between employing model-driven or data-driven SHM systems, or in tandem depends on factors like the system's requirements, the complexity of the application, and whether the existing data and models can effectively support and provide valuable insights into the structure's health state. For instance, if a hybrid approach is preferred, the predictive accuracy of the system depends on the performance of the physics-based model and the relevance and usability of the measured data from the data-driven approach for training and validation.

1.2 Anomaly Definition and Identification

A vertical hierarchy is commonly employed to identify and categorize damage in structures. This damage typology, as pioneered by Rytter (1993), comprises four main levels of damage assessment [13]:

1. Detection of damage.
2. Locating the position of damage.
3. Assessing the extent or severity of damage.
4. Predicting the future prognosis of damage.

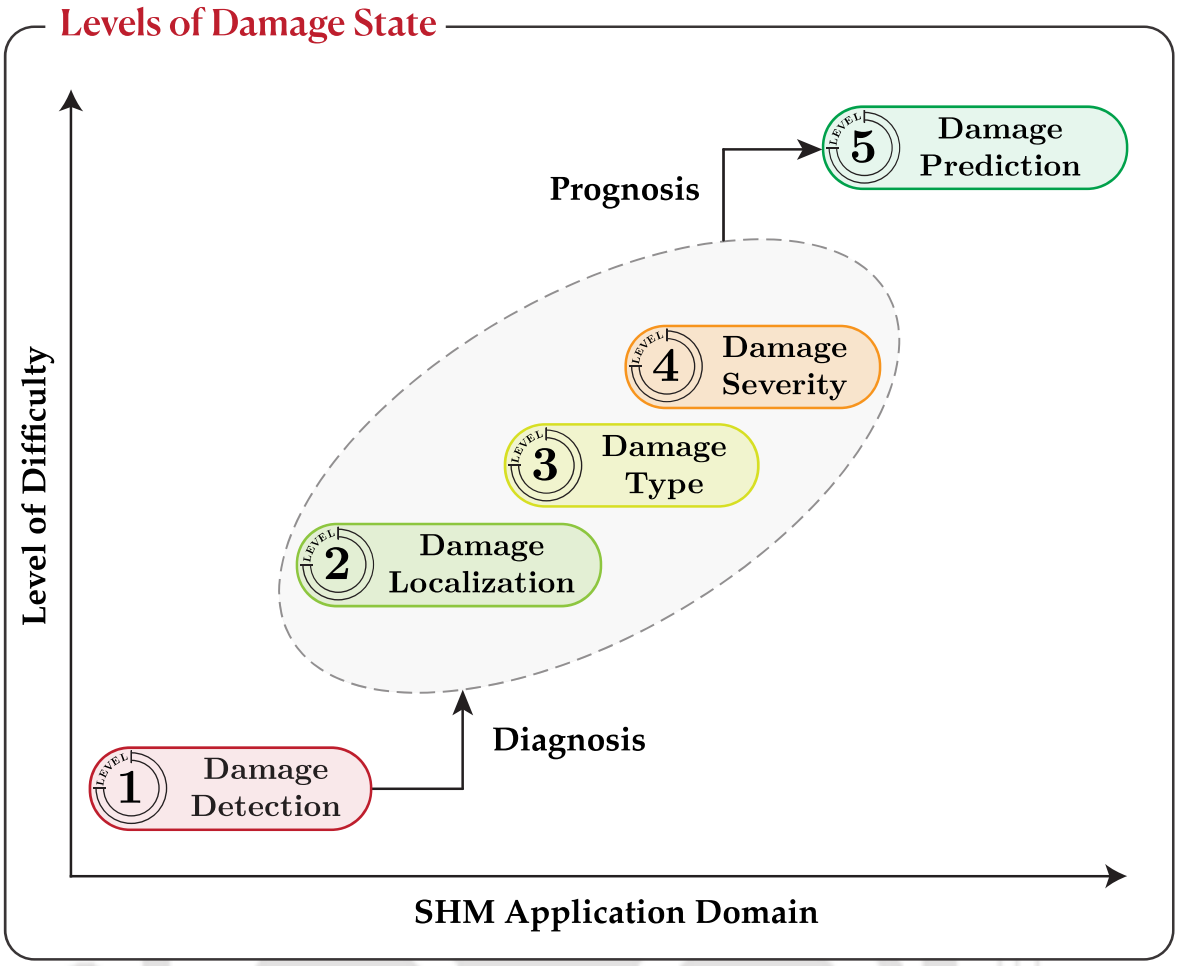

Figure 1.3 Five level hierarchical structure of damage identification strategy.

In this hierarchical approach, knowledge of the previous level is often essential for the successful identification of damage at a higher level. With the introduction of ML and pattern recognition (PR) algorithms, a new level has been added to this hierarchy. It involves determining the type or classification of damage, and it falls between the second and third steps of the original hierarchy. This results in a 5-step hierarchical process for damage identification, spanning from detection to prediction, as illustrated in Figure 1.3. Damage identification should be as detailed as possible to describe its impact on the structural system. Broadly, developments in damage identification can be divided into three areas: damage detection, damage diagnosis, and damage prognosis. However, damage diagnosis can be further subdivided to better characterize damage in terms of location, type, and severity.

In situations where both damaged and undamaged data are available, a supervised learning algorithm can effectively navigate all five levels of damage detection.

However, this requires the availability of extensive data from sensing systems, physical models, or experiments, which may not be feasible in many cases.

For such scenarios, unsupervised learning methods come into play. Instead of learning models and training on data, these methods employ a relatively simple approach, such as novelty or outlier detection [14]. Initially, a baseline model is established, assuming normal operational conditions. Subsequently, when new data is received from sensing systems during operation, the algorithm identifies any outliers based on a predefined threshold [15]. An example of an unsupervised algorithm's application involved testing it on an aircraft fuselage and a multi-layered carbon fibre-reinforced polymer (CFRP) plate for damage detection [16]. Unsupervised learning methods are particularly useful when labelled data is scarce or unavailable. They do not require predefined labels for training, making them ideal for early-stage damage detection where collecting and labelling data is challenging. These methods work by identifying deviations from the normal behaviour of the structure, which can indicate potential damage. Techniques such as clustering, principal component analysis (PCA), and autoencoders are commonly used to detect anomalies in the data. By focusing on changes in the statistical properties of sensor signals, unsupervised methods can flag unusual patterns that may correspond to structural damage [11].

In contrast to supervised learning, unsupervised methods offer an advantage by not necessitating prior knowledge of a structure's damaged state. However, unsupervised learning is primarily suitable for detecting damage and, occasionally, but not consistently, for locating it [17]. Many ML approaches used for damage detection often overlook environmental and operational factors (EOFs), focusing solely on severe damages. These factors, such as temperature variations and traffic loading, significantly influence the response of in-service structures [18]. Some studies have explored the impact of these variabilities over extended periods, ranging from 1 to 2 years [19-21]. As a result, an unsupervised approach alone may not be effective when considering external factors' influence in damage identification [22]. Instead, a combined approach that integrates both model-driven and data-driven algorithms can be employed to achieve a more comprehensive and reliable level of damage identification [23].

1.3 Background

In this era where the complexity of engineering structures is ever-increasing, the imperative for ensuring their operational integrity and safety is paramount. The advent of novel materials and the evolution of construction methodologies have given rise to structures with enhanced performance characteristics; however, these advancements also bring about new challenges in monitoring and maintenance. However, it is the older structures, which have been exposed to prolonged environmental stressors and wear, that require more rigorous SHM to ensure their continued safety and functionality. Plate structures, an important element within many engineering systems, are no exception. Their ubiquitous presence in key industries—from aerospace to civil infrastructure—demands a monitoring approach that is both sophisticated and reliable.

Historically, SHM has been reliant on periodic inspections and conservative design approaches to guarantee safety. Nevertheless, the limitations of such strategies are becoming apparent, particularly as the drive for efficiency necessitates the optimization of material usage and structural design. The detection of anomalies, such as cracks, delamination, or other forms of material degradation, requires more than just the traditional non-destructive evaluation (NDE) techniques; it requires a proactive, continuous monitoring strategy that can provide actionable insights in real-time.

The integration of piezoelectric materials into structural components has opened new avenues for SHM. These materials' unique properties enable them to act as both sensors and actuators, potentially providing a collection of data about the health of a structure. However, the analysis of this data is non-trivial. The multi-modal and dispersive nature of wave propagation through these materials introduces complexities that conventional analysis techniques are ill-equipped to handle.

Concurrently, anisotropic plates exhibit varying mechanical properties in different directions, a characteristic that can pose challenges when analysing and characterizing structural behaviour [24]. They are extensively used in aerospace composites, civil infrastructure, and medical devices, emphasizing the significance of robust SHM techniques tailored to their unique properties. Anisotropic materials, due to their directional dependency, require specialized monitoring approaches to accurately detect and diagnose potential issues. Traditional SHM methods might struggle to

account for the complex behaviour of these materials, leading to the need for more sophisticated techniques [25, 26].

The emergence of ML and data-driven methodologies presents a promising alternative for addressing these challenges. By leveraging vast computational power, we can develop frameworks that not only interpret the intricate data collected from these smart materials but also learn from it, improving their diagnostic capabilities over time. ML algorithms can analyse large datasets to identify patterns and anomalies that might be missed by conventional methods. Additionally, data-driven approaches can adapt to new data, making them ideal for monitoring the evolving state of anisotropic materials [9, 11].

For instance, in aerospace applications, where the integrity of composite materials is crucial, ML algorithms can predict failure modes and maintenance needs more accurately than traditional methods. In civil infrastructure, these technologies can help in monitoring bridges and buildings made from anisotropic materials, providing early warnings of potential failures. Similarly, in medical devices, ensuring the reliability of materials can significantly enhance patient safety and device performance [27, 28].

Despite the promising potential of these technologies, their application in SHM is still in its infancy. There are challenges to be addressed, such as the need for high-quality data, the development of robust algorithms capable of handling complex material behaviours, and the integration of these systems into existing SHM frameworks. However, as research in this area progresses, it is expected that ML and data-driven approaches will play an increasingly vital role in the effective monitoring and maintenance of anisotropic structures [29].

This thesis is set against this backdrop, where there is a clear and present need for advanced SHM systems that can keep pace with the evolving landscape of engineering structures. Through a systematic exploration of data-driven and ML frameworks, **this research aims to contribute to the field of SHM by developing methodologies that elevate our understanding and capabilities in the condition assessment of plate structures.**

1.4 Objectives and Methodology of the Study

1.4.1 Objectives

The objectives for this thesis is anchored in the critical need for robust SHM systems capable of ensuring the safety and longevity of engineering structures. With the increasing complexity of modern infrastructures and the prevalence of advanced materials, such as piezoelectric substrates and anisotropic composites, traditional SHM techniques are often found lacking.

Driven by this need, the thesis has the goal to harness and advance data-driven and ML methodologies to enhance the accuracy, sensitivity, and reliability of SHM frameworks. The research is specifically pronounced towards addressing the challenges posed by the intricate wave propagation behaviours in complex materials, aiming to develop sophisticated algorithms that can accurately detect minute anomalies and characterize material properties with unprecedented precision.

Moreover, the integration of computational models that can consider the uncertainties of empirical data presents an opportunity to significantly improve the predictive capabilities of SHM systems. By contributing novel approaches to anomaly detection and material characterization, the thesis aspires to fill existing gaps in SHM practices and offer scalable, practical solutions that can be readily applied in various sectors of civil, mechanical and aerospace engineering. The ultimate objective lies in bridging the gap between theoretical research and practical applications.

The primary objectives of this thesis are as follows:

- **Innovate SHM Methodologies for Anomaly Detection in Piezoelectric material**: To develop and validate cutting-edge computational algorithms that enhance the capability to detect, localize, and characterize anomalies and defects in piezoelectric material.
- **Advanced Diagnostic Techniques for PZT sensor**: By employing DL models to create robust frameworks for improved identification of anomalies in PZT sensors.
- **Optimize Material Characterization Techniques**: To improve and advance material characterization methods that minimize the need for destructive testing and can adapt to the accurate properties of advanced composite materials.

- **Enhance Probabilistic Estimation Models**: To establish and enhance probabilistic frameworks that account for uncertainties in measurement and modelling, thereby providing more reliable predictions of material properties and structural integrity.
- **Multi-fidelity Framework for Acoustic Emission Source Localization**: To integrate data-driven ML models with physics-informed principles to create robust frameworks for SHM for localizing acoustic emission sources in anisotropic composite materials.

By meeting these objectives, the thesis aims to contribute substantially to the field of SHM, providing both theoretical insights and practical tools that can be adopted by industry professionals and researchers to monitor and maintain the integrity of structural systems.

1.4.2 Methodology

The methodology adopted in this dissertation is rooted in the application of data-driven techniques and ML algorithms to address the challenges of SHM for plate structures. This multifaceted approach is comprised of several distinct yet interrelated computational strategies, each contributing to the overarching aim of enhancing the precision, efficiency, and reliability of SHM practices.

First, a novel experimental setup based on Coulomb coupling is employed across multiple studies to facilitate the visualization and analysis of ultrasonic wave interactions within piezoelectric materials and anisotropic composites. Further, to acquire wavefield propagation data in composite material scanning laser Doppler vibrometer is employed. These setups serve as the foundation for the subsequent application of advanced computational techniques.

The thesis then progresses through a series of methodological advancements:

- **Multiresolution Dynamic Mode Decomposition (mrDMD)**: This technique is leveraged to capture the spatiotemporal dynamics of elastic waves, facilitating the detection and localization of microscale defects within piezoelectric substrates.
- **Deep Learning based Autoencoder**: A deep autoencoder neural network is employed to isolate and identify anomalies within complex waveform datasets, enhancing the diagnostic capabilities of SHM systems.

- **Unscented Kalman Filter (UKF)**: The UKF is applied within a Bayesian framework to probabilistically estimate the stiffness tensor of anisotropic materials, integrating empirical data with physics-based modelling.
- **Multi-output Gaussian Process Regression (moGPR)**: moGPR is utilized to estimate the elastic constants of composite materials based on Lamb wave dispersion curves, contrasting computational predictions with experimental observations.
- **Multi-fidelity Physics-informed Neural Network (mfPINN)**: The thesis introduces an innovative mfPINN framework, combining low-fidelity physical models and sparse high-fidelity data to localize acoustic emission (AE) sources within composite structures. This approach acts as the central component for the thesis. This study of detecting AE source serves as a validation tool for the efficacy of all previous methodologies, showcasing their collective potential in a cohesive, real-world application for SHM.

Throughout these methodological advancements, the thesis maintains a commitment to addressing real-world applicability and scalability within the SHM domain.

1.5 Structure of the Dissertation

The dissertation unfolds systematically across nine chapters, beginning with an introduction (this chapter) that establishes the scope, background, and objectives of the research in the domain of SHM. Chapter 2 provides a comprehensive review of existing literature and the state-of-the-art in SHM methodologies, highlighting gaps and underscoring the need for specialized approaches. In Chapter 3, the experimental procedures used to collect the data necessary for the subsequent computational analysis are detailed. It describes the equipment, materials, and methodologies employed. Chapter 4 delves into the application of mrDMD for detecting anomalies in piezoelectric materials. It discusses the algorithmic development, implementation, and the experimental validation of the method. Chapter 5 explores the use of a DL based autoencoder network for anomaly detection in piezoelectric substrates. It presents the theoretical basis for the technique, and the characteristics of its implementation. Chapter 6 presents the research involving the UKF for the probabilistic estimation of stiffness tensors in anisotropic materials. It outlines the

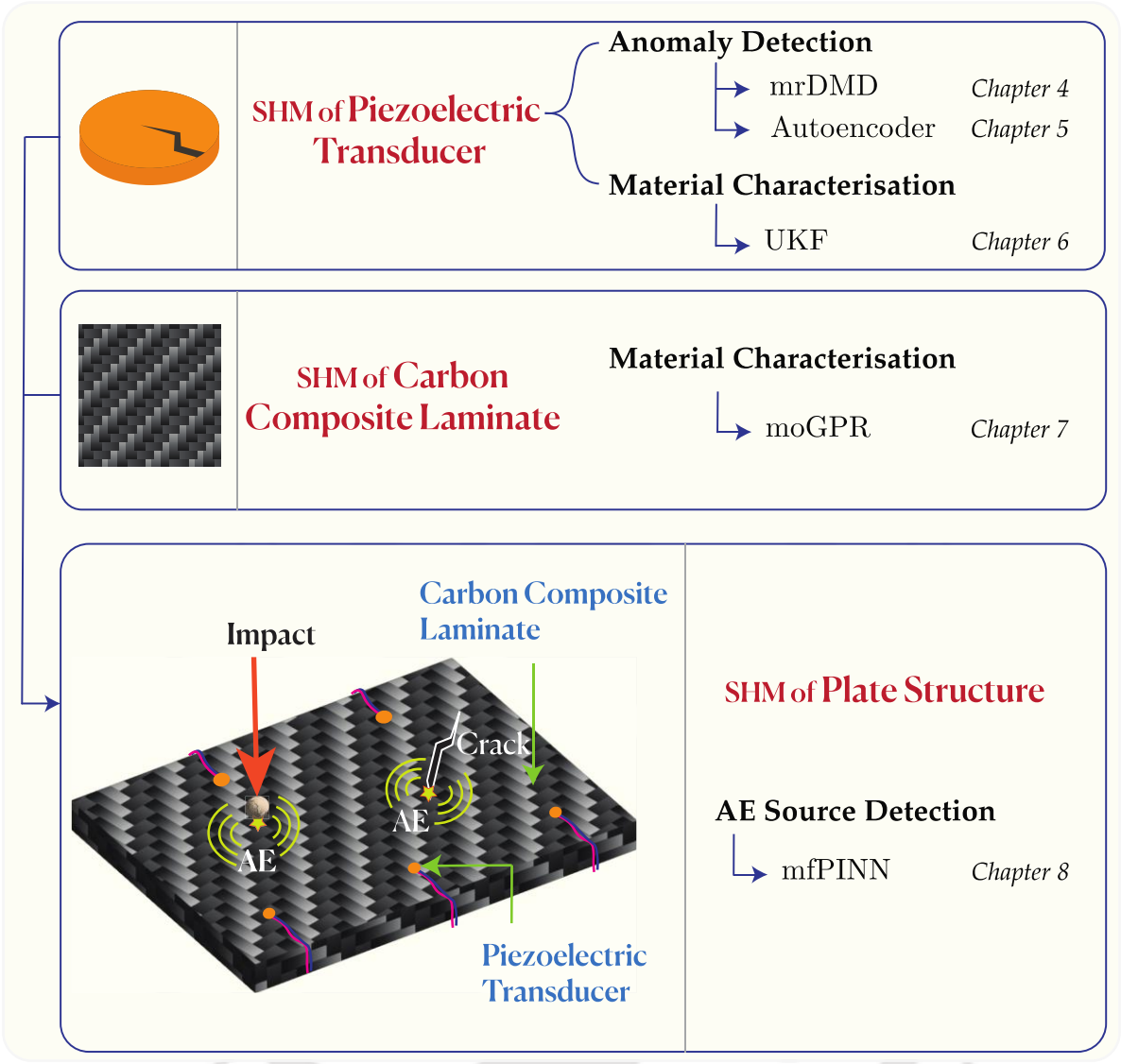

Figure 1.4 Overall research theme and structure of the dissertation.

algorithm's integration with the experimental data and its efficacy on material characterization accuracy. In Chapter 7, the application of moGPR to estimate the elastic constants of composite materials is discussed. It focuses on the method's ability to correlate experimental observations with model predictions. Chapter 8 highlights the development of a framework based on mfPINN for AE source localization within composite panels. It validates the application as a cornerstone tool that combines the methodologies developed in previous chapters. The final chapter, i.e., Chapter 9 concludes the dissertation by summarizing the key findings and contributions. It reflects on the implications of the research for the SHM field and proposes directions for future research, suggesting how the methodologies developed could be expanded

or applied to new challenges. The classification of thesis chapters along with overall research theme is illustrated in Figure 1.4.

1.6 Contribution to Knowledge

This thesis contributes significantly to the field of SHM, primarily advancing the understanding and application of data-driven techniques in the assessment of structural integrity. At its core, the research addresses the multifaceted challenges of SHM, ranging from the precise detection of anomalies to the comprehensive characterization of complex engineering materials. By focusing on the integration of recent advanced computational models and probabilistic frameworks, the thesis provides a pathway to enhance the predictive accuracy of SHM systems. The outcomes of this research emphasize the pivotal role of ML and data analysis in shaping future monitoring strategies that are both robust and adaptive to varying structural conditions.

The broader implications of this work are manifold. It establishes a new benchmark for the utilization of high-fidelity data in the development of advanced SHM strategies, accentuating the potential for real-world application across various domains of civil and aerospace engineering. Overall, the knowledge accumulated from this research enriches the SHM discourse, bridging theoretical innovation with practical application, and providing the connection for the next generation of intelligent monitoring systems that ensure the safety and resilience of engineering structures.

Chapter 2

Literature Review

This chapter discusses the historical overview of guided wave based methods in SHM, and data-driven and ML algorithms within a pattern recognition framework for SHM in civil, mechanical, and aerospace structures as illustrated in Figure 2.1. Guided waves are ultrasonic mechanical waves that propagate through bounded structural mediums, differing from traditional bulk wave propagation used in non-destructive evaluation (NDE). These waves have been extensively studied due to their sensitivity to small-scale damage and their ability to inspect large areas with minimal sensor deployment. However, their complex propagation characteristics, including multi-modal, dispersive, and attenuating behaviour, present significant analytical challenges.

The integration of guided wave-based methods into SHM frameworks has gained traction due to their effectiveness in detecting damage in thin-walled structures such as aircraft panels and pipelines. This approach leverages the unique advantages of guided waves, such as their long-range propagation capabilities and sensitivity to various types of structural anomalies.

ML based approaches scientifically play a critical role in learning and understanding structural behaviour. They are particularly relevant when damage-sensitive features derived from structural responses are influenced by operational and environmental variations, as well as damage-related changes. The chapter introduces state-of-the-art ML and data-driven algorithms, including Gaussian mixture models (GMMs), principal component analysis (PCA), Kalman filter, dynamic mode decomposition (DMD) and artificial neural networks (ANN). These algorithms differ in their working principles but share the common goal of establishing a baseline for

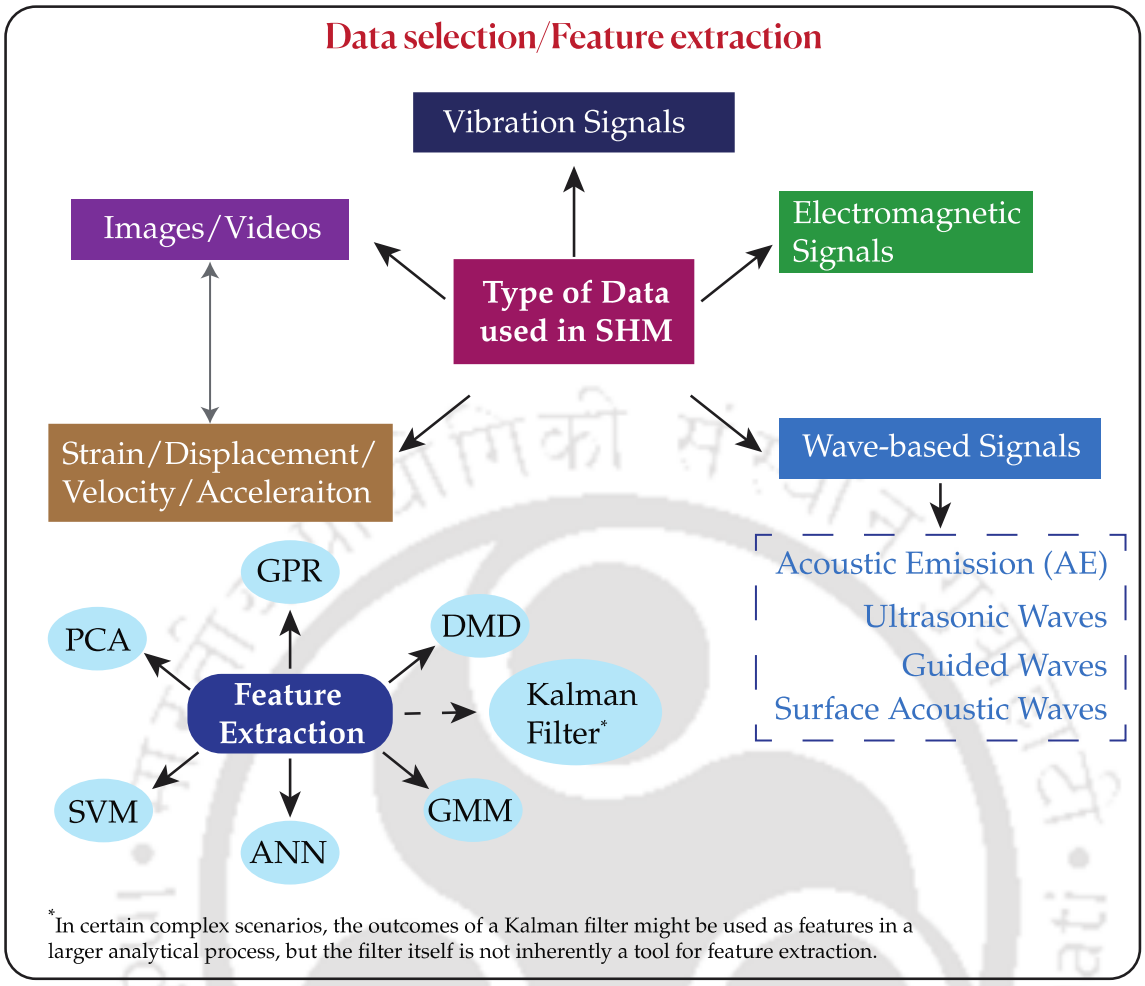

Figure 2.1 Illustration of various types of data and feature extraction algorithm used in SHM.

normal structural conditions and identifying deviations from this baseline, which may indicate damage.

2.1 Guided Wave based SHM

In SHM, guided waves refer to ultrasonic mechanical waves that propagate through confined structural mediums, differing from bulk wave propagation used in traditional NDE. Guided waves often exhibit multi-modal, dispersive, and attenuating characteristics due to the bounded nature of the waveguide, making their analysis and implementation more complex.

Various types of guided waves have been explored for SHM applications. The Lamb wave, frequently utilized in aircraft due to its propagation through thin plates and shells with stress-free surfaces, is among the most common. There's also significant research on Rayleigh waves, which travel near the surface of a medium and

can transform into Lamb waves under certain conditions like higher frequencies or in thicker plates. The shear-horizontal (SH) wave is another type often studied, particularly in laminated composite plates [30].

2.1.1 Simulation and modelling of guided waves

Since the early 1990s, simulation and modelling of guided waves for SHM have been a significant focus in the field. Research in this area covers a range of topics, including the characteristics and dispersion of waves, interactions between waves and damage, and coupling between transducers and structures. The approaches to modelling have been diverse, encompassing numerical, analytical, and semi-analytical techniques. In the last several decades, the computation of Lamb waves' dispersion in the multi-layered composite has been an active area of research. Leveraging the three-dimensional theory of elasticity, Nayfeh and Chimenti (1989) initially formulated a method to calculate Lamb waves dispersion within a uniform homogeneous plate [31]. Nayfeh (1991) further refined this approach resulting the transfer matrix method (TMM) by incorporating the Thomson-Haskell technique for layered composites [32, 33]. This method was subsequently enhanced by Hosten and Castaings (1993) to include viscoelastic properties and by Wang and Yuan (2007) to determine wave group velocities [34, 35]. Despite its utility, TMM faced challenges with numerical stability at larger values of frequency × thickness (or fd value) [36].

The global matrix method (GloMM) serves as an alternative to the TMM, collecting the response of each layer of a composite material into a global matrix [37]. One can determine the material's resonant modes by analysing the determinant of this matrix. The GloMM has been adapted for materials with different directional properties due to its consistent stability [38, 39]. Despite its reliability, the method's demand for computational resources increases with the number of composite layers, which can lead to inefficiency for composites with many layers. Pavlakovic and Lowe (2003) have incorporated the GloMM into an interactive licensed software called DISPERSE™, which can analyse various wave-related phenomena in layered materials [40]. Further, Ramasawmy, *et al.* (2020) developed a tool in MATLAB™ called 'Elastic Matrix' to model wave propagation in anisotropic media [41].

Rokhlin and Wang (2002) improved the analytical process for studying wave propagation in materials by proposing the stiffness matrix method (SMM) and its recursive formula, which enhanced stability and improved computational speed [42].

Huber (2018) developed an open source toolbox based on this method, called 'Dispersion Calculator,' in MATLAB™ [43]. The semi-analytical finite element (SAFE) method presents an alternative to exact 3D elasticity theory based method as discussed above for analysing Lamb wave behaviour in material [44]. This approach involves discretising a structure's thickness using one-dimensional elements to define stiffness and mass matrices. It transforms the problem into a generalized eigenvalue problem, which addresses challenges like the root search problem and numerical instabilities found in 3D elasticity methods. SAFE's adaptability and dependability have led to its application in various contexts, including anisotropic and laminated composite structures, and piezoelectric materials [45, 46].

2.1.2 Anomaly detection using guided Waves

The application of Lamb waves in SHM is often complicated due to their multi-modal nature. To simplify, the excitation frequency is usually kept below the cut-off frequencies of higher Lamb wave modes, which, however, reduces the sensitivity for detecting small-scale damage. As an alternative, Rayleigh waves, also known as surface acoustic waves (SAW), are considered due to their mostly single-mode, near non-dispersive propagation [47, 48]. While there are several studies on Rayleigh waves' dispersion characteristics, their use is limited to detecting surface-level cracks and defects [49]. Rayleigh waves have been applied in geophysical studies and for detecting damage in both metallic and civil structures [50-52].

SH waves are another type of guided wave, particularly useful for monitoring composite structures and adhesive bonds. Castaings and Hosten (2001) have conducted both experimental and theoretical studies on generating and detecting SH waves in anisotropic composites using air-coupled ultrasonic transducers [53]. Su, *et al.* (2007) have demonstrated SH wave-based delamination detection in composite beams, where SH wave propagation arises from the mode conversion of the S0 Lamb wave [30]. SH waves are also investigated in periodically layered composite structures with defects [54]. Their application is especially relevant in aerospace structures for monitoring adhesively bonded joints, given SH waves' sensitivity to shear stiffness, a crucial factor in bonded structures. Castaings (2014) and Le Crom and Castaings (2010) have contributed extensive theoretical and experimental work on SH wave-based monitoring in these contexts [55-57].

2.1.3 Application in real-world structures

Guided wave based method is recognized for its potential in SHM, notably for its ability to inspect large areas, its compatibility with lightweight and integrable transducers, and its sensitivity to small-scale damage. However, its application is hindered by the inherent difficulties of wave propagation, including multi-modal phenomena, reflections, and mode conversions at discontinuities. These challenges have largely confined the use of guided wave techniques to laboratory settings, and efforts to adapt the technology for practical, real-world use have been scarce. This is the case despite significant advancements in understanding guided wave propagation for damage detection. In contrast, traditional non-destructive testing (NDT) methods have been utilized in industrial contexts for many years. This section will explore reported cases of guided wave applications in actual structures, particularly those with more complex geometries.

The excitation and detection of guided waves in cylindrical structures and pipes have acquired considerable attention due to the need for scanning large areas prone to wave attenuation. In such scenarios, It's crucial to generate axial and/or circumferential wave modes, especially when the wall thickness exceeds the criteria for thin-walled assumptions. Piezoelectric transducers are commonly used, though the potential of magneto-strictive and laser-based sensors has been explored [58-61]. There has also been progress in visualizing damage through laser-based imaging in larger pipes [61]. Significant studies have been made in addressing complex, real-world conditions in cylindrical structures. This includes accounting for fluid flow within the structures, encountering discontinuities like welds, bends, elbows, and collars, and dealing with pipes that are supported, embedded, or submerged [62-65]. These advancements reflect the evolving capability of SHM systems to handle the intricacies of practical applications.

Some researchers have explored potential application of guided wave propagation for health monitoring in civil structures. For instance, Timoshenko beam theory was applied to a high-rise building model to detect damage based on wave propagation, with a case study involving earthquake acceleration data from a 54-story steel frame building in Los Angeles [66, 67]. Similar techniques have been used to detect damage in multi-story steel frame buildings by measuring changes in the velocities of longitudinal waves and employing analytical impulse response functions [67, 68].

Quintana, *et al.* (2014) introduced a global search method for detecting damage in a cable-stayed bridge by comparing flexural wave responses to the simulated responses of an undamaged bridge [69]. There has also been investigation into damage detection in large trusses using multivariate damage detection schemes [70]. Additionally, Wang, *et al.* (2009) developed a concrete-steel spectral element model that characterizes guided wave propagation through interface damages, with subsequent experimental validation [71]. The potential for guided stress wave-based damage detection in concrete piles has been explored using piezoceramic transducers [72]. In this study, a piezoceramic-based smart aggregate embedded between rebar was used to generate and record stress waves, with changes in wave amplitude and transmission energy indicating cracks in the concrete piles. This was illustrated by comparing time responses from healthy and damaged piles recorded by the smart aggregate piezoceramic transducer. Furthermore, guided wave propagation in reinforced concrete for damage detection was examined by Lu, *et al.* (2013) [73]. This involved the use of circular piezoceramic patches on the surface of the beam, along with piezoceramic patches at the ends of the rebars, to differentiate between damaged and undamaged response during experimental studies.

The application of guided wave-based method for detecting damage in complex aircraft structures initially focused on stiffened metallic and composite panels [74, 75]. In recent years, this technique has been applied to actual aircraft components, as documented in several studies [76, 77]. Senyurek (2015) demonstrated the application of surface wave-based damage detection on the wing slats of a Boeing 737, which consists of aluminium and a composite honeycomb core, using PZT discs as transducers to identify cuts and impact damage through strategic transducer placement [77]. Haynes, *et al.* (2013) developed a statistical model that employs a likelihood ratio test to distinguish between damaged and undamaged structures based on the responses of guided waves [76]. This model's effectiveness was verified on a commercial aircraft's fuselage rib section, which exhibited both holes and cracks.

2.2 Data-Driven and ML Algorithms for Statistical Pattern Recognition

2.2.1 Gaussian mixture model

The GMM is a parametric probability density function (pdf), which is similar to kernel density estimates with fewer components. It can be employed in bridge monitoring to identify the primary component representing the bridge's healthy state amidst varying environmental factors. In a case study of the Z-24 bridge in Switzerland, Figueiredo and Cross (2013) implemented an integration of supervised and unsupervised learning techniques for nonlinear long-term bridge monitoring [78]. This approach combined supervised nonlinear principal component analysis (NLPCA) for mapping the interdependencies of features and factors in environmental conditions, with unsupervised GMM for detecting damage through outlier analysis. Another study by Figueiredo, *et al.* (2019) on the Z-24 bridge examined using a hybrid method by integrating model-driven and data-driven systems for damage detection [21]. The FEM data utilised to enhance the GMM's damage classification and validation. Additionally, Farhidzadeh, *et al.* (2013) employed GMM for monitoring crack development in reinforced concrete shear walls, successfully differentiating between shear and tensile crack modes through the model [79].

2.2.2 Principal component analysis

In SHM and non-destructive evaluation (NDE), one often face a situation where there's a large amount of data points from a limited number of available measurements. The high-dimensionality of the data arises from the specific SHM/NDE methods used. For instance, a single high-resolution image could be comprised of a large matrix of data points, or a continuous wave might be represented by an extensive series of sampled points. Furthermore, as technology advances, the capability to capture data at higher sampling rates and resolutions escalates, leading to an even greater expansion in the size and complexity of the data.

Numerous techniques have been devised for reducing the dimensionality of data, known as dimensionality reduction tools [80, 81]. For instance, principal component analysis (PCA) is a prominent technique that reduces data to a space having a lower dimension by identifying the correlation among the original features [82]. PCA is widely used in data analysis to identify the most significant features of the data through principal components as illustrated in Figure 2.2. However, one challenge

with PCA, as with many statistical techniques, is its vulnerability to anomalies or outliers. These outliers may arise from faulty measurements due to equipment breakdown, human error, or mishandling of data, as well as external factors like environmental or measurement noise. Robust PCA (RPCA) is an advancement to PCA for high-dimensional data, offering improved robustness against outliers. RPCA has found its utility in numerous areas such as video surveillance, semantic indexing, ranking, and collaborative filtering, and is especially promising in the domain of SHM/NDE due to its ability to handle data with outliers and noise [82, 83]. For instance, the technique has been employed to robustly classify stress states in materials affected by environmental conditions like temperature. RPCA successfully distinguished the sparse components due to temperature variations related to stress states [84, 85].

In SHM/NDE, damage is often represented as outlier data. RPCA has proven useful in extracting and isolating this sparse data, facilitating in the detection, categorization, and localization of damage [86]. Applications have included the analysis of guided waves in aircraft turbine blades and the discernment of structural integrity in pipe-like structures using ultrasonic methods [87-89]. The methods such as approximated non-convex RPCA have been explored for their efficacy in identifying defects in structures like thin-walled plates through the analysis of lamb wave signals [90]. RPCA is also effective at identifying sparse patterns of damage, such as cracks

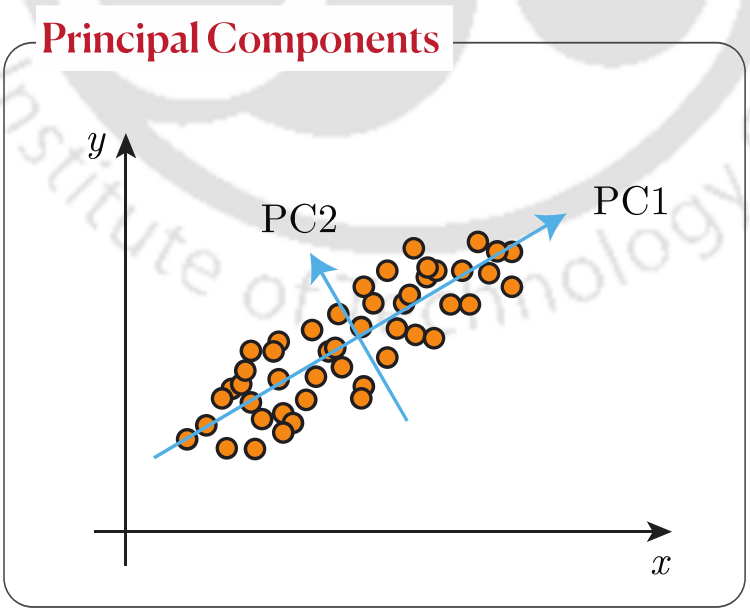

Figure 2.2 Orthogonal coordinate system of the data is determined by principal components.

in reinforced concrete or weld defects, using various imaging techniques [91-93]. The versatility of RPCA extends to its application in emerging data acquisition technologies like LIDAR or drone-captured videos for autonomous damage detection and localization in SHM/NDE [94].

The integration of RPCA in the framework of NDE 4.0 and digital twins signifies its potential in processing data from IoT devices and edge computing [95]. It plays a pivotal role in enhancing the resilience and efficiency of these devices by addressing the challenges posed by the volume of data and the necessity of noise removal, as well as the limitations of computational resources. Consequently, RPCA stands out as a valuable method for extracting relevant data features in the central models of digital twins.

2.2.3 Dynamic mode decomposition

The field of data-driven modelling and control of complex systems, encompassing engineering, biology, and physical sciences, is rapidly advancing due to the extensive availability of high-fidelity measurements from various sources. Despite the abundance of data, modelling these systems remains challenging. These systems are often high-dimensional, nonlinear, and exhibit complex multiscale behaviours. However, they typically evolve on low-dimensional attractors characterized by coherent spatiotemporal structures. The dynamic mode decomposition (DMD), a novel method for discovering dynamical systems from high-dimensional data [96].

Since its inception, the DMD algorithm was developed as a tool for analysing complex fluid dynamics [97, 98]. Its primary capability lies in extracting crucial low-rank spatiotemporal features from high-dimensional systems, yielding results that can be physically interpreted in terms of spatial configurations and their temporal behaviours. Despite its evolution, this diagnostic aspect of DMD remains its main application across various fields. It facilitates the data-driven identification of fundamental, low-rank structures in intricate systems, similar to the role of proper orthogonal decomposition (POD) analysis in fluid mechanics, plasma physics, atmospheric modelling, and other areas [96].

System identification methods from the control community are closely linked to DMD. Prior research has established connections between DMD and the eigensystem realization algorithm (ERA) [99, 100]. Further, DMD with control (DMDc) was connected with the observer Kalman filter identification methods (OKID) [101]. ERA,

and OKID algorithms are designed to construct input-output models using specific types of response data and are particularly useful in aerospace applications where systems often have a higher rank than the number of sensor measurements [99, 102-106]. In contrast, DMD and DMDc are tailored for systems with numerous measurements and low-rank dynamics, and have also been applied to analyse nonlinear complex systems [98, 107-109].

The domain of ML, compressed sensing, and data science has introduced nonlinear techniques for system identification. Genetic programming (symbolic regression) proven effective in identifying nonlinear dynamics from measurement data [110, 111]. The sparse identification of nonlinear dynamics (SINDy) algorithm employs sparse regression in a nonlinear function space to pinpoint key dynamic terms, recently connecting to DMD and the Koopman operator theory [112, 113]. Other methods focus on understanding causality in dynamical systems using techniques like time-delay embedding, related to delay coordinates [114, 115]. Exploring the relationship between DMD and these advanced system identification methods presents an exciting research avenue for dissecting complex nonlinear systems.

The mrDMD algorithm is an extension of DMD with multiresolution analysis (MRA) in time. The mrDMD is ideally suited for the decomposition of complex data and extract coherent spatiotemporal features. The detailed mathematical background of the mrDMD method is discussed in section 4.3. In a recent computer vision algorithm, DMD has been utilised to extract spatiotemporal features and applied to separate the foreground and background of video frames in real-time [116]. Bilal, *et al.* (2019) employed the mrDMD algorithm to detect the epileptic seizure [117]. Further, Sikha and Soman (2020) detected the salient region in noisy images by utilising the mrDMD algorithm [118]. The well-suited methods to perform MRAs are windowed Fourier transform [119], Hilbert-Huang Transform [120] and wavelet-based methods [121, 122]. These techniques are limited in implementation in both space and time simultaneously. However, the mrDMD overcomes the limitation and separates the multiscale spatiotemporal features.

2.2.4 Kalman filter

The Kalman filter comes in various forms to deal to different types of physical systems and their associated challenges. The ensemble Kalman filter (EnKF) is suitable for systems with a large number of variables often described by partial differential

equations (PDEs) [123]. For nonlinear systems, specialized versions like the extended Kalman filter (EKF), the unscented Kalman filter (UKF), and the particle filter (PF) are utilized for state and parameter estimation. Section 6.4 details the mathematical background of Kalman filter, particularly UKF.

The EKF is a prevalent method used for estimating states and parameters of nonlinear systems through measured data. It operates by linearizing the system's nonlinear equations via Taylor series expansion, allowing it to work on these linearized systems through a prediction-correction cycle. EKF can provide reliable estimates for systems with weak non-linearity under less noisy conditions. Zhang, *et al.* (2017) explored the integration of an extended Kalman filter (EKF) with ℓ_1 regularization to identify structural damage using free vibration data [124]. They transformed the standard optimization problem to include an ℓ_1-norm constraint, incorporating it into the EKF through a pseudo-measurement technique. In a separate advancement, Huang, *et al.* (2019) improved upon the EKF by introducing ℓ_p regularization, determining the optimal value of p through a novel L-surface method. Their method demonstrated superior performance in terms of accuracy and required fewer measurements compared to traditional EKF methods. Yun and Shinozuka (1980) employed the EKF for identifying parameters in nonlinear, multi-degree-of-freedom (MDOF) models, showing its efficacy even with noise [126]. A stabilization method within EKF was devised through a weighted global iteration, which proved effective in parameter tracking for various structural systems [127]. Further additional variables were introduced by Toki, *et al.* (1989) to this scheme for ground motion identification, and this modified approach was also used for input and parameter estimation in different contexts, such as in SDOF systems simulated under earthquake excitation [128, 129]. Kalman filters have been widely used for time-series analysis and parameter identification. Lei, *et al.* (2012) applied an extended Kalman estimator to identify both structural parameters and unknown excitations, particularly focusing on large-scale structures [130]. They managed to estimate the interconnection effects between substructures without needing measurements at the interface degrees of freedom (DOFs), an approach that outperformed previous methods requiring comprehensive interface data.

Wang and Haldar (1997) introduced a two-stage procedure (ILS-EKF-UI) that first estimates the input and then identifies structural parameters, working

satisfactorily with limited data [131]. Further improvements to the EKF algorithm allowed for the detection of structural damage that primarily affects stiffness, characterizing damping through Rayleigh's model [132, 133]. To identify input forces on nonlinear systems, a combined method of EKF with recursive least squares was proposed [134]. Yang, *et al.* (2006) introduced an adaptive tracking technique within this framework to optimize parameter tracking, showing special effectiveness in detecting sudden structural changes [135]. Dealing with a large number of parameters, traditional EKF can face divergence issues. To address this, Lei, *et al.* (2015) developed a two-step Kalman filter technique to enhance convergence and reduce the number of parameters needing estimation at each step [136]. This was successfully applied to detect damage in frame structures by separately estimating the structural state vector and the structural parameters [137]. Despite these advancements, EKF's convergence can suffer from numerical instability. To counter this, constraints were introduced to maintain parameter estimates within reasonable limits, showcasing the method's robustness in damage identification for various structures [138]. Moreover, EKF and its variants often depend highly on the initial guess of the unknown parameter estimates. To mitigate this, Yun, *et al.* (2021) proposed a hybrid extended Kalman filter (HEKF) that integrates a genetic algorithm with the EKF, enhancing its performance as demonstrated on a steel frame structure [139].

The EKF linearizes non-linear systems using a Taylor series approximation around the current state by truncating after the first derivative, which can lead to significant numerical errors. The UKF improves this by generating 'sigma points' around the current estimate, which follow a Gaussian distribution [140]. These points help to minimize error covariance in the correction step, making UKF a more accurate and robust algorithm, particularly in the presence of noise. Sitz, *et al.* (2002) showed that UKF could effectively estimate states and parameters in noisy, non-linear dynamical systems, but convergence depends mainly on the initial covariance choice [141]. Popescu and Wong (2003), as well as Mariani and Ghisi (2007), found that UKF outperformed EKF in joint state and parameter estimation for non-linear systems [142, 143].

Astroza, *et al.* (2017) applied an UKF to navigate nonlinear state-space equations, bypassing the need for finite element (FE) response sensitivity computations regarding model parameters and input excitations [144]. Chatzi and Smyth (2009) compare UKF

with the particle filter revealed UKF's efficiency and lower computational cost for inverse parameter estimation [145]. UKF's effectiveness was further highlighted by Chatzi, *et al.* (2010) for online parameter estimation in non-linear systems with additional non-linear terms [146]. Despite these advancements, the success of UKF still heavily depends on the accuracy of initial parameter estimates. To address this, Bayesian optimization and weighted adaptive strategies have been proposed, like the weighted adaptive constrained UKF (WACUKF), which integrates adaptive noise evaluation and genetic algorithms for more reliable initial guesses, demonstrating effectiveness on complex hysteretic systems [147].

The EnKF integrates measurements into a Monte Carlo simulation, using an ensemble-derived covariance matrix instead of the actual one, and propagating state vector samples with the precise non-linear model. Evensen (1994) introduced this method to address the EKF's inadequate covariance handling [148]. EnKF propagates by evolving a set of state vector samples over time to estimate the probability distribution of the state vector. Ghanem and Ferro (2006) showcased its efficacy for identifying non-linear system characteristics amidst Gaussian noise, exemplified through a 4-storey building model [149]. They successfully estimated the location and timing of damage despite noise interference. EnKF proved to be more effective than EKF, especially in dealing with significant non-linearities. Additionally, Slika and Saad (2016) applied EnKF for predicting the lifespan of concrete structures damaged by chloride, highlighting its predictive capabilities in structural health monitoring [150].

Classical non-linear filters like the EKF utilize a parametric form to express the conditional pdf, often Gaussian distribution. The state characteristics are depicted by updating its parameters—mean and covariance. These methods efficiently manage general non-linearities and Gaussian noise. Particle filtering takes a more direct approach, representing the pdf non-parametrically with a set of samples or "particles," avoiding the need for an approximate analytical representation. These particles, each with an associated weight, are propagated to represent the evolving distribution, adjusting state and weight based on predicted responses and measurements. Nasrellah and Manohar (2011) explored dynamic state and parameter estimation in non-Gaussian noise scenarios using a particle filter with finite element models, demonstrating their approach on structures analysed with diagnostic loads [151]. Sen,

et al. (2017) applied particle-based stochastic filters for localizing acoustic emissions in plates, using Bayesian methods to incorporate various uncertainties [152]. Wan*, et al.* (2018) developed a particle filter for identifying augmented states and unknown inputs, combining standard particle filtering with least squares for simultaneous estimation [153].

In summary, particle filtering and its variants offer robust alternatives to parametric filters like EKF, with a broad application range from structural analysis to state and parameter identification, even in complex and noisy environments. Particle filter stand out for flexibility in handling non-Gaussian noise and the ability to incorporate unknown inputs into filter's estimations.

2.2.5 Gaussian process

Gaussian process (GP) models have gained significant traction in ML for their ability to address complex problems. GP stands out as a Bayesian approach that defines a prior distribution over function spaces, rather than relying on the physical structure of the system [154-156]. This non-parametric method uses Mercer kernel functions within a Bayesian framework for probabilistic inference, enabling the modelling of function distributions based on defined mean and covariance functions. It provides mean predictions for test points, along with associated uncertainty levels like 95% confidence intervals. However, a limitation of standard GPs, known as homoscedastic GPs, assume a uniform noise level across the input space [157]. The detailed mathematical background of the GP is discussed in section 7.2.2.

To address this, the heteroscedastic GP (HGP), introduced by Goldberg*, et al.* (1997), assumes variable observation noise and seeks to model both mean and variance distributions [158]. In HGP, two models are used: one for estimating the mean and another for assessing log-noise power. HGP inference is more complex than standard GPs because its predictive posterior distribution also accounts for noise rates as independent latent variables, complicating the analytical handling of the predictive posterior distribution integral. Various numerical methods have been developed to address this challenge, including Markov chain Monte Carlo (MCMC), *maximum a posteriori* (MAP) HGP, sparse GP (GPz), and most likely HGP. MCMC approximates the posterior distribution but is computationally intensive, especially for large datasets [158]. Kersting*, et al.* (2007) used a most likely noise approach, which maximizes likelihood through an iterative process similar to Expectation

Maximization updates, though it may not always converge [159]. Recently, Almosallam, *et al.* (2016) introduced GPz for heteroscedastic uncertainty estimation, using a Bayesian machine learning approach for joint optimization of predictive mean and variance [160]. This model accounts for intrinsic uncertainty due to data density and uncertainty due to training data limitations.

In the field of SHM, applications of GP are relatively sparse. Hensman, *et al.* (2010) demonstrated the use of GP for acoustic emission (AE) source in complex structures using thermoelastic expansion and high-power lasers, simplifying damage detection without the need for complex basis function placement [161]. The GP model, employing radial basis function (RBF) kernels, was trained for relationship regression using time differences across various sensor combinations as inputs and AE source locations as outputs. This model successfully learned to map and generalize for effective prediction. Torres-Arredondo and Fritzen (2012) explored the monitoring of impact stress waves and developed an automated method for estimating impact magnitude and localization in isotropic structures using single-target GP in a Bayesian framework [162]. Anderson, *et al.* (2014) combined GP into structural dynamic framework employing spatial maps of frequency-domain features [163].

GP has also been applied as a prognostic tool in SHM. As a data-driven method, GP can predict system status under unobserved conditions or future scenarios based on monitoring data, beneficial for complex system. Mohanty, *et al.* (2009) proposed a life prognosis method using a nonlinear GP model to study the relationship between variables affecting fatigue and crack growth in metallic structures [164]. Liu, *et al.* (2010) developed a real-time approach to estimate the remaining useful life (RUL) of composite specimens, employing an offline GP model for cumulative fatigue damage estimation [165]. Mohanty, *et al.* (2011) later used GP regression (GPR) for damage progression prediction in aluminium specimens with cracks [166].

2.2.6 Support vector machine

Support vector machine (SVM) are among the most popular ML algorithms is used both as classifiers and regressors. The schematic presentation of SVM is shown in Figure 2.3. It functions by mapping data (linear or nonlinear) onto an n-dimensional feature space, where a hyperplane effectively separates different classes by maximizing the distance between them. The transformation of data into this higher-dimensional

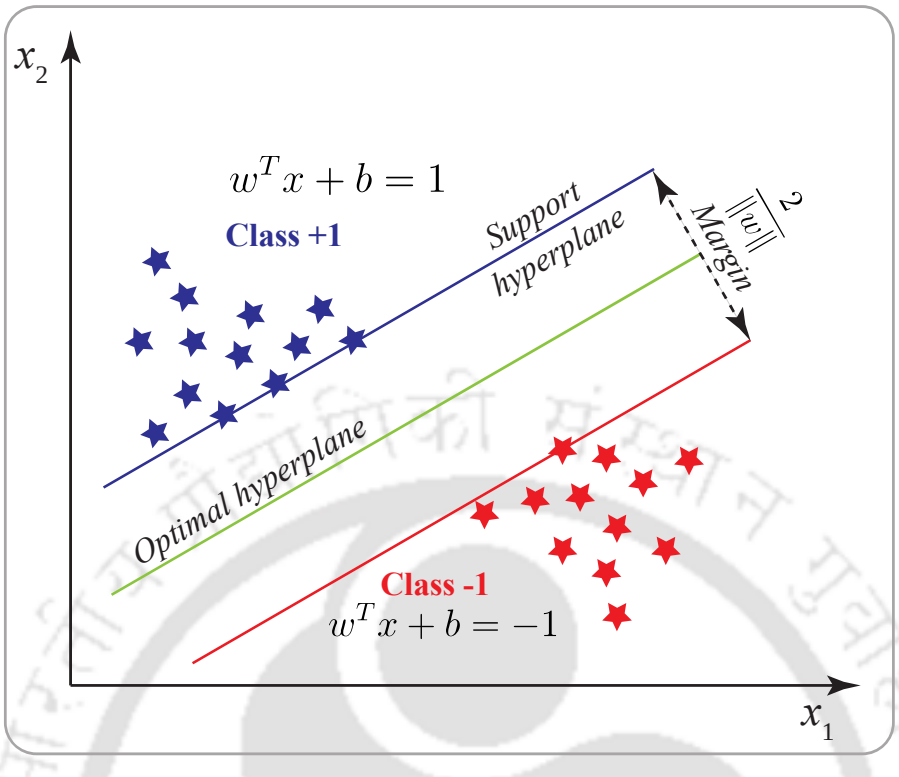

Figure 2.3 Concept of support vector machine.

space is facilitated by kernel functions, and the accuracy of SVM largely dependent on the appropriate choice of these kernels.

In SHM applications, where data features are both numerous and high-dimensional, SVM often outperforms over other supervised ML techniques with the correct kernel selection. This was demonstrated in studies carried by Lu, *et al.* (2020) and further supported by Gordan, *et al.* (2020), who successfully applied a polynomial kernel function for damage identification in slab-on-girder bridges, showing SVM's superiority over methods like classification and regression tree (CART) due to its capacity to perform high-quality predictions [167, 168].

However, SVM has its challenges; notably, training times can increase exponentially with larger data sets. To address this, the least-squares SVM (LS-SVM) was developed, which optimizes a set of linear equations instead of the quadratic programming approach used in traditional SVM. Deng, *et al.* (2021) applied LS-SVM in a hybrid model-driven and data-driven SHM system, demonstrating its effectiveness in assessing daily fatigue damage in highway bridge hangers using weigh-in-motion data and the SVM regressor function [169].

SVM also enhances DL in damage detection. One issue in DL is the potential misclassification of unlearned patterns as learned ones. Kohiyama, *et al.* (2020) validated a method using a deep NN and SVM to detect unlearned damage patterns in a steel frame structure [170]. Additionally, Chong, *et al.* (2014) proposed an efficient and precise nonlinear multiclass SVM for time-varying structures, trained with wavelet-based autoregressive coefficients from healthy and damaged structures [171]. Beyond these applications, SVM is versatile, also being useful in aspects like sensor placement optimization, data normalization, and feature extraction/selection, showcasing its extensive utility in various stages of machine learning procedures.

2.2.7 Artificial neural network

ANN techniques are inspired by the human brain's functioning and typically comprise at least three layers: an input layer, one or more hidden layers, and an output layer. ANNs with multiple hidden layers are known as multilayer perceptron (MLP). These networks function as optimization processes, adjusting network parameters such as weights biases to minimize a cost function [172]. This method is extensively utilized due to its ability to its adaptability to various inputs and outputs.

In feed-forward ANNs, independent variables at each input neuron affect processing and calculations at hidden and output layers. Training of ANN involves an error propagation algorithm, categorizing it as supervised learning. The mathematical background of ANN is presented in section 8.5.1. For instance, HekmatiAthar, *et al.* (2020) collected sensor data using both contact and contactless methods to detect damage on a scaled bridge model using ANN [173]. Another study by Malekjafarian, *et al.* (2019) employed a two-stage approach for bridge damage detection using vehicle responses [174]. The first stage involved training the ANN with backpropagation to predict the vehicle's response on the bridge. In the second stage, changes in the prediction error distribution were identified using a Gaussian process to indicate damage.

While MLP and backpropagation are common in civil infrastructure damage detection, unsupervised neural network like self-organizing map (SOM) are also used. SOMs show high-dimensional data in two-dimensional (2D) or three-dimensional (3D) maps while maintaining the original feature properties, differ from traditional ANNs as their training relies on the internal structure of inputs rather than target-defined input-output samples [175]. For example, Tibaduiza, *et al.* (2013) utilized SOM with

PCA data reduction in a two-stage process to classify damage on an aluminium plate [176]. Avci, *et al.* (2020) applied SOM to a grid structure, focusing on stiffness reduction and boundary condition changes for damage identification and quantification [177]. Despite their effectiveness, ANNs can be computationally demanding and time-consuming in training, which may limit their application in some SHM contexts.

In addition to ANN and MLP, a variety of both shallow and deep NN algorithms are found in research, though only a few are widely used in SHM. Convolutional NN (CNN) are currently the most prevalent DL approach in SHM, extensively discussed in several review papers [178-183]. However, there's growing interest in other deep NN methods, which, when combined with CNN, can offer enhanced results compared to using CNN alone.

A key area in many SHM systems is sequential data or time series analysis, where Recurrent Neural Networks (RNN) are particularly useful. Unlike conventional feed-forward ANNs, RNNs have an internal memory that allows them to loop outputs back into their predictions, maintaining a continuous sequence. This feature is advantageous in SHM for recognizing damage patterns, especially when correlations exist between various signal sources and external factors, such as environmental and operational factors (EOFs). For instance, Mousavi and Gandomi (2021) utilized RNN to track and predict temperature variations, showing that significant deviations in prediction errors could indicate damage [184]. Similarly, in another study by Mousavi and Gandomi (2021) used RNN to identify damage under EOF conditions when Johansen cointegration failed to find relationships among the frequency signals [185]. Despite performing well under noisy conditions, RNNs have challenges, including the risks of gradient vanishing and exploding, as noted by Zhang, *et al.* (2020) [186]. These issues can impede the learning process or destabilize the network, reflecting the need for careful management of network parameters in RNN applications.

To address the issue of gradient-vanishing in neural networks, the long short-term memory (LSTM) network was developed. This network type is designed to retain information over extended periods, enabling the learning of long-term temporal dependencies. Zhang, *et al.* (2019) were among the first to implement LSTM networks, particularly for modelling the seismic responses of highly nonlinear dynamic systems with limited data [187]. To manage the data scarcity, they employed K-means

clustering to divide the data for training and testing purposes. Their stacked LSTM network demonstrated effective performance, achieving prediction errors within ±10% with confidence levels of 91%, 86%, and 84%. However, this method required extensive computational resources, involving training over 50,000 epochs. Li, *et al.* (2021) introduced an innovative deep RNN encoder-decoder model that incorporated LSTM in a sequence-to-sequence (seq2seq) framework [188]. This model was applied for online SHM monitoring, particularly under seismic excitation, and proved to be effective in predicting dynamic responses for future earthquakes. When compared with seven other advanced methods for sequence learning and prediction, it showed a significant reduction in prediction error and standard deviation, by at least 13% and 15%, respectively. A notable limitation of LSTM, however, is its demand for considerable computational resources and lengthy training periods for optimal performance.

Gated recurrent units (GRU), a simplified version of the LSTM architecture with one lesser gate, offers easier and quicker training, particularly beneficial for smaller datasets. In specific contexts like detecting structural damage in offshore wind turbine blades, GRU has proven to be more accurate than LSTM and stacked LSTM, with improvements in accuracy ranging from 10 to 30%, as evidenced in a research by Choe, *et al.* (2021) [189]. To overcome the limitation of traditional RNNs, which only use past input data for current output predictions, bidirectional RNNs were developed. These networks incorporate both past and future input data for each time step, enhancing prediction accuracy. Tian, *et al.* (2021) employed this concept in a bidirectional LSTM model that successfully linked girder vertical movement with cable tension, achieving a notable relative root mean square error of 3.24% while maintaining stable performance in diverse conditions [190]. However, despite their advantages, bidirectional deep neural networks are not extensively used in SHM. Their limited adoption might stem from the need to have the entire data sequence before prediction and the significant computational resources required to operate these sophisticated models, a challenge particularly pronounced in contrast to their prevalent use in natural language processing (NLP).

Generative adversarial network (GAN) represents a unique deep NN framework composed of two parts: a generator and a discriminator-that are trained simultaneously through adversarial processes as shown in Figure 2.4. The generator

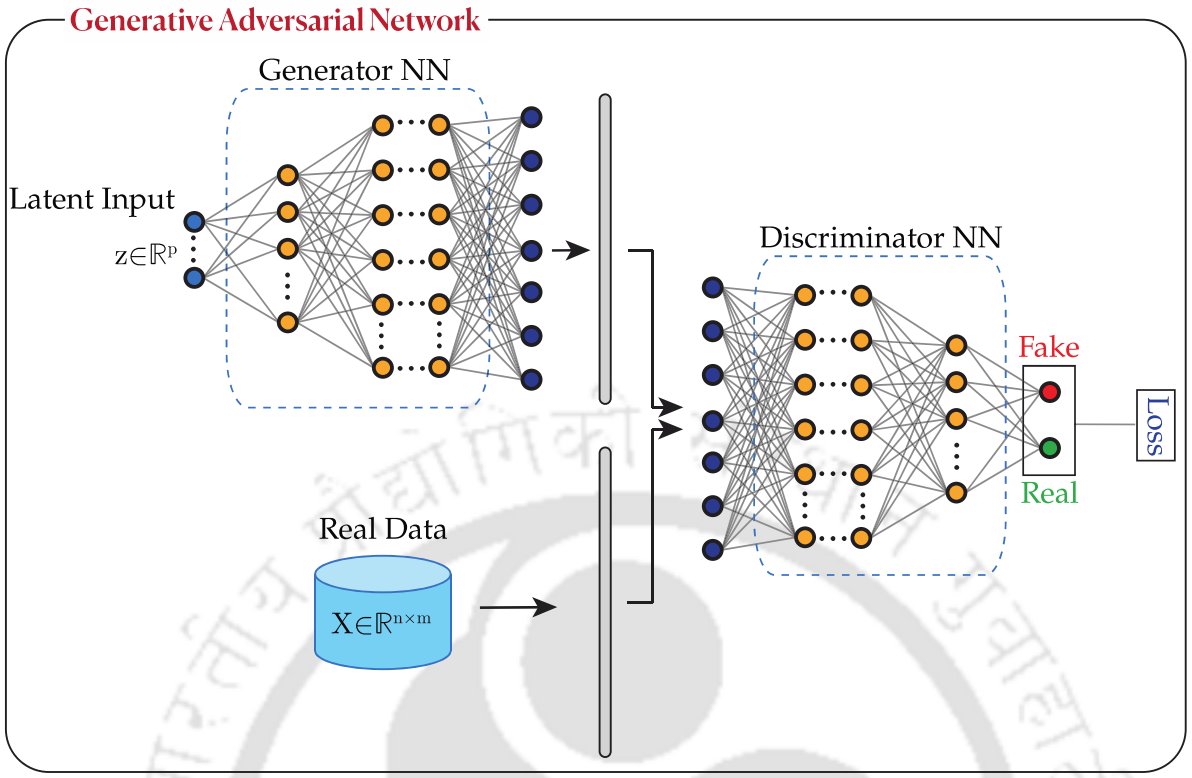

Figure 2.4 General architecture of GAN.

creates new data instances from random noise while the discriminator tries to distinguish between real and synthetic data. The generator aims to produce data that the discriminator will classify as real [191]. The discriminator enhances the generator's ability to produce realistic outputs through this process. Ideally, by the end of training, the generator should be effective at simulating the true data distribution, making it challenging for the discriminator to differentiate between real and fake data. The training is deemed successful when both networks achieve a Nash equilibrium, where neither can improve unilaterally. Tsialiamanis, *et al.* (2020) explored the application of GANs in SHM systems, showing their potential to discern damage characteristics, even in the presence of extraneous factors, using both categorical and continuous variables [192]. This makes GANs a promising tool for managing large datasets in SHM. Recently, Fan, *et al.* (2021) demonstrated GAN's utility in reconstructing structural dynamic responses under various conditions, such as ambient or seismic excitations [193]. While the primary focus was not on damage detection, their findings suggest GAN's potential in this area, as evidenced by a significant reduction in reconstruction error (15.7%) compared to traditional CNN models (69%). This indicates that GANs could significantly enhance SHM systems by

effectively identifying damage through advanced data analysis and reconstruction techniques.

2.2.8 Deep autoencoder neural network

The deep autoencoder network focuses on discovering a low-dimensional space where data instances can be effectively reconstructed. It is commonly used for data compression or dimensionality reduction [194, 195]. The underlying strategy for employing this method in anomaly detection is that by learning key regularities within the data, the feature representations are optimized to minimize reconstruction errors. Consequently, anomalies, which do not conform to these regular patterns, are harder to reconstruct and therefore stand out due to their larger reconstruction errors. The mathematical background of deep autoencoder is explained in section 5.2.

The introduction of various regularized autoencoders designed to capture more complex and informative feature representations [196-199]. For instance, sparse autoencoders are trained to promote sparsity within the hidden layers' activation units, such as by retaining only the most active units [196]. Denoising autoencoders focus on learning representations that are stable against minor variations by reconstructing data from intentionally corrupted data instances [197]. Contractive autoencoders go a step further by learning features that are insensitive to small shifts in data points, accomplished by incorporating a penalty term derived from the Jacobian matrix of the encoder activations [198]. Variational autoencoders introduce a prior distribution over the latent space for regularization, which helps prevent overfitting and ensures generative properties for creating meaningful data instances [199].

Autoencoders are relatively straightforward to implement and intuitively appealing for anomaly detection, leading to extensive exploration in research. The Replicator neural network is a pioneering model in this domain, using a multi-layer perceptron structure to detect anomalies in static, multidimensional data by effectively clustering data points [200]. Subsequent research has sought to improve upon this approach. RandNet, for instance, employs an ensemble of autoencoders with random dropout connections and adapts the training batch size dynamically, specifically catering to tabular data [201].

Beyond tabular data, autoencoders are utilized for anomaly detection in sequence, graph, and image/video data [202]. Adapting to these complex data types involves

either modifying the network architecture to fit the data, as seen with CNN-autoencoder, LSTM-autoencoder, Conv-LSTM-autoencoder, and graph convolutional network-autoencoder, or using autoencoders to learn low-dimensional representations and then predicting these learned representations in two distinct steps [203-206].

2.2.9 Physics informed machine learning

Physics-informed machine learning (PIML) efficiently combines physics-based insights with data from imperfect or noisy datasets, especially in forward and inverse problem-solving. This approach excels even with limited or noisy data, which is notably evident in SHM, where the conventional techniques may fail to produce meaningful results [207]. The integration of physics knowledge into ML not only aligns results with physical laws and thereby reducing computational efforts, but also facilitates learning from unlabelled or incomplete data sets [208]. One instance of this approach's success is the use of physics-informed NN (PINN) in SHM problems involving partial differential equations (PDEs), such as the Euler–Bernoulli beam equation [209]. The schematic illustration of PINN is shown in Figure 2.5. Section 8.5.2 discusses the mathematical background of PINN. Despite limited or noisy data, PINN demonstrated superiority over traditional data-driven methods, with a maximum error of 1.9%, compared to 30.3% error in conventional approaches. Similarly, the

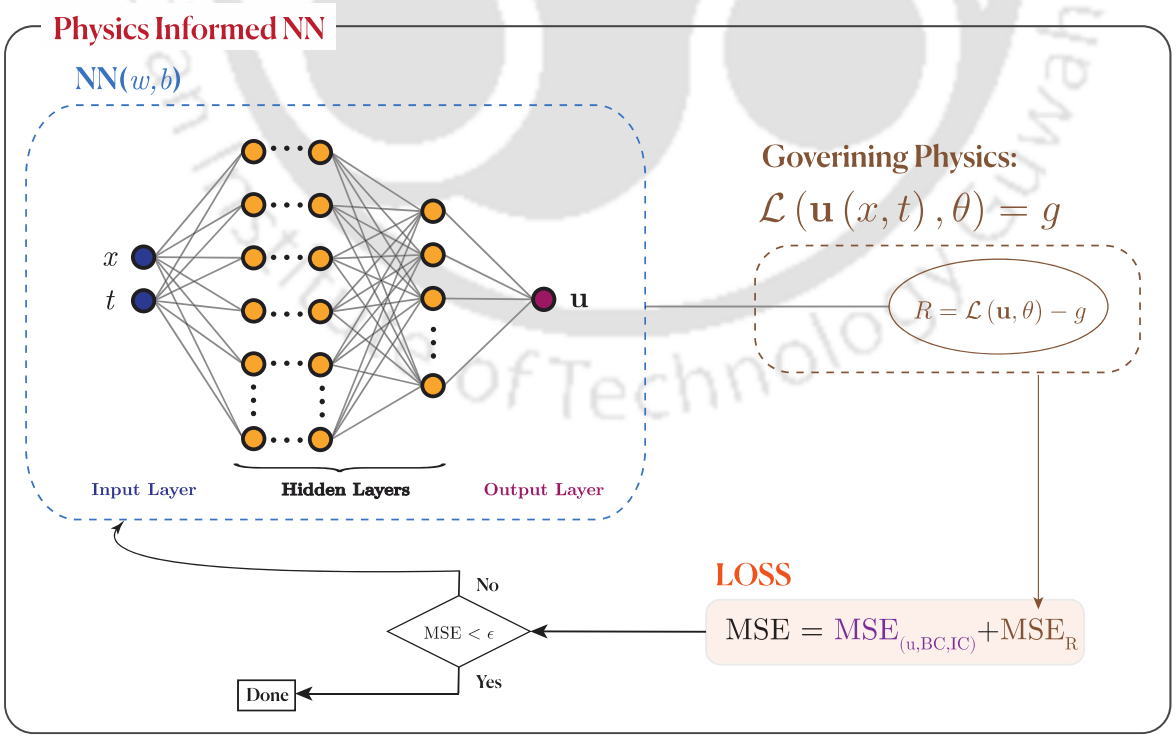

Figure 2.5 Schematic illustration of PINN.

physics-informed Gaussian process (PIGP) outperforms in modelling non-linear functions under data constraints. Gaussian processes (GP), characterized by mean and covariance functions aligned with physical laws, effectively capture complex patterns and manage missing or corrupted data [210-212]. For instance, Jones, *et al.* (2023) implemented a PIGP for acoustic emission (AE) time maps, enhancing predictive accuracy by incorporating physical constraints [213]. This method ensured physically consistent predictions by including information about structural geometry and boundary condition in the learning process. Another application of PIGP employed to predict structural responses considering the factors such as temperature and traffic loading effects on the Tamar Bridge situated in the West of England [214]. By integrating physics-based insights into the prior mean function, the model's predictive accuracy was significantly improved compared to using a GP alone. These examples highlight the effectiveness of PIML in handling complex and real-world SHM problems, particularly when data quality is a challenge.

The Bayesian PINN (B-PINN) acts similar to the PIGP, is effective at handling high-dimensional challenges in the presence of noisy and incomplete data sets. In the study done by Yang, *et al.* (2021) merges the Bayesian NN (BNN) with PDE constraints, serving as a prior framework for the model [215]. Further, the authors highlighted the effectiveness of B-PINN where it excelled in generating accurate predictions despite the presence of significant noise and spurious elements in the data. This method is particularly promising for SHM applications and addresses the issues that arise from the inherent stochastic nature of data in high-dimensional and noisy datasets. B-PINN's robustness in such scenarios marks it as a valuable tool in the field of SHM.

The challenge of handling high-dimensional data, known as the “curse of dimensionality,” presents significant difficulties for conventional ML techniques, often leading to their failure to fit and predict reliable outcomes. When DL is fused with insights from physics that emerges as a potent solution to this challenge. This integration presumes that the desired function comprises hierarchical composites of local functions [216, 217]. By applying physical laws or symmetries to ML, the dimensionality of the dataset can be effectively reduced, facilitating more accurate feature representation. Training models with limited data but without any physical constraints or domain expertise can lead to results that are physically inconsistent or

exhibit good local accuracy but poor generalization [218]. Alternatively, physics-informed autoencoders have been utilized, where physical laws are integrated into the loss function. This method enhances the performance and robustness of models, even with noisy and limited high-dimensional data, and it can also reduce computational costs. Jagtap, *et al.* (2020) introduced a conservative PINN (cPINN), which partitions a domain into sub-domains where separate neural networks operate and interact through boundary conditions at the interfaces [219]. This method ensures the continuity of the solution and the conservation of physical quantities across different regions, improving the efficiency of the model, particularly for complex problems involving nonlinear conservation laws. Similarly, the extended PINN (XPINN) approach divides both spatial and temporal domains [220]. It offers benefits like parallel processing and efficient hyperparameter optimization, making it suitable for multi-scale and multi-physics problems and addressing the curse of dimensionality in high-dimensional problems [221].

The recent advancement of the separable PINN (SPINN) further reduces computational demands for solving multi-dimensional PDEs [222]. SPINN employs separate sub-networks for each one-dimensional coordinate, which are combined to produce the output. This method was demonstrated to save significant time—up to 98% compared to traditional PINN methods—while maintaining accuracy, as seen in its application to the Klein–Gordon equation.

The process of collecting data for SHM is often slow, costly, and resource-intensive. DL models typically require large amounts of data to achieve satisfactory results and generalization, benefit significantly from the PINN approach when only limited data are available. In PINN models, physics can be integrated into the network as a soft constraint and effectively increasing the dataset size [223]. For instance, Zhang, *et al.* (2019) employed a physics-informed DL framework to create a metamodel that accurately simulates nonlinear structural responses to seismic activity using multi-layer LSTM networks [187]. This framework successfully predicted structural responses and non-observable nonlinear state variables, even with limited data.

GANs have been employed for the reconstruction of structural responses, but effectiveness depends on the variety of the input data [224, 225]. The GAN can learn better and generalize from the dataset when more diverse real data are provided. However, GANs may encounter issues when the discriminator becomes optimal,

leading to a diminishing gradient for the generator and failure in learning. To counteract this, a physics-informed GAN (PI-GAN) has been developed, which incorporates physical laws and invariance properties into its framework to avoid training collapses and improve scalability. Physical constraints are added to the generator's loss function, which not only prevents the vanishing gradient issue but also expedites the convergence of the generator, facilitating the discriminator in reaching a state of equilibrium more efficiently.

In the context of SHM, sensor data from various points on a structure are used to gather comprehensive information. Moreover, as mentioned in a study by Yang, *et al.* (2019), adding more stochastic variables to the model also scales up computational demands [226]. The authors in this study address this by applying a domain decomposition approach within the PI-GAN framework, utilizing one generator and several discriminators, each assigned to a different subdomain. This method enables each discriminator to focus on the sensor data relevant to its subdomain, optimizing the learning process.

Furthermore, another method for enhancing datasets is through extrapolation. PINNs have shown capabilities for spatial extrapolation to a certain degree, potentially widening the scope of the dataset [215]. Nonetheless, extrapolation in ML is generally not recommended due to the necessity for careful consideration of model assumptions and limitations. Extrapolation can lead to unreliable predictions if the model steps too far outside the range of data it was trained on.

2.3 Summary of Literature Review and Research Gaps

A comprehensive review of prior studies has presented on guided wave based SHM, and on various pattern-recognition algorithm used in SHM. This review led to identification of research gap on anomaly detection and system identification when noisy measurements available. Based on the review, numerous examples are available for damage detection and system identification of various civil and mechanical structures without diagnosing the sensors used. The previous research have not adequately established the extension of research on diagnosing the sensors in the SHM framework and development of inversion algorithm for noisy/uncertain data.

Despite significant advancements, several gaps remain in the current research, which this thesis aims to address:

- There is limited research on SHM techniques specifically for piezoelectric materials, despite their widespread use in sensors and actuators.
- Existing studies often struggle with the complexities of guided wave propagation in anisotropic composite materials due to their directional dependence and heterogeneity.
- There is a lack of robust hybrid models that effectively integrate physics-based principles with data-driven ML algorithms for SHM.
- Current SHM practices often do not adequately account for uncertainties in measurement and modelling, leading to less reliable predictions.

To this end, a research effort for the condition assessment of plate structures is undertaken as the research problem. This dissertation presents several studies on advanced data-driven and ML frameworks for damage detection and system identification of piezoelectric transducer and composite laminate with noisy/uncertain measurements. The developed frameworks rigorously tested by performing experiments, and the same is presented in the subsequent chapters.

Chapter 3

Experimental Setup

This chapter outlines the experimental methodologies utilized in the research, focusing on addressing critical gaps in SHM by developing frameworks for advanced materials like piezoelectric substrates and carbon composites. The experimental techniques aids in acquiring meaningful data for monitoring these advanced materials. A novel experimental technique known as the point contact method is presented for the excitation and detection of ultrasonic waves in piezoelectric materials. This technique is significant because it offers an efficient method to study wave propagation in piezoelectric materials, which are extensively used in various engineering applications. However, its application is limited to piezoelectric materials. To acquire comprehensive wavefield data for carbon composite laminates, a scanning laser Doppler vibrometer (SLDV) is employed. The SLDV provides non-contact, high-resolution measurements of surface vibrations, making it an ideal tool for studying wave propagation in complex anisotropic materials like carbon composites. These methods are elaborated upon in the subsequent sections of the chapter. Based on the data acquired through these experiments, the study conducts damage detection and parameter estimation on piezoelectric and carbon composite materials.

3.1 Point Contact Method

The innovative experimental technique for point contact excitation and detection is based on Coulomb coupling and is designed for the excitation and detection of ultrasonic waves in a piezoceramic. A Coulomb coupling technique is based on electro-mechanical excitation to generate an electric field that induces stress waves. The experimental method was designed for effective electric field coupling with elastic modulus and permittivity of piezoceramics. The experimental setup for point contact

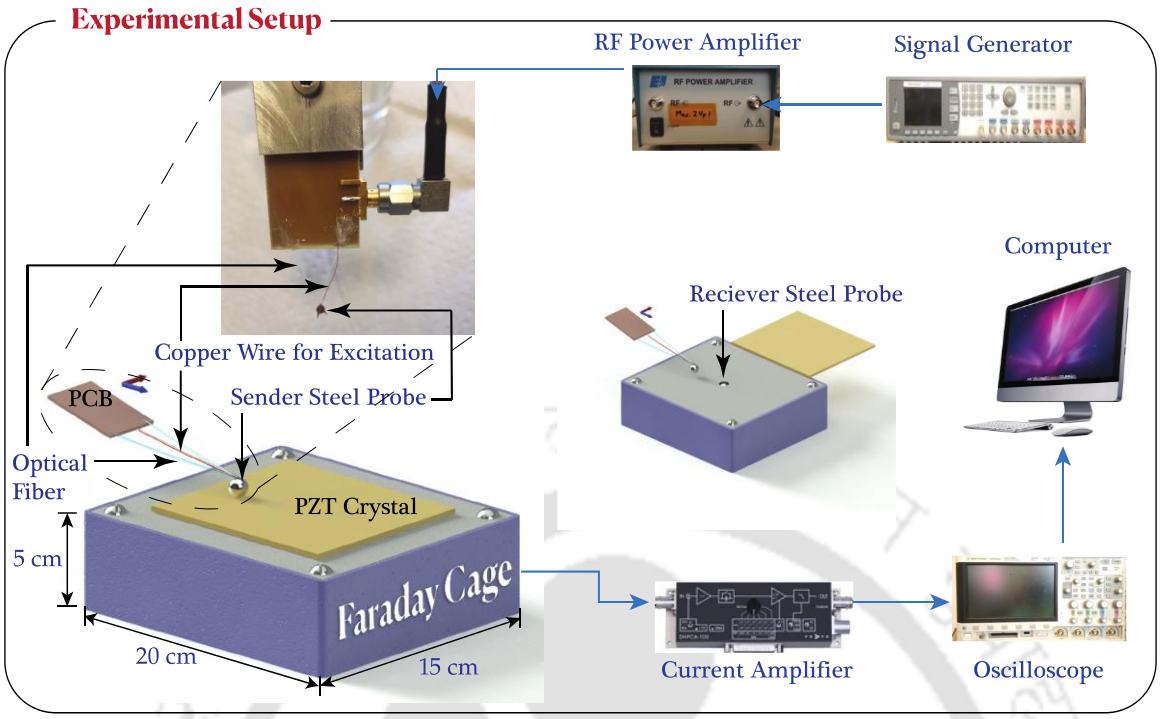

Figure 3.1 Experimental setup for point contact excitation and detection method.

excitation and detection in PZT ceramic sample is depicted in Figure 3.1. A comprehensive overview of the excitation and detection probes fabrication, as well as the experimental setup can be found in [227-229].

The excitation pulse, approximating a Dirac delta function with a time width of 70 ns was produced using an off-the-shelf function generator (Agilent 81150A). The excitation signal was routed to a radio-frequency (RF) amplifier (Electronics and Innovation: 403LA, New York, USA) for signal amplification. The amplified signal was sent to the excitation steel probe. The steel sphere made gentle contact with the sample's surface. The excited signal produced the acoustic waves in the PZT ceramic specimen. An identical steel sphere was employed on the opposite side of the PZT ceramic plate specimen to acquire the propagated signal, which was then amplified by a trans-impedance amplifier (DHPCA-100). A trans impedance amplifier of this kind transforms current into voltage using an adjustable amplification factor. Finally, the amplified signal was captured using an oscilloscope (Agilent 3024A) capable of digitising up-to 12 bits. The data collection sampling interval was 25 ns. The oscilloscope averages 256 pulse shots and digitises the signal, which is then saved in a personal computer (PC) via a USB port. The PC also controls the mechanical scanner

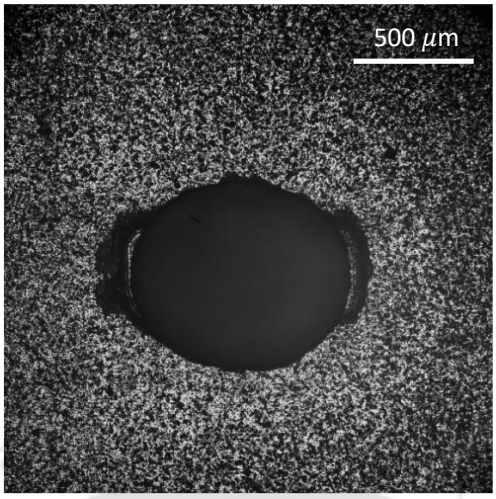

Figure 3.2 Optical image for the surface flaw of the PZT ceramic sample. The size of the defect is 1.2 mm × 1.3 mm and 1.5 mm in depth.

in the XY plane, i.e., the step size is 50 μm in both directions and a scanning area of 10 mm × 10 mm.

The objective of the experiment was to visualise the wave propagation in the PZT sample and localise the defect in the sample. At first, a healthy PZT sample as a reference was placed in the experimental setup, and the measurement was performed. Following the completion of healthy state experiment, a calibrated damage was introduced on the surface of PZT ceramic with a high-speed diamond drill. The damage was approximately 1.2 mm × 1.3 mm and 1.5 mm in depth. The optical image of the drilled PZT, acquired by a microscope (Olympus) with a 4x objective lens in reflection mode, can be seen in Figure 3.2. The interaction of the ultrasonic wave with the damage was visualised by performing the experiment again.

Closing this section, it is worth mentioning that the limit of the point contact excitation and detection method primarily depends upon few parameters, that is, the diameter of the probe, time gating of the excitation pulse, to mention a few. The obtainable resolution of the Coulomb excitation method as mentioned in the study carried by Habib, *et al.* (2007) is $\lambda/_2$, where λ is the acoustic wavelength [230]. Further, it is mentioned that to obtain a resolution equivalent to Abbe limit, the approximate diameter of the probe is given as $D = \lambda/_{0.24}$. While scanning the PZT sample, the resolution equivalent to the diffraction limit is computed approximately as 308 μm.

3.2 Scanning Laser Doppler Vibrometer

Analysis of guided wave propagation was conducted on a carbon/epoxy laminate, reinforced with 16 layers of plain weave fabric. The specimen was fabricated using GG 205 P prepregs (comprising Toray FT 300–3K 200 tex fibres) from G. Angeloni and IMP503Z-HT epoxy resin from Impregnatex Compositi in an autoclave. The composite laminate measured 1200 × 1200 mm with an average thickness of 3.9 ± 0.1 mm.

The total weight of the specimen was 8550 g, yielding a density of approximately 1522.4 kg/m³ based on its volume. The geometric and other parameters for the plain weave textile-reinforced composite are discussed in details in Chapter 7.

The experimental setup, as shown in Figure 3.3, included a waveform generator, signal amplifier, piezoelectric actuator, specimen, and scanning laser Doppler vibrometer (SLDV) head operated by controller and software. A 10 mm diameter piezoelectric transducer disc was affixed to the specimen's centre. A chirp signal with

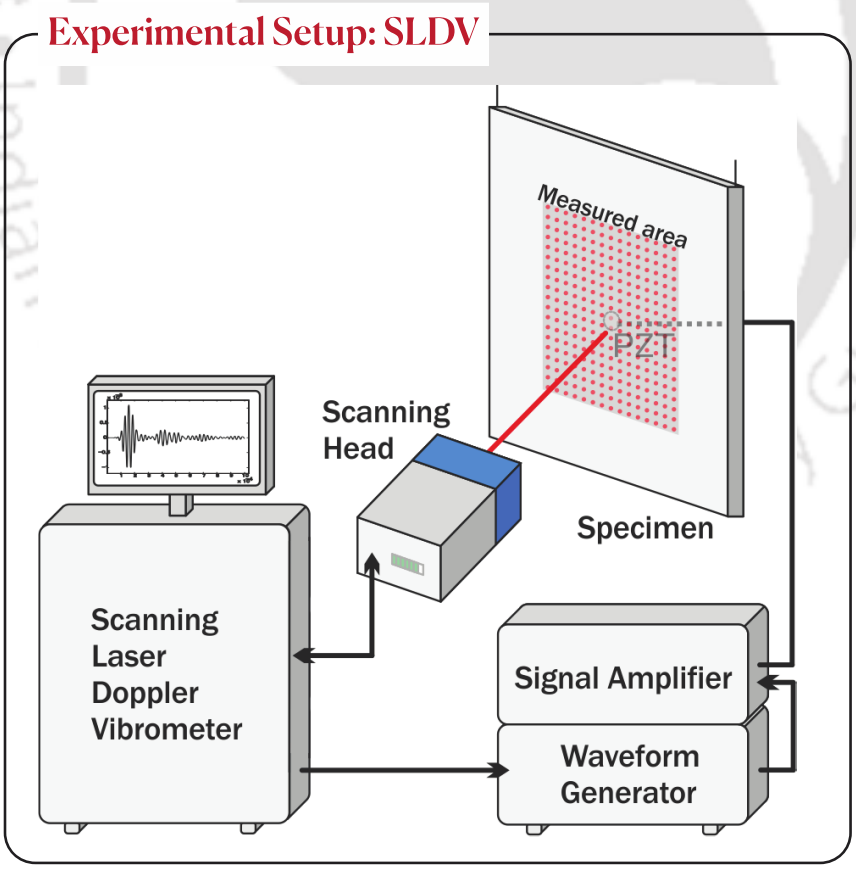

Figure 3.3 Illustration of experimental setup used to acquire full wave-field data in woven fabric reinforced carbon composite laminate.

a frequency range of 0–500 kHz lasting 200 μs was applied to the piezoelectric transducer at a sampling frequency of 1.28 MHz. Full wavefield measurements of guided waves were taken using an SLDV (Polytec PSV-400) over a central area measuring 0.726 m by 0.726 m. A grid with 499 × 499 measurement points covered the specimen's surface. Retro-reflective tape was applied to enhance the laser signal quality. Measurements were acquired 40 times at each grid point and averaged to enhance the signal-to-noise ratio.

Chapter 4

Anomaly Detection in PZT Sensor using mrDMD

The performance of piezoelectric sensors deteriorated due to the presence of defect, delamination, and corrosion that needed to be diagnosed for the effective implementation of the SHM framework. A novel experimental approach based on Coulomb coupling is devised to visualise the interaction of ultrasonic waves with microscale defects in the Lead Zirconate Titanate (PZT). mrDMD technique in conjunction with image registration, and Kullback Leibler (KL) divergence is utilised to diagnose and localise the surface defect in the PZT. The mrDMD technique extracts the spatiotemporal coherent mode and provides an equation-free architecture (i.e., the governing equation of the system dynamics may actually be unknown) to reconstruct underlying system dynamics from the data. Additionally, due to the strong connection between mrDMD and Koopman operator theory, the proposed technique is well suited to resolve the nonlinear and dispersive interaction of elastic waves with boundaries and defects. The mrDMD sequentially decomposes the three-dimensional (3D) spatiotemporal data into low and high frequency modes. The spectral modes are sensitive to defects based on the scaling of wavelength with the size of the defect. The error due to offset and distortion was minimised with ad hoc image registration technique. Further, localisation and quantification of defect are performed by evaluating the distance metric of the probability distribution of coherent data of mrDMD acquired from healthy and defected samples. In the arena of big-data that is ubiquitous in SHM, this chapter demonstrates an efficient damage localisation algorithm that explores the nonlinear system dynamics using spectral multi-mode resolution techniques by sensitising the damage features.

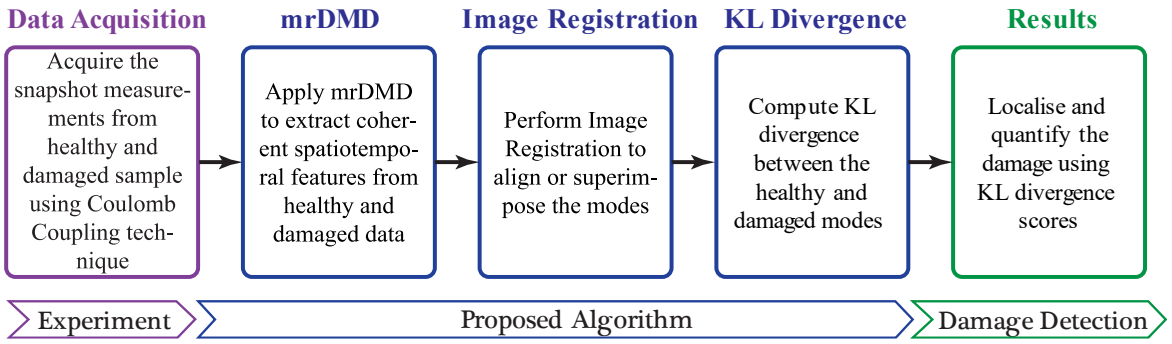

Figure 4.1 Flowchart of the proposed novel damage detection framework

4.1 Proposed Scheme

We propose an advanced damage detection method based on mrDMD [231], image registration, and KL divergence [232]. The mrDMD algorithm is an extension of DMD with multiresolution analysis (MRA) in time. The mrDMD is ideally suited for the decomposition of complex waveforms and extract coherent spatiotemporal features.

The proposed damage detection algorithm has numerous advantages for high dimensional wave field images acquired by the Coulomb coupling technique. At the very outset, the data-driven and equation-free framework of the mrDMD algorithm reconstructs the underlying dynamics alone from the snapshot measurements [97, 100, 233, 234]. Additionally, due to the strong connection between mrDMD and Koopman operator theory, the proposed technique is well suited to resolve the nonlinear and dispersive interaction of elastic waves with boundaries and defects [98, 107, 109, 235]. Finally, one can modify the DMD algorithm to take advantage of the sparse or limited measurement of the complex system [236, 237]. The experimental method based on the Coulomb Coupling technique is a well suited method for the detection of surface cracks. Further, the proposed novel damage detection algorithm is a data-driven and equation-free technique. Recently data-driven breakthroughs are transforming how we detect, model and control damages in the SHM framework. Most of the techniques available are based on empirical models or derivation based on first principles. In SHM, the systems depict as nonlinear, high-dimensional, dynamic, and multi-scale in space and time. With unprecedented accessibility of data and expanding computational resources make the novel data-driven algorithm robust and ease of use in real-life scenarios. The algorithm is divided into two-phase, i.e., (i) spatiotemporal feature extraction using mrDMD, and (ii) damage localisation using distance measure of the probability density of 2D wavefield image data-set of healthy state and damaged

state. The advantages mentioned above of mrDMD combined with image registration and KL divergence mandate the developed data-driven algorithm as robust, accurate and computationally viable for the SHM framework. The schematic representation emphasising the damage-detection algorithm comprising of mrDMD, Image registration and KL divergence is shown in Figure 4.1. While the presented work focuses on the data driven multi-resolution extension of DMD i.e., mrDMD, it is important to note the underlying theory behind modal decomposition techniques as a whole.

4.2 Singular Value Decomposition

In DMD, as well as other decomposition techniques like POD, the Singular Value Decomposition (SVD) is the core mathematical technique used to extract low-rank patterns from high-dimensional data. The SVD is a well-known, robust, numerically stable, and efficient method for data-driven matrix decomposition that is commonplace in engineering and scientific applications. Since SVD is the driving force of the DMD and mrDMD algorithms, it is worthwhile to briefly explore the SVD. The SVD is formally defined as

$$\mathbf{X} = \mathbf{U}\mathbf{\Sigma}\mathbf{V}^{*}, \tag{4.1}$$

where $\mathbf{X}$, is a general $n \times m$ matrix, $\mathbf{U}$ is an $n \times m$ matrix comprised of the left singular vectors, $\mathbf{\Sigma}$ is an $m \times m$ diagonal matrix containing the singular values, and $\mathbf{V}^{*}$ is an $m \times m$ matrix containing the right singular vectors. Matrices of these sizes allow for the most efficient computation of the SVD since only the first m non-zero singular values are considered, and as such this method is called the 'economy sized' SVD. It should be noted that $\mathbf{U}$ and $\mathbf{V}$ matrices are both unitary and have orthonormal columns, and $\mathbf{\Sigma}$ only contains positive, real valued entries. The $\mathbf{U}$ and $\mathbf{V}$ matrices provide a column basis and row basis of the original $\mathbf{X}$ matrix, and can be thought of as storing the column and row patterns from the original matrix respectively. When regarding a time-series of snapshots, the left singular vectors can be thought of as containing the spatial patterns of the snapshot series, while the right singular vectors contain the temporal patterns.

4.3 Multiresolution Dynamic Mode Decomposition (mrDMD)

The DMD represents a way to approximate the dynamics of a non-linear system through a finite dimensional linear operator [238]. To successfully implement the DMD method, the dynamical system being examined is modelled as the differential equation,

$$\frac{d\mathbf{x}}{dt} = \boldsymbol{\mathcal{F}}\mathbf{x}, \tag{4.2}$$

here, $\mathbf{x}$ represents the current state of the system and $\boldsymbol{\mathcal{F}}$ represents the linear model of the continuous time dynamics. This form of differential equation can be solved with the eigenfunction expansion method, yielding a solution with the form:

$$\mathbf{X}(t) = \sum_{k=1}^{n} \phi_k \exp(\omega_k t) b_k = \boldsymbol{\Phi} \exp(\boldsymbol{\Omega}\mathbf{t})\mathbf{b}, \tag{4.3}$$

where ϕ_k and ω_k are the eigenvectors and eigenvalues of the matrix $\boldsymbol{\mathcal{F}}$, the coefficients b_k are the coordinates of the system's initial conditions, $\mathbf{x}(\mathbf{0})$, projected onto the eigenvector basis, and n represents the bound on dimensionality introduced by the discretization of the dynamical system into n spatial points.

To discuss the mathematical background of mrDMD, let us assume $\mathbf{S}$ be a matrix that represents a collection of two dimensional (2D) snapshots given in (4.4). The spatial dimension of each snapshot is $p \times q$, and there exists M number of such snapshots along the time axis. It is possible to unwrap each frame to a higher dimensional matrix, for instance, $N-$dimensional ($N = p \times q \gg 1$) column vector of a large data matrix $\mathbf{X}$. Corresponding to each frame, the columns of $\mathbf{X}$ are sampled regularly at Δt in time as given in (4.5).

$$\mathbf{S} = [\mathbf{i}_{t_1}, \mathbf{i}_{t_2}, \dots, \mathbf{i}_{t_M}]_{(p\times q)\times M}, \tag{4.4}$$

$$\mathbf{X} = [\mathbf{x}_1, \mathbf{x}_2, \dots, \mathbf{x}_M]_{N\times M}, \tag{4.5}$$

To apply DMD, we can arrange the data matrix $\mathbf{X}$ into two matrices $\mathbf{X}_1$ and $\mathbf{X}_2$ as given in (4.6) and (4.7).

$$\mathbf{X}_1 = [\mathbf{x}_1, \mathbf{x}_2, \dots, \mathbf{x}_{M-1}]_{N\times(M-1)}, \tag{4.6}$$

$$\mathbf{X}_2 = [\mathbf{x}_2, \mathbf{x}_3, \dots, \mathbf{x}_M]_{N\times(M-1)}, \tag{4.7}$$

The DMD algorithm assumes that there exists a best-fit linear operator $\mathbf{F}$ relating both the $\mathbf{X}_1$ and $\mathbf{X}_2$ matrices as given in (4.8).

$$\mathbf{X}_2 = \mathbf{F}\mathbf{X}_1, \tag{4.8}$$

where, $\mathbf{F} = \exp(\mathcal{F}\Delta t)$ represents the system dynamics and is also referred to as the Koopman operator [231]. The matrix $\mathbf{F}$ can be computed by pseudo-inverse or eigen decomposition as given in (4.9).

$$\mathbf{F} = \underset{\mathbf{F}}{\operatorname{argmin}} \|\mathbf{X}_2 - \mathbf{F}\mathbf{X}_1\|_2 = \mathbf{X}_2\mathbf{X}_1^{\dagger}, \tag{4.9}$$

where, $\|\cdot\|_2$ is the Frobenius norm and $\dagger$ denotes the Moore-Penrose pseudo-inverse.

An important assumption when using DMD is that the individual snapshots $\mathbf{x}_k$ in the matrix $\mathbf{X}$ are high dimensional, making the matrices $\mathbf{X}_1$ and $\mathbf{X}_2$ tall and skinny. This assumption is usually valid when using snapshots generated from the Coulomb coupling technique, where the number of spatial points N is typically $\mathcal{O}(10^6)$ and above,while the number of snapshots M is typically $\mathcal{O}(10^2)$ to $\mathcal{O}(10^3)$ at most. If $\mathbf{F}$ were to be directly computed from the matrices $\mathbf{X}_1$ and $\mathbf{X}_2$ of this size, the number of elements in $\mathbf{F}$ would be $\mathcal{O}(10^{12})$ or higher. Thus, a direct computation of $\mathbf{F}$ is intractable when N is large. The DMD method takes advantage of the fact that $M \ll N$, which in turn means that the matrix $\mathbf{F}$ is at most rank $M-1$. A low rank subspace can be defined by a set of $M-1$ POD spatial modes, and within this subspace a low rank representation of $\mathbf{F}$ can be computed. This low rank representation, defined as $\widetilde{\mathbf{F}}$, contains at most $(M-1)^2$ elements, but still accurately captures how the dynamics of the system evolve across snapshots. The low rank dynamics are then reprojected into the full dimensions spanned by the dataset. This full dimensional reprojection of $\widetilde{\mathbf{F}}$ contains an accurate reconstruction of the leading, dominant eigenvalues and eigenvectors of the original $\mathbf{F}$ matrix. Therefore, the DMD method can accurately capture the behaviour of the $\mathbf{F}$ matrix, without an explicit computation of $\mathbf{F}$.

Further, to apply mrDMD, the samples of spatiotemporal data are selected such that all possible low and high-frequency contents are available. The mrDMD is a recursive approach of DMD, which extract the low-frequency features from the given spatiotemporal data. At first, the mrDMD removes m_1 modes and m_2 is the number of slow modes at level 1. The remaining modes are considered as the fast modes at level 1. Mathematically, mrDMD solution can be approximated as given in (4.10).

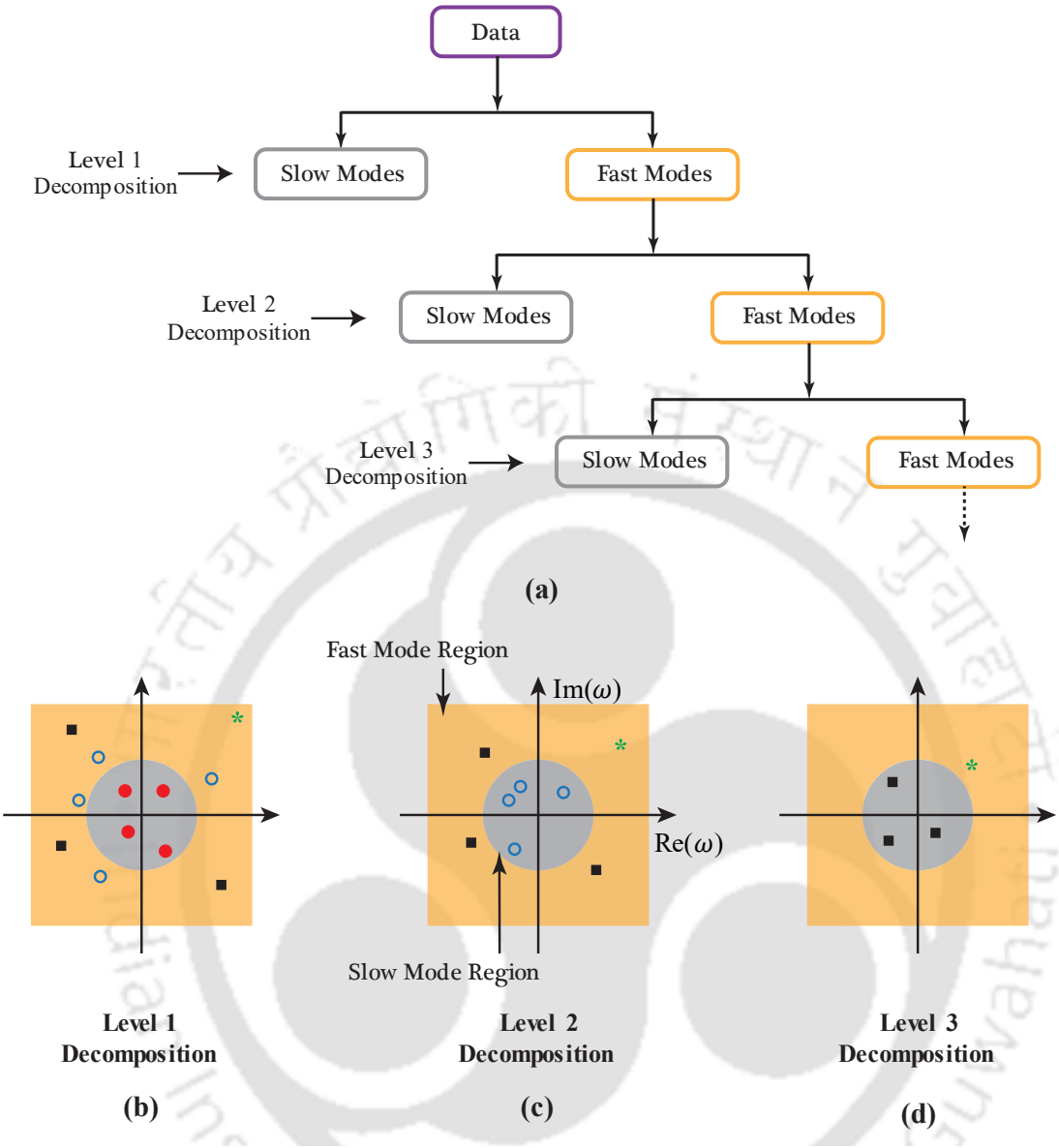

Figure 4.2 (a) The general structure of the mrDMD decomposition tree. Illustration of eigen value on a complex plane corresponding to the dynamic modes at b) level 1, c) level 2, and d) level 3 of decomposition. The yellow and grey shaded regions represent slow and fast mode region at that level respectively.

$$\mathbf{x}_{\text{mrDMD}}(t) = \underbrace{\sum_{k=1}^{m_1} b_k(0)\phi_k^{(1)}(\xi)\exp(\omega_k t)}_{\text{(slow modes)}} + \underbrace{\sum_{k=m_1+1}^{M} b_k(0)\phi_k^{(1)}(\xi)\exp(\omega_k t)}_{\text{(fast modes)}}, \tag{4.10}$$

where, ξ are the spatial coordinates, $b_k(0)$ is the initial amplitude of each mode. $\phi_k^{(1)}$ is DMD mode or eigenvector of full snapshot matrix, and $\exp(\omega_k t)$ is the corresponding eigenvalue. After the first level of decomposition, the time window is reduced for the second level. The DMD algorithm can be performed again with a

reduced time window on the second sum, representing the fast modes of (4.10). However, the fast modes are again separated into two matrices.

$$\mathbf{X}_{M/2} = \mathbf{X}^{(1)}_{M/2} + \mathbf{X}^{(2)}_{M/2}. \tag{4.11}$$

The first matrix of the right-hand side in (4.11) has the first $M/2$ snapshots, and the remaining snapshots are in the second matrix. At this level of decomposition, the m_2 slow-DMD modes are represented by $\phi_k^{(2)}$ are computed separately from the first- or second-time interval. This removal of slow modes is repeated recursively till the desired truncation level is achieved. This process is also represented in Figure 4.2. The general mrDMD decomposition structure is illustrated in Figure 4.2(a). The eigen value of (4.10) corresponding to a dynamic-mode represents a particular point on a complex plane. Referring to Figure 4.2(b), Figure 4.2(c) and Figure 4.2(d), the slow dynamic-modes at a certain level of decomposition are represented by the points near to the origin of the complex plane. There exists m_1 slow modes at 1st level of decomposition which are shown by red dots on a complex plane in Figure 4.2(b). The m_2 (blue circles) and m_3 (black squares) represent the slow dynamic-modes at 2nd and 3rd level of decomposition as shown in Figure 4.2(c) and Figure 4.2(d). The grey region

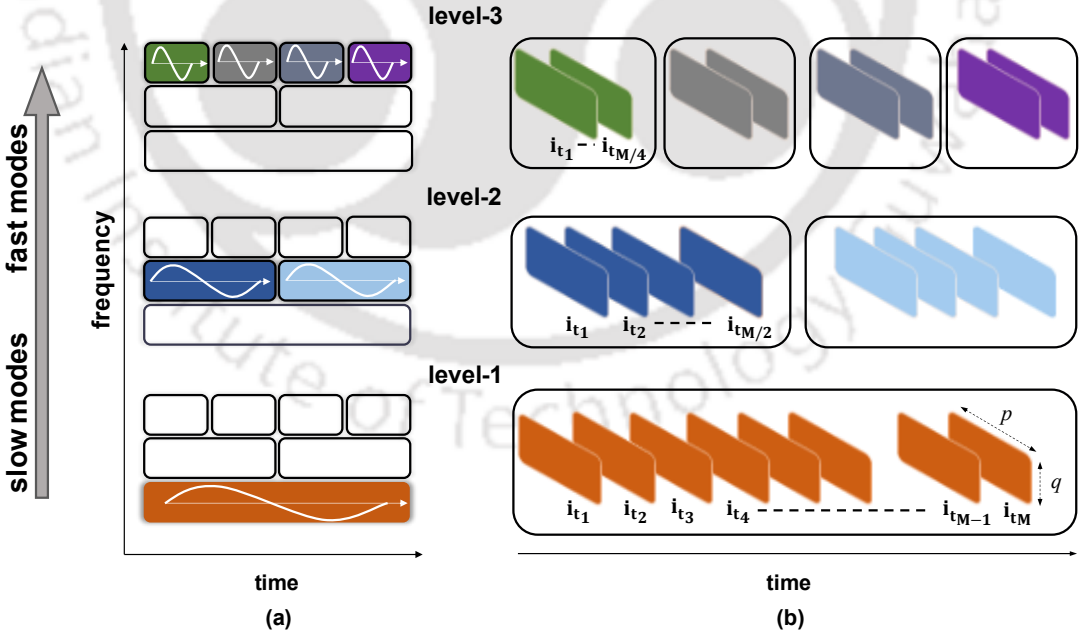

Figure 4.3. Illustration of mrDMD algorithm demonstrating sampling strategy of snapshots at various levels. a) time-frequency decomposition up to level-3 colour-coded with the snapshots, and b) snapshots of decomposition up to level-3 decomposition.

illustrates the slow modes which are removed at that level. In Figure 4.2(d), the green stars represent some dynamic-modes which can be extracted beyond 3rd level of decomposition.

The schematic diagram of the mrDMD technique is explained in Figure 4.3. A three-level decomposition of mrDMD (left) and the sampling strategy of snapshots (right) at each level is shown in Figure 4.3. The mrDMD extracts the slow varying features at level-1 (the bottom panel), and the fast scale features are successively extracted at a higher level of decomposition. The mrDMD method initially adapts M snapshots to capture slow scale features. At each higher level, successively, the sample size of the data is reduced to half of its previous level. The level 1 has the lowest frequencies of the dynamic-modes and increases as the level of decomposition an increase.

Formally, one can define the mrDMD solution in a generalised form as

$$\mathbf{x}_{\mathrm{mrDMD}}(t) = \sum_{l=1}^{L}\sum_{j=1}^{J}\sum_{k=1}^{m_L} f^{l,j}(t) b_k^{(l,j)} \phi_k^{(l,j)}(\xi) \exp\left(\omega_k^{(l,j)} t\right), \tag{4.12}$$

where,

$$l = 1,2,\ldots,L : \text{number of decomposition levels,} \tag{4.13}$$

$$j = 1,2,\ldots,J : \text{number of time bins per levels,} \quad (J = 2^{(l-1)}), \tag{4.14}$$

$$k = 1,2,\ldots,m_L : \text{number of modes extracted at level L.} \tag{4.15}$$

$f^{l,j}(t)$ is known as indicator function acts as a sifting function and is defined as:

$$f^{l,j}(t) = \begin{cases} 1, & t_j \le t \le t_{j+1} \\ 0, & elsewhere \end{cases} \tag{4.16}$$

Eq. (4.12) represents the mrDMD solution containing the information about time bins, the number of decomposition levels and the modes extracted at various levels.

The detailed algorithm of mrDMD [231] is explained in brevity in the following section.

4.3.1 The mrDMD algorithm

Step 1: Construct the data matrices $\mathbf{X}_1$ and $\mathbf{X}_2$ at level l and time bin j of the decomposition as referred to in (4.6) and (4.7).

Step 2: Take the singular value decomposition (SVD) of $\mathbf{X}_1$

$$\mathbf{X}_1 = \mathbf{U}\mathbf{\Sigma}\mathbf{V}^*, \tag{4.17}$$

where, $*$ denotes the conjugate transpose, $\mathbf{U} \in \mathbb{C}^{(n\times r)}$, $\mathbf{\Sigma} \in \mathbb{C}^{(r\times r)}$, and $\mathbf{V} \in \mathbb{C}^{(m\times r)}$. Here, r is the rank of the reduced SVD approximation to $\mathbf{X}_1$; the left singular vectors of $\mathbf{U}$ are POD modes.

Step 3: Next, compute $\widetilde{\mathbf{F}}^{(l,j)}$, the $r \times r$ entire matrix $\mathbf{F}^{(l,j)}$ onto POD modes:

$$\begin{aligned} \mathbf{F}^{(l,j)} &= \mathbf{X}_2\mathbf{V}\mathbf{\Sigma}^{-1}\mathbf{U}^*, \\ \widetilde{\mathbf{F}}^{(l,j)} &= \mathbf{U}^*\mathbf{F}^{(l,j)}\mathbf{U} = \mathbf{U}^*\mathbf{X}_2\mathbf{V}\mathbf{\Sigma}^{-1}. \end{aligned} \tag{4.18}$$

Step 4: Compute the Eigen decomposition of $\widetilde{\mathbf{F}}^{(l,j)}$

$$\widetilde{\mathbf{F}}^{(l,j)}\mathbf{W} = \mathbf{W}\mathbf{\Lambda}, \tag{4.19}$$

where, the columns of $\mathbf{W}$ are eigenvectors and $\mathbf{\Lambda}$ is a diagonal matrix with the corresponding eigenvalues λ_k.

Step 5: At this level of decomposition, collect the slow eigen values to construct slow modes, if present, where $\|\lambda_j\| < \rho$, and ρ is chosen in such a way to extract slow modes.

Step 6: Finally, reconstruct the Eigen decomposition of $\widetilde{\mathbf{F}}^{(l,j)}$ from $\mathbf{W}$ and $\mathbf{\Lambda}$. Specifically, the eigen values of $\mathbf{F}^{(l,j)}$ are presented by $\mathbf{\Lambda}$, and the eigenvectors of $\mathbf{F}^{(l,j)}$ (DMD modes) are the same as the columns of $\mathbf{\Phi}^{(l,j)}$:

$$\mathbf{\Phi}^{(l,j)} = \mathbf{X}_2\mathbf{V}\mathbf{\Sigma}^{-1}\mathbf{W}, \tag{4.20}$$

Step 7: Halve the initial sampling window at level $l+1$, and repeat the procedure for each subsequent sample.

In step 2, the rank r may be chosen by the optimal hard threshold technique; the principled way of truncation is discussed briefly in the following section.

4.3.2 Optimal Hard Threshold to Obtain Singular Value Truncation

Noise is an unavoidable part of data collected from an experiment. In such case, a principle way to truncate singular values of a data matrix $\mathbf{X}$ under the assumption that it has a low-rank matrix $\mathbf{X}_t$ with additive white noise error matrix $\mathbf{X}_n$ and noise magnitude ν is given by the recent theoretical discovery by Gavish and Donoho (2014) [239] that determines the optimal hard threshold τ

$$\mathbf{X} = \mathbf{X}_t + \nu\mathbf{X}_n. \tag{4.21}$$

When the noise magnitude ν is known

$$\tau = \eta\sqrt{N}\nu \,, \tag{4.22}$$

a. For a square matrix, $\mathbf{X} \in \mathbb{R}^{N\times N}$:

$$\eta = \frac{4}{\sqrt{3}}, \tag{4.23}$$

b. For a rectangular matrix, $\mathbf{X} \in \mathbb{R}^{N\times M}$ and $M \ll N$ with $\beta = {}^{M}/_{N}$:

$$\eta(\beta) \triangleq \sqrt{2(\beta+1) + \frac{8\beta}{(\beta+1)+\sqrt{\beta^2+14\beta+1}}}, \tag{4.24}$$

When the noise magnitude ν is unknown, this is usual in real-life scenarios

a. For a rectangular matrix, $\mathbf{X} \in \mathbb{R}^{N\times M}$

$$\tau = \omega(\beta)\sigma_{med}, \tag{4.25}$$

Here, σ_{med} is the median singular value; $\omega(\beta) = {}^{\eta(\beta)}/_{\mu(\beta)}$, $\mu(\beta)$ can be approximated numerically by solving:

$$\int_{(1-\sqrt{\beta})^2}^{\mu(\beta)} \frac{\sqrt{((1+\sqrt{\beta})^2-t)(t-(1-\sqrt{\beta})^2)}}{2\pi t}\, dt = \frac{1}{2}, \tag{4.26}$$

The rank r of the reduced SVD approximation can be determined by using the technique as discussed in this section.

4.4 Image Registration

Image registration is the method of superimposing two or several images of the same event from various perspectives or sensors [240, 241]. With respect to the reference image, the sensed image is geometrically aligned. Image registration is utilised in the application where different way of image acquisition is considered such as (a) Images of the same scene acquired from different viewpoints, (b) Images of the same scene acquired at different times, (c) Images of the same scene acquired by different sensors, and (d) Scene to model registration. Universal method of image registration is not practical because of the variation of images and several types of degradation. The image registration should take into account factors such as geometric deformation among the images, required accuracy and the noise content. Nonetheless, registration methods mostly comprise of the following four steps [240] (see Figure 4.4):

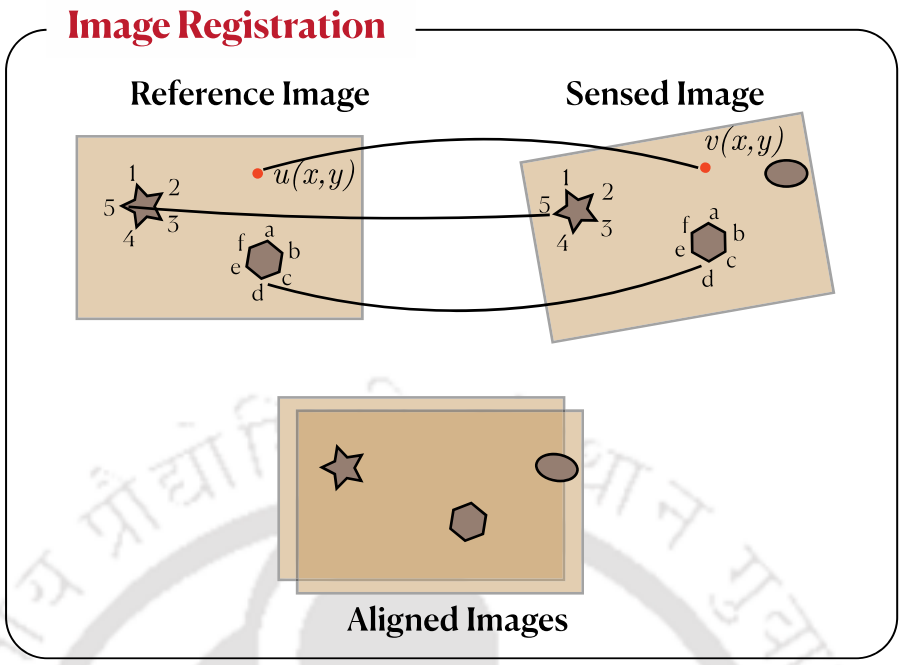

Figure 4.4. A schematic diagram representing the four steps of image registration.

a. Feature detection: Salient and distinctive features are manually or automatically detected.
b. Feature matching: A spatial relationship among the detected features in the sensed image $v(x, y)$ and those in reference image $u(x, y)$ is established.
c. Transform model estimation: The parameters of the mapping functions are computed with the help of established spatial relationship among the features.
d. Image resampling and transformation: Mapping functions formed in the previous step are employed to transform the sensed image. The necessary interpolation technique is used to calculate image value in the co-ordinate where the information is missing after the transformation.

Finding the similarity is an important component in the proposed damage detection algorithm. An mrDMD mode from the healthy data is considered as a reference image and from the damage data is considered as a sensed image. After registering these images, they are compared based on the content. Here in this work, the author used KL divergence for comparison of the images. In the following section, the KL divergence is briefly discussed.

4.5 KL Divergence

The Kullback Leibler (KL) divergence measures the distance between the two probability density functions $h(x)$ and $u(x)$ [232]. In statistics, it characterises the entropy, and it is defined as:

$$D_{KL}(h \parallel u) \triangleq \int h(x) \log \frac{h(x)}{u(x)} dx, \tag{4.27}$$

KL divergence can be used efficiently to measure the similarity between images [56]. In information theory, it measures the information loss in the fitted model $u(x)$ relative to that in the reference model $h(x)$. Note that, $D_{KL}(h \parallel u) = 0$, if $h(x) = u(x)$ (since $\log 1 = 0$) which indicates the self-identification and $D_{KL}(h \parallel u) > 0$ for all $h(x)$ and $u(x)$.

4.6 Results

In this chapter, the results are presented by implementing the proposed damage detection algorithm. Figure 4.5 shows the visualisation of two dimension (2D) acoustic waves propagation in the PZT ceramic. The time interval of the 2D image is 125 ns. The total acquisition time of the temporal images was 1 μs, corresponding to 365 time-varying snapshots. The dimension of the spatiotemporal data matrix $\mathbf{S}$ is $200 \times 200 \times 365$. Referring to Figure 4.5 (H1-H2), the maximum intensity was observed at the centre of the image attributing to strong coupling of the electric-field. The outward radiating longitudinal wave generates circular wave fringe due to the isotropic property of the PZT ceramic.

Upon completion of the Coulomb scanning of the healthy specimen, a controlled surface damage was introduced in the PZT ceramic. The damaged ceramic was reoriented to ensure minimum scanning offset (translation/rotation) with respect to a healthy state. Figure 4.6 shows the time-sequential images of wave propagation in damaged PZT ceramic. The surface defect in the PZT ceramic behaves as a reflector and impedes the transmission of the elastic wave. The forward propagating wave reflects from the surface defect and plate boundaries. The wave experience multiple interferences between the forward propagating and back-propagating reflected waves, as evident from Figure 4.6 (D4-D9). Further, the interaction of ultrasonic wave with the defect cause attenuation of the bulk wave.

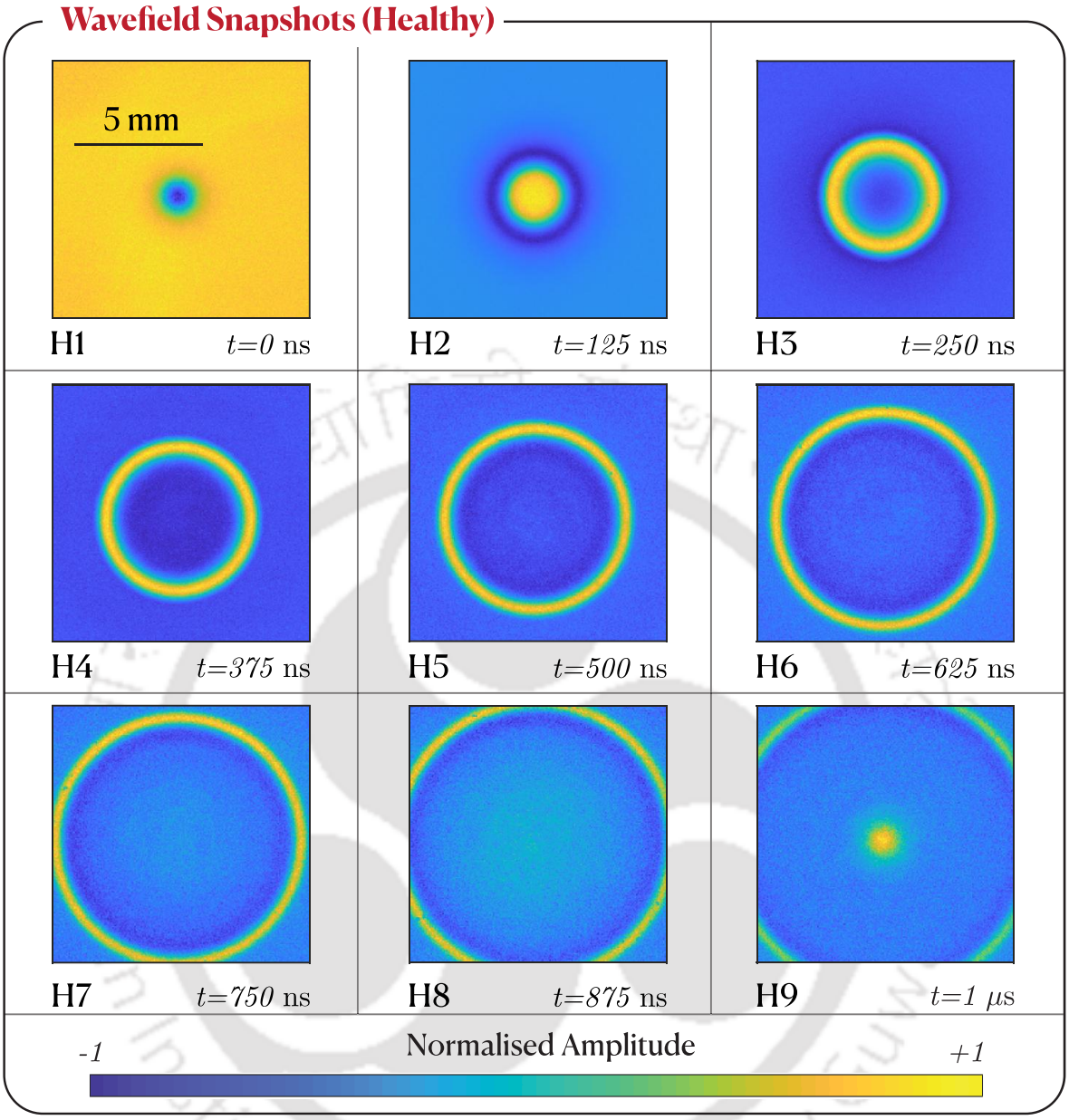

Figure 4.5 The sequential images of propagation of acoustic wave at an interval of 125 ns in a 3 mm thick sintered PZT ceramic plate (healthy state). The scanning region was 10 mm × 10 mm.

The precise detection and quantification of the defect directly from the experimental images are difficult due to the multiple interferences between the forward and reflected waves. To overcome the challenge, here we demonstrated an algorithm that separates spatiotemporal features emanating from the wave interaction with the defect. The main objective is to develop a time-frequency based feature detection algorithm for damage detection and localisation of damage. The mrDMD is ideally suited for decomposition of complex waveform and extract spatiotemporal

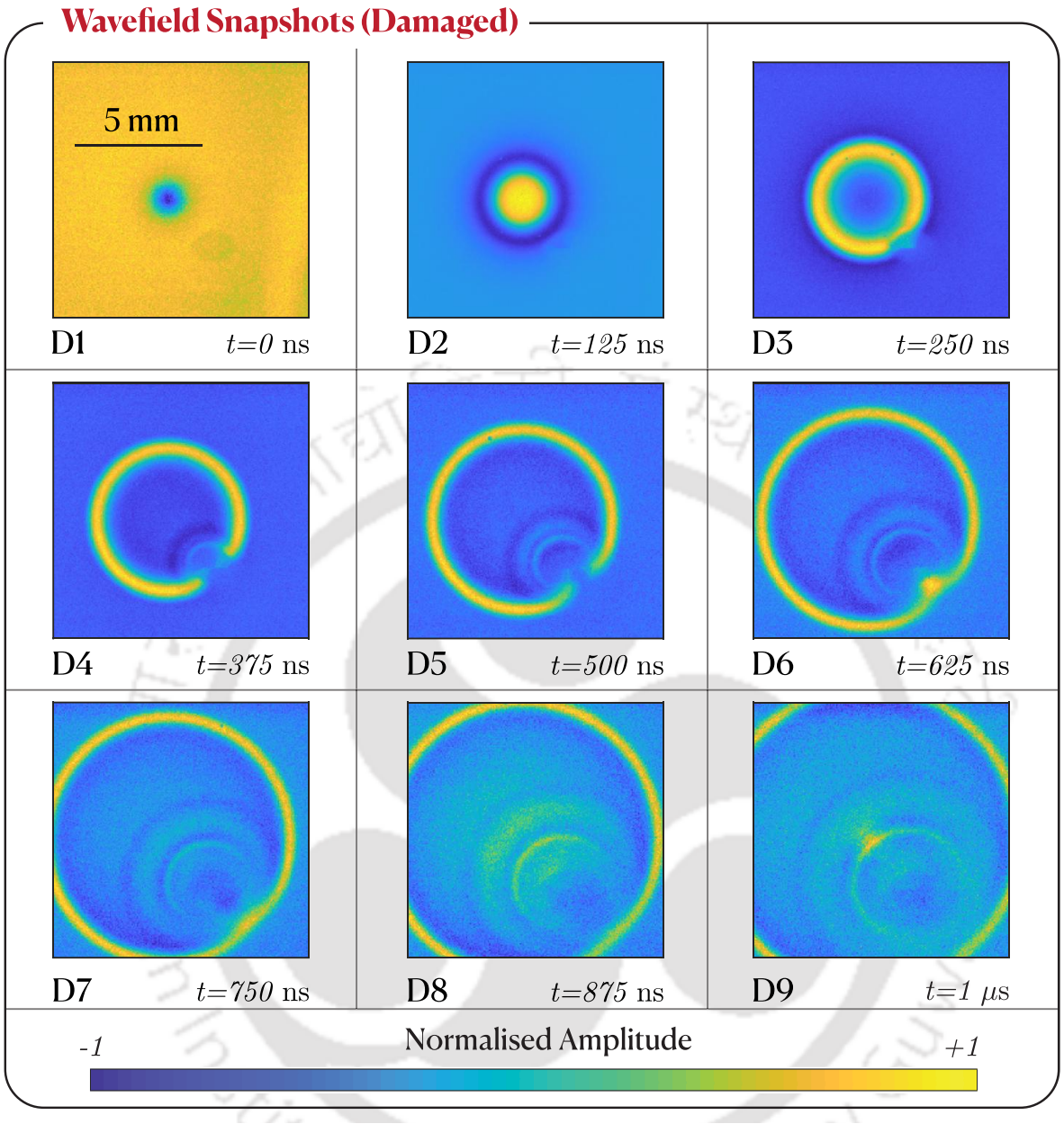

Figure 4.6 The sequential images of propagation of acoustic wave at an interval of 125 ns in a 3 mm thick sintered PZT ceramic plate (with surface defect). The scanning region was 10 mm × 10 mm.

features of damage. The algorithm is divided in two phases i.e., (i) spatiotemporal feature extract using mrDMD, and (ii) damage localisation using distance measure of probability density of 2D wave field image dataset of healthy state and damaged state.

Figure 4.7 and Figure 4.8 represent the results obtained by applying the mrDMD algorithm in the healthy and damaged state, respectively [96, 231]. Figure 4.7(b) and Figure 4.8(b) shows first level of decomposition, representing slowest wave mode for healthy and damaged state, respectively. Refer to Figure 4.7(b) and Figure 4.8(b),

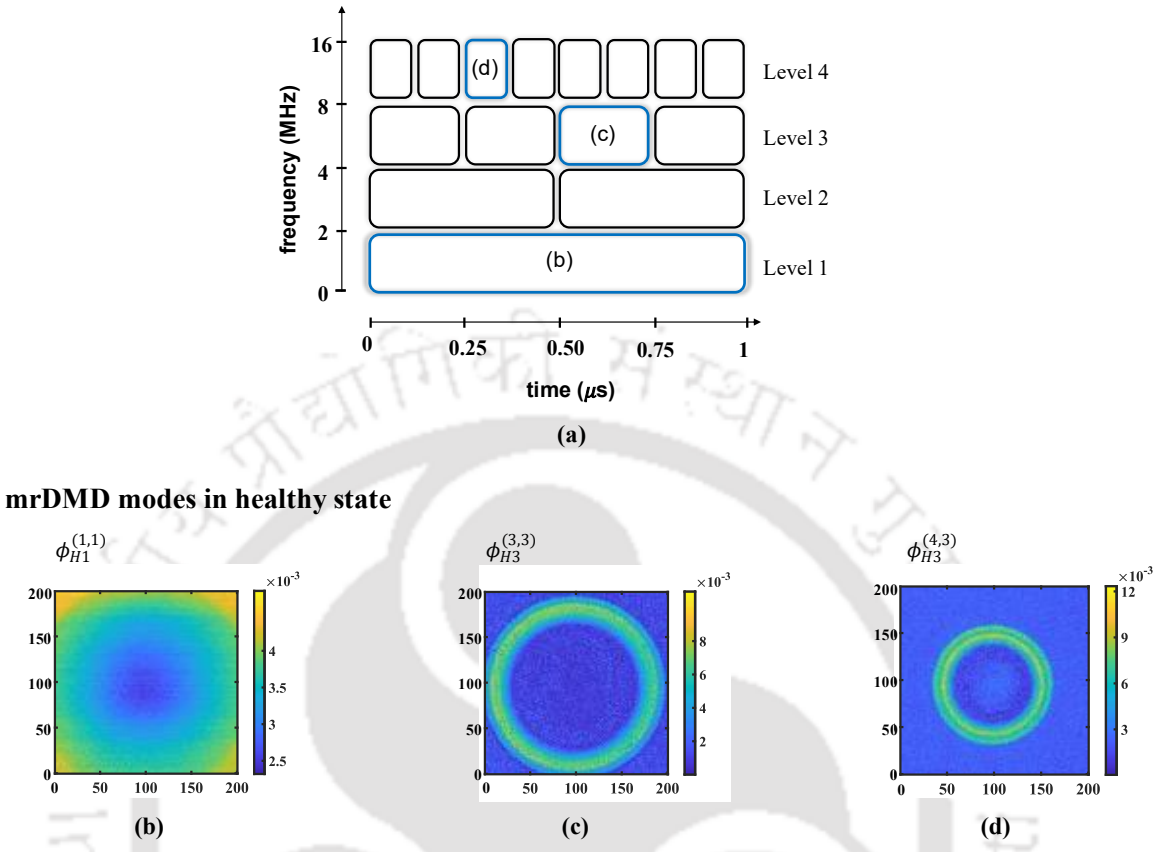

Figure 4.7 Results of mrDMD applied on 2D wave propagation in healthy PZT ceramic. a) Four-level of time frequency decomposition (top panel), b) level 1, c) level 3, and d) level 4 of mrDMD modes (bottom panel).

the slowest wave mode is denoted by $\phi_{H1}^{(1,1)}$ and $\phi_{D1}^{(1,1)}$ that represent the long time period. In this mode, the strong intensity at the centre is observed due to the strong coupling of the electric field. Figure 4.7(c) and Figure 4.7(d) represent level 3 and level 4 of mrDMD modal decomposition for healthy sample. The higher-order modes represent fast-varying features of acoustic wave propagation in PZT that are sensitive to surface and subsurface defects.

The data-driven approach of mrDMD extracts sensitive spatiotemporal features of the wave interaction with the defect. Figure 4.8 shows the four-level of mrDMD decomposition of spatiotemporal wavefield imaging in the defective PZT. Further, at the first level of decomposition, the extracted mode, $\phi_{D1}^{(1,1)}$, of the damaged state shows the impression of the surface defect (Figure 4.8(b)). However, the lowest order mode has long wavelength that restricts the spatial resolution. The level-3, $\phi_{D3}^{(3,3)}$ of mrDMD decomposition, shows extracted feature of the reflected wave from the edge of the

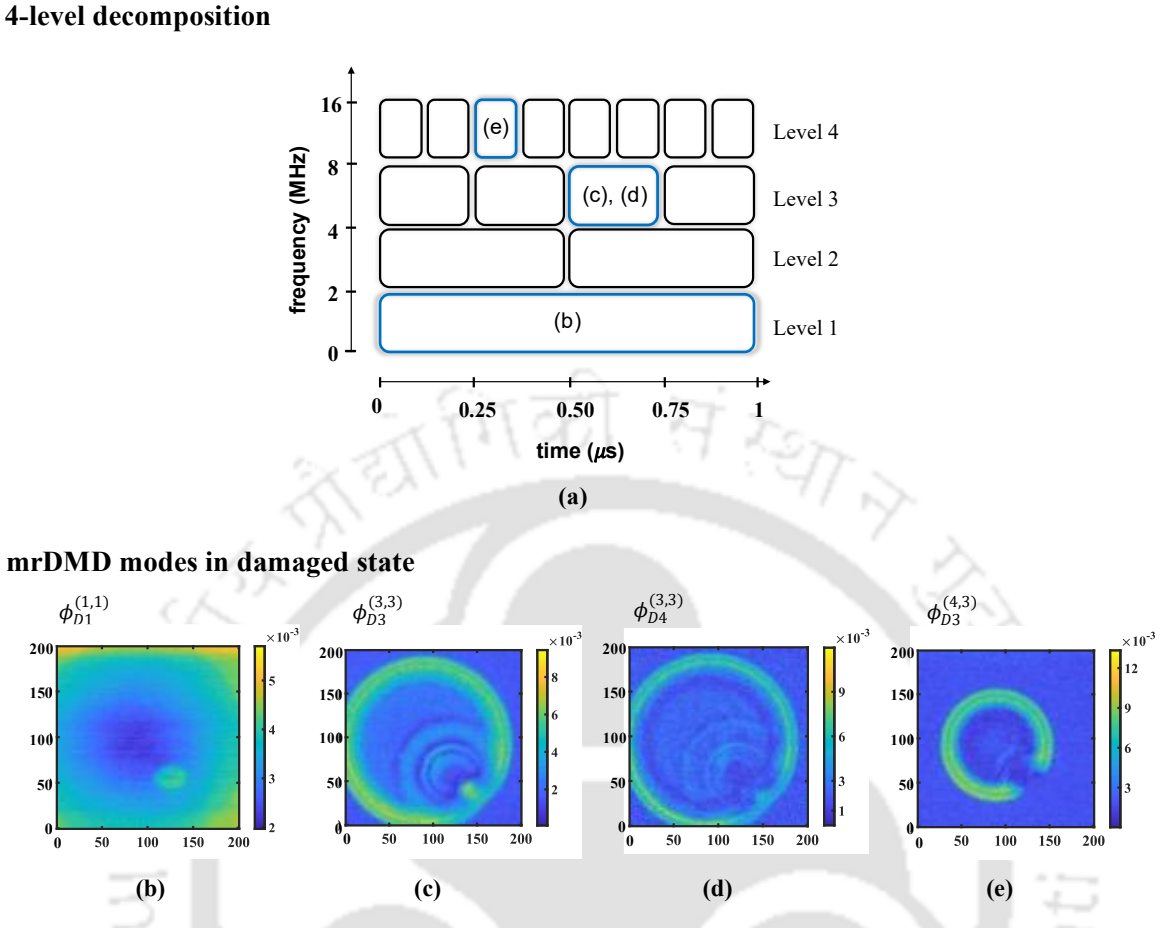

Figure 4.8 Results of mrDMD applied on 2D wave propagation in damage PZT ceramic. a) Four-level of time frequency decomposition (top panel), b) level 1, c) and d) level 3, and e) level 4 of mrDMD modes (bottom panel).

defect along with the forward propagating acoustic waves (Figure 4.8(c)). Further, Figure 4.8(d) illustrates the mrDMD level 3 mode, $\phi_{D4}^{(3,3)}$ that shows considerably low intensity of the reflected wave. Upon, comparison of the original wavefield image, (refer Figure 4.6-D4), with level-3 mrDMD mode shows a similar observation of reduced intensity. For both healthy and damaged situation, a 4-level decomposition is sufficient to extract spatiotemporal sensitive features.

Considering, the decomposition of mrDMD modes, the subsequent objective is to localise and quantify the damage in the PZT. To achieve this, we considered the slowest mode, $\phi_{H1}^{(1,1)}$ and $\phi_{D1}^{(1,1)}$ at level 1 of the decomposition from both the healthy and damaged data. Since, the healthy and damaged data are disjoint and acquired independently, hence, it is presumed that the 2D wave filed image will possess geometrical offset and rotation. As, the mrDMD modes are extracted from raw images,

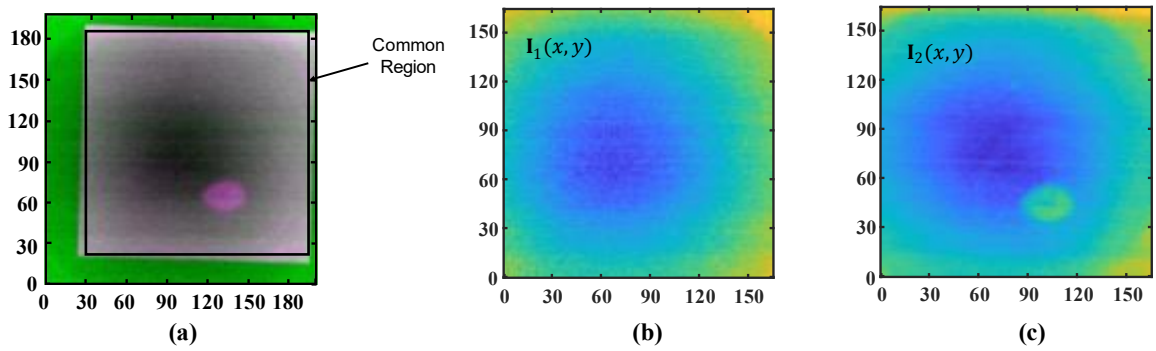

Figure 4.9 Results of intensity-based image registration. a) The damage mode (magenta) is registered and overlaid on the healthy mode (green), b) the aligned cropped image of healthy mode, and c) the aligned cropped image of damage mode.

the offset or rotation will also present in such modes. A minor offset or rotation can lead to a considerable error in the quantification of the defect. To overcome the errors arising due to offset in the considered modes, the intensity-based image registration technique is employed. In the intensity-based image registration, the healthy mode is considered as a reference image (green) and the damage mode as translated/rotated image (magenta) (refer to Figure 4.9(a)). Figure 4.9 shows the outcome of offset correction obtained through the image registration technique. The common region of Fig. 11(a) is selected and masked for quantifying the defect. Figure 4.9(b) and Figure 4.9(c) show the resulting aligned cropped images for healthy and damaged mode, respectively.

Once the process of image registration is performed, the localisation and quantification of damage are performed by computing the KL divergence. The key idea of computing KL divergence is computing the statistical distance between the modes of healthy and damaged states. The mrDMD mode of damage state almost exhibits the mode of healthy state with some loss of information at the damage location. Consider $\mathbf{I}_1(x,y)$ and $\mathbf{I}_2(x,y)$ represent the output masked image of the healthy and damaged state respectively; the dimension of each image is $w \times h$. As discussed in Section 4.5, KL divergence scores are minimum for similar modes (i.e $\mathbf{I}_1(x,y) \approx \mathbf{I}_2(x,y)$). Here, we computed KL divergence strip-wise; first a horizontal strip is considered and sliding the strip along the vertical direction $(\mathbf{I}_k(x,j); 1 \leq k \leq 2; 1 \leq j \leq h)$ and vice versa $(\mathbf{I}_k(x,i); 1 \leq k \leq 2; 1 \leq i \leq w)$. The computation of KL divergence scores by considering both directions are illustrated in Figure 4.10.

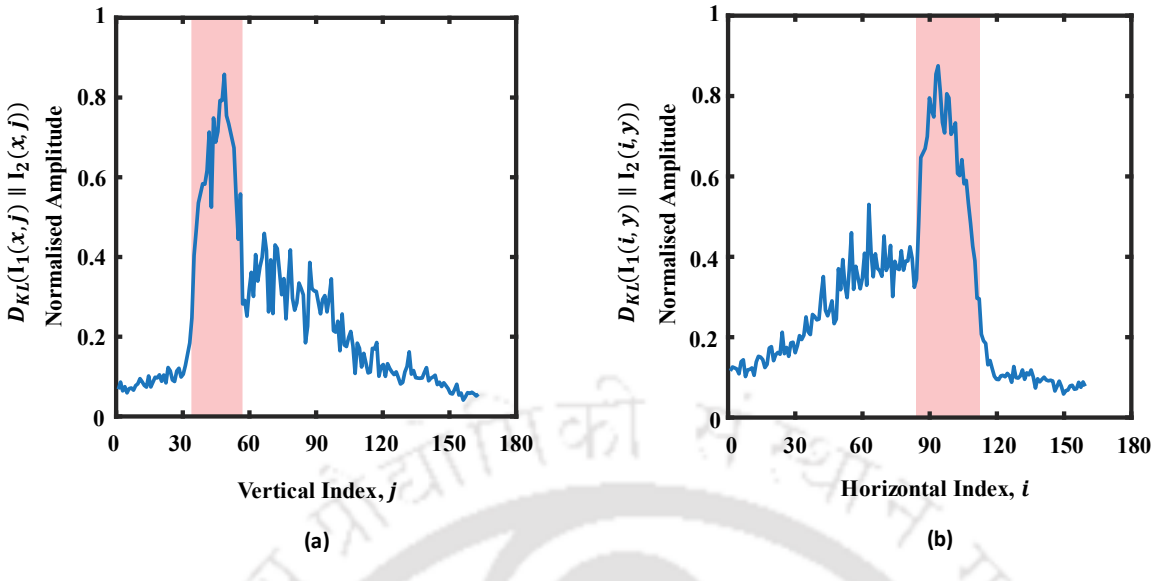

Figure 4.10 Plot of normalized KL Divergence scores. (a) The scores are computed by first considering the horizontal strip and sliding across along the vertical direction, and (b) the vertical strip sliding across along the horizontal direction.

Referring to Figure 4.10(a), sliding strip along the vertical direction, the KL divergence scores suddenly escalate in the domain from $j = 34$ to $j = 56$. Similarly, from Figure 4.10(b), the strip along the horizontal direction, in the domain from $i = 87$ to $i = 116$ the KL divergence scores are again increased abruptly. Referring to Figure 4.11, a rectangular region is compartmentalised between $j = 34$ to 56 and $i = 87$ to 116 which conforms to the location of the defect. The size of the surface flaw is quantified approximately 1.1 mm $\times$ 1.4 mm. The original size of the defect was approximately 1.2 mm $\times$ 1.3 mm. To evaluate the accuracy the error function is defined as follows:

$$\varepsilon_r = \frac{\left|(\text{Area of Damage})_{\text{original}} - (\text{Area of Damage})_{\text{detected}}\right|}{(\text{Area of Damage})_{\text{original}}} \times 100\ \%. \tag{4.28}$$

Therefore, the proposed algorithm is efficient for localisation and quantification of the damage with an error of about 1.3%.

Further, we implemented the algorithm repeatedly by varying several parameters to illustrate the reliability of the proposed algorithm. The first parameter considered here is the rank r that has significant importance in the mrDMD algorithm. It depends on the factors such as the amount of noise and the distribution of the singular values. Often, one selects the rank r of the SVD by identifying ‘‘elbows’’ or ‘‘knees’’ in the plots of singular values on the logarithmic scale. The ‘‘elbows’’ or ‘‘knees’’ may

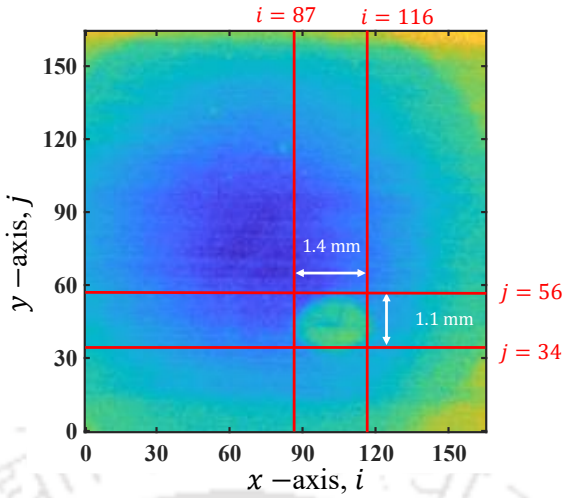

Figure 4.11 Localization of the surface defect in a rectangular region between $i =$ 87 to 116 and $j = 34$ to 56 unit. The size of the surface defect is quantified as approximately 1.4 mm $\times$ 1.1 mm.

represent the transition of important patterns from noise. Another way of truncating the singular values at the rank r that captures a pre-defined energy such as 80% or 90% in the original data [96]. Despite primitive, these techniques are commonly used. To overcome this, a principled approach to obtaining rank reduced SVD is discussed in Section 4.3.2. We also implemented the algorithm by setting the rank r on identifying the ‘‘elbows’’ from the distribution of singular values in a logarithmic scale. The damage is identified with an accuracy of about 97%. As stated earlier, the accuracy is further improved when the optimal truncation value is employed using the optimal hard threshold technique as discussed in Section 4.3.2. The second parameter considered to illustrate the reliability is ρ in step 5 of the mrDMD

Table 4.1 Comparison of error while detecting damage by varying different parameters.

Parameter	Method of selection / Value	Error (%)
r	Identifying the “elbows”	3 %
	Optimal hard threshold	1.3 %
ρ	1	1.8 %
	2	1.3 %
	3	2.1%

algorithm. The parameter ρ is chosen to extract slow modes. There is some liberty in the selection of ρ. This value is selected based on the length of the sampling window. The results presented in this work chooses the value of ρ in such a way that to extract modes with fewer than two cycles within the sampling window. However, the algorithm is repeated by setting the various values of ρ, such as one cycle and three cycles of oscillations. In each repetition, the damage is identified with an error of less than 5%. Finally, defining the limits of the escalating region in the plot of the KL divergence score is a contentious choice. However, one can define the limit by threshold crossing of the KL divergence score. Table 4.1 presents the error in detecting damage by varying different parameters of the mrDMD algorithm.

4.7 Concluding Remarks

Multiresolution dynamic mode decomposition is an equation- free data-driven technique that explores the underlying system dynamics by extracting spatiotemporal coherent mode. The unique ability of mrDMD is leveraged to extract higher-order dynamic-modes of the ultrasonic wave. The point source technique based on Coulomb coupling is employed for the excitation and detection of ultrasonic waves in PZT sensors. The two-dimensional spatial temporal evolution of waves in the PZT is imaged for diagnosis and localisation of surface defects in the PZT. The mrDMD provides input-output models for the interaction of waves with complex geometries. The coherent mode of propagation of elastic waves are filtered, and modes sensitive to defect are considered for localisation. Further, KL divergence method in two-dimensional scanning mode is used to localise the detects from the mrDMD defect sensitive modes. The proposed algorithm exhibits good accuracy in detecting and quantifying damage with an error of around 1.3%. Albeit, the technique being implemented on full-field transient imaging, has still poised itself to perform scientifically in situations of data sparsity, which can occur due to high costs or practical limitations in the data capture setup used for the experiments, may lead to inaccurate damage detection that needs further investigation.

Chapter 5

Anomaly Detection in PZT Sensor using Deep Learning

The implementation of piezoelectric sensors is degraded due to surface defects, delamination, and extreme weathering conditions, to mention a few. Hence, the sensor needs to be diagnosed before the efficacious implementation in the SHM framework. To rescue the problem, a novel experimental method based on Coulomb coupling is utilised to visualise the evolution of elastic waves and interaction with the surface anomaly in the lead zirconate titanate (PZT) substrate. Recently, machine learning (ML) has been expeditiously becoming an essential technology for scientific computing, with several possibilities to advance the field of SHM. This study employs a deep learning-based autoencoder neural network in conjunction with image registration and peak signal-to-noise ratio (PSNR) to diagnose the surface anomaly in the PZT substrate. The autoencoder extracts the significant damage-sensitive features from the complex waveform big data. Further, it provides a nonlinear input–output model that is well suited for the non-linear interaction of the wave with the surface anomaly and boundary of the substrate. The measured time-series waveform data is provided as input into the autoencoder network. The mean absolute error (MAE) between the input and output of the deep learning model is evaluated to detect the anomaly. The MAEs are sensitive to the anomaly that lies in the PZT substrate. Further, the challenge arising from offset and distortion is addressed with ad hoc image registration technique. Finally, the localisation and quantification of the anomaly are performed by computing PSNR values. This chapter proposes an advanced, efficient damage detection algorithm in the scenario of big data that is ubiquitous in SHM.

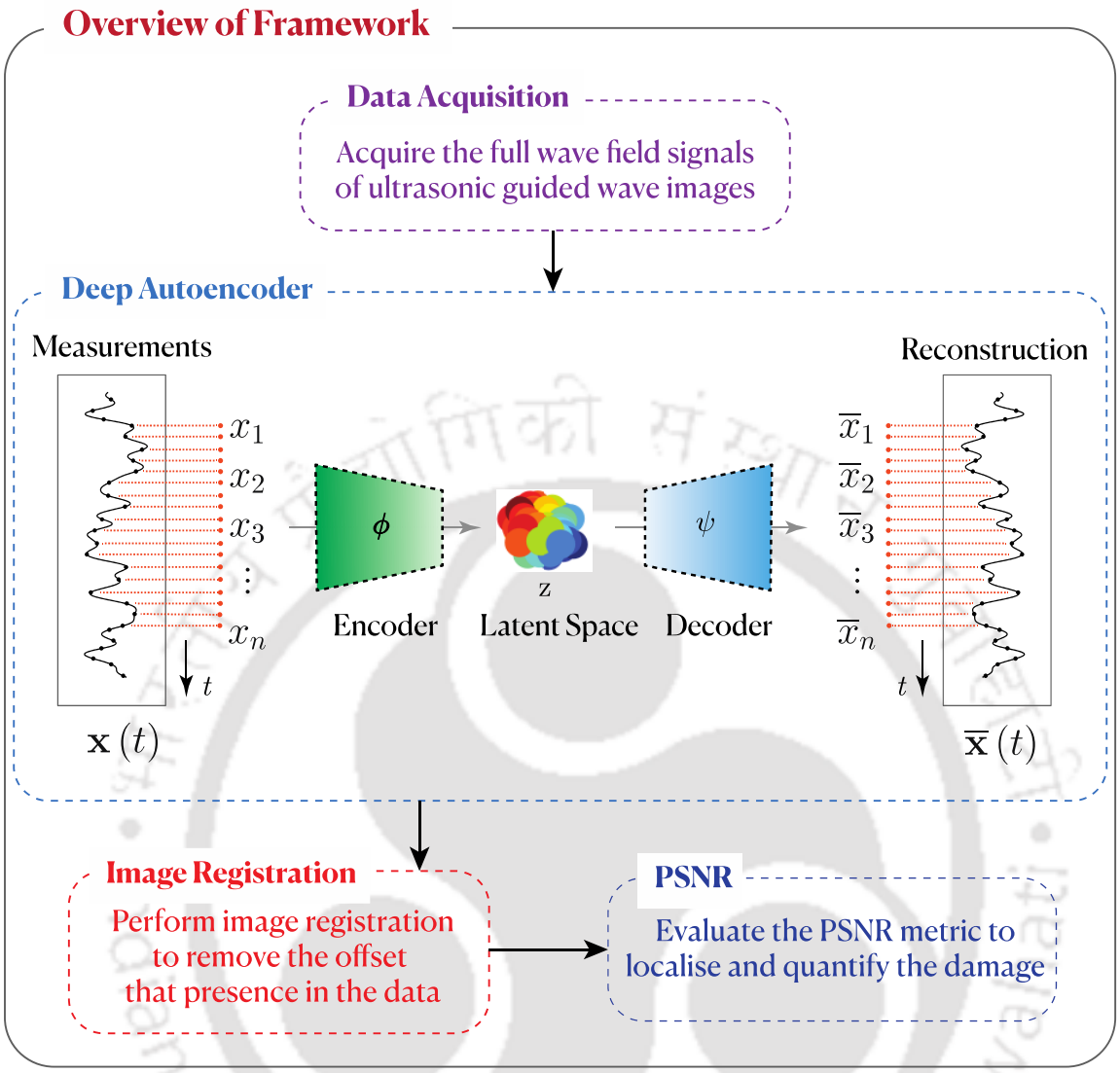

Figure 5.1 The overview of the proposed damage detection algorithm.

5.1 Proposed Scheme

This chapter presents a novel damage detection framework based on a deep autoencoder NN, image registration [240] and peak signal-to-noise ratio (PSNR) [242]. The proposed method is applied for the diagnosis of PZT substrate using propagation of the ultrasonic wave. The results show that the proposed method is robust, reliable and effective for the SHM framework. The advantages of the building block used in the proposed frameworks are as follows:

- In order to avoid conventional signal processing techniques and diagnose experience, a damage detection framework is proposed primarily based on the deep autoencoder feature learning method to learn the necessary damage-sensitive features from the experimental measurement automatically.

- In order to nullify the error due to the offset presented in the experimental data and to enhance the performance, the image registration technique is employed.
- In order to localisation and quantify the damage, the PSNR metric is adopted.

The overview of the proposed framework is illustrated in Figure 5.1.

5.2 Mathematical Background of Deep Autoencoder

To discuss the mathematical background of deep autoencoder, let us first discuss the construction spatiotemporal data matrix, $\boldsymbol{\mathcal{D}}$. The time domain signals are recorded by employing point contact excitation and detection method by placing the sender probe at p points along the x-direction and q points along y-directions, which is the total $(p \times q)$ number of spatial points on the substrate. By stacking all the $(p \times q)$ number of signals, the data matrix $\boldsymbol{\mathcal{D}}$ is constructed given in Eq. (5.1)

$$\boldsymbol{\mathcal{D}} = \{\mathbf{S}_1, \mathbf{S}_2, \mathbf{S}_3, \dots, \mathbf{S}_m\}_{(p \times q \times m)}. \tag{5.1}$$

One can create a two-dimensional (2D) matrix by collecting the measurement at the ith index $(1 \leq i \leq m)$ of the time domain signal. This matrix represents the 2D snapshots of the wavefield denoted by $\mathbf{S}_i$ in Eq. (5.1). $\boldsymbol{\mathcal{D}}$ represents the collection of the 2D snapshot of wavefield images. The dimension of each snapshot is $(p \times q)$, where p, q represent the number of pixels along x- and y-directions, respectively. There exist m such snapshots along the time axis. It is possible to vectorise each snapshot matrix, $\mathbf{S}_i$ to a higher dimensional, for instance, n-dimensional $(n = p \times q \geq 1$ column vector, $\mathbf{x}_i$. Each column of the matrix $\mathbf{X}$ represents the vectorised form of each snapshot as given in Eq. (5.2)

$$\mathbf{X} = \{\mathbf{x}_1, \mathbf{x}_2, \mathbf{x}_3, \dots, \mathbf{x}_m\}_{(n \times m)}. \tag{5.2}$$

A deep autoencoder NN is an amenable and expedient framework for exploiting low-dimensional meaningful features from high-dimensional data. The autoencoder generalises the linear subspace embedding of singular value decomposition or principal component analysis to a nonlinear manifold embedding, often of a lower dimension [238, 243]. Specifically, for the given training data $\mathbf{X} = \{\mathbf{x}_1, \mathbf{x}_2, \mathbf{x}_3, \dots, \mathbf{x}_m\}$ (for each sample $\mathbf{x}_i$, $\mathbf{x}_i = [x_1, x_2, \dots, x_n]^T$), the encoder maps the original high-dimensional input vector $x_i \in \mathbb{R}^n$ to a low-dimensional latent representation $\mathbf{Z} = \{\mathbf{z}_1, \mathbf{z}_2, \mathbf{z}_3, \dots, \mathbf{z}_m\}$ (for each $\mathbf{z}_i \in \mathbb{R}^r$, $\mathbf{z}_i = [z_1, z_2, \dots, z_r]^T$). Then the latent

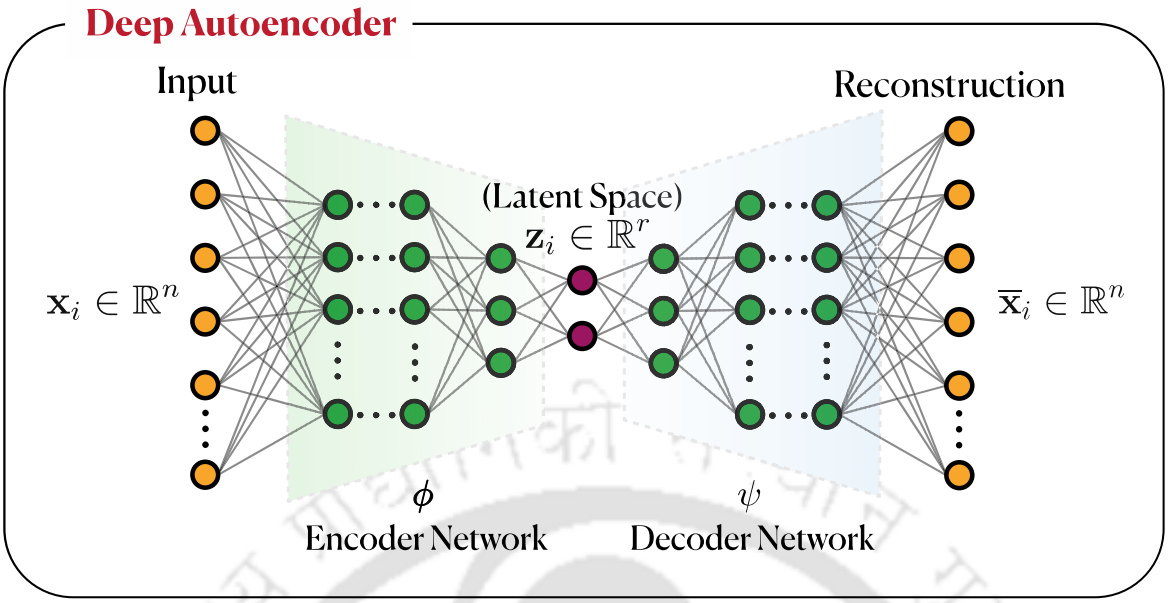

Figure 5.2 Illustration of an autoencoder network architecture.

representation $\mathbf{Z}$ is transformed back to the high dimensional space $\overline{\mathbf{X}} = \{\overline{\mathbf{X}}_1, \overline{\mathbf{X}}_2, \ldots, \overline{\mathbf{X}}_m\}$ (for each $\overline{\mathbf{X}}_i \in \mathbb{R}^n$, $\overline{\mathbf{X}}_1 = [\bar{x}_1, \bar{x}_2, \ldots, \bar{x}_n]^T$) by the decoder, which is technically the output of the network. The objective of the autoencoder is to map the output back to itself, i.e. $\|\overline{\mathbf{x}} - \mathbf{x}\|_2 \approx 0$ [238, 244]. Usually, $r \ll n$ for autoencoding and mathematically, the encoding is represented as

$$\mathbf{Z} = \phi(\mathbf{X}), \tag{5.3}$$

where $\mathbf{Z}$ is the latent space data and $\mathbf{X}$ is the training high-dimensional input data. Decoding is represented as

$$\overline{\mathbf{X}} = \psi(\mathbf{Z}), \tag{5.4}$$

where the NN parameters are tuned so that the output $\overline{\mathbf{X}}$ is as accurate as possible to the input $\mathbf{X}$,

$$\underset{\theta}{\operatorname{argmin}} \|\mathbf{X} - \overline{\mathbf{X}}\|_2^2 = \underset{\theta}{\operatorname{argmin}} \|\mathbf{X} - \mathbf{f}_\theta(\mathbf{X})\|_2^2, \tag{5.5}$$

where θ are the learnable parameters of the autoencoder network $\mathbf{f}_\theta(\mathbf{x}) = \psi(\phi(\mathbf{x}))$.

From a mathematical point of view, the autoencoder allows a mapping, as shown in Figure 5.2, so that

$$\begin{aligned} &\phi: \boldsymbol{\mathcal{X}} \rightarrow \boldsymbol{\mathcal{Z}}, \\ &\psi: \boldsymbol{\mathcal{Z}} \rightarrow \boldsymbol{\mathcal{X}}, \end{aligned} \tag{5.6}$$

where the input $\mathbf{x} \in \boldsymbol{\mathcal{X}} \subseteq \mathbb{R}^n$ and output $\mathbf{z} \in \boldsymbol{\mathcal{Z}} \subseteq \mathbb{R}^r$ are defined in high- and low-dimensional spaces, respectively. The final NN optimisation is composed around the loss function as represented in Eq. (5.7)

$$\underset{\phi,\psi}{\operatorname{argmin}} \|\mathbf{X} - (\psi \circ \phi)\mathbf{X}\|. \tag{5.7}$$

5.3 PSNR

PSNR is a measure of the quality of reconstructed or compressed data. It is widely used to measure the image quality of image compression and image restoration system. The PSNR is usually defined via the mean squared error (MSE). It is typically expressed in decibels (dB). Given a reference image $I_1(m \times n)$ and the sensed image $I_2(m \times n)$ of size $M \times N$, the MSE and thus PSNR (in dB) is defined as

$$\text{MSE} = \frac{1}{MN} \sum_{M,N} [I_1(m,n) - I_2(m,n)]^2, \tag{5.8}$$

$$\text{PSNR} = 10 \log_{10} \left(\frac{\text{Max}_i^2}{\text{MSE}} \right). \tag{5.9}$$

Here, Max_i is the maximum possible pixel value of the image. The higher the PSNR, the better the similarity between the sensed and reference images since a higher PSNR indicates a lower MSE and, thus, less distortion. Note that, PSNR $= \infty$, if $I_1(m,n) = I_2(m,n)$ (since MSE $= 0$) indicates self-identification and PSNR $< \infty$ for all $I_1(m,n)$ and $I_2(m,n)$.

5.4 Results and Discussion

This section presents the results by implementing the proposed novel and robust anomaly detection algorithm. The visualisation 2D acoustic wave propagation in the PZT ceramic is already discussed in previous chapter (Section 4.6).

The precise detection and quantification of anomalies from the sequential wavefield snapshots are challenging, and the multiple interferences among the forward and reflected waves further compound the challenge. Coming to the rescue, a novel algorithm based on a deep autoencoder is manifested to identify the anomaly in the PZT crystal. The main thrust of this study is to develop a deep learning-based algorithm to detect and localise the damage. The deep autoencoder is ideally suited to extract damage-sensitive features from the complex waveform data. The proposed

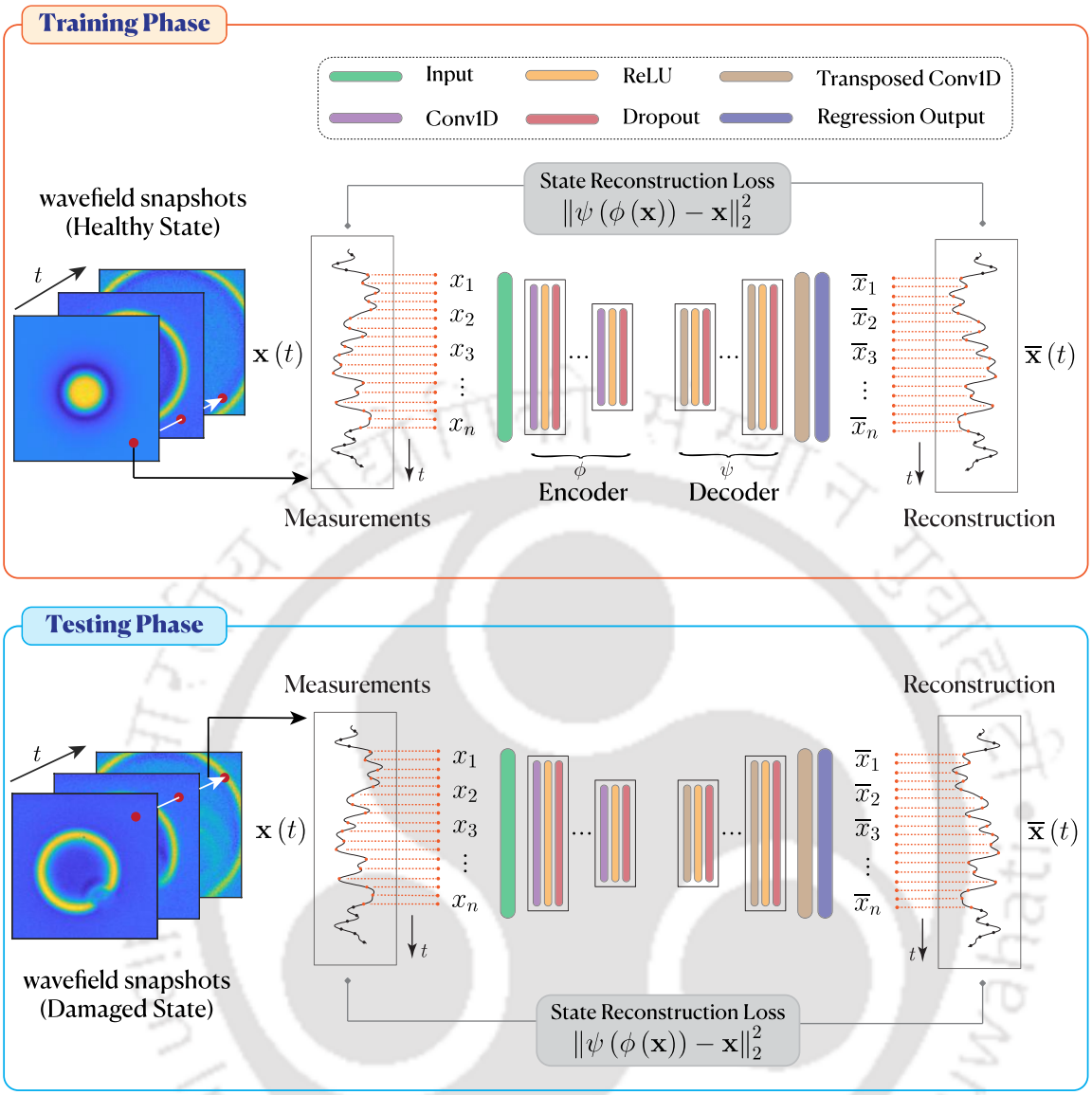

Figure 5.3 Schematic illustration of the proposed damage detection framework based on deep autoencoder for identifying anomalies in the PZT material.

novel damage detection algorithm has two phases, i.e. (a) damage-sensitive features extraction by employing deep autoencoder, (b) damage localisation by measuring PSNR between the damaged features in the form of images of the healthy and damaged state.

Here, we propose to employ a deep autoencoder to detect anomalous regions in a collection of time series wavefield data. An autoencoder is a type of NN trained to reconstruct the input. This can be achieved by encoding and decoding steps. The encoder transforms the input into a lower dimensional space and reconstruction the

input from the lower dimensional space by the decoder. One must note that training an autoencoder does not require labelled data.

The autoencoder itself does not identify anomalies. The basic idea here is training an autoencoder using only a healthy dataset to yield a deep learning model that can reconstruct its input data by using features learned from the trained data only. To detect anomaly in the observed data using an autoencoder, the observed measurement is provided as an input into the trained network, and the error between the input and the reconstructed measurement is evaluated. A significant error between the input and reconstructed measurement indicates that the input measurement consists of features unrepresentative of the data used to train the network; thus, the input measurement is anomalous. By evaluating the region-wise error among the input measurement and reconstructed measurement, one can identify the localised region of defect. The proposed network architecture is illustrated in Figure 5.3. Out of the available healthy time series data in 40000 ($= 200 \times 200$) spatial locations, the 2500 time series data are selected by uniform sampling to train the autoencoder. The data are partitioned into training and validation partitions. The autoencoder network is trained 90% of the data, and 10% is kept aside for validation.

The encoder of the autoencoder network considered in this work recursively down-samples the temporal dimension of the data by a factor of two. Then, the decoder up-samples the data by a factor of two the same number of times. Before providing the data into the network, the time series data is truncated to have a length of the nearest multiple of 2^j, where j is the number of down-sampling operations to ensure the network can reconstruct the data unmistakably. In this study, $j = 2$ is considered, i.e. the autoencoder network down-samples the data twice.

The input data are normalised using Z-score normalisation to have a better performance in the training process. The encoder network is designed by repeating blocks of 1D convolution, rectified linear unit (ReLU) and dropout layers to down-sample the data. Whereas the decoder is designed by the same number of blocks of 1D transposed convolution, ReLU and dropout layers to up-sample the data, as illustrated in Figure 5.3. The network down-samples and up-samples the data evenly by a factor of 2, specifying the stride equal to 2. Finally, a 1D transposed convolution and regression output layers are included to get the output of the same size as the input. Then, the network is trained with the Adam solver for 17 iterations per epoch.

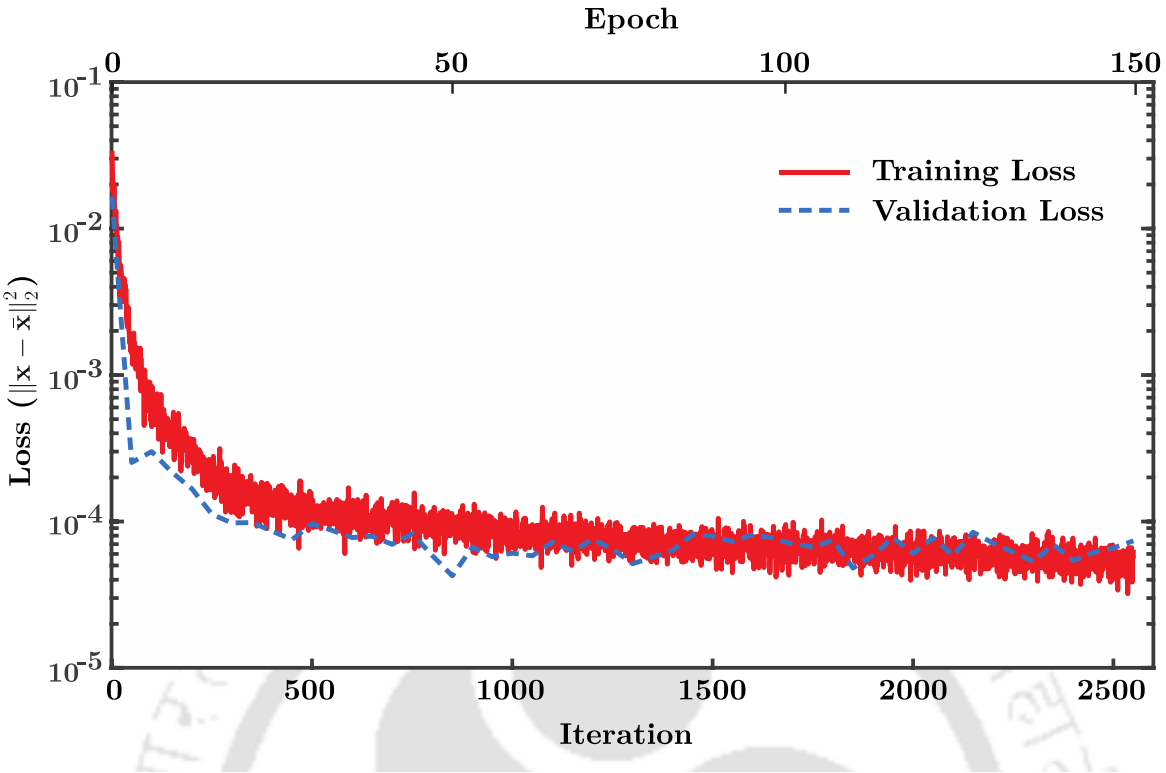

Figure 5.4 The plot of the performance summary of the optimization algorithm (red line) during the training and the performance summary of the autoencoder in validation (dashed blue line) during the training process.

A total number of 2550 iterations corresponding to 150 epochs are required to finish the training process. The validation data are used to validate the network. The variation of training loss and validation loss to the number of iterations and the epochs are illustrated by the red and dashed blue lines, respectively, in Figure 5.4.

After training the deep learning model, the objective is to detect the anomaly in the PZT sensor. Towards that, the MAE between the input sequence and the reconstructed sequence is considered damage sensitive feature. The data collected from the damaged PZT by experimenting are provided as input to the trained deep autoencoder. The MAE is evaluated for each sequence of the damaged PZT data. One must note that the size of the damaged data matrix is $200 \times 200 \times 365$, i.e. 40000 ($= 200 \times 200$) number of time sequences are reconstructed by the trained autoencoder network and corresponding MAE are calculated. To compare with the healthy PZT dataset of size $200 \times 200 \times 365$, the similar steps are repeated. Figure 5.5(a) and (b) illustrate the visualisation of the MAE matrix obtained by applying the deep autoencoder network on healthy and damaged states, respectively.

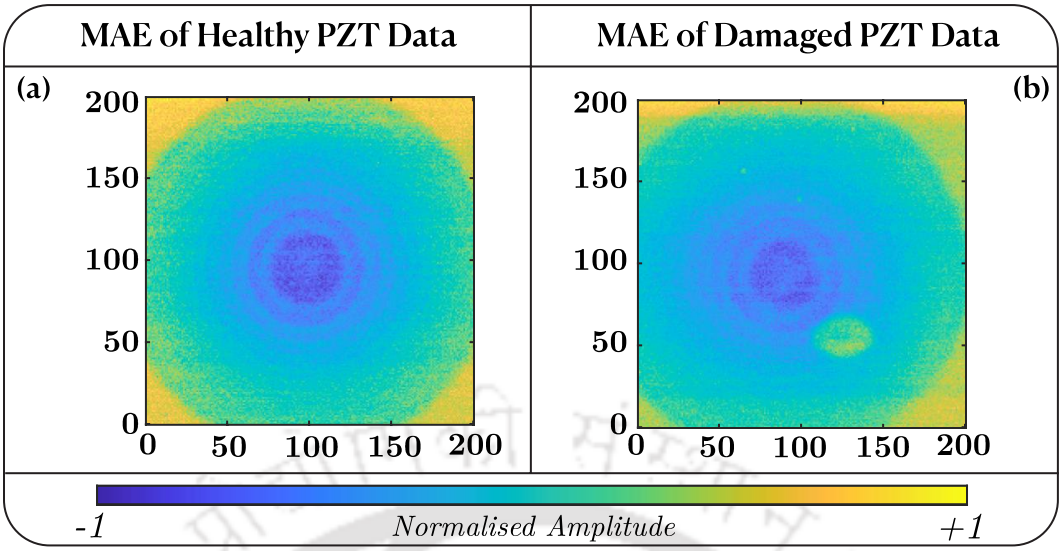

Figure 5.5 Illustration of the MAE of the autoencoder representation for (a) healthy PZT data and (b) damaged PZT data.

The deep autoencoder network extracts the damage-sensitive features of the wave interaction with the surface defect. Further, referring to Figure 5.5(b), the MAE image of the damaged state shows the impression of the surface defect. In addition to detecting the defect, the subsequent objective is to quantify and localise the anomaly in the PZT. Towards this objective, the MAE images of the healthy and damaged data are considered. Since the experimental measurement of healthy and damaged data are disjoint and measured independently, it is evident that the 2D wave field images will have geometrical offset and rotation. The MAE images will also possess

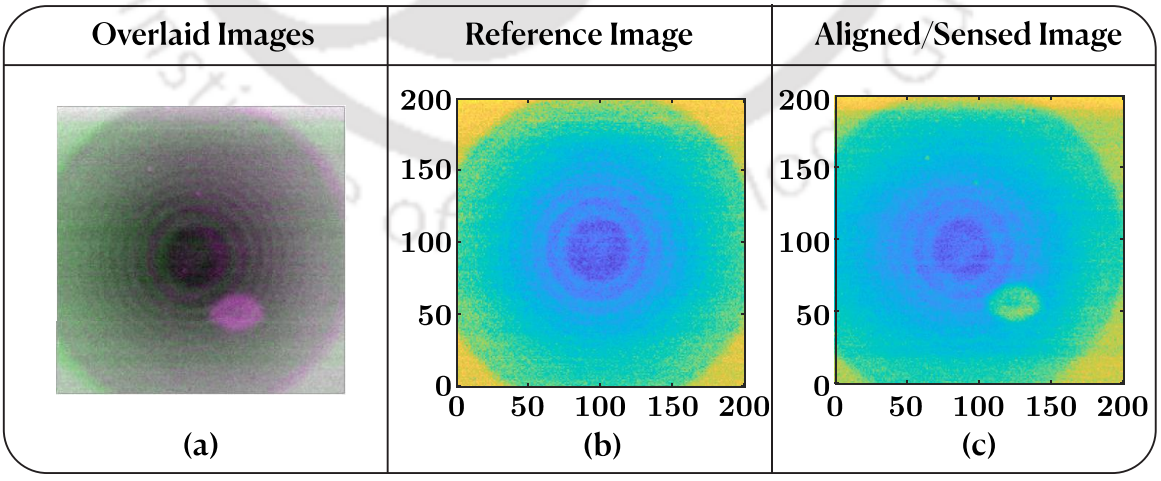

Figure 5.6 Results of intensity-based image registration. (a) The damaged MAE image (magenta) is overlaid on the healthy MAE image (green), (b) the aligned reference image, and (c) the aligned MAE image of damaged data.

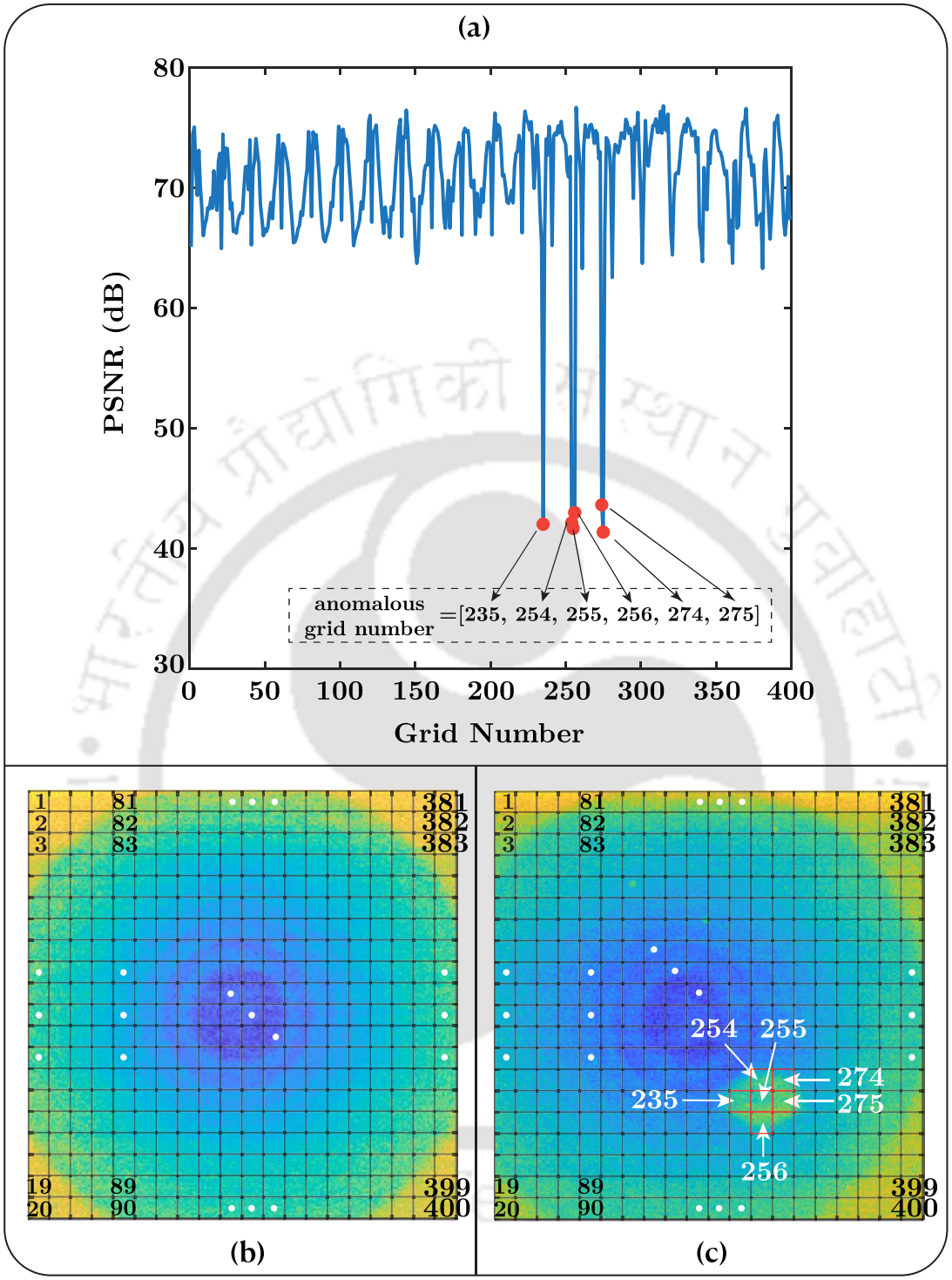

Figure 5.7 (a) The plot of PSNR values in dB to the grid number, (b) an illustration of the grids used on the MAE image of the healthy state, and (c) identification of anomalous grids on the MAE image of the damaged state.

the offset or rotation as they are extracted from such raw data. A slight offset or rotation can induce a substantial error in anomaly quantification. Intensity-based image registration is employed to address the challenge arising due to offset. From

Figure 5.6(a), it can be observed that the MAE image of the damaged data is considered a sensed image (magenta) and the MAE image of healthy data as a reference image (green) in the intensity-based image registration. The result of the offset correction is illustrated in Figure 5.6.

After the registration process is performed, the quantification and localisation of the surface anomaly are done by computing PSNR values. The key idea of evaluating the PSNR value is computing the difference between healthy and dam- aged MAE images. The MAE image of the damaged state almost exhibits the MAE image of the healthy state with the loss of some information at the damaged location. The MAE images are divided into 400 grids, and the dimension of each grid is 10 pixels $\times$ 10 pixels (0.5 mm $\times$ 0.5 mm) as shown in Figure 5.7(b). The PSNR is computed between the healthy and damaged MAE images on each grid. As discussed in Section 5.3, the PSNR value will be maximum for similar grids. The computation of PSNR values in dB by considering the grids is illustrated in Figure 5.7(a).

Referring to Figure 5.7(a), the PSNR values suddenly abate for the grid numbers 235, 254, 255, 256, 274 and 275. These grids are identified on the MAE image of the damaged state, which conforms to the location of the defect, as illustrated in Figure 5.7(c). The size of these anomalous six grids is quantified as 1.5 mm^2 (= 6 $\times$ 0.5 mm $\times$ 0.5 mm). The original size of the surface defect is approximately 1.56 mm^2 (= 1.2 mm $\times$ 1.3 mm). Therefore, the proposed algorithm is accurate for the detection, localisation and quantification of the surface anomaly on PZT sensors with an accuracy of about 96%. However, testing the proposed framework on multiple scenario to evaluate the model's efficiency can be a scope of future work.

5.5 Concluding Remarks

The autoencoder NN is a data-driven deep learning technique that learns the crucial features from healthy data. The unique learning ability of the autoencoder NN is leveraged to extract the damage-sensitive features from the data. The novel experimental technique based on Coulomb coupling is employed to visualise the spatial–temporal evolution of the ultrasonic waves in the PZT sensor. The received sequential temporal signals of the excited ultrasonic wave in the PZT are considered for detecting and quantifying the surface defect in the PZT. The autoencoder provides an input-output deep learning model for the interaction of waves with complex geometries. The MAE between the input signal and reconstructed signal by the

autoencoder NN is sensitive to defect and is considered for quantification and localisation. Further, PSNR is computed between the MAE images of healthy and damaged datasets to localise the anomaly. The proposed robust algorithm manifests good accuracy in detecting and quantifying the anomaly with an accuracy of about 96%. Albeit, the proposed framework being implemented on full-field transient signals of healthy and damaged states has still poised itself to perform satisfactorily in situations of data sparsity and without healthy state data that needs further investigation.

Chapter 6

Parameter Estimation of Anisotropic Substrate using Kalman Filter

The potential application of Lithium Niobate ($LiNbO_3$) crystal is immense, specifically in the domain of *meta*-surfaces and nano-resonators. However, the practical application of LiNbO3 is impeded due to unreliable experimental techniques and inaccurate inversion algorithms for material characterization. In the current research, material characterization of anisotropic crystal is proposed by exploring the wavefield evolution in the spatial and temporal domains. The presented framework has three major components: a physics-based mathematical model (Christoffel equation), a novel experimental technique, and an inversion algorithm based on Bayesian filtering. An experimental technique based on Coulomb coupling is devised to visualize the propagation of ultrasonic waves in an anisotropic crystal. The crystal is characterized by measuring the directional-dependent acoustic wave velocity from the spatial–temporal information of the wave propagation. The anisotropic constitutive properties of the crystal are estimated by exploring the wave velocity in the Bayesian filtering algorithm. The proposed algorithm is based on the probabilistic framework that integrates the experimental measurement in a physics-based mathematical model for optimal state prediction of stiffness tensor through the Bayesian filtering algorithm. In particular, we utilize the unscented Kalman filter (UKF) in conjunction with the plane-wave Eigen solution to estimate the constitutive parameters. In the presence of measurement uncertainties, the performance of the optimal prediction algorithm is illustrated by comparing the estimated parameter with the corresponding theoretical value. The comparison demonstrates that the proposed inversion algorithm is efficient

and robust and performs satisfactorily even with significant measurement uncertainties.

6.1 Proposed Scheme

Lithium Niobate is an anisotropic single crystal most preferable for photonic, electronic and sensor applications. It has been extensively employed in optical fibres, optical modulators, beam deflectors and thin film photonic devices. In these applications, various cuts of Lithium Niobate are used. Further, the accurate and complete characterisation of the material is essential prior to the usage of the substrate. The piezoelectric substrates are characterised by elastic, piezoelectric, and dielectric material constants. However, the challenge is that crystal growth and chemical composition can largely change the acoustical physical constants compared to the initial stage of the research and development, which can change the velocity of the bulk and guided waves. The main thrust of this study is to develop a robust and reliable framework that can estimate the constitutive parameters of the crystal from the noisy/uncertain velocity profile. We would like to remark that the proposed framework is generic that can be extended to estimate the constitutive parameters of any other anisotropic material.

A novel approach based on a non-linear Bayesian filter is proposed to estimate the constitutive tensor of anisotropic $LiNbO_3$ crystal from wavefield images. Point contact excitation and detection scheme is explored for visualization of the acoustic wave in piezoelectric crystal. One must note that the proposed procedure is modular, so different experimental techniques can also be used to create the measurement dataset. The Bayesian filter is a probabilistic framework; hence it provides a confidence interval of the estimated parameters, which gives an advantage in decision-making. Kalman filter is one of the Bayesian filtering techniques widely accepted in many engineering disciplines, such as climate prediction, spacecraft tracking, and localization of acoustic source emission [245-248]. In this study, we used an unscented Kalman filter among the Bayesian filter available in the literature. The Kalman filtering framework requires a set of physics-based equations and measurement equation that depicts the real-world model.

In the current context, if the constitutive parameter describes the state of a system, then the Christoffel equation can be considered the measurement equation that relates the state to the measurement. However, in practice, these physics-based

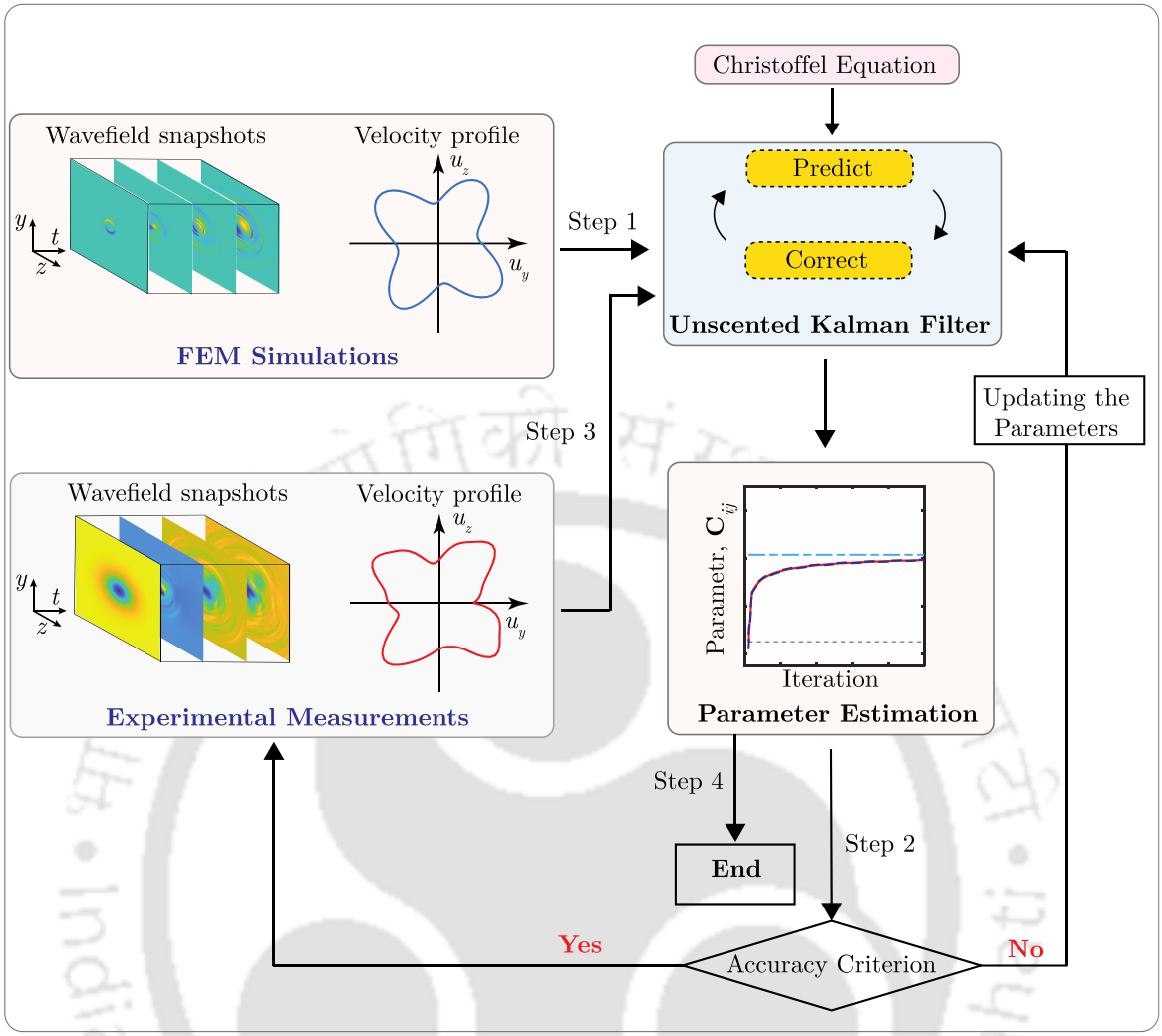

Figure 6.1 The general approach for constitutive parameter estimation, emphasizing the unscented Kalman filter framework.

mathematical equations alone do not prescribe the real-world model accurately. For a highly non-linear system that is prevalent in a real-world case, a small perturbation of noise and/or uncertainties can lead to significant changes in the system's behaviour, stability, and predictability. Kalman filtering is a technique that attempts to mitigate the effect of noise and uncertainties present in the system. The main thrust of the current research is to develop a unified framework for the parameter estimation of the stiffness tensor of the piezoelectric material. The idea is to utilize the measurement information, such as the velocity of ultrasonic waves and integrate it with the numerical model prediction to better estimate the constitutive parameters. Prior to that, the framework of the algorithm is calibrated and verified with the FEM simulation data. The current work conceives the experimental technique using a local electric field probe in conjunction with the Bayesian filter for the estimation of the

constitutive parameters of an anisotropic piezoelectric material. The schematic representation of the overview of the framework accentuating the constitutive parameter estimation framework based on the unscented Kalman filter is shown in Figure 6.1.

6.2 Finite Element Method Simulation

The main aim of conducting numerical finite element method (FEM) analysis is to generate angular velocity maps for anisotropic solids, which further be used for calibration of the proposed UKF algorithm. The accuracy and efficacy of the UKF algorithm for parameter estimation of Lithium Niobate crystal is benchmarked using FEM velocity profile results. The FEM is widely used to simulate ultrasonic wave propagation in an anisotropic substrate. The simulation parameters, such as material properties and excitation waveform, play a significant role in the visualization of transient wave propagation and the modal analysis of waves.

In piezoelectric materials, acoustic wave propagation is governed by two systems of equations; (a) the mechanical equation of motion and (b) Maxwell's equation for electric behaviour. The constitutive characteristics of piezoelectric materials couple these two systems of equations in the elastic range of the material.

$$\begin{aligned} T_{ij} &= C_{ijkl} S_{kl} - e_{kij} E_k, \\ D_i &= e_{ikl} S_{kl} + \varepsilon_{ik} E_k, \end{aligned} \tag{6.1}$$

where, T_{ij} are the stress components, C_{ijkl} the elastic constant, S_{kl} the strain, E_k the electric field intensity, e_{ikl} the piezoelectric constant, and ε_{ik} the permeability. In typical piezoelectric substrates, the acoustic wave propagates five times slower than the electromagnetic waves. Hence, one can assume the piezoelectric coupled field as quasistatic. Therefore, Maxwell's equations can be reduced to

$$\frac{\partial D_i}{\partial x_i} = 0, \tag{6.2}$$

and

$$E_i = -\frac{\partial \varphi}{\partial x_i}, \tag{6.3}$$

where, D_i are the electric field displacement components and φ the electric field potential. The electric charge inside the piezoelectric substrate is assumed to be zero

Table 6.1 Value of the constitutive parameters of the $LiNbO_3$ crystal.

Material	Constitutive Parameters (10^{10} N/m^2)					Density, ρ
	C_{11}	C_{13}	C_{14}	C_{33}	C_{44}	(kg/m^3)
Lithium Niobate	20.3	7.5	0.9	24.5	6	4700

because the substrates are supposed to be perfect insulators. The equation of motion can be expressed in the absence of internal body force as

$$\frac{\partial T_{ij}}{\partial x_j} - \rho \frac{\partial^2 u_i}{\partial t^2} = 0, \tag{6.4}$$

where, ρ is the density of the medium and u_i are the displacement field components. Further, one can define the components of strain as

$$S_{ij} = \frac{1}{2}\left(\frac{\partial u_i}{\partial x_j} + \frac{\partial u_j}{\partial x_i}\right). \tag{6.5}$$

Now, substituting the Eqs. (6.3) and (6.5) into Eq. (6.1) and hence Eqs. (6.2) and (6.4) results in a system of coupled wave equations for the electric potential and displacement in piezoelectric substrates,

$$\begin{aligned} -\rho \frac{\partial^2 u_i}{\partial t^2} + C_{ijkl} \frac{\partial^2 u_k}{\partial x_j \partial x_l} + e_{kij} \frac{\partial^2 \varphi}{\partial x_k \partial x_j} = 0, \\ e_{ikl} \frac{\partial^2 u_k}{\partial x_i \partial x_l} - \varepsilon_{ik} \frac{\partial^2 \varphi}{\partial x_i \partial x_k} = 0. \end{aligned} \tag{6.6}$$

Conveniently these equations are solved using finite element analysis. In this work, 3D FEM simulation of ultrasonic wave in the time domain is conducted in an anisotropic $LiNbO_3$ crystal using commercially available FEM solver COMSOL Multiphysics 5.6 version. The simulated geometry considered here is 8 mm × 8 mm X-cut $LiNbO_3$ substrate having a thickness of 300 μm. Table 6.1 presents the mean theoretical value of the constitutive parameter of $LiNbO_3$ crystal [249]. The piezoelectricity physics is added under the electromagnetic structure interaction menu available in the physics tab of the COMSOL Multiphysics program. This adds both Physics nodes and Multiphysics nodes. Under the physics nodes, the Solid Mechanics and Electrostatics effects are added, and the Piezoelectric effect is considered under the Multiphysics coupling node. In Solid Mechanics physics, the low reflecting

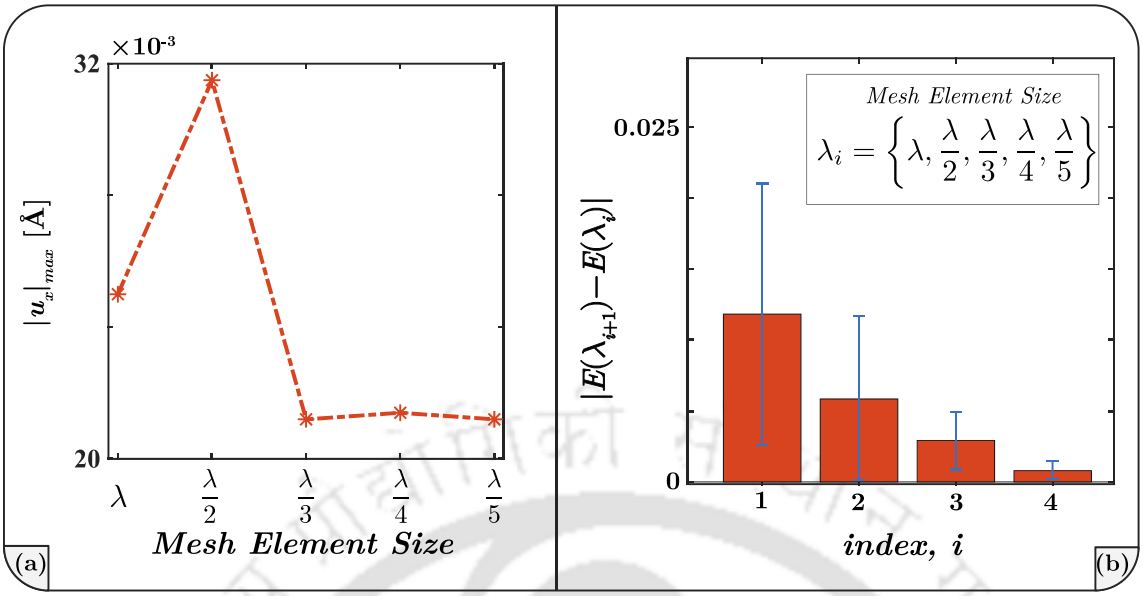

Figure 6.2 Illustration of the convergence of the finite element model for various mesh element sizes, (a) variation of absolute maximum displacement with respect to the different mesh element sizes, and (b) absolute difference of the energy content in the time domain output signal between two consecutive mesh element sizes.

boundary condition is applied at all edges along the bottom boundary to absorb the outgoing waves. Thus, no reflection occurs, and interference among the waves can be avoided. The electrostatic potential and ground boundary conditions are added at the top and bottom flat surfaces under the Electrostatics physics. The time-dependent equations are solved for the low-reflecting boundary given in Eq. (6.7).

$$\sigma \cdot \mathbf{n} = -\mathbf{d}_{\text{im}}(\rho, c_s, c_p)\frac{\partial \mathbf{u}}{\partial t}, \tag{6.7}$$

where, $\mathbf{n}$ is the unit normal vector at the boundary, c_s and c_p are the speeds of pressure and shear waves respectively, and $\mathbf{d}_{\text{im}}$ is the mechanical impedance matrix.

$$\mathbf{d}_{\text{im}} = \rho\frac{c_p + c_s}{2}\mathbf{I}, \tag{6.8}$$

where, $\mathbf{I}$ is the identity matrix.

The excitation rectangular pulse of 20 ns width at an input voltage of 10 V is employed as an input excitation signal. The mesh is generated with tetrahedral elements. To avoid numerical instability, the integration time step (Δt) was selected as $\Delta t = {}^{1}\!/_{20 f_{\max}}$, where $f_{\max}$ is maximum frequency that controls the integration time step and element size. The maximum element size employed in the simulation is less than $\lambda/5$, which corresponds to, five mesh elements per wavelength. Here, λ is

the shortest wavelength of the ultrasonic wave. However, for the convergence study, the maximum mesh element size is kept as $\lambda/factor$, where the *factor* at denominator is varied from 1 to 5, corresponding to 1 to 5 mesh elements per wavelength. To investigate the convergence properties of the FEM model, two metrics are considered: (a) the absolute maximum displacement of the output displacement signal and (b) The absolute difference of the energy content in the output signal. The maximum displacement along the perpendicular direction of the substrate plane at an arbitrarily chosen point (0, 1, 1) is illustrated in Figure 6.2(a). This can be observed that the result converges for a *factor* value of more than 2. Figure 6.2(b) illustrates the absolute difference of the energy content in the output time-domain displacement signals for two consecutive mesh element sizes. The outputs are taken from 10 arbitrarily chosen points on the FEM model for the various mesh element sizes. The blue bar in Figure 6.2(b) depicts the $\mu \pm \sigma$ where μ is average value and σ is the standard deviation of the ten samples considered in the study. For instance, $E(\lambda/3)$ indicates the energy of the output signal corresponding to the mesh element size of $\lambda/3$. Note that the energy difference approaches zero ($|E(\lambda/5) - E(\lambda/4)| \rightarrow 0$) ,that indicates the model converges with sufficient accuracy for the mesh element size of $\lambda/5$. In the simulation, time-dependent analysis and time-dependent solver are used for the solution. The directional-dependent velocity profile is extracted and used for UKF code calibration, as discussed in Section 6.5.3.

6.3 Theory

6.3.1 Christoffel equation

The stiffness tensor $\mathbf{C}$ is an elementary characteristic of a material. It relates stresses and strains within the elastic limit by generalizing the three-dimensional Hooke's law.

$$T_{ij} = \sum_{mn} C_{ijmn} S_{mn}, \tag{6.9}$$

where, T is the stress tensor and S is the strain tensor. The generalized stiffness matrix $\mathbf{C}$ is a second-order tensor, and for non-polar material, it is expressed by 6×6 matrix.

$$\mathbf{C} = \begin{bmatrix} C_{11} & C_{12} & C_{13} & C_{14} & C_{15} & C_{16} \\ C_{21} & C_{22} & C_{23} & C_{24} & C_{25} & C_{26} \\ C_{31} & C_{32} & C_{33} & C_{34} & C_{35} & C_{36} \\ C_{41} & C_{42} & C_{43} & C_{44} & C_{45} & C_{46} \\ C_{51} & C_{52} & C_{53} & C_{54} & C_{55} & C_{56} \\ C_{61} & C_{62} & C_{63} & C_{64} & C_{65} & C_{66} \end{bmatrix}. \tag{6.10}$$

In addition to the information about static deformations, the propagation of the elastic wave in a material is governed by the structural form of the stiffness tensor. The evolution and propagation of the longitudinal and transversal bulk wave in an anisotropic crystal are illustrated with the Christoffel equation [250].

$$[\Gamma_{ij} - \rho\omega^2\delta_{ij}]U_j = 0. \tag{6.11}$$

For a monochromatic wave with frequency ω, polarisation $\bar{U}$ and wave vector $\mathbf{n}$ propagating through a material of density ρ, then the Christoffel matrix Γ is defined as:

$$\Gamma_{ij} = n_m C_{imnj} n_j. \tag{6.12}$$

The Eq. (6.11) is a simple Eigenvalue problem that can be solved systematically for any value of $\mathbf{n}$. The Eigenvalue solution consists of three frequencies that ultimately lead to the three phase velocities for each value of $\mathbf{n}$. For $LiNbO_3$, which is a trigonal crystal, in the yz plane polarisation along the *x-axis,* the velocity of the pure shear wave, $u^{(2)}$ along the propagation angle ϕ is given by [249]

$$u^{(2)} = \frac{1}{\rho^{1/2}\{C_{66}\sin^2\phi + C_{44}\cos^2\phi + C_{14}\sin 2\phi\}^{1/2}}. \tag{6.13}$$

The velocity of the Quasi-shear wave, $u^{(1)}$ is described by

$$u^{(1)} = \frac{1}{(2\rho)^{1/2}\left\{P - \sqrt{Q^2+R}\right\}^{-1/2}}. \tag{6.14}$$

The velocity of the Quasi-longitudinal wave, $u^{(3)}$ is described by

$$u^{(3)} = \frac{1}{(2\rho)^{1/2}\left\{P + \sqrt{Q^2+R}\right\}^{-1/2}}, \tag{6.15}$$

where,

$$\begin{aligned} P &= C_{44} + C_{11}\sin^2\phi + C_{33}\cos^2\phi - C_{14}\sin 2\phi, \\ Q &= (C_{44} - C_{11})\sin^2\phi + (C_{33} - C_{44})\cos^2\phi + C_{14}\sin 2\phi, \end{aligned} \tag{6.16}$$

$$R = \{(C_{13} + C_{14}) \sin 2\phi - 2C_{14} \sin^2 \phi\}^2.$$

6.3.2 Calculation of wave velocity

Considering an arbitrary Cartesian coordinate system in the plane of an anisotropic substrate, a particular wave mode travelled at time t_i from a location (y_i, z_i), and it reached the location (y_j, z_j) at time t_j. The velocity of a wave along an angle ϕ can be computed as:

$$u_\phi^{\{k\}} = \frac{\sqrt{(y_j - y_i)^2 + (z_j - z_i)^2}}{(t_j - t_i)}. \tag{6.17}$$

The velocity is computed repeatedly in several adjacent points along a particular radial direction $(k = 1,2,\dots,n)$ to evaluate the uncertainty in the velocity measurement. For anisotropic material, the wave velocity depends on the direction of propagation ϕ and can be defined as:

$$\phi = \arctan\left(\frac{z_j - z_i}{y_j - y_i}\right), \tag{6.18}$$

$$\mathbf{u}_\phi = \left[u_\phi^{\{1\}}, u_\phi^{\{2\}}, \dots, u_\phi^{\{n\}}\right], \tag{6.19}$$

where, $\mathbf{u}_\phi$ is a vector representing a collection of all the velocities calculated at various points along the propagation ϕ. An illustration of the steps involved in the computation of the velocity and the corresponding uncertainty is presented in Figure

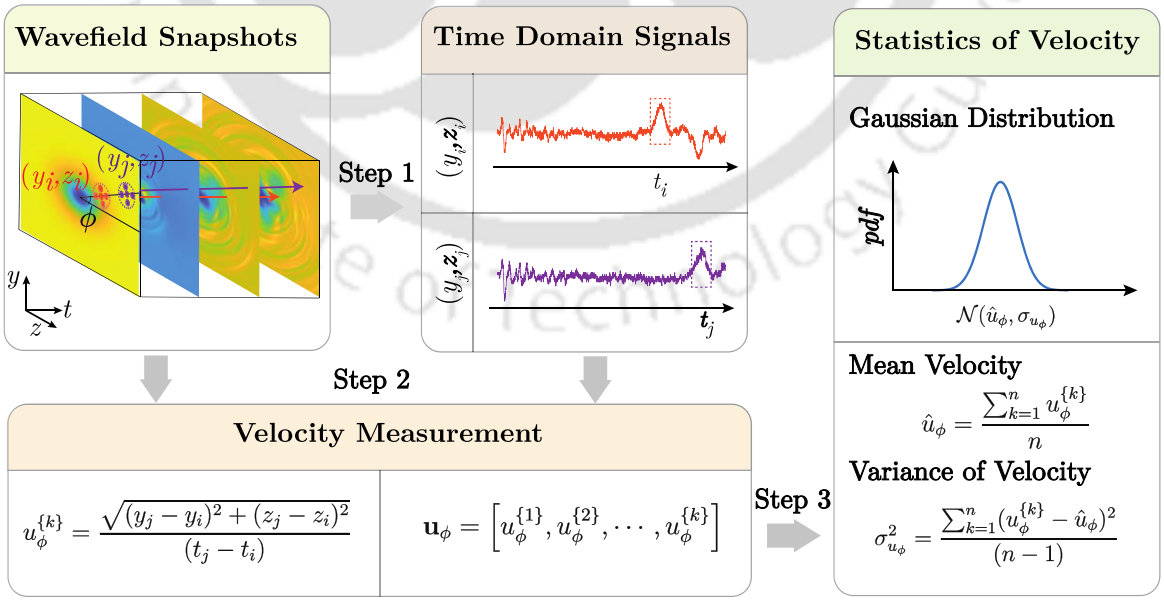

Figure 6.3 Illustration of the steps involved in the computation of the statistical velocity.

6.3. It is assumed that the probability distribution function of the velocity follows the Gaussian distribution. The sample mean, $\hat{u}_\phi$ and sample variance, $\sigma^2_{u_\phi}$ can be computed as follows:

$$\hat{u}_\phi = \frac{\sum_{k=1}^{n} u_\phi^{\{k\}}}{n}, \tag{6.20}$$

$$\sigma^2_{u_\phi} = \frac{\sum_{k=1}^{n} \left(u_\phi^{\{k\}} - u_\phi\right)^2}{(n-1)}. \tag{6.21}$$

6.4 Unscented Kalman Filter

One of the key components in the development of the proposed framework is to estimate the constitutive parameters from the velocity profile. This is can be considered as a classical parameter estimation problem, and this study proposes to employ the Bayesian filter to achieve the objective. Bayesian filters utilise Bayesian inference to formulate a framework that can be used for parameter estimation. Bayesian inference differs from the conventional frequentist approach (e.g., maximum likelihood estimation (MLE)). The Bayesian inference takes the uncertainty of an event in a single trial as the probability of an event. In contrast, the frequentist approach considers it as the proportion of the event in probability space, despite the fact that the full posterior estimation in the Bayesian approach is accurate but computationally expensive and is often intractable. The first-order Markovian process assumption simplifies the computational intricacy. Using assumptions of the Markovian model, the recursive Bayesian filter can be established, and the Kalman filter emerges [251, 252]. The Kalman filter is a particular type of recursive Bayesian filter applied for a linear model. The extended Kalman filter (EKF) [251] and unscented Kalman filter (UKF) [251, 253] are advancements over the Kalman filter to apply for non-linear models. In this study, UKF is used as a Bayesian filter of choice over the other Bayesian filter and the conventional frequentist approach. It is to be noted that the UKF is computationally expensive as compared to the EKF and MLE; however, the performance of the UKF in the case of non-linear systems and small observed data regime is Indeed, powered by the increased computational resources, the proposed UKF based framework results as robust and reliable for the parameter estimation task.

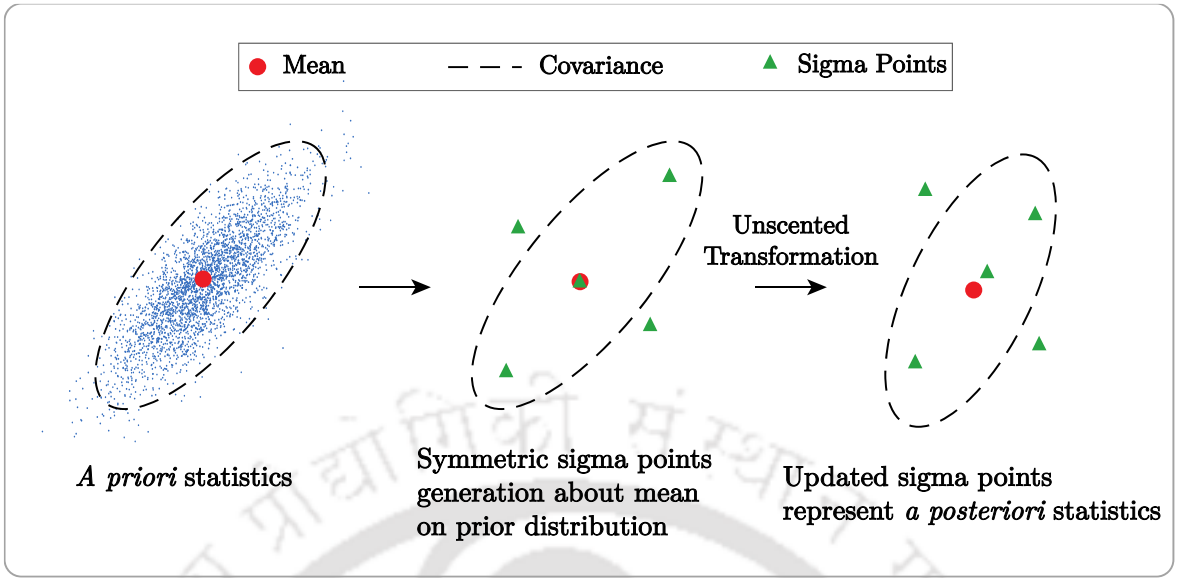

Figure 6.4 Illustration of unscented transformation of a distribution using sigma points.

The solution of the Christoffel equation prescribes a set of mathematical models of the velocity of a wave in a material. For instance, the governing equation describes the velocity of the Quasi-shear wave in Lithium Niobate crystal in the YZ plane given in the Eq. (6.14) is a complex non-linear system. The UKF is a versatile filter appropriate for complex non-linear systems first developed by Julier, *et al.* (1995) [140]. It utilizes the concept of unscented transformation to approximate the statistics of fairly complex non-linear systems. In the unscented transformation, the statistical properties of a random variable are approximated by choosing a set of sample points deterministically. These points are known as sigma points. Each sigma point is propagated through the non-linear systems to apply the non-linear transformation. These transformed sets of points represent the statistical properties of the transformed random variable. Figure 6.4 illustrates how sigma points are employed in the unscented transformation to represent *a posteriori* statistic.

Let us consider a general discrete non-linear dynamical system modelled as

$$\begin{aligned} \mathbf{x}_{k+1} &= \mathbf{F}(\mathbf{x}_k) + \mathbf{w}_k, \\ \mathbf{y}_k &= \mathbf{H}(\mathbf{x}_k) + \mathbf{v}_k \end{aligned} \tag{6.22}$$

where, $\mathbf{F} : \mathbb{R}^N \longmapsto \mathbb{R}^N$ is the vector-valued state prediction function of the system, $\mathbf{H} : \mathbb{R}^N \longmapsto \mathbb{R}^M$ is the observation function that transforms a state vector into the proper measurement vector. The $\mathbf{x}_k \in \mathbb{R}^N$ is the state variable, $\mathbf{y}_k \in \mathbb{R}^M$ is the measured

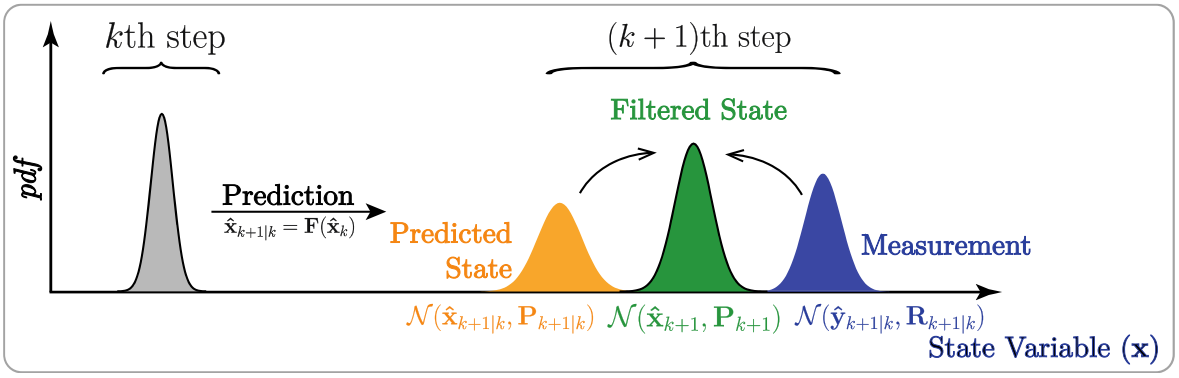

Figure 6.5 Schematic presentation of the steps involved in the unscented Kalman filter algorithm.

value, and $\mathbf{w}_k \in \mathbb{R}^N$ and $\mathbf{v}_k \in \mathbb{R}^M$ are additive process noise with covariance $\mathbf{Q}$ and measurement noise with covariance $\mathbf{R}$, respectively, as in the Eq. (6.23). The subscript $k \in \mathbb{N}$ denotes the kth discrete step.

$$\begin{aligned} \mathbf{w}_k &\sim \mathcal{N}(\mathbf{0}, \mathbf{Q}_k), \\ \mathbf{v}_k &\sim \mathcal{N}(\mathbf{0}, \mathbf{R}_k), \\ \mathbb{E}[\mathbf{w}_k \mathbf{v}_k^T] &= \mathbf{0}. \end{aligned} \tag{6.23}$$

It is assumed that the state variable $\mathbf{x}_k \in \mathbb{R}^N$ obeys a normal distribution with its mean $\hat{\mathbf{x}}_k$ and covariance $\mathbf{P}_k$ denoted by $\mathbf{x}_k \sim \mathcal{N}(\mathbf{x}_k, \mathbf{P}_k)$. We also suppose that the initial state, $\hat{\mathbf{x}}_0$, is known with the corresponding initial error covariance matrix, $\mathbf{P}_0$. The UKF algorithm is discussed briefly in the following Section 6.4.1. A probabilistic approach to the key steps involved within the UKF framework is shown schematically in Figure 6.5.

6.4.1 UKF algorithm

Step 1: Calculation of weights for sigma points

A set of weights $\mathbf{W}^{(i)}$ corresponds to each sigma point are defined as follows:

$$\begin{aligned} \mathbf{W}^{(0)} &= \frac{\kappa}{N+\kappa}, \\ \mathbf{W}^{(i)} &= \frac{1}{2(N+\kappa)}, \quad i = 1,2,\ldots,2N \end{aligned} \tag{6.24}$$

where, the parameter κ is the scaling parameter that controls the spread of the sigma point about the mean, $\hat{\mathbf{x}}_{k|k}$ and N is the length of the state vector. κ can take any positive or negative value such that $N + \kappa \neq 0$. In this study, it has been chosen $\kappa = 0$.

Step 2: Define noise

$$\begin{aligned}\mathbf{Q}_k &= \mathbb{E}[\mathbf{w}_k\mathbf{w}_k^T],\\ \mathbf{R}_k &= \mathbb{E}[\mathbf{v}_k\mathbf{v}_k^T].\end{aligned} \tag{6.25}$$

Step 3: Initialization

Define the initial state vector and corresponding error covariance matrix as:

$$\begin{aligned}\hat{\mathbf{x}}_0 &= \mathbb{E}[\mathbf{x}_0],\\ \mathbf{P}_0 &= \mathbb{E}[(\mathbf{x}_0-\hat{\mathbf{x}}_0)(\mathbf{x}_0-\hat{\mathbf{x}}_0)^T].\end{aligned} \tag{6.26}$$

Step 4: Generate the sigma points

A set of $2N+1$ sigma points $\boldsymbol{\chi}_k^{(i)}$ are defined as follows:

$$\begin{aligned}\boldsymbol{\chi}_k^{(0)} &= \hat{\mathbf{x}}_k,\\ \boldsymbol{\chi}_k^{(i)} &= \hat{\mathbf{x}}_k + \sqrt{N+\kappa}(\sqrt{\mathbf{P}_k})_i,\\ \boldsymbol{\chi}_k^{(i+N)} &= \hat{\mathbf{x}}_k - \sqrt{N+\kappa}(\sqrt{\mathbf{P}_k})_i,\end{aligned} \tag{6.27}$$

where $(\sqrt{\mathbf{P}_k})_i$ is the ith column of the matrix square root of the error covariance matrix $\mathbf{P}_k$. The weighted covariance matrix of $\boldsymbol{\chi}$ is $\mathbf{P}_k$ can be computed as:

$$\mathbf{P}_k = \sum_{i=0}^{2N}\mathbf{W}_k^{(i)}\left(\boldsymbol{\chi}_k^{(i)}-\hat{\mathbf{x}}_k\right)\left(\boldsymbol{\chi}_k^{(i)}-\hat{\mathbf{x}}_k\right)^T. \tag{6.28}$$

Step 5: Prediction

Propagate each sigma points through the prediction model

$$\boldsymbol{\chi}_{k+1|k}^{(i)} = \mathbf{F}\left(\boldsymbol{\chi}_k^{(i)}\right), \quad i = 0,1,\ldots,2N \tag{6.29}$$

Calculate the mean $\hat{\mathbf{x}}_{k+1|k}$ and covariance $\mathbf{P}_{k+1|k}$ of the predicted state as given by:

$$\begin{aligned}\hat{\mathbf{x}}_{k+1|k} &= \sum_{i=0}^{2N}\mathbf{W}^{(i)}\boldsymbol{\chi}_{k+1|k}^{(i)},\\ \mathbf{P}_{k+1|k} &= \sum_{i=0}^{2N}\mathbf{W}^{(i)}\left(\boldsymbol{\chi}_{k+1|k}^{(i)}-\hat{\mathbf{x}}_{k+1|k}\right)\left(\boldsymbol{\chi}_{k+1|k}^{(i)}-\hat{\mathbf{x}}_{k+1|k}\right)^T+\mathbf{Q}_{k+1}.\end{aligned} \tag{6.30}$$

Step 6: Observation

Propagate each sigma point through observation

$$\boldsymbol{\Psi}_{k+1|k}^{(i)} = \mathbf{H}\left(\boldsymbol{\chi}_{k+1|k}^{(i)}\right), \quad i = 0,1,\ldots,2N \tag{6.31}$$

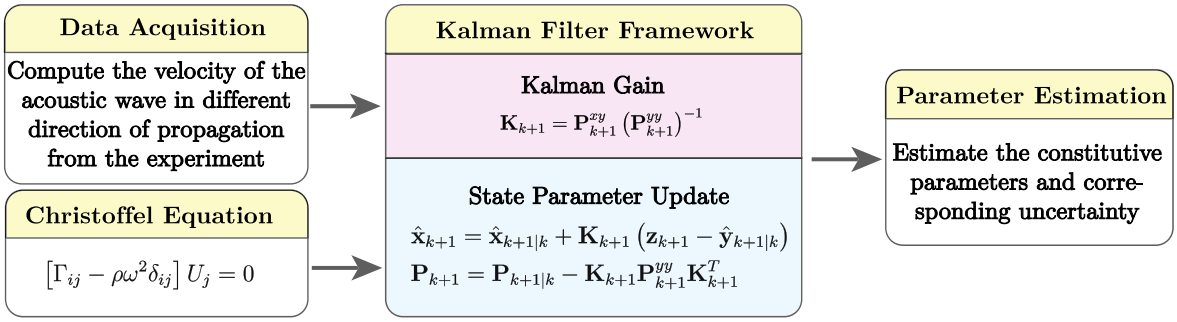

Figure 6.6 Flowchart representing key components of the proposed parameter estimation algorithm.

Calculate the mean $\hat{\mathbf{y}}_{k+1|k}$, covariance of predicted output $\mathbf{P}^{yy}_{k+1}$ and cross-covariance of state and output $\mathbf{P}^{xy}_{k+1}$ as given by:

$$\begin{aligned}
\hat{\mathbf{y}}_{k+1|k} &= \sum_{i=0}^{2N} \mathbf{W}^{(i)} \boldsymbol{\Psi}^{(i)}_{k+1|k}, \\
\mathbf{P}^{yy}_{k+1} &= \sum_{i=0}^{2N} \mathbf{W}^{(i)} \left(\boldsymbol{\Psi}^{(i)}_{k+1|k} - \widehat{\mathbf{y}}_{k+1|k}\right) \left(\boldsymbol{\Psi}^{(i)}_{k+1|k} - \widehat{\mathbf{y}}_{k+1|k}\right)^T + \mathbf{R}_{k+1}, \\
\mathbf{P}^{xy}_{k+1} &= \sum_{i=0}^{2N} \mathbf{W}^{(i)} \left(\boldsymbol{\chi}^{(i)}_{k+1|k} - \widehat{\mathbf{x}}_{k+1|k}\right) \left(\boldsymbol{\Psi}^{(i)}_{k+1|k} - \widehat{\mathbf{y}}_{k+1|k}\right)^T.
\end{aligned} \tag{6.32}$$

Step 7: Update

Compute Kalman gain $\mathbf{K}_k$, filtered state mean $\hat{\mathbf{x}}_{k+1}$ and error covariance $\mathbf{P}_{k+1}$ provided the sensor measurement $\mathbf{z}_{k+1}$ as follows:

$$\begin{aligned}
\mathbf{K}_{k+1} &= \mathbf{P}^{xy}_{k+1} (\mathbf{P}^{yy}_{k+1})^{-1}, \\
\hat{\mathbf{x}}_{k+1} &= \hat{\mathbf{x}}_{k+1|k} + \mathbf{K}_{k+1} (\mathbf{z}_{k+1} - \hat{\mathbf{y}}_{k+1|k}), \\
\mathbf{P}_{k+1} &= \mathbf{P}_{k+1|k} - \mathbf{K}_k \mathbf{P}^{yy}_{k+1} \mathbf{K}^T_{k+1}.
\end{aligned} \tag{6.33}$$

The UKF is used for the estimation of constitutive parameters of an anisotropic crystal. The essential parts of the robust algorithm are illustrated in Figure 6.6.

6.5 Results and Discussion

6.5.1 FEM simulation results

The transient time domain signals obtained at various points from the simulation are used to visualise the ultrasonic wave in the $LiNbO_3$ crystal. Figure 6.7 shows the visualisation of wave propagation in the $LiNbO_3$ crystal acquired through FEM simulation. The total acquisition time of the temporal images of 1 μs corresponding

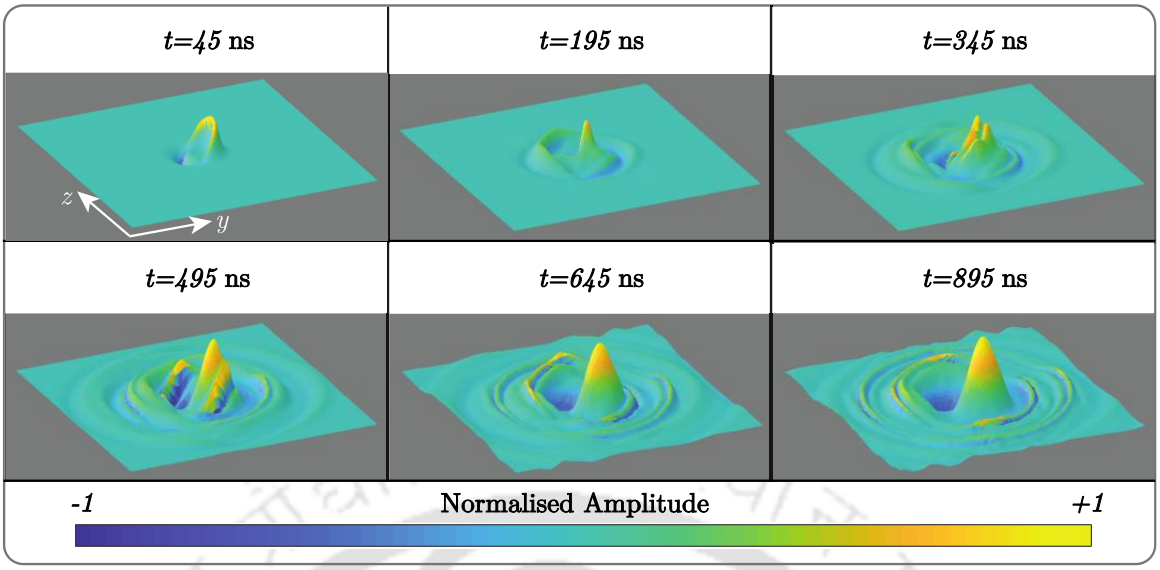

Figure 6.7 Pseudo-3D representation of the ultrasonic wave propagation on X-cut 300 µm thick $LiNbO_3$ crystal obtained for the finite element method simulation case. Each frame dimension is 8 mm × 8mm.

to 201 time-varying snapshots. Each frame of Figure 6.7 corresponds to 150 ns in the transient signals. The numerical velocity results are incorporated in the UKF algorithm for establishing the accuracy of the parameter estimation.

The Kalman filter utilized the combined information of field measurement and governing mechanistic equation for the estimation of state parameters. However, to illustrate the efficiency of the Kalman filter algorithm, we measured the velocity at an angular spacing of 15° varying from 0° to 360°.

In Figure 6.8, the blue line represents the theoretical velocity profile for the Quasi-shear wave in $LiNbO_3$ crystal, which is computed by the Eigen solution of the Christoffel equation. Further, the circle legends represent the numerical average velocity of the ultrasonic wave calculated along a particular direction of propagation. Upon computing discrete velocity in different directions, a cubic Hermite interpolation was performed to approximate the velocity in all directions. The resulting profile is shown by the red dashed line in Figure 6.8. However, this approximate velocity profile does not require in the UKF framework.

6.5.2 Experimental results

We present the visualization of propagation of the ultrasonic wave in $LiNbO_3$ acquired through the Coulomb Coupling method. After the acquisition of the transient signals

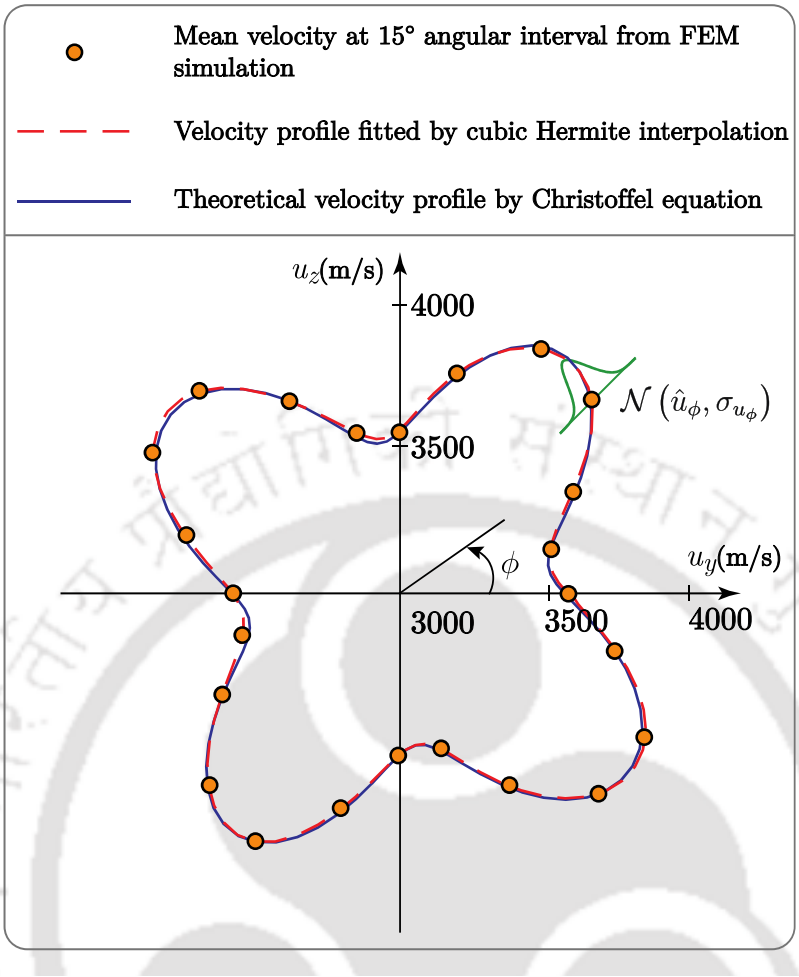

Figure 6.8 The ultrasonic velocity profile computed from finite element method simulation in various directions for Lithium Niobate crystal.

for every position of the scanner, time gating was performed to construct the snapshot of the ultrasound waves.

Figure 6.9 shows the pseudo-3D evolution of ultrasonic waves in $LiNbO_3$ crystal at an excitation gate width of 35 ns. The speed of the ultrasonic wave in an anisotropic solid is directional dependent and evident from Figure 6.9. Each frame of Figure 6.9 corresponds to 13.3 μs in the transient signal. The brightness of the images indicates wavefront on the crystal surface at the corresponding gating time. The velocity of the ultrasonic wave in each direction is calculated from the evolution of spatiotemporal snapshots. The advantage of the Coulomb coupling technique is it provides complete field transient imaging, so it is possible to compute the velocity in every direction.

The theoretical velocity profile computed by the Eigen solution of the Christoffel equation for the Quasi-shear wave in $LiNbO_3$ crystal is presented by the blue line in Figure 6.10. The circle legends in Figure 6.10 illustrate the average experimental

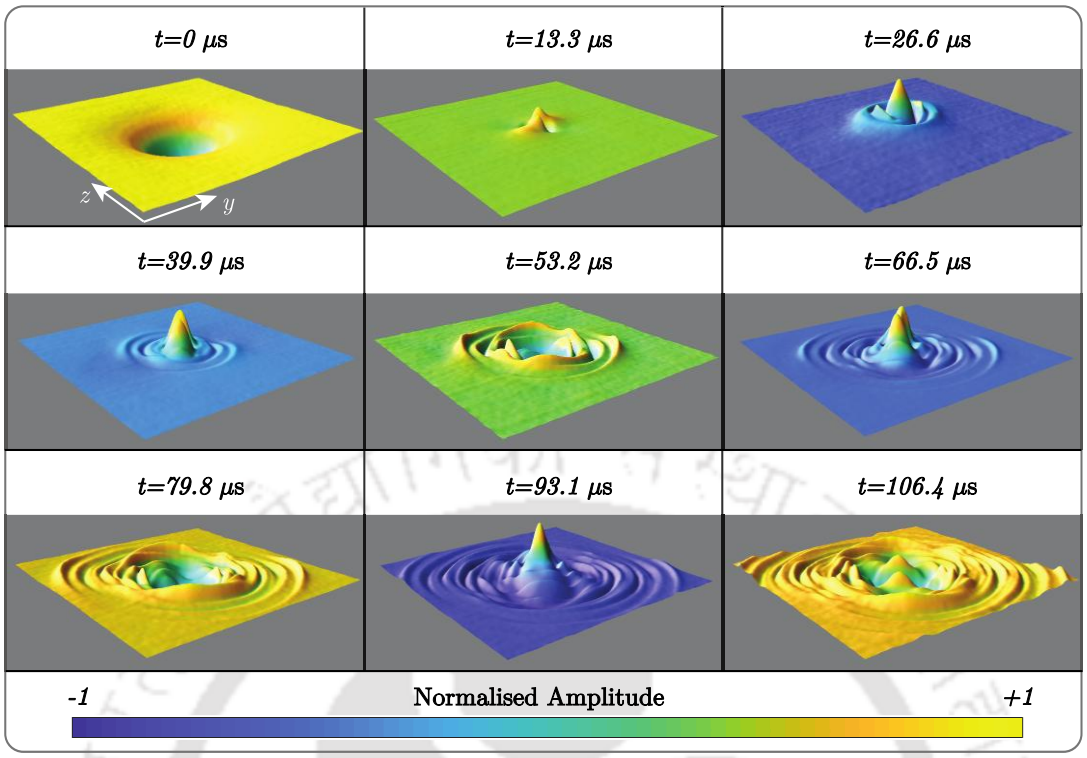

Figure 6.9 Pseudo-3D representation of the spatial and temporal evolution of the ultrasonic wave amplitude of images on X orientation 1 mm thick, $LiNbO_3$ crystal at a gate width of 35 ns for the experimental case. Each image frame dimension is 20 mm × 20 mm.

velocities calculated in a particular direction of propagation. The dashed red line in Figure 6.10 shows the interpolated velocity profile.

6.5.3 Verification of UKF algorithm using FEM simulation data

The transient time domain signals obtained at various points from the simulation are used to visualise the ultrasonic wave in the $LiNbO_3$ crystal, as shown in Figure 6.7. The velocity of the propagated wave along different directions is computed from the simulation data. The constitutive parameters estimation of the crystal from the velocity data is an ill-posed inverse problem, and the noisy/uncertain velocity data compounds this challenge.

Usually, the data obtained from the simulation are more accurate and noise-free compared to the data collected from real field experiments. Moreover, in the case of simulation, the parameters to be estimated are known *a priori*. In general, starting with a problem where the solution is known is important to evaluate the performance and verify the architecture of the proposed algorithm. Thus, we evaluate the

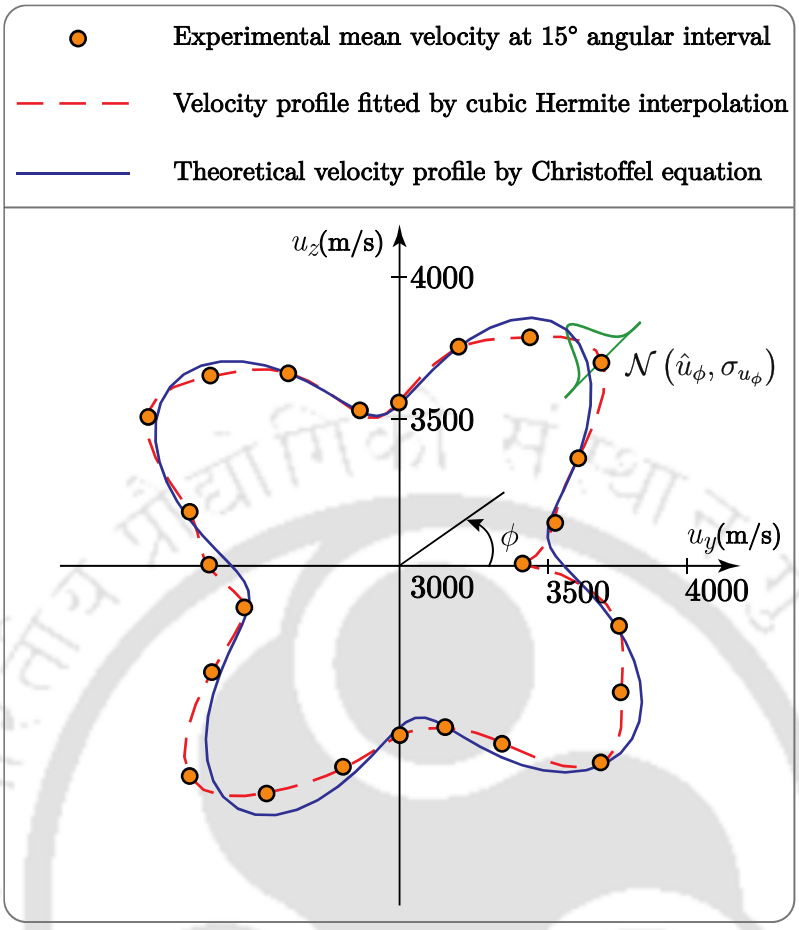

Figure 6.10 The variation of ultrasonic velocity in different directions evaluated from the experiment for Lithium Niobate crystal.

performance of the algorithm by comparing the estimated parameters with the known parameters (theoretical value) used in the FEM simulation.

To illustrate the performance of the UKF in parameter estimation, we considered the non- linear characteristic model for Quasi-shear wave propagation as expressed in the Eq. (6.14). We considered that the velocity measurements are available in different directions. The objective here is to estimate the constitutive parameters accurately by diffusing the mathematical model and the experimental measurements available in the UKF framework. Figure 6.8 shows the variation of mean velocity, $\hat{u}$ with respect to the angle ϕ extracted from the FEM simulation.

For the parameter estimation using UKF, an augmented state vector $\mathbf{x}$ is defined as:

$$\mathbf{x} = \begin{bmatrix} x_1 \\ x_2 \\ x_3 \\ x_4 \\ x_5 \end{bmatrix} = \begin{bmatrix} C_{11} \\ C_{13} \\ C_{14} \\ C_{33} \\ C_{44} \end{bmatrix}. \tag{6.34}$$

Then the state space is formulated as follows:

$$\dot{\mathbf{x}} = \begin{bmatrix} \dot{x}_1 \\ \dot{x}_2 \\ \dot{x}_3 \\ \dot{x}_4 \\ \dot{x}_5 \end{bmatrix} = \begin{bmatrix} 0 \\ 0 \\ 0 \\ 0 \\ 0 \end{bmatrix}. \tag{6.35}$$

The derivatives with respect to the time of the constitutive parameters are all zero because they are assumed to be constant over time. A discrete form of the Eq. (6.35) is given by:

$$\mathbf{x}_{k+1} = \mathbf{F}(\mathbf{x}_k) + \mathbf{w}_k = \begin{bmatrix} x_{1,k} \\ x_{2,k} \\ x_{3,k} \\ x_{4,k} \\ x_{5,k} \end{bmatrix} + \mathbf{w}_k, \tag{6.36}$$

where a process noise $\mathbf{w}$ has been added.

If the velocity of the wave propagation in a crystal is measured, the observation equation can be expressed as:

$$y = u + v, \tag{6.37}$$

where u is the velocity and v represents the measurement noise.

The vector-valued non-linear function $\mathbf{H}$ in Eq. (6.22) can be defined by Eq. (6.14) written as follows:

$$\mathbf{y}_k = \mathbf{H}(\mathbf{x}_k) + \mathbf{v}_k = \frac{1}{(2\rho)^{1/2}\left\{P - \sqrt{Q^2 + R}\right\}^{-1/2}} + v_k. \tag{6.38}$$

By combining the Eqs. (6.16) and (6.34), the P, Q and R of the Eq. (6.38) are re-written as follows:

$$\begin{aligned} P &= x_{5,k} + x_{1,k}\sin^2\phi + x_{4,k}\cos^2\phi - x_{3,k}\sin 2\phi, \\ Q &= (x_{5,k} - x_{1,k})\sin^2\phi + (x_{4,k} - x_{5,k})\cos^2\phi + x_{3,k}\sin 2\phi, \\ R &= \{(x_{2,k} + x_{3,k})\sin 2\phi - 2x_{3,k}\sin^2\phi\}^2. \end{aligned} \tag{6.39}$$

To perform the parameter estimation using the UKF, the iteration process initiates within the UKF framework by initializing the state vector estimate $\hat{\mathbf{x}}_0$ and its error covariance matrix $\mathbf{P}_0$. It was observed that naively applying UKF to data with uncertainty for parameter estimation would often result in incorrect estimation, as the effects of noise variance in the data set. Hence, we configure the initial state vector estimate $\hat{\mathbf{x}}_0$ and the initial covariance matrix $\mathbf{P}_0$ to ensure that the UKF can be applied as follows:

$$\begin{aligned}\hat{\mathbf{x}}_0 &= [C_{11,0}, C_{13,0}, C_{14,0}, C_{33,0}, C_{44,0}]^T \\ &= [10, 0.2, 0.3, 12, 3]^T \times 10^{10}\mathrm{N/m^2}, \\ \mathbf{P}_0 &= diag\left(\sigma^2_{C_{11,0}}, \sigma^2_{C_{13,0}}, \sigma^2_{C_{14,0}}, \sigma^2_{C_{33,0}}, \sigma^2_{C_{44,0}}\right) \\ &= diag(1.58, 1.58, 1.00, 1.58, 1.58) \times 10^{22}(\mathrm{N/m^2})^2,\end{aligned} \tag{6.40}$$

where $diag(\cdot)$ is a diagonal matrix with arguments along the main diagonal. Further, the process noise covariance matrix $\mathbf{Q}$ is set to be null, since the state $\mathbf{x}$ has no superimposed noise. The measurement noise is assumed to be a Gaussian white noise process with zero mean and covariance matrix $\mathbf{R}$ with the terms along the main diagonal are defined in the Eq. (6.21).

$$\mathbf{R} = \begin{bmatrix} \sigma^2_{u_{0^\circ}} & 0 & \cdots & 0 \\ 0 & \sigma^2_{u_{15^\circ}} & & \vdots \\ \vdots & & \ddots & 0 \\ 0 & \cdots & 0 & \sigma^2_{u_{360^\circ}} \end{bmatrix}. \tag{6.41}$$

In the context of the general experimental procedure, it is assumed that the wave velocity measurements ($\mathbf{z}_k$) in different directions are available by extracting data at every 15° angular spacing varying from 0° to 360°.

$$\mathbf{z}_k = \{\hat{u}_{0^\circ}, \hat{u}_{15^\circ}, \ldots, \hat{u}_{360^\circ}\}^T. \tag{6.42}$$

The UKF algorithm starts by generating eleven ($2N+1$, here $N=5$) sigma points deterministically based on $\hat{\mathbf{x}}_0$ and $\mathbf{P}_0$ as defined in the Eq. (6.27). In the following step, each sigma point is employed to compute the wave velocity in the directions where field measurements are present. The algorithm will correct the initial guess in the first iteration by incorporating the innovations $(\mathbf{z}_{k+1} - \hat{\mathbf{y}}_{k+1|k})$ (difference between measurement and predicted measurement). This process continues recursively till the truncation criterion is achieved. The truncation criterion is achieved in this study by setting the minimum number of iterations to 50 ($k = 1,2,\ldots,50$). However, one can

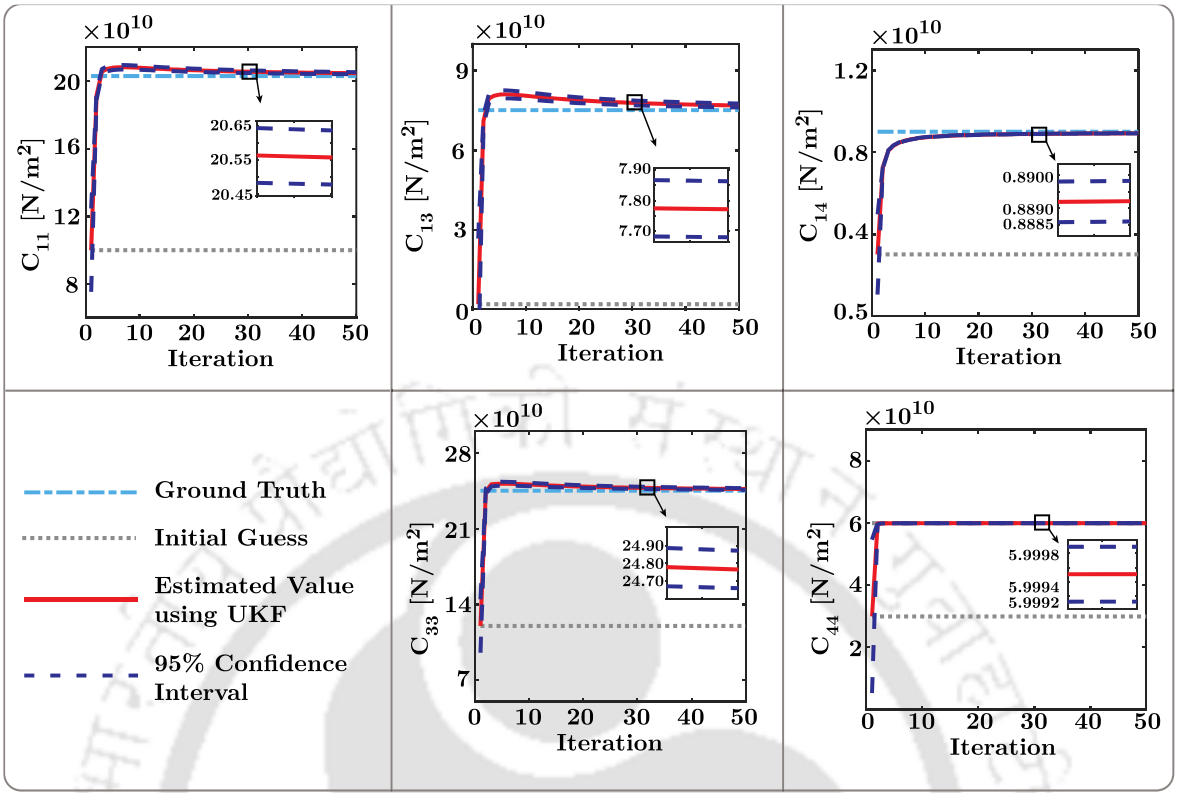

Figure 6.11 Constitutive parameter estimation results for the Lithium Niobate crystal for finite element method simulation case. The velocity with uncertainty computed from the finite element method simulation is provided to the unscented Kalman filter as a measurement.

achieve the truncation criterion by defining a tolerance limit ε as the absolute difference between the state vector estimates given by two successive Kalman Filter iterations (i.e. $\hat{\mathbf{x}}_{k+1} - \hat{\mathbf{x}}_k < \varepsilon$). The output of the UKF algorithm is the corrected state vector which is the mean $\hat{\mathbf{x}}_k$ of the multivariate Gaussian distribution with the covariance matrix $\mathbf{P}_k$. Specifically, $\mathbf{P}_k$ stands for the uncertainty in estimating the constitutive parameters at kth step.

Table 6.2 Sigma points of the initial state vector in unscented Kalman filter framework for the finite element method simulation case.

Sigma Point	1	2	3	4	5	6	7	8	9	10	11
$C_{11}(\times 10^{10}\mathrm{N/m^2})$	10	12.815	10	10	10	10	7.185	10	10	10	10
$C_{13}(\times 10^{10}\mathrm{N/m^2})$	0.2	0.2	3.015	0.2	0.2	0.2	0.2	-2.615	0.2	0.2	0.2
$C_{14}(\times 10^{10}\mathrm{N/m^2})$	0.3	0.3	0.3	0.524	0.3	0.3	0.3	0.3	0.076	0.3	0.3
$C_{33}(\times 10^{10}\mathrm{N/m^2})$	12	12	12	12	14.815	12	12	12	12	9.185	12
$C_{44}(\times 10^{10}\mathrm{N/m^2})$	3	3	3	3	3	5.815	5	5	5	5	0.185

Table 6.3 Summary of the constitutive parameter estimation for the finite element method simulation case.

Constitutive Parameters	Theoretical Values	Initial Guess	Estimated	Relative % Error (±)
$C_{11}(\times 10^{10}\mathrm{N/m^2})$	20.3	10	20.47	0.84%
$C_{13}(\times 10^{10}\mathrm{N/m^2})$	7.5	0.2	7.67	2.27%
$C_{14}(\times 10^{10}\mathrm{N/m^2})$	0.9	0.3	0.89	1.11%
$C_{33}(\times 10^{10}\mathrm{N/m^2})$	24.5	12	24.66	0.65%
$C_{44}(\times 10^{10}\mathrm{N/m^2})$	6.0	3	5.99	0.20%

For ease of reference, Table 6.2 and Table 6.4 present the generated sigma points, $\boldsymbol{\chi}_0^{(i)}$ corresponding to the initial state vector within the UKF algorithm. Figure 6.11 and Figure 6.12 illustrate the parameter estimation results in terms of theoretical value and estimated parameters in every iteration. The dashed lines in Figure 6.11 and Figure 6.12 indicate the 95% confidence interval (CI), implying the actual parameter lies between this interval with a probability of more than 0.95. The UKF being a Bayesian filter that has the capability to provide a level of confidence for the estimate, makes the algorithm superior to the other deterministic algorithms. We summarise the estimation of the constitutive parameter and corresponding absolute error in Table 6.3 and Table 6.5. It can be observed from Table 6.3 and Table 6.5 that the maximum error in the estimation of the stiffness parameters corresponds to the estimation of C_{13}, that is less than 3%.

6.5.4 Parameter estimation using UKF from experimental data

The performance and verification of the UKF algorithm are first examined in Section 6.5.3. To assess the performance of the proposed algorithm in the real experimental case, the mean velocity is computed from five samples along a particular direction of propagation. To that end, the velocity vector with uncertainty shown by circles in Figure 6.10 is provided as the measurement in the UKF framework. For ease of reference, Table 6.4 shows the generated sigma points, $\boldsymbol{\chi}_0^{(i)}$ corresponding to the initial state vector within the UKF algorithm for the experimental case.

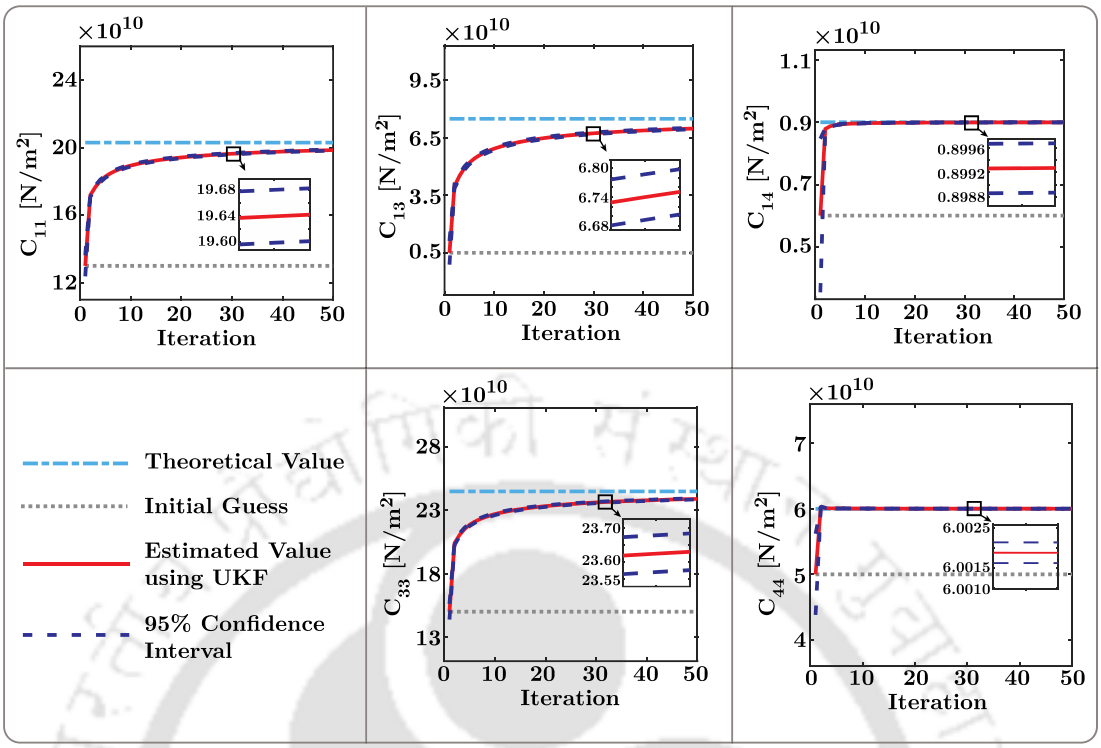

Figure 6.12 Constitutive parameter estimation results for the Lithium Niobate crystal for the experimental case. The velocity measurement perturbated with uncertainty from the experiment is provided to the unscented Kalman filter as a measurement.

The initial state vector estimate $\hat{\mathbf{x}}_0$ and the initial covariance matrix $\mathbf{P}_0$ is configured to estimate the parameters within the UKF framework for the experimental case as follows:

$$\begin{aligned}\hat{\mathbf{x}}_0 &= [C_{11,0}, C_{13,0}, C_{14,0}, C_{33,0}, C_{44,0}]^T \\ &= [13, 0.5, 0.6, 15, 5]^T \times 10^{10}\mathrm{N/m^2}, \\ \mathbf{P}_0 &= diag\left(\sigma^2_{C_{11,0}}, \sigma^2_{C_{13,0}}, \sigma^2_{C_{14,0}}, \sigma^2_{C_{33,0}}, \sigma^2_{C_{44,0}}\right) \\ &= diag(1,1,0.158,1,1) \times 10^{22}(\mathrm{N/m^2})^2.\end{aligned} \tag{6.43}$$

The state parameter estimation results obtained by the proposed UKF algorithm are shown in Figure 6.12. Figure 6.12 illustrates the parameter estimation results in terms of theoretical value and estimated parameters in every iteration. The dashed lines in Figure 6.12 indicate the 95% confidence interval. It can be observed that the UKF algorithm provides remarkably accurate estimates of the constitutive parameters. As for the parameter estimation, C_{11}, C_{14}, C_{33} and C_{44} converge more accurately to the corresponding theoretical values, as given in Table 6.1. As for C_{13}, the proposed

Table 6.4 Sigma points of the initial state vector in the unscented Kalman filter framework for the experimental case.

Sigma Point	1	2	3	4	5	6	7	8	9	10	11
$C_{11}(\times 10^{10}\mathrm{N/m^2})$	13	13.707	13	13	13	13	12.293	13	13	13	13
$C_{13}(\times 10^{10}\mathrm{N/m^2})$	0.5	0.5	1.207	0.5	0.5	0.5	0.5	-0.207	0.5	0.5	0.5
$C_{14}(\times 10^{10}\mathrm{N/m^2})$	0.6	0.6	0.6	5.055	0.6	0.6	0.6	0.6	0.318	0.6	0.6
$C_{33}(\times 10^{10}\mathrm{N/m^2})$	15	15	15	15	15.707	15	15	15	15	14.293	15
$C_{44}(\times 10^{10}\mathrm{N/m^2})$	5	5	5	5	5	5.707	5	5	5	5	4.293

method acquires an accuracy of around 93%. The estimation of the constitutive parameter and corresponding absolute error is summarised in Table 6.5.

From Table 6.3 and Table 6.5, two important observations can be drawn: (a) the error in the estimation of C_{44} is least as compared to the other parameters for both FEM and experimental cases. The least error in C_{44} is due to its sensitivity to the shape of the measured velocity profile and C_{44} is more sensitive; in other words, a slight change in the value of C_{44}, there is a significant change in the velocity profile shape. Further, the rapidity of convergence and the error in the estimate of each parameter depends upon their sensitivity to the measurement provided in the UKF framework. The parameter C_{44} performs well in the estimation and has the minimum error; on the contrary, the constitutive parameter C_{13} has the maximum error as compared to the rest of the parameters for both FEM and experimental cases. However, the performance can further be improved by increasing the measurement size, i.e., a better representation of the velocity profile and by increasing the number

Table 6.5 Summary of the constitutive parameter estimation for the experimental case.

Constitutive Parameters	Theoretical Values	Initial Guess	Estimated	Relative % Error (±)
$C_{11}(\times 10^{10}\mathrm{N/m^2})$	20.3	13	19.86	2.17%
$C_{13}(\times 10^{10}\mathrm{N/m^2})$	7.5	0.5	6.99	6.80%
$C_{14}(\times 10^{10}\mathrm{N/m^2})$	0.9	0.6	0.89	1.11%
$C_{33}(\times 10^{10}\mathrm{N/m^2})$	24.5	15	23.91	2.41%
$C_{44}(\times 10^{10}\mathrm{N/m^2})$	6.0	5	6.001	0.02%

of Kalman filter iterations. The aim of this work is to estimate the parameters optimally in the sparse measurement situation. (b) Some parameters, for instance, C_{11} and C_{13}, are over-estimated for the FEM simulation case but under-estimated in the experimental case. The under- and over-estimation of these parameters for both cases do not have any physical sense. Since the measured velocity profile and the amount of noise/uncertainty present in the measurement for FEM and experimental cases are different. Hence, each parameter does not need to follow a similar trend to converge its theoretical value in both cases. However, it is worth noting that the estimation error for each parameter should lie within the acceptable limit. From Table 6.3 and Table 6.5, one can observe that the parameters converge satisfactorily and the error corresponding to each estimation lies within the allowable limit.

6.6 Concluding Remarks

The estimation of the mechanical properties of the anisotropic Lithium Niobate is conducted using the Coulomb coupling technique and Bayesian filtering. The point contact method based on Coulomb coupling is employed for the excitation and detection of ultrasonic waves in the Lithium Niobate crystal. The spatial-temporal wavefield imaging is utilized for the extraction of direction-dependent wave velocity. The direction wave velocity is a function of the stiffness tensor and is theoretically computed by a plane wave Eigenvalue solution. The stiffness parameter is considered as a state variable and predicted using the UKF. At first, the architecture of the inversion algorithm is verified with the FEM simulation data, as the true values are known in the case of numerical simulation. In this case, the accuracy in the estimation of the parameter is more than 97%. The UKF is a data-driven hybrid technique that takes advantage of the data collected from a field experiment in conjunction with the physics-informed mathematical model. The prediction results obtained from the UKF technique are compared with the theoretical state parameters. The UKF, being a Bayesian filter, accounts for measurement uncertainties, thereby providing a confidence level on the estimate to facilitate the decision-making process. It has been demonstrated through the experimental investigation that the velocity measurements are sufficient to estimate the parameter with an accuracy of more than 93%. It is worth noting that the velocity of a wave in any direction can be extracted from the full-field transient images. However, the UKF algorithm needs limited experimental velocity information along the angular direction that may even be perturbed by

measurement uncertainty/noise. Further, the proposed algorithm is generic that utilizes available physics-informed mathematical models and relevant experimental techniques with limited measurements. The compatibility of different experimental procedures and the suitability of non-linear systems within the UKF framework makes the proposed methodology robust, reliable and applicable in other real-life scenarios.

Chapter 7

Parameter Estimation of Anisotropic Composite using Gaussian Process Regression

The potential uses of carbon composite material are vast, particularly in the civil, mechanical and aero-structures. Nonetheless, the practical utilization of carbon composite faces challenges due to complex experimental methods and imprecise algorithms for inverting material properties. Characterization of full set of stiffness tensor for an anisotropic material in particular orthotropic material can be considered as a complex non-linear inversion problem. Inversion process requires a robust optimization algorithm and forward models. The complexity of this inversion process impedes the practical utility in large-scale automation and in real-time SHM application. To cater this, in this work an advanced probabilistic machine learning framework based on multi-output Gaussian process regression (moGPR) is proposed as an inversion algorithm. The inversion algorithm proposed is based on probabilistic framework that utilises the dispersion of Lamb waves as an input for optimal estimation of stiffness tensor. Experimental measurements of full wavefield data of propagating waves are conducted by scanning laser Doppler vibrometer. Further, an optimal training dataset is generated by employing a forward model based on stiffness matrix method (SMM). In the presence of measurement uncertainties, the effectiveness of the optimal prediction algorithm is showcased through a comparison between the estimated parameter and its ground truth. This comparison reveals that the proposed inversion algorithm is both efficient and robust, delivering satisfactory performance even in the presence of substantial measurement uncertainties.

7.1 Proposed Scheme

In this chapter, a novel framework based on probabilistic machine ML is proposed to estimate the stiffness matrix of woven fabric composite to address the research gap. A forward model based on SMM is explored to generate Lamb waves' dispersion curve to train the ML model. It is to be noted that the proposed approach is modular, so various forward model can be employed to create the training dataset. The main thrust of this study is to develop a robust and reliable framework that can estimate the stiffness parameters of the composite from the noisy/uncertain experimental measurement. We would like to remark that the proposed framework is generic that can be extended to estimate the constitutive parameters of any other anisotropic material. Gaussian process regression (GPR) is one of the probabilistic ML techniques widely used in many engineering domains [254-256]. In this work, multi-output GPR (moGPR) is employed among the probabilistic ML available in the literature. The results show that the proposed method is robust, reliable and effective for the SHM framework. The major advantages of the building block used in the proposed framework over other deterministic framework are three folds:

- To begin with, the inherent Gaussian structure of moGPR makes highly amenable to incorporate uncertainty/noise in the training data, which is prevalent in real-life scenarios.
- Further, since the proposed framework is probabilistic in nature, therefore, it provides a confidence interval of the estimated stiffness parameter unlike other heuristic algorithm which gives an advantage in decision making.
- Finally, moGPR require less data as compared to DNN, only need to optimize few hyperparameters, and robust to phenomena like exploding and vanishing gradient. This makes the framework ease of use in situations like data sparsity.

7.2 Methodology

7.2.1 Forward Model: SMM

This study adopts the SMM to effectively compute dispersion curves of Lamb waves for effectively use in training dataset of the ML model. The forward model is implemented in an open-source MATLAB™ implementation of the SMM, which is available as the 'Dispersion Calculator' [43]. The method's precision and computational efficiency are well-documented in the literature [257].

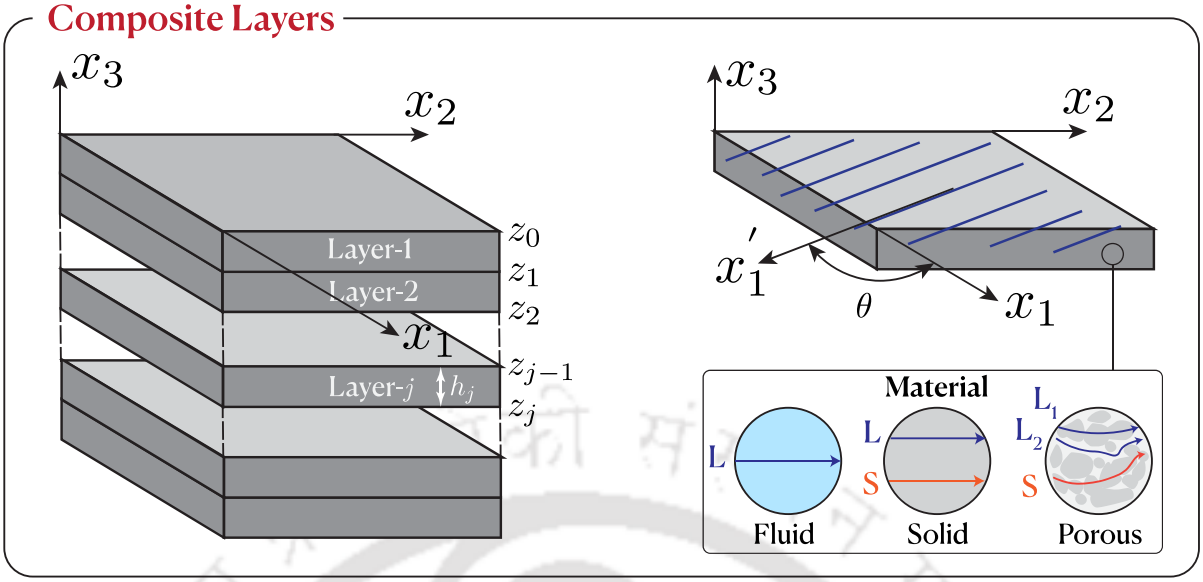

Figure 7.1 Illustration of multi-layered medium with various layers for wave propagation. The medium consists of n layers bonded with two half-spaces on both sides. There is only longitudinal L wave in fluid, longitudinal L and shear S waves in solid, and fast L_1 and slow L_2 longitudinal and shear S waves in porous medium.

Considering a general problem of wave propagation in an arbitrary multi-layer as illustrated in Figure 7.1. The multilayer contains n layers with infinite dimensions in x_1- and x_2-directions. The jth layer is defined by two interfaces z_{j-1} and z_j in the x_3-direction having a thickness of $h_j = z_j - z_{j-1}$.

The formulation of SMM begins by establishing a stiffness matrix relation for a layer j by Wang and Rokhlin (2001) [258]

$$\begin{aligned}\begin{bmatrix}\boldsymbol{\sigma}_j\\ \boldsymbol{\sigma}_{j-1}\end{bmatrix} &= \begin{bmatrix}\mathbf{D}^+ & \mathbf{D}^-\mathbf{H}\\ \mathbf{D}^+\mathbf{H} & \mathbf{P}^-\end{bmatrix}_{j-1}\begin{bmatrix}\mathbf{P}^+ & \mathbf{P}^-\mathbf{H}\\ \mathbf{P}^+\mathbf{H} & \mathbf{P}^-\end{bmatrix}^{-1}_{j-1}\begin{bmatrix}\mathbf{u}_j\\ \mathbf{u}_{j-1}\end{bmatrix},\\ &= \begin{bmatrix}\mathbf{K}_{11}^{j-1} & \mathbf{K}_{12}^{j-1}\\ \mathbf{K}_{21}^{j-1} & \mathbf{K}_{22}^{j-1}\end{bmatrix}\begin{bmatrix}\mathbf{u}_j\\ \mathbf{u}_{j-1}\end{bmatrix}.\end{aligned} \tag{7.1}$$

where subscript $j-1$ means the top surface of the jth layer and subscript j means the bottom surface of the jth layer.

Further, $\boldsymbol{\sigma}$, $\mathbf{u}$ denotes the stress field and displacement filed, respectively. In this context, $\mathbf{P}$, $\mathbf{D}$ and $\mathbf{H}$ represent the matrix of polarization vectors, the matrix of stress vectors along the surface normal and propagation matrix, respectively [259]. $\mathbf{K}_{pq}^{j-1}(p,q \in \{1,2\})$ are submatrices. The superscript sign indicates the propagation

direction: a positive sign (+) for downward and a negative sign (−) for upward direction.

Subsequently, employing the recursive algorithm formulated by Rokhlin and Wang (2002), one can compute the global stiffness matrix that correlates the fields in medium 1 to fields in medium $n+1$ as [42, 260]

$$\widetilde{\mathbf{K}}_{n+1} = \begin{bmatrix} \mathbf{K}_{11}^{n} + \mathbf{K}_{12}^{n}(\mathbf{K}_{11}^{n+1} - \mathbf{K}_{22}^{n})^{-1}\mathbf{K}_{21}^{n} & -\mathbf{K}_{12}^{n}(\mathbf{K}_{11}^{n+1} - \mathbf{K}_{22}^{n})^{-1}\mathbf{K}_{12}^{n+1} \\ -\mathbf{K}_{21}^{n}(\mathbf{K}_{11}^{n+1} - \mathbf{K}_{22}^{n})^{-1}\mathbf{K}_{21}^{n+1} & \mathbf{K}_{22}^{n+1} - \mathbf{K}_{21}^{n+1}(\mathbf{K}_{11}^{n+1} - \mathbf{K}_{22}^{n})^{-1}\mathbf{K}_{12}^{n+1} \end{bmatrix} \tag{7.2}$$

The recursive algorithm enables a fast computation of the global stiffness matrix for layered media. Further, SMM is quick and maintains numerical stability at high frequency-thickness (fd) values [261].

7.2.2 Inverse Model: Gaussian Process Regression

GPR is a non-parametric, Bayesian approach to regression that provides a probabilistic framework for modeling the underlying functions. The observations are assumed to be the subset of the Gaussian distribution and can be modeled using the multivariable normal distribution [262]. Let the observations be modeled through mean function $m(\mathbf{x})$ and covariance or kernel function $k(\mathbf{x}, \mathbf{x}')$ of a real process $f(\mathbf{x})$ as [263]

$$\begin{aligned} m(\mathbf{x}) &= \mathbb{E}[f(\mathbf{x})], \\ k(\mathbf{x}, \mathbf{x}') &= \mathbb{E}[\big(f(\mathbf{x}) - m(\mathbf{x})\big)\big(f(\mathbf{x}') - m(\mathbf{x}')\big)], \end{aligned} \tag{7.3}$$

and the Gaussian process as

$$f(\mathbf{x}) \sim \mathcal{GP}\big(m(\mathbf{x}), k(\mathbf{x}, \mathbf{x}')\big). \tag{7.4}$$

Thus, for the finite set of observations, this process is jointly Gaussian,

$$p(f|X) = \mathcal{N}(f|\mu, K), \tag{7.5}$$

where, $K_{ij} = k(\mathbf{x}_i, \mathbf{x}_j)$ and $\mu = \big(m(\mathbf{x}_1), m(\mathbf{x}_2), \dots, m(\mathbf{x}_n)\big)$. For the noise free observation $f_i \triangleq f(\mathbf{x}_i)$ evaluated at $\mathbf{x}_i$, that is we know $\{(\mathbf{x}_i, f_i)|i = 1,2,\dots,n\}$. The joint distribution of training outputs, $\mathbf{f}$, and test outputs $\mathbf{f}_*$ corresponding to test inputs X_* according to the prior is

$$\begin{bmatrix} \mathbf{f} \\ \mathbf{f}_* \end{bmatrix} \sim \mathcal{N}\left(\begin{bmatrix} \mu \\ \mu_* \end{bmatrix}, \begin{bmatrix} K(X, X) & K(X, X_*) \\ K(X_*, X) & K(X_*, X_*) \end{bmatrix} \right). \tag{7.6}$$

By computing mean and covariance matrix the function values $\mathbf{f}_*$ can be sampled from the joint posterior distribution given as

$$\mathbf{f}_*|X_*, X, \mathbf{f} \sim \mathcal{N}\left(\mu(X_*) + K(X_*, X)K(X, X)^{-1}\big(\mathbf{f} - \mu(X)\big), \\ K(X_*, X_*) - K(X_*, X)K(X, X)^{-1}K(X, X_*)\right). \tag{7.7}$$

In case of noisy observation $y = f(\mathbf{x}) + \varepsilon$, the observed values y differ from the function values $f(\mathbf{x})$ by additive noise. This noise follows an independent, identically distributed Gaussian distribution with zero mean and variance σ_n^2

$$\varepsilon \sim \mathcal{N}(0, \sigma_n^2). \tag{7.8}$$

The prior on the noisy observation becomes

$$\text{cov}(\mathbf{y}) = K(X, X) + \sigma_n^2 I, \tag{7.9}$$

where, I is the identity matrix. The squared-exponential kernel function in one dimension can be expressed as

$$k_y(x_p, x_q) = \sigma_f^2 \exp\left(-\frac{1}{2\ell^2}(x_p - x_q)^2\right) + \sigma_n^2 \delta_{pq}, \tag{7.10}$$

where, $\ell > 0$ is the characteristic length-scale, $\sigma_f^2 > 0$ is the signal variance and δ_{pq} is a Kronecker delta which is one iff $p = q$ and zero otherwise. Here, it should be noted that only single dimension of the output (y) can be predicted using single kernel function. In current context, we want to estimate nine parameters of stiffness matrix of the carbon woven laminate. Thus, albeit multi-output Gaussian process regression (moGPR) is beneficial.

7.2.3 Multi-output Gaussian process regression

Multi-output Gaussian process regression (moGPR) learns a multi-output function $\boldsymbol{f}(\cdot)\colon \mathcal{X} \to \mathbb{R}^P$ and the input space $\mathcal{X}$ to be $\mathbb{R}^D$. The pth output of $\boldsymbol{f}(\cdot)$ at the input $\mathbf{x}$ is denoted by $f_p(\mathbf{x})$. A prior over such functions is a multi-output Gaussian process [264] when the distribution of a vector of values

$$\mathbf{f} = \{f_{p_n}(\mathbf{x}_n)\}_{n=1}^N, \qquad f \in \mathbb{R}^N, \tag{7.11}$$

is Gaussian distributed. Here $\mathbf{x}_n$ is the input and the corresponding output is p_n. The kernels for the multioutput Gaussian process on the input space $\mathcal{X}$ is written as

$$k\colon \mathcal{X} \times \mathcal{X} \to \mathbb{R}^{P \times P}, \qquad k(\mathbf{x}, \mathbf{x}') = \mathbb{C}_{\boldsymbol{f}(\cdot)}[f(\mathbf{x}), f(\mathbf{x}')], \tag{7.12}$$

where a covariance matrix for all outputs is returned [265]. An alternative view is that the matrix-valued kernel obeys the same positive definiteness properties of a single-output kernel where the index of the output is treated simply as another input.

In other words, multi-output kernels as functions on the input space $\mathcal{X}$ extended by the index of the output

$$\begin{aligned} &k\colon (\mathcal{X},\mathbb{N})\times(\mathcal{X},\mathbb{N})\to\mathbb{R},\\ &\mathbb{C}_{\boldsymbol{f}(\cdot)}[f(\mathbf{x}),f(\mathbf{x}')]=\mathbb{E}_{\boldsymbol{f}(\cdot)}[f(\mathbf{x}),f(\mathbf{x}')]=k(\{\mathbf{x},p\},\{\mathbf{x}',p'\}). \end{aligned} \tag{7.13}$$

There exists various choices for priors on the correlations between multiple outputs [264]. Linear model of coregionalization is a simple way of introducing correlations in the outputs is to construct our multi-output function $\boldsymbol{f}(\cdot)$ from a linear transformation $W\in\mathbb{R}^{P\times L}$ of L independent functions $g_\ell(\cdot)$ as

$$g_\ell(\cdot)\sim\mathcal{GP}\big(0,k_\ell(\cdot,\cdot')\big),\quad \boldsymbol{g}(\mathbf{x})=\{g_\ell(\mathbf{x})\}_{\ell=1}^{L},\quad \boldsymbol{f}(\mathbf{x})=W\boldsymbol{g}(\mathbf{x}), \tag{7.14}$$

with $\boldsymbol{f}(\mathbf{x})\in\mathbb{R}^P$ and $\boldsymbol{g}(\mathbf{x})\in\mathbb{R}^L$. Thus, the covariance is

$$k(\{\mathbf{x},p\},\{\mathbf{x}',p'\})=\mathbb{E}\big[[W\boldsymbol{g}(\mathbf{x})\boldsymbol{g}(\mathbf{x}')^\top W^\top]_{pp'}\big]=\sum_{\ell=1}^{L}W_{p\ell}k_\ell(\mathbf{x},\mathbf{x}')W_{p'\ell}. \tag{7.15}$$

The training, validation and testing of the inversion algorithm are carried out in a computer with M1Pro processor and 32 GB system memory.

7.3 Results and Discussion

This section presents two sets of results of material characterization using the moGPR model. The results in first set using synthetic data to validate the ML model and on experimental data to demonstrate its practical utility.

Initially, simulations for an orthotropic carbon woven composite plate are carried out using the SMM forward model. A preliminary study is then employed to determine the optimal size for the training dataset. The wavenumbers in the training and testing datasets are perturbed with various levels of random noise to simulate real-world measurement uncertainties. This intentional perturbation of noise is crucial for training models that can differentiate actual signal features from noise, thereby enhancing their ability to generalize. After numerically validating the inversion method, the study illustrates its effectiveness in characterizing the stiffness of a real-

Table 7.1 Initial values of stiffness parameters used in numerical study (units: GPa).

C_{11}	C_{12}	C_{13}	C_{22}	C_{23}	C_{33}	C_{44}	C_{55}	C_{66}
50	5	5	50	5	9	3	3	3

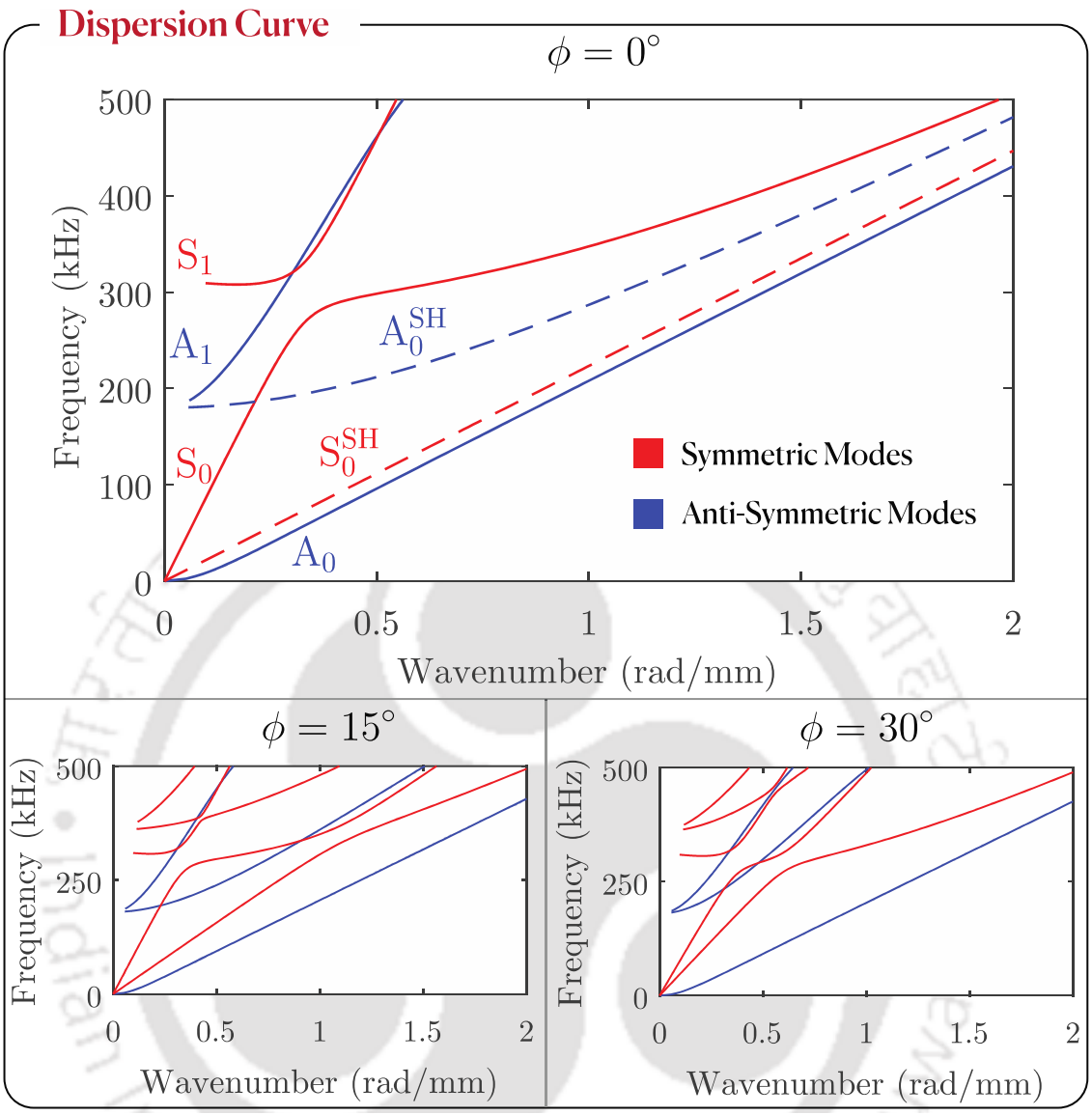

Figure 7.2 Dispersion curves for Lamb waves evaluated in a 3.9 mm thick plate having stiffness value given in Table 7.1 and 0°, 15° and 30° propagation angle.

world composite material: a woven fabric reinforced composite laminate, using an experimental wavefield dataset.

7.3.1 Validation of moGPR using forward simulation

To evaluate the efficacy of the proposed approach, a numerical case study is performed on an orthotropic plate. The SMM facilitated to create the training dataset by generating dispersion curve. The initial values of stiffness parameter characterising the plate is presented in Table 7.1. It is assumed in the numerical study that the plate is composed of 8 layers of a total thickness of 3.9 mm with same orientation angle (0°) for each ply. To this end, propagation direction (ϕ) of 0°, 15°, and 30° are

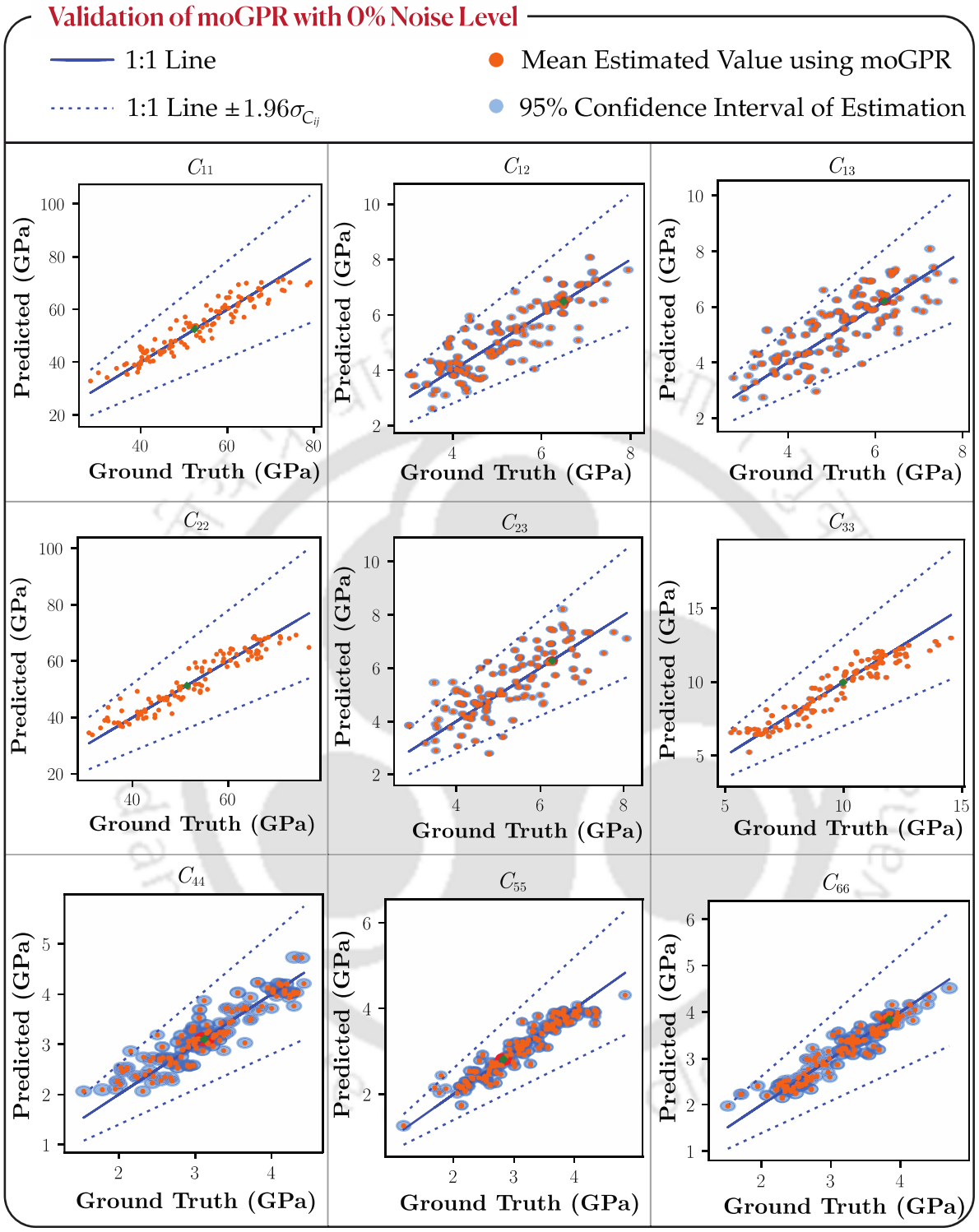

Figure 7.3 A comparison between predicted stiffness parameters with ground truth is illustrated for moGPR based inversion of validation dataset with 0% noise level. The orange dot represents the mean estimated value and blue circle represents 95% confidence interval of the estimation. The 1:1 line in this representation serves as the exact match.

considered. The dispersion curve in these angles are subsequently used to estimate 9 stiffness parameters. Figure 7.2 illustrates numerical dispersion curves for Lamb waves in the composite plate for a propagation angle of $\phi = 0°, 15°$ and $30°$.

To construct an optimal set of data for training and testing, the SMM was used to simulate dispersion curves of Lamb waves with stiffness variations from – 30% to + 40% to the initial values in Table 7.1. Asymmetric parameter limits were set because conventional inversion algorithms often have prone to use middle values as initial solutions. The datasets were generated with stiffness parameters uniformly distributed within the defined bounds. The dataset contains 135 data corresponding to each propagation angle which in turn a total of 405 data. The advantage of using ML based algorithm is the training can be done beforehand. Once the ML is trained, it can efficiently predict the properties of a stiffness tensor based on a set of dispersion data, provided that these data are within the range used during training. This process paves the way for real-time stiffness estimation and model updating in a fraction of second. Figure 7.3 presents a comparison between the predicted and actual stiffness parameters for the validation datasets, showing a strong correlation for most

Table 7.2 Summary of the stiffness parameter estimation for synthetic dataset perturbed with various level of noise.

Noise		C_{11}	C_{12}	C_{13}	C_{22}	C_{23}	C_{33}	C_{44}	C_{55}	C_{66}
	True	50	5	5	50	5	9	3	3	3
0 %	Pred.	50.033	4.995	4.954	49.940	4.938	8.982	2.984	3.008	2.998
	%Error	0.066	0.100	0.920	0.120	1.240	0.200	0.533	0.267	0.067
1 %	Pred.	50.105	4.986	5.005	50.036	4.961	8.952	2.992	3.003	2.996
	%Error	0.210	0.280	0.100	0.072	0.780	0.533	0.267	0.100	0.133
2 %	Pred.	50.258	4.978	5.042	48.715	4.791	9.009	3.008	3.007	3.005
	%Error	0.516	0.440	0.840	2.570	4.180	0.100	0.267	0.233	0.167
3 %	Pred.	50.541	5.077	4.976	51.661	5.194	9.088	3.042	3.040	3.037
	%Error	1.082	1.540	0.480	3.322	3.880	0.978	1.400	1.333	1.233
5 %	Pred.	52.039	4.542	4.331	50.777	4.286	9.254	3.088	3.040	3.155
	%Error	4.078	**9.160**	**13.380**	1.554	**14.280**	2.822	2.933	1.333	**5.167**

parameters. Notably, the off-diagonal stiffness parameters (C_{12}, C_{13} and C_{23}) exhibit higher error margins. This aligns with the findings from sensitivity analyses of guided wave modes by Kudela*, et al.* (2020) and of natural frequencies by Gsell*, et al.* (2007) [266, 267].

For the synthetic dataset of a 3.9 mm thick composite plate with stiffness values given in Table 7.1, it is to be noted that the estimated stiffness parameters typically exhibit an average error of about 1.24% compared to the true values when no noise is present as presented in Table 7.2. In practical situations, the introduction of noise could degrade the accuracy of these estimations, potentially while the error level increases. To assess the robustness of the models under such conditions, additional studies were conducted where random noise was introduced to the training and testing datasets to predict the accuracy in the presence of noise. The noise affected data is defined as follows:

$$\mathfrak{D}_{noise} = \mathfrak{D}_{SMM} + \varepsilon, \tag{7.16}$$

where $\mathfrak{D}_{noise}$ is the noise perturbed dispersion data, $\mathfrak{D}_{SMM}$ is dispersion data simulated by SMM, and ε is a Gaussian noise as defined in Eq. (7.8). In this study, noise level of 1, 2, 3, and 5% are considered. From Table 7.2, one can observe that the prediction error lies between 0.066% to 14.280% depending on the considered noise level. Under the condition of measurement uncertainty/noise, the two sets of validation sets perturbed with 2% and 5% noise levels are illustrated for brevity in Figure 7.4 and Figure 7.5 respectively. With increased noise level, the moGPR estimates the parameters with larger confidence interval which is evident from Figure 7.5. This ability of providing confidence interval of estimation with input uncertainty facilitates the better decision-making process.

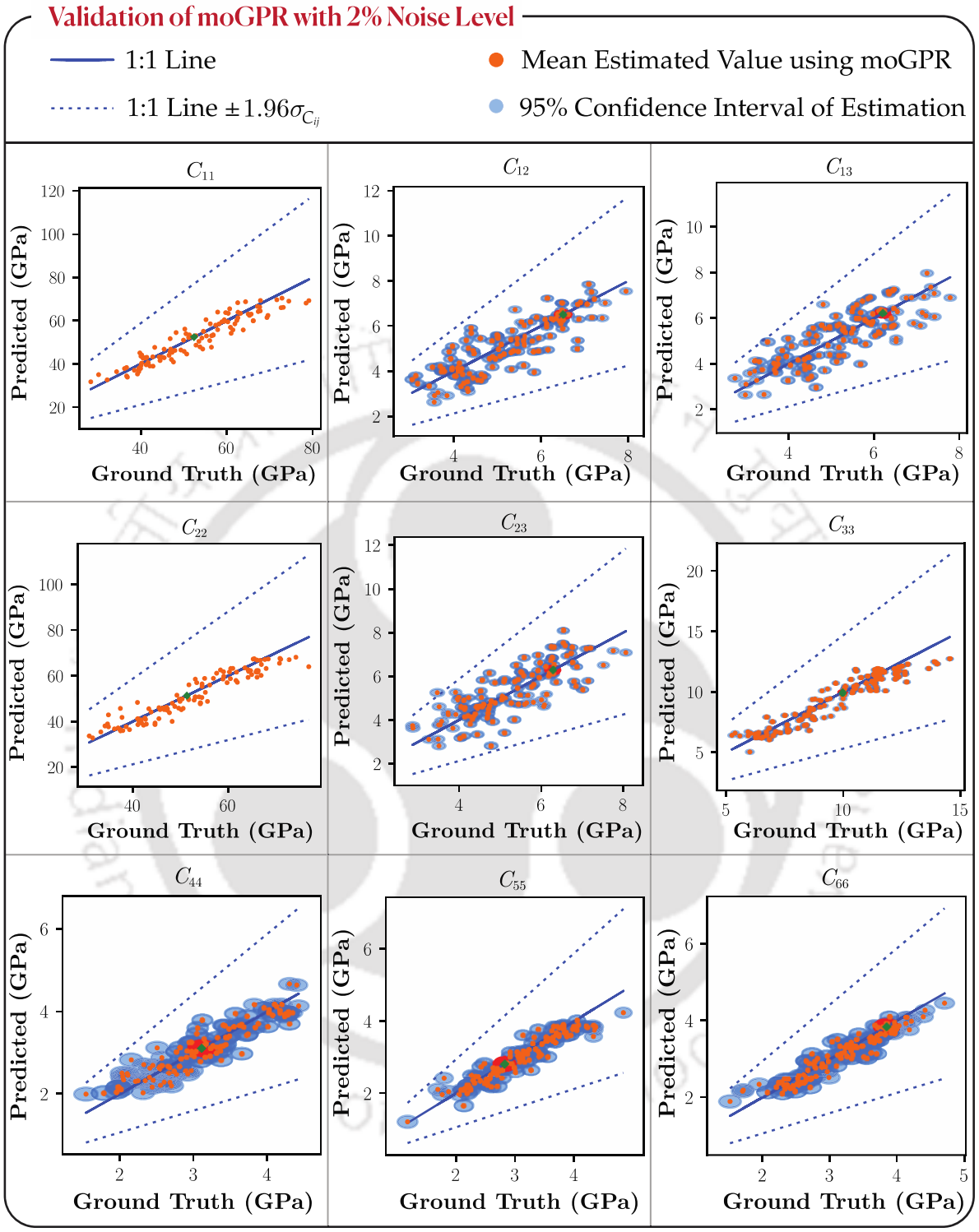

Figure 7.4 A comparison between predicted stiffness parameters with ground truth is illustrated for moGPR based inversion of validation dataset with 2% noise level. The orange dot represents the mean estimated value and blue circle represents 95% confidence interval of the estimation. The 1:1 line in this representation serves as the exact match.

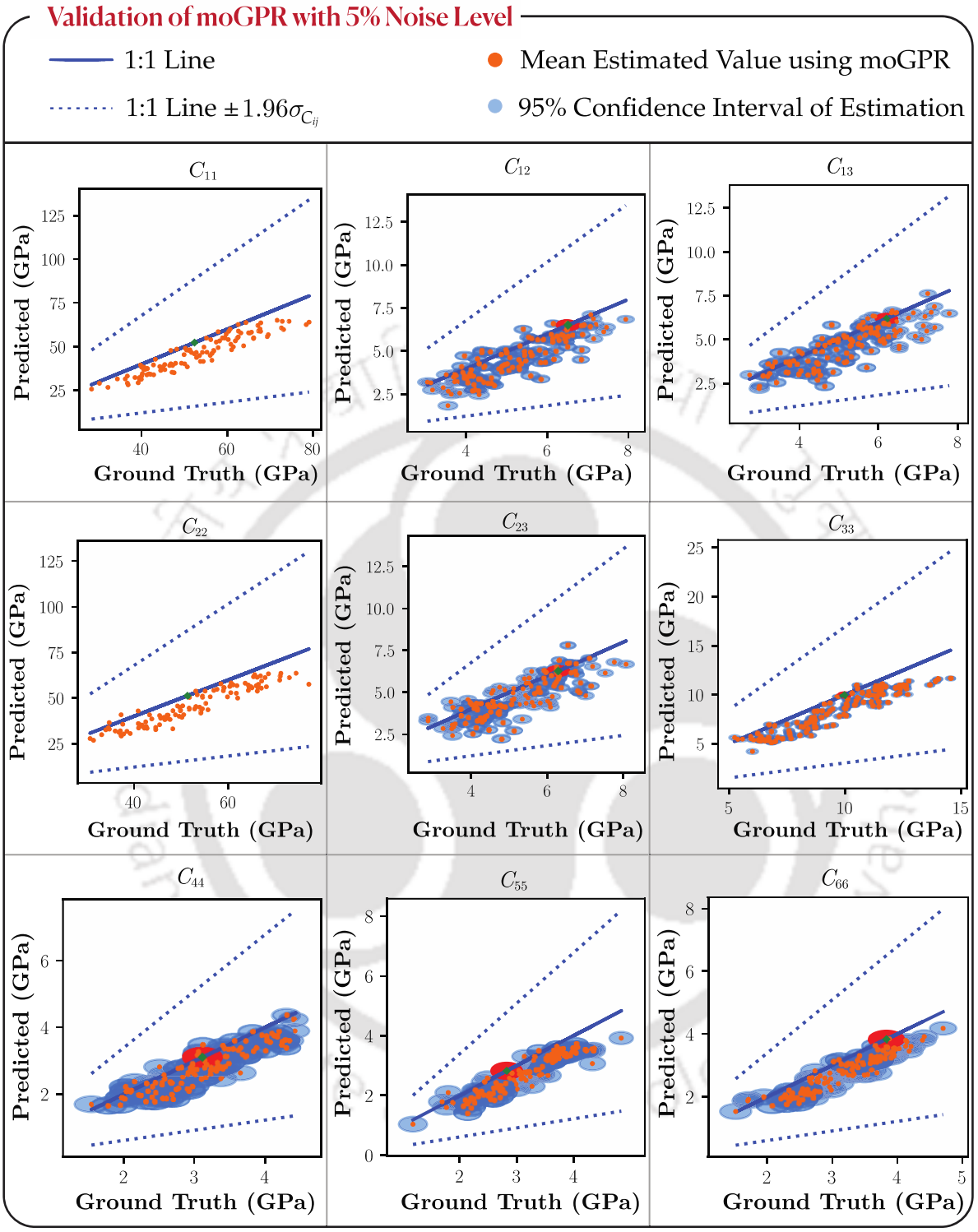

Figure 7.5 A comparison between predicted stiffness parameters with ground truth is illustrated for moGPR based inversion of validation dataset with 5% noise level. The orange dot represents the mean estimated value and blue circle represents 95% confidence interval of the estimation. The 1:1 line in this representation serves as the exact match.

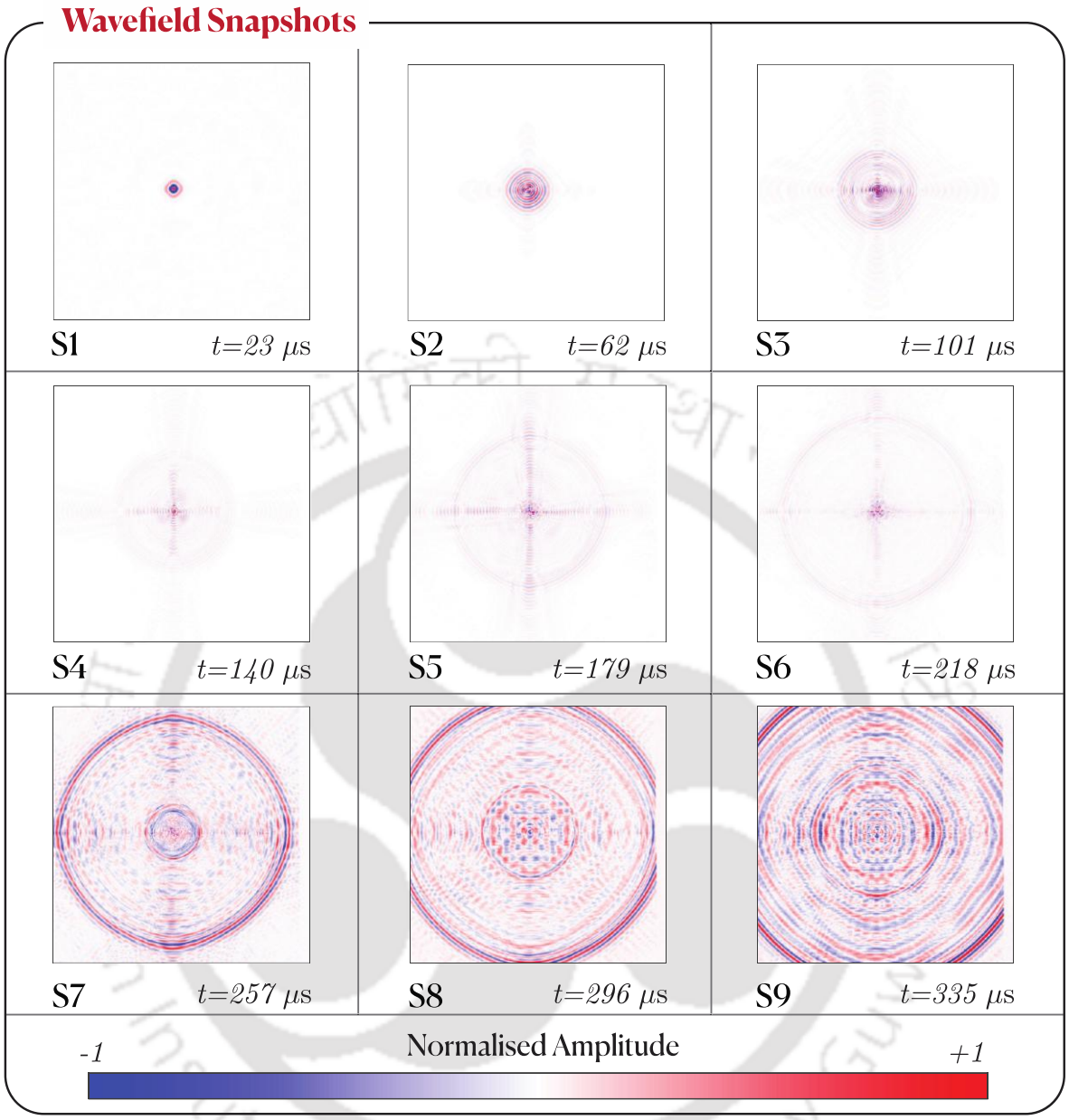

Figure 7.6 Sequential snapshots illustrating the spatial and temporal propagation of Lamb waves at an interval of 39 μs in 3.9 $\pm$ 0.1 mm thick woven fabric carbon composite laminate. The size of each snapshot is 0.726 m $\times$ 0.726 m.

7.3.2 Experimental case study: woven fabric reinforced composites

For the experimental case study, Lamb wave propagation data have been acquired on the surface of carbon/epoxy laminate reinforced by 16 layers of plain weave fabric. Figure 7.6 illustrates the visualisation of 2D Lamb wave evolution in the woven fabric carbon composite laminate. The time interval of each snapshot as presented in Figure 7.6 is 39 μs. The spatial-temporal data matrix has dimension of 499 $\times$ 499 $\times$ 1024. Each snapshot's spatial size is 499 pixels $\times$ 499 pixels, equivalent to a physical space

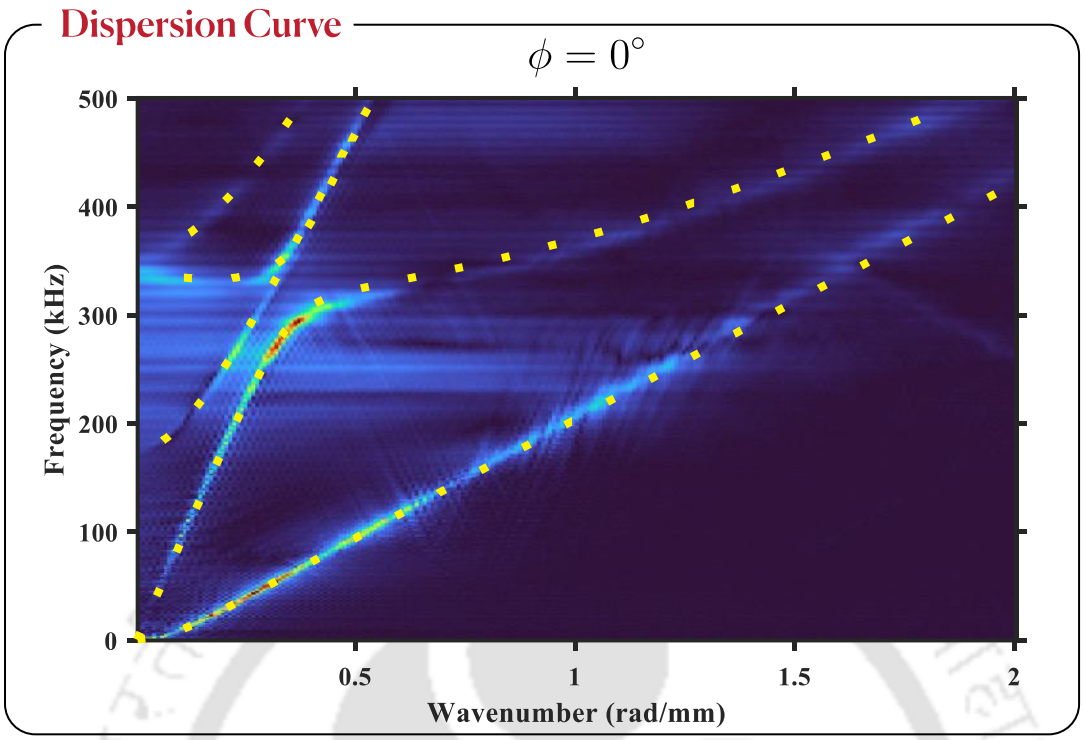

Figure 7.7 Wavenumber–frequency pairs for in-plane direction $\phi = 0°$ corresponding to the moGPR optimized stiffness values (dots) superimposed on the dispersion landscape for a 3.9 mm thick carbon/epoxy plate deduced from the experimental Lamb wave propagation data.

of 0.726 m $\times$ 0.726 m. A total of 1024 time-varying snapshots, corresponding to a total acquisition duration of 799 μs, are collected through experimental procedures as discussed in Section 3.2. The outward radial propagation of the wave fringe are moving fast in two orthogonal axes can be observed from the snapshots S4 to S6 of Figure 7.6, is attributed to the orthotropic nature of the composite laminate.

The full wavefield data was processed using a 3D Fourier transform in the temporal and spatial domains (t, x, y). This data was then converted from Cartesian (ω, k_x, k_y) to cylindrical coordinates (f, k, ϕ). The 2D images (f, k) are obtained through interpolation represents dispersion curves $f(k)$ at specific angles ranging from 0° to 90°. The moGPR-based inverted stiffness parameters are summarized in the second column of Table 7.3, and are in reasonable agreement with the inversion results obtained by using a traditional heuristic inversion algorithm based on genetic algorithm [266]. Furthermore, in Figure 7.7, the computed dispersion curves calculated from the moGPR-optimized stiffness parameters (best match using SMM) are

Table 7.3 Summary of the stiffness parameter estimation for experimental data.

C_{ij}	moGPR C_{ij} (GPa)		Traditional Inversion C_{ij} (GPa) [266]	% Deviation
	Mean $\left(\mu_{C_{ij}}\right)$	95 % Confidence Interval		
C_{11}	53.66	50.76 – 55.56	52.55	2.12
C_{12}	5.95	5.66 – 6.24	6.51	8.60
C_{13}	5.71	5.43 – 5.99	5.94	3.87
C_{22}	49.33	46.51 – 52.15	51.83	4.82
C_{23}	5.63	5.33 – 5.93	5.88	4.25
C_{33}	11.10	10.52 – 11.68	10.28	7.98
C_{44}	3.00	2.86 – 3.14	2.93	2.39
C_{55}	2.96	2.81 – 3.11	2.92	1.37
C_{66}	3.65	3.50 – 3.8	3.86	5.44

superposed on the experimentally recorded dispersion landscape. An excellent match is obtained, confirming the high accuracy of the inverted stiffness parameters.

7.4 Concluding Remarks

This work has demonstrated inversion technique that utilizes a probabilistic machine learning (ML) to determine the elastic stiffness parameters of orthotropic plates, based on experimental data coming from the scanning laser Doppler vibrometer SLDV measurements. The benefit of this approach is that it enables one-sided, non-contact measurement with contact excitation, allowing for direct application on current structures without the need for preparing specialized samples.

Initially, the approach involves using the 3D Fourier transform to extract frequency values as function of real wavenumber from recorded experimental wave movement across various in-plane directions. Simultaneously, the dispersion curves for numerous materials featuring range of orthotropic elastic stiffness metrics are calculated using a fast stiffness matrix method (SMM). This generates a dataset of directional wavenumber–frequency pairings, which serves as the training data for the ML model, finally enabling the accurate prediction of specific orthotropic elastic stiffness parameters.

The novel inversion technique was initially tested using a simulated dataset for a composite plate generated through the SMM. This test showed a remarkably less error of 1.24% without noise, and increasing up to 14.28% error with 5% noise introduced. Finally, experimental validation was also performed using SLDV data on a 3.9 mm thick woven fabric reinforced carbon composite plate. The inverted stiffness parameters were closely aligned with those obtained by conventional inversion methods, with less than a 6.8% deviation.

As a probabilistic framework, the moGPR incorporates measurement uncertainties, offering a level of confidence in its estimates that aids in the better decision-making process The primary advantage of the moGPR-based inversion strategy is its efficiency after training, yields accurate and rapid estimations of elastic properties of orthotropic plates in under a second. This rapid assessment capacity yields the method particularly valuable for real time SHM.

Chapter 8

Acoustic Emission Source Detection using Transfer Learning based mfPINN

The practical application of data-driven frameworks like deep neural network in acoustic emission (AE) source localization is impeded due to the collection of significant clean data from the field. The utility of the such framework is governed by data collected from the site and/or laboratory experiment. The noise, experimental cost and time consuming in the collection of data further worsen the scenario. To address the issue, this work proposes to use a novel multi-fidelity physics-informed neural network (mfPINN). The proposed framework is best suited for the problems such as AE source detection, where the governing physics is known in an approximate sense (low-fidelity model), and one has access to only sparse data measured from the experiments (high-fidelity data). This work further extends the governing equation of AE source detection to the probabilistic framework to account for the uncertainty that lies in the sensor measurement. The mfPINN fuses the data-driven and physics-informed deep learning architectures using transfer learning. The results obtained from the data-driven artificial neural network (ANN) and physics-informed neural network (PINN) are also presented to illustrate the requirement of a multi- fidelity framework using transfer learning. In the presence of measurement uncertainties, the proposed method is verified with an experimental procedure that contains the carbon-fibre-reinforced polymer (CFRP) composite panel instrumented with a sparse array of piezoelectric transducers. The results conclude that the proposed technique based on a probabilistic framework can provide a reliable estimation of AE source location with confidence intervals by taking measurement uncertainties into account.

8.1 Proposed Scheme

A novel probabilistic framework is proposed to estimate the AE source location. One of the key components of the proposed framework is to develop a probabilistic approach to account for the uncertainty present in the TOF measurements. The proposed approach utilises a multi-fidelity physics-informed neural network (mfPINN) to achieve the goal. The underlying idea here is initially to train the neural network with the low-fidelity model and then update it with sparse high-fidelity data. The low-fidelity model is the approximate governing physics-based equations, and the high-fidelity data are collected by either performing laboratory experiments or direct field measurements. This is accomplished by the newly evolved physics-informed deep learning algorithm [268-270].

The advantages of the proposed framework over other deterministic data-driven approaches are three-fold.

- To begin with, this study proposes a novel cost function extended from the physics-based governing equations of AE source localisation using a probabilistic approach to incorporate the uncertainty/noise in the TOF data, which is prevalent in real-life scenarios.
- Further, as the proposed framework is probabilistic in nature, hence it provides a confidence interval of the estimated AE location, which gives an advantage in decision-making.
- Finally, the proposed method is a data-driven hybrid technique that takes advantage of the few measurements from a field experiment in conjunction with the physics-informed mathematical model to train the network as compared to the other data-hungry algorithm. This makes the algorithm ease of use in situations of data sparsity.

8.2 Mathematical Background of AE Source Location

Consider a sparse array of n piezoelectric transducers instrumented on an anisotropic plate-like structure. The coordinates of the unknown AE source (x_s, y_s) and the fixed sensors are located at the coordinates (x_i, y_i), as shown in Figure 8.4. The time of flight (TOF) from the unknown source to the ith sensor is t_i. Conventionally, the unknown coordinates of the AE source can be expressed with the TOF and velocity as

$$(x_s - x_i)^2 + (y_s - y_i)^2 = [t_i v(\theta_i)]^2, \tag{8.1}$$

where, i is the sequence number of sensors. In the anisotropic plate, $v(\theta_i)$ is the functional relationship between the wave propagation velocity and propagation direction θ_i defined as [271]:

$$\theta_i = \arctan\left(\frac{y_s - y_i}{x_s - x_i}\right). \tag{8.2}$$

The TOF from the AE source to the first sensor (t_1) is considered as a reference because the velocity of the stress wave cannot be exactly determined. The following sets of equations can be expressed with the time difference of arrival (TDOA)

$$(x_s - x_i)^2 + (y_s - y_i)^2 = [(t_1 + \Delta t_{1i}) v(\theta_i)]^2, \tag{8.3}$$

where, $\Delta t_{1i} = t_i - t_1$ is defined as TDOA between the ith and the first sensors. By combining Eqs. (8.1) and (8.3), the following sets of nonlinear equations can be obtained [271]

$$\Delta t_{1i} = t_i - t_1 = \frac{\sqrt{(x_s - x_i)^2 + (y_s - y_i)^2}}{v(\theta_i)} - \frac{\sqrt{(x_s - x_1)^2 + (y_s - y_1)^2}}{v(\theta_1)}, \tag{8.4}$$

where, θ_i and θ_1 are the angle of propagation from the AE source to the ith and the first sensors, respectively. This set of nonlinear equations is not sufficient to solve the AE source coordinates for the anisotropic structures as the number of equations available $(n-1)$ is less than the number of unknowns $(n+2)$, i.e. AE source coordinates (x_s, y_s) and n-wave velocities.

In the past few decades, several number of TOF-based strategies have been developed to overcome this limitation. Kundu, *et al.* (2007) used a known velocity profile to reduce the number of unknowns in Eq. (8.4) [271]. In such a case, a minimum number of three sensors ($n = 3$) are required to compute the AE source coordinates (x_s, y_s). Several techniques are reported in the literature on the localization of AE sources in anisotropic material without knowing its material properties [272-275]. Ciampa and Meo (2010) also proposed a technique in which the information on the velocity profile is not required, where the clusters of sensors are used [276]. In this approach, the n sensors are placed in n_c clusters in such a way that $n - 1 \geq n_c + 2$ in order to solve the system of equations. It is assumed that the wave velocity from

the source to each sensor in a cluster is the same. Further, in TOF-based strategies, the accuracy of TOF measurement is crucial as the erroneous measurement will lead to a considerable error in estimating the AE source location.

This work proposes a novel probabilistic approach comprised of a deep neural network to estimate the AE source location from the noisy measurement. The proposed network takes the TDOA of all the sensors along with the TOF uncertainties of each sensor as input and gives the AE source coordinates and corresponding uncertainties. It is considered that the TOF, t_i and AE source coordinates (x_s, y_s) are correlated random variables since they are related by Eq. (8.4); the unknowns x_s and y_s are mutually independent Gaussian random variables. Further, the TOF t_i is considered as a mutually independent Gaussian random variable under the condition that the probable AE event occurs far enough away from the sensor locations (i.e., $\sqrt{(\mu_{x_s} - x_i)^2 + (\mu_{y_s} - y_i)^2} \gg 0$). The μ_{x_s} and μ_{y_s} are defined in Eq. (8.5). Based on the above assumptions, the Based on the above assumptions, the probability density function of TDOA is also a Gaussian random variable $\big(\mathcal{N}(\mu, \sigma)\big)$ parameterized by mean (μ) and standard deviation (σ) [245, 277, 278].

$$\begin{aligned} t_i &\sim \mathcal{N}(\mu_{t_i}, \sigma_{t_i}), \\ x_s &\sim \mathcal{N}(\mu_{x_s}, \sigma_{x_s}), \\ y_s &\sim \mathcal{N}(\mu_{y_s}, \sigma_{y_s}), \\ \Delta t_{1i} &\sim \mathcal{N}(\mu_{\Delta t_{1i}}, \sigma_{\Delta t_{1i}}). \end{aligned} \tag{8.5}$$

The mean of TDOA, $\mu_{\Delta t_{1i}}$ and variance of TDOA, $\sigma^2_{\Delta t_{1i}}$ are defined as

$$\mu_{\Delta t_{1i}} = \mu_{t_i} - \mu_{t_1}, \quad \sigma^2_{\Delta t_{1i}} = \sigma^2_{t_1} + \sigma^2_{t_i}. \tag{8.6}$$

One can write the Eq. (8.1) as follows

$$t_i^2 = \frac{(x_s - x_i)^2 + (y_s - y_i)^2}{\{v(\theta_i)\}^2}. \tag{8.7}$$

In Eq. (8.7), t_i, x_s and y_s are the random variables. However, it is to be noted that, t_i^2 in Eq. (8.7) is actually a (scaled) generalized chi-squared random variable. In particular, if $\sigma_{x_s} = \sigma_{y_s}$ then t_i^2 has a (scaled) non-central chi-squared distribution with two degrees of freedom. Now applying the expectation operator $\mathbb{E}[\cdot]$ on both sides of the Eq. (8.7) we get

$$\begin{aligned}\mathbb{E}[t_i^2] &= \mathbb{E}\left[\frac{(x_s - x_i)^2 + (y_s - y_i)^2}{\{v(\theta_i)\}^2}\right] \\ &= \frac{\mathbb{E}[(x_s - x_i)^2] + \mathbb{E}[(y_s - y_i)^2]}{\{v(\theta_i)\}^2} \\ &= \frac{\mathbb{E}[x_s^2 - 2x_s x_i + x_i^2] + \mathbb{E}[y_s^2 - 2y_s y_i + y_i^2]}{\{v(\theta_i)\}^2} \\ &= \frac{\mathbb{E}[x_s^2] - 2\mathbb{E}[x_s]x_i + x_i^2 + \mathbb{E}[y_s^2] - 2\mathbb{E}[y_s]y_i + y_i^2}{\{v(\theta_i)\}^2}.\end{aligned} \tag{8.8}$$

The statistical moments of t_i are known. Considering $\text{var}[t_i] = \sigma_{t_i}^2$ then one can write as

$$\mathbb{E}[t_i^2] = \mu_{t_i}^2 + \sigma_{t_i}^2. \tag{8.9}$$

Similarly, $\mathbb{E}[x_s^2] = \mu_{x_s}^2 + \sigma_{x_s}^2$ and $\mathbb{E}[y_s^2] = \mu_{y_s}^2 + \sigma_{y_s}^2$. Now, substituting the value of $\mathbb{E}[t_i^2]$, $\mathbb{E}[x_s^2]$ and $\mathbb{E}[y_s^2]$ in Eq. (8.8) one gets

$$\mu_{t_i}^2 + \sigma_{t_i}^2 = \frac{\mu_{x_s}^2 + \sigma_{x_s}^2 - 2\mu_{x_s}x_i + x_i^2 + \mu_{y_s}^2 + \sigma_{y_s}^2 - 2\mu_{y_s}y_i + y_i^2}{\{v(\theta_i)\}^2}, \tag{8.10}$$

$$\Rightarrow \mu_{t_i} = \sqrt{\frac{\mu_{x_s}^2 + \sigma_{x_s}^2 - 2\mu_{x_s}x_i + x_i^2 + \mu_{y_s}^2 + \sigma_{y_s}^2 - 2\mu_{y_s}y_i + y_i^2}{\{v(\theta_i)\}^2} - \sigma_{t_i}^2}. \tag{8.11}$$

Similarly,

$$\mu_{t_1} = \sqrt{\frac{\mu_{x_s}^2 + \sigma_{x_s}^2 - 2\mu_{x_s}x_1 + x_1^2 + \mu_{y_s}^2 + \sigma_{y_s}^2 - 2\mu_{y_s}y_1 + y_1^2}{\{v(\theta_1)\}^2} - \sigma_{t_1}^2}. \tag{8.12}$$

Substituting the value of μ_{t_i} and μ_{t_1} in the expression of $\mu_{\Delta t_{1i}}$ given in Eq. (8.6) one can get

$$\begin{aligned}\mu_{\Delta t_{1i}} = &\sqrt{\frac{\mu_{x_s}^2 + \sigma_{x_s}^2 - 2\mu_{x_s}x_i + x_i^2 + \mu_{y_s}^2 + \sigma_{y_s}^2 - 2\mu_{y_s}y_i + y_i^2}{\{v(\theta_i)\}^2} - \sigma_{t_i}^2} \\ &- \sqrt{\frac{\mu_{x_s}^2 + \sigma_{x_s}^2 - 2\mu_{x_s}x_1 + x_1^2 + \mu_{y_s}^2 + \sigma_{y_s}^2 - 2\mu_{y_s}y_1 + y_1^2}{\{v(\theta_1)\}^2} - \sigma_{t_1}^2}.\end{aligned} \tag{8.13}$$

It should be noted that the direction dependent velocity $v(\theta)$ is a deterministic quantity as the velocity profile is known *a priori* to make the Eq. (8.13) solvable. The low-fidelity physics-based model given in Eq. (8.13) is employed to train the network initially.

8.3 Time of Flight Measurements

The accuracy of the AE source estimation depends upon the precision of the TOF measurements. It is contentious to measure the exact arrival time of the signal from the time-history plot. Because the time domain signals are perturbed by the low-level and high-frequency noise that creates an uncertainty in the signal, first time of arrival and this noise obscures the actual arrival time. Consequently, the actual arrival time may deviate from the measured time of arrival. However, the cost function used in this study given in Eq. (8.13) is based on TDOA; hence, these minor errors get mutually nullified, and the final estimation should not be affected considerably. Several techniques comprising threshold crossing by fitting the envelope, wavelet transform, cross-correlation, and curve fitting, to mention a few are available in the literature to measure the time of arrival from the time domain acoustic signal [279-281]. This study employs a principled way to measure the arrival time by threshold

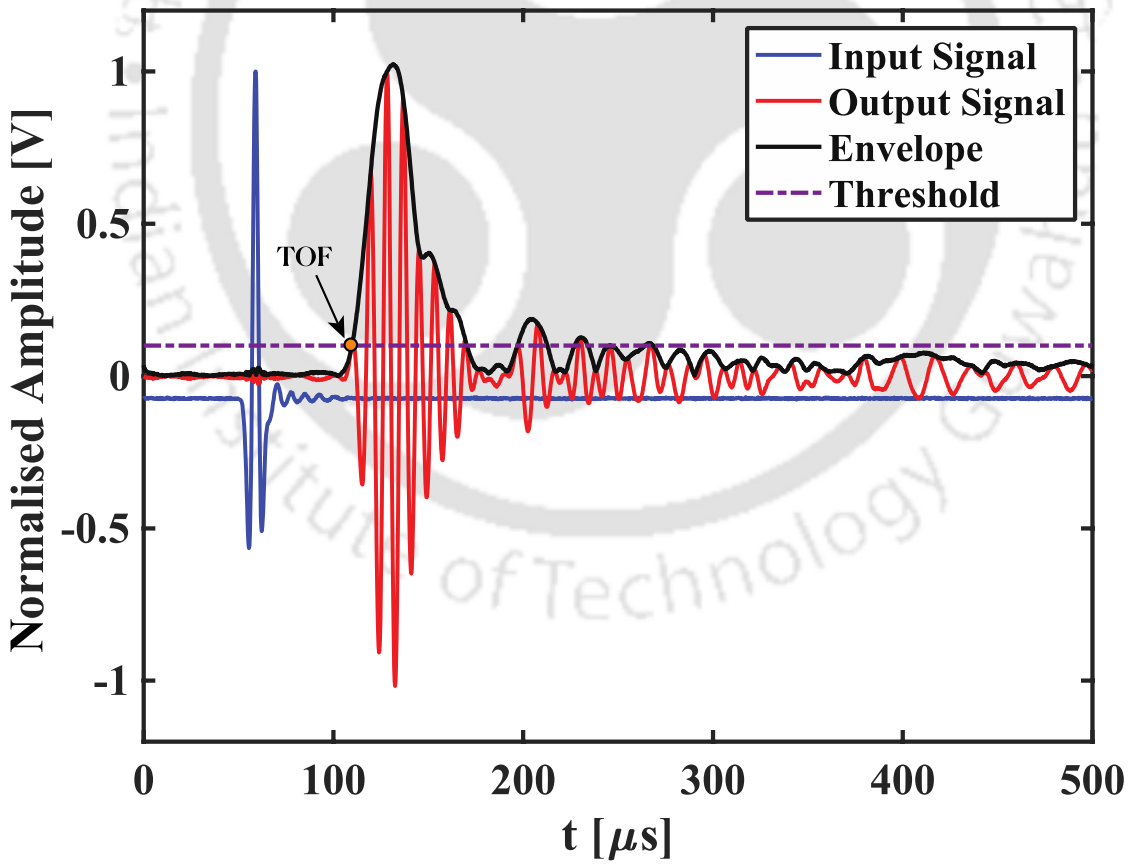

Figure 8.1 Illustration of the arrival time measurement by threshold crossing of the time history signal envelope.

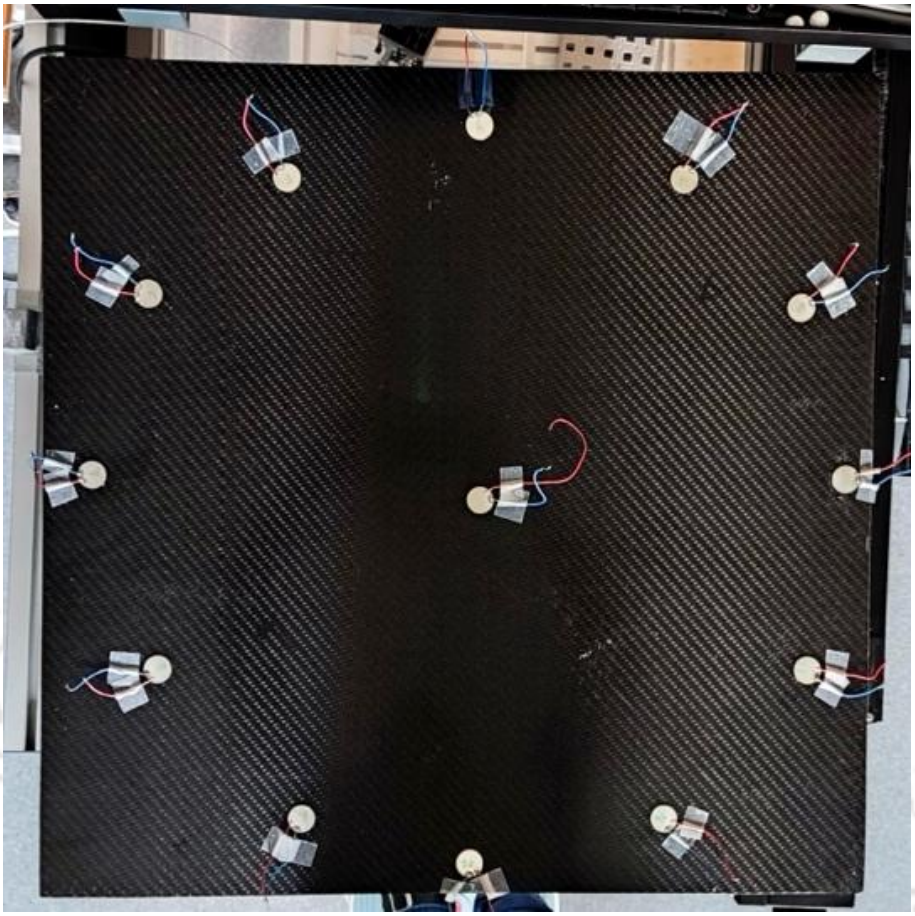

Figure 8.2 Experimental setup of wave velocity profile measurement.

crossing of the signal envelope. The envelope can be computed by using the definition of an analytic signal $x_A(t)$ of an actual signal $x(t)$:

$$x_A(t) = x(t) + ix_H(t), \tag{8.14}$$

where, $i = \sqrt{-1}$ is the imaginary unit and $x_H(t)$ is the Hilbert transform of $x(t)$ defined as:

$$x_H(t) = \frac{1}{\pi}\int_{-\infty}^{\infty} x(\tau)\frac{1}{t-\tau}d\tau. \tag{8.15}$$

Now, the envelope $A(t)$ can be computed as:

$$A(t) = \sqrt{x(t)^2 + x_H(t)^2}. \tag{8.16}$$

The time of flight is measured when the envelope of a signal crosses the defined threshold (A_t). In this study, a threshold A_t was defined as 0.1 V [245, 279]. Figure 8.1 illustrates the arrival time measurement from the threshold crossing of the envelope of a signal.

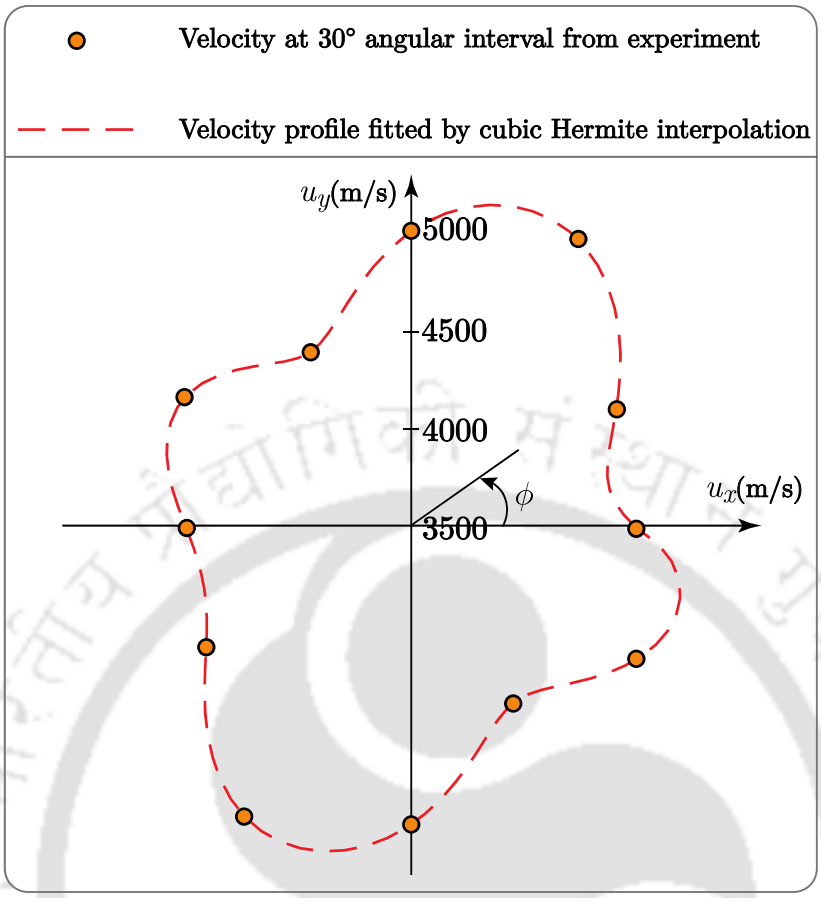

Figure 8.3 The variation of wave velocity in different directions for the composite plate.

8.4 Acquisition of High-Fidelity Data

Experimental tests were conducted using a 60 cm × 60 cm CFRP composite panel to collect high-fidelity data and to evaluate the efficacy of the proposed framework. The anisotropic panel had a nominal thickness of 2 mm. In order to simulate the impact on a plate, a Teflon ball of diameter 13.4 mm was dropped on the composite plate. The ball weighs approximately 10 g and dropped from a height of 0.3 m. The velocities in different directions are calculated by placing twelve PZT sensors in a circle with a radius of 27.5 cm at 30° angular spacing varying from 0° to 360° as shown in Figure 8.2.

A guided ultrasonic wave was excited at the centre of the circle through central PZT. The signal is received simultaneously by all the sensors placed at the circumference of the circle. In Figure 8.1, the blue and red signals are the input signal excited at the centre and the signal received by the sensor at the circumference,

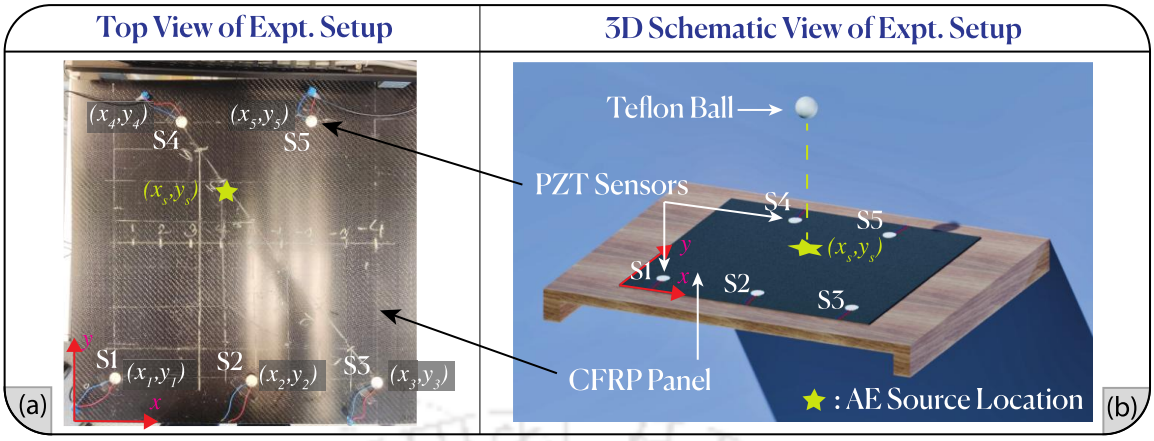

Figure 8.4 (a) Top view of the experimental setup, and (b) a 3D schematic view of the experimental setup.

respectively. The time difference between the input signal and TOF of the received signal is the time taken to propagate the wave from the centre to the circumference. By measuring the time of arrival and dividing the radius of the circle by the time of arrival, the wave velocities in different directions are computed. After experimentally measuring the wave velocity in discrete angular directions, the wave velocity at any

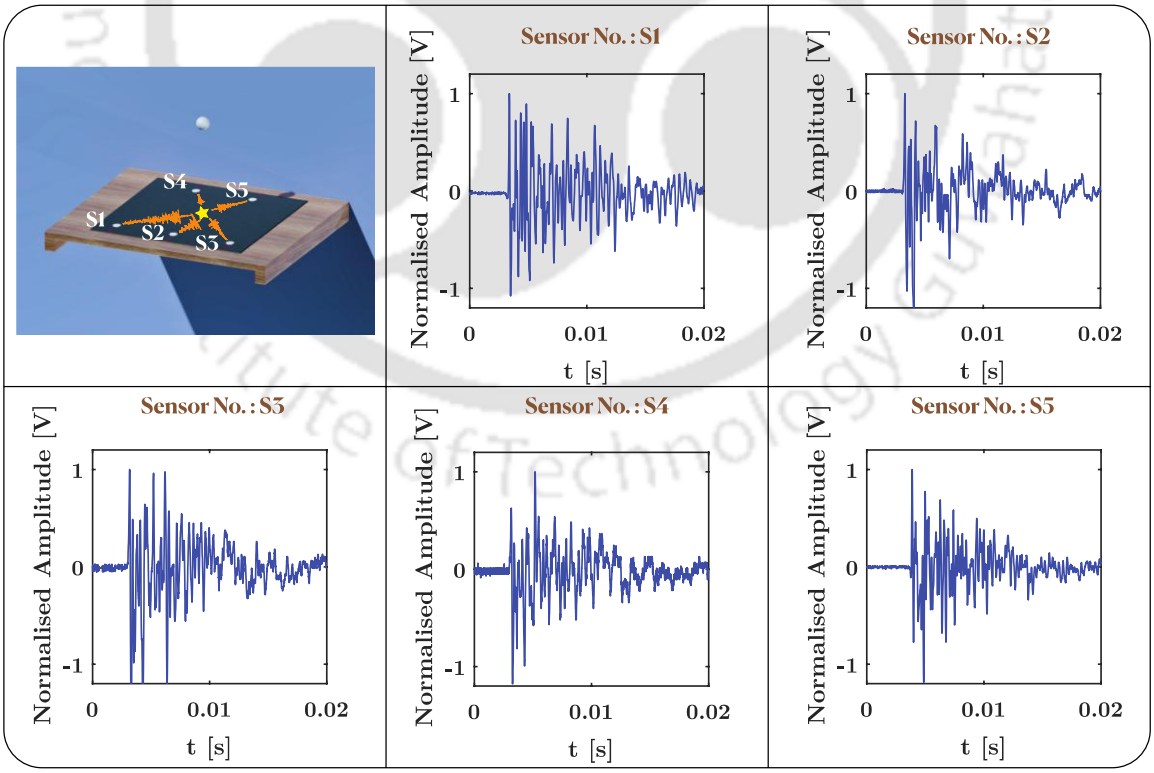

Figure 8.5 Plots of time domain signals were received at different sensors due to the drop of the Teflon ball.

Table 8.1 Location of sensors placed on CFRP plate to detect the AE source in the experiment.

Sensor No	Sensor Location	
	x_s (cm)	y_s (cm)
1	7.5	7.5
2	30.5	7.5
3	53.5	7.5
4	19	53.5
5	42	53.5

angle ϕ can be obtained by performing the cubic Hermite interpolation. The resulting velocity profile is shown in Figure 8.3.

After obtaining the velocity profile, the sparse array of five sensors were installed on the plate, as shown in Figure 8.4. A point on the plate was selected randomly, and the Teflon ball was dropped at that point to generate high-fidelity data. The signals received by the five sensors were recorded to estimate the AE source. Figure 8.5 illustrates the plots of time domain signals received at different sensors due to the Teflon ball being dropped at a location of $x = 30$ cm and $y = 35$ cm. Table 8.1 summarises the location of sensors placed on the plate to detect the AE source.

8.5 Mathematical Background of mfPINN

The data-driven ANN and PINN are the cornerstone of the proposed mfPINN. In the following sections, a brief background on the ANN and PINN are presented.

8.5.1 Data-driven ANN

An ANN is a smart data processing system that imitates the biological neural network of the animal brain [282]. It is a robust technique that is extensively used in the domain of ML [283]. An ANN is comprised of input, output and hidden layers in between. These layers are interconnected by the number of neurons. The connectivity between the neurons depicts the functionality of the ANN [284]. ANNs have effectively been utilised to understand complex engineering systems and to extract important and meaningful features from the data.

The nodes of a layer are parameterised by weights ($\mathbf{w}$) and biases ($\mathbf{b}$). Each input parameter $\mathbf{x}$ is multiplied by its weights prior to reaching the hidden layer node. The

weighted sum ($\mathbf{z}$) of the weighted parameters collected at the nodes is computed. The weighted sum can be defined as

$$\mathbf{z} = \mathbf{w}\mathbf{x} + \mathbf{b}. \tag{8.17}$$

Subsequently, the weighted sum is transmitted to the next layer using the activation function and finally to the output layer as the target data. The activation function $f(\cdot)$ is defined as [285]

$$\mathbf{u} = f(\mathbf{z}). \tag{8.18}$$

In a feedforward NN, the input data is propagated through the input, hidden and output layers. However, in the backpropagation algorithm, the output loss is propagated back in the opposite direction of the output, hidden and input layers. During the training process in a data-driven setting, the network parameters, i.e., weights and biases, are updated by minimising the loss function. The loss function $\mathcal{L}_{\mathbf{u}}$ for this is given by

$$\mathcal{L}_{\mathbf{u}} = \sum_{k=1}^{N_H} \|\mathbf{u} - \tilde{\mathbf{u}}\|, \tag{8.19}$$

where, N_H is the number of high-fidelity data points available, $\mathbf{u}$ is the observed response and $\tilde{\mathbf{u}}$ is the neural network predicted response. Despite the fact that ANN architectures are employed to learn physics, there exist crucial issues related to interpretability, generalizability, overfitting and demands for significant data. These factors limit their utility and computational tractability for data- driven models. It is to be noted that for the current work, the high-fidelity data collected from the experiment is very sparse. Thus, the direct application of data-driven ANN is inconceivable to get adequate results.

8.5.2 PINN

One of the key components of the proposed framework is building physics-informed learning machines. In this section, we first delineate how to embed physics in an ML model and how various physics can steer in developing novel NN architectures. Currently, there are three approaches that can be pursued individually or in tandem to expedite training and enhance the generalization of ML models by embedding physics in them [223]. (a) Training ML systems on data that embody the underlying physics allow them to learn functions, vector fields or operators that contemplate the physical structure of the data by introducing observational biases. (b) Another

pathway of embedding physics is by introducing inductive biases to incorporate the prior assumptions in tailored interventions to an ML architecture in such a way that the predictions of the ML models are ensured to implicitly satisfy the governing physical laws, often expressed in the form of certain mathematical constraints. The implementation of this approach is complex and difficult to scale. (c) Last but not least approach of embedding physics is by proper selection of loss functions, constraints and inference algorithms. The learning biases can be introduced that can regulate the training phase of the ML system to explicitly favour convergence towards solutions that comply with the governing physics. This enables a very adaptable platform of embedding physics that can be expressed in the form of integral, differential or even fractional equations. These various methods of embedding physics in a learning algorithm towards physically coherent solutions are not mutually exclusive and can be adequately merged together to yield a very broad class of hybrid approaches for developing physics-informed learning machines. From these available pathways of embedding physics, the current work followed the learning biases mode to impose the underlying physics in a soft manner by properly defining the loss function of conventional NN. This variation of NN is also known as a PINN.

Recently, PINNs have become an excellent solution technique for solving various physics-based models pioneered by Raissi, *et al.* (2019) [269]. Several works are reported in the literature where the PINNs are leveraged to solve various engineering and scientific problems when the underlying physics is in the form of differential equations [223, 268, 286]. Despite this fact, one can extend the capability of PINN to solve the problem when the underlying physics is in the form of fractional equations. However, in such a scenario, the application of PINN is sparse in the literature. Recently, Pun, *et al.* (2019) proposed to employ PINN to predict interatomic potential energy surface in a large atomistic model [287]. They combine the physics-based model of bond order potential, which is in the form of a fractional equation with an NN. Further, they compared the results of PINN with a conventional NN and concluded that the accuracy of the PINN is better and performs well in the extrapolation regime. Several studies have made similar claims that PINN performs better than the conventional NN trained in a data-driven setting [223, 268, 286, 287]. However, one can generate data based on the underlying physics and train a conventional NN on such data by using the observational biases mode of embedding physics on a learning model. This type of model is not generalizable and does not offer any flexibility.

In the current impact detection problem, the governing physics contains parameters like the properties of the material in the form of the velocity of the wave $\big(v(\theta)\big)$, the location of sensors (x_i, y_i) and the uncertainty of the sensors (σ_t). For certain parameters one can generate data that embody the underlying physics and train a conventional neural network on such data to get the intended output from the NN. However, any changes in the parameter, for instance, the material is changed, and the positions of sensors are changed; in such a scenario, one has to generate the data and train the network again. This data generation task could be time-consuming and computationally expensive in many engineering applications. In this work, we proposed to use PINN over a conventional NN to avoid the data generation step, as PINN can be directly trained by using the underlying physics as expressed in Eq. (8.13) without generating data from it, as the governing physics is directly embedded in the PINN. The leading motivation for employing PINN in the proposed framework is that the embedding underlying physics can yield more interpretable DL architecture that remain robust in the presence of imperfect data and can provide accurate and physically consistent prediction even for extrapolatory or generalization task.

Most real engineering systems suffer from limited high-fidelity or experimental data. In such cases, the conventional NN does not perform well because of its data intensiveness nature and the huge training data requirement. The advantage of PINN over the conventional NN is that the PINN performs very well in the sparse data scenario as it takes advantage of the underlying physics-based mathematical model.

To be mathematically precise, we again generalized the representation of the Eq. (8.13) as

$$\mathbf{N}\Big(\mathbf{u}\Big(\mu_{x_s}, \sigma_{x_s}, \mu_{y_s}, \sigma_{y_s}\Big), \beta\Big) = g, \tag{8.20}$$

where,

$$\begin{aligned}\mathbf{N}(\mathbf{u}(\mu_{x_s}, \sigma_{x_s}, \mu_{y_s}, \sigma_{y_s}), \beta) \\ = \sqrt{\frac{\mu_{x_s}^2 + \sigma_{x_s}^2 - 2\mu_{x_s}x_i + x_i^2 + \mu_{y_s}^2 + \sigma_{y_s}^2 - 2\mu_{y_s}y_i + y_i^2}{\{v(\theta_i)\}^2} - \sigma_{t_i}^2} \\ - \sqrt{\frac{\mu_{x_s}^2 + \sigma_{x_s}^2 - 2\mu_{x_s}x_1 + x_1^2 + \mu_{y_s}^2 + \sigma_{y_s}^2 - 2\mu_{y_s}y_1 + y_1^2}{\{v(\theta_1)\}^2} - \sigma_{t_1}^2},\end{aligned} \tag{8.21}$$

$g = \mu_{\Delta t_{1i}}$.

$\mathbf{N}(\cdot)$ prescribe the nonlinear function as defined in Eq. (8.21) and β represents the other parameters of Eq. (8.21). The goal is to find an NN approximation $\tilde{\mathbf{u}}$ to the observed data $\mathbf{u}$. The approximation should satisfy the governing physics defined in Eq. (8.13) and in turn Eq. (8.20). The NN is then trained to minimize the physics-informed loss function given by

$$\mathcal{L}_R = \sum_{k=1}^{N_L} \|\mathbf{N}(\mathbf{u}, \beta) - g\|, \tag{8.22}$$

where, N_L is the number of points for the input and R is the residual of the governing equation corresponding to the collocation points and is defined as

$$R = \mathbf{N}(\mathbf{u}, \beta) - g. \tag{8.23}$$

The advantage of PINN is the training is fast as compared to the data-driven ANN because the PINN needs no simulation data. The governing equation of the system is satisfied during the training process; thus, the other physical properties of the system are also satisfied. One must note that the governing equation under consideration is available to apply the PINN successfully. However, numerous cases exist in science and engineering where the underlying equation is unknown [112]. Albeit, the equation is known, it is usually derived based on certain assumptions and approximations. The governing equation merely depicts the actual case in an approximate manner. It is expected that the results obtained from PINN would necessarily be erroneous.

8.5.3 Proposed Approach

The overarching goal of this work is to leverage the capabilities of PINN and ANN to estimate the AE source location under the condition of sparse and noisy data. The proposed approach is driven by the requirement for an efficient parsimonious model that evades overfitting and exploits the underlying physics of the problem. Unlike previous deep learning approaches, the proposed network architecture is designed particularly to handle a ubiquitous class of sparse data perturbed by noise and uncertainty.

The proposed network architecture is shown in Figure 8.6. The objective of this network is to estimate the location (μ_{x_s}, μ_{y_s}) of the AE source and the corresponding uncertainty $(\sigma_{x_s}, \sigma_{y_s})$ estimated from the TDOA information $(\mu_{\Delta t_{1i}})$ perturbed with

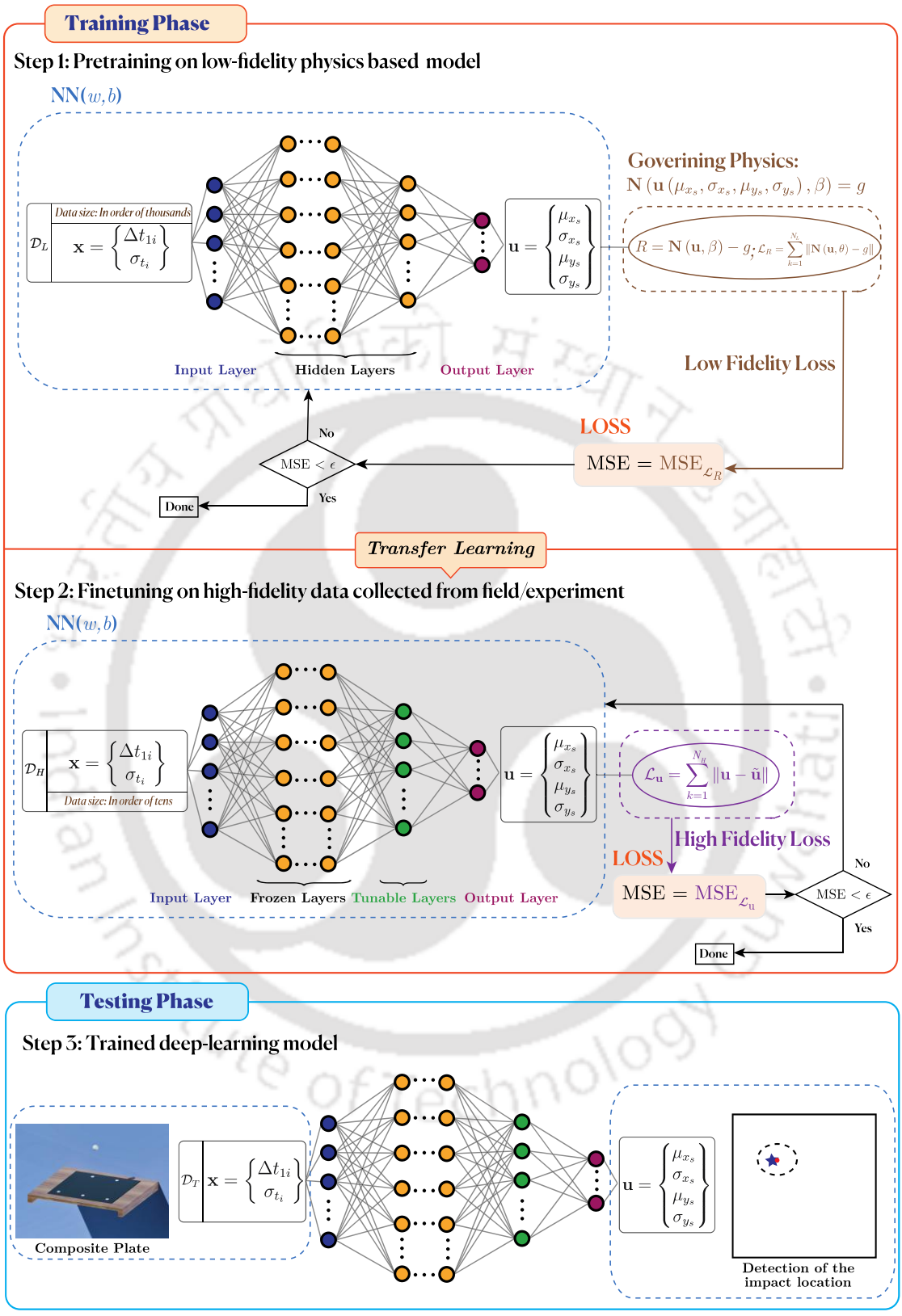

Figure 8.6 Schematic representation of proposed mfPINN framework for estimating AE source location and corresponding uncertainty.

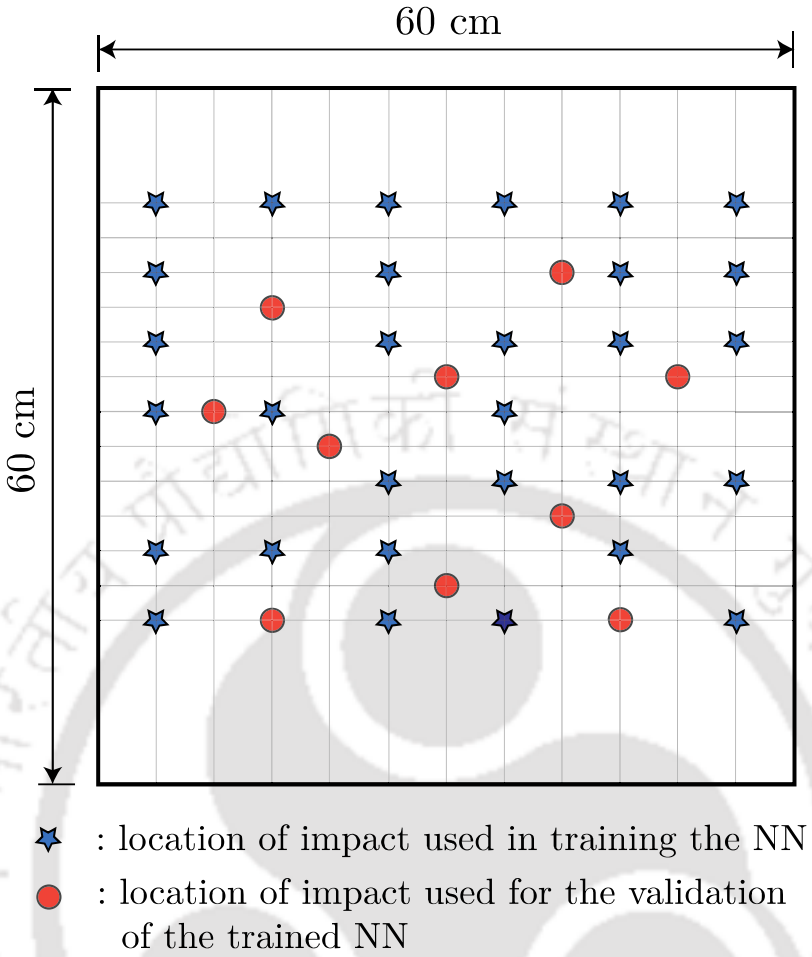

Figure 8.7 Illustration of the impact location to generate high-fidelity data by performing the experiment.

noise/uncertainty (σ_{t_i}). Neither data-driven ANN nor the PINN is competent in estimating the AE source from the sparse, noisy data collected from field/real experiments. The ANN fails as the data available is sparse. Moreover, NNs have considerable potential for overfitting data. Simultaneously, PINN fails because the governing physics in Eq. (8.13) merely portrays the real scenario in an approximate manner.

To overcome the problem, a novel framework based on mfPINN is presented in this study. The presented approach employs both ANN and PINN. Towards this goal, a single deep NN is first trained for the low-fidelity model and then updated based on the high-fidelity data. The idea of transfer learning is employed to tune the network on high-fidelity data. The usage of transfer learning in the multi-fidelity framework is found in the literature [288]. The concept of data-driven ANN is used to update the

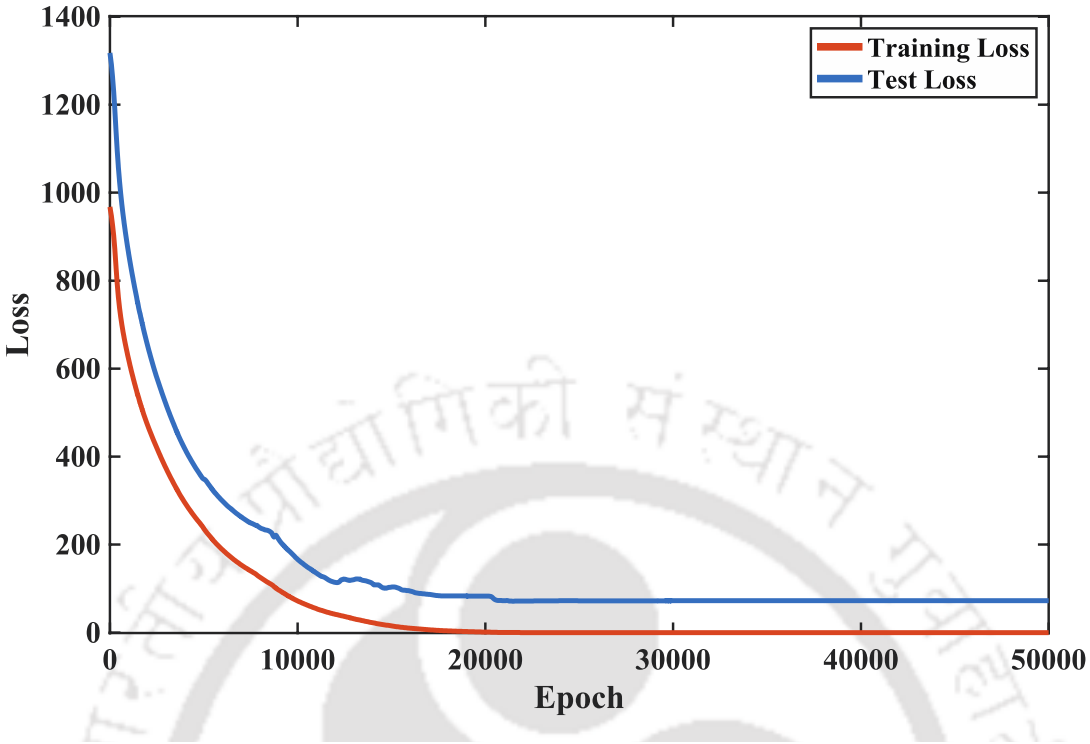

Figure 8.8 The plot of the performance summary (red line) of the optimization algorithm during the training and the performance summary of ANN (blue line) in prediction during the process.

low-fidelity PINN on the high-fidelity data. While updating the network, two crucial factors are considered. To begin with, the training starts on the high-fidelity data by retaining the initial value of the network parameters obtained from the training on low-fidelity PINN. Finally, using the concept of transfer learning [286] the parameters corresponding to the last one or two layers are updated instead of all the network layers. The transfer learning accelerates the training process of the network as the number of parameters to be updated is decreased. Freezing the initial layers ensures the knowledge gained from the low-fidelity model is retained in the DL model. Further, transfer learning avoids the overfitting of the network on high-fidelity data.

Closing this section, it is worth mentioning that mfPINN involves a significant number of hyperparameters, that is, the number of layers, the types of activation functions, and the neurons per layer, to mention a few, need to be tuned carefully in order to get optimal results. The universal approximation theorem promises that a neural network comprised of at least one hidden layer and a large enough number of neurons, and the differentiable activation function is competent in depicting any arbitrary function or dataset [289-291]. Hanin (2019) presented expressions for the

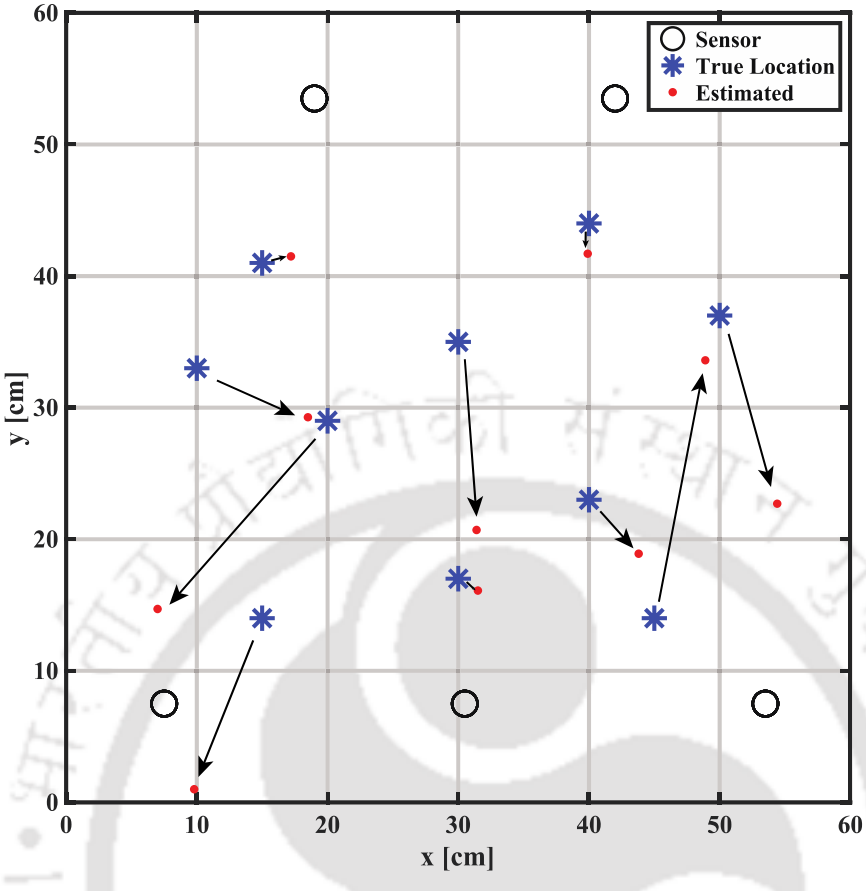

Figure 8.9 Impact location results showing true and estimated locations using data-driven ANN.

optimal neural network parameters required to depict a function within a desired accuracy when ReLU activation functions are used [292]. There are several methods, such as grid search or random search, Bayesian hyperparameter optimisation procedure [293] etc., are often used to tune the NN hyperparameters. Despite these theoretical guarantees, the training algorithm might not be able to find optimal values of the network parameters to achieve the desired accuracy. In practice, with few numbers of hidden layers and a significant number of neurons per layer might be needed. Further, often more than one layer with a small number of neurons per layer is used. For the activation function $f(\cdot)$ in Eq. (8.18), there are various alternatives available. One common option is the rectified linear unit (ReLU). For an input z, the output from ReLU is given as

$$f_{\text{ReLU}}(z) = \max\ (0, z). \tag{8.24}$$

It is worth noting that the derivative of the output from ReLU vanishes for $z < 0$. This conceives a difficulty in training using gradient descent for negative inputs and

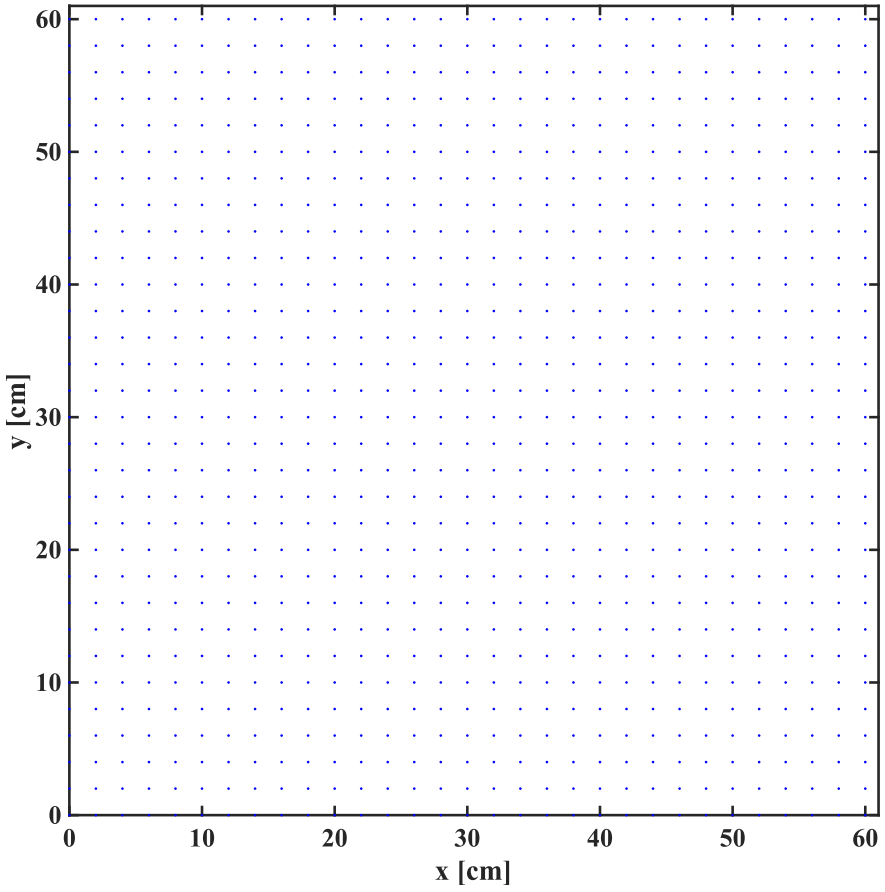

Figure 8.10 The collocation points are used to train the low-fidelity model of the neural network.

is called a *dying ReLU* problem. In order to avoid this problem, the applicability of another activation function is explored, namely, hyperbolic tangent or tanh. For this activation function, the output is given as

$$f_{\tanh}(z) = \tanh(z) = \frac{e^z - e^{-z}}{e^z + e^{-z}}. \tag{8.25}$$

For the last layer, we employed the linear activation function, where the output is given as

$$f_{\text{Linear}}(z) = z. \tag{8.26}$$

One should note that there exist different alternatives for activation functions, e.g., logistic sigmoid, leaky ReLU, and exponential linear unit (ELU), to mention a few. However, we found the combination of tanh and linear activation provides an excellent result for the AE detection problem. Further, in this work, we use 50 neurons per layer based on a preliminary investigation, where the performance is monitored with

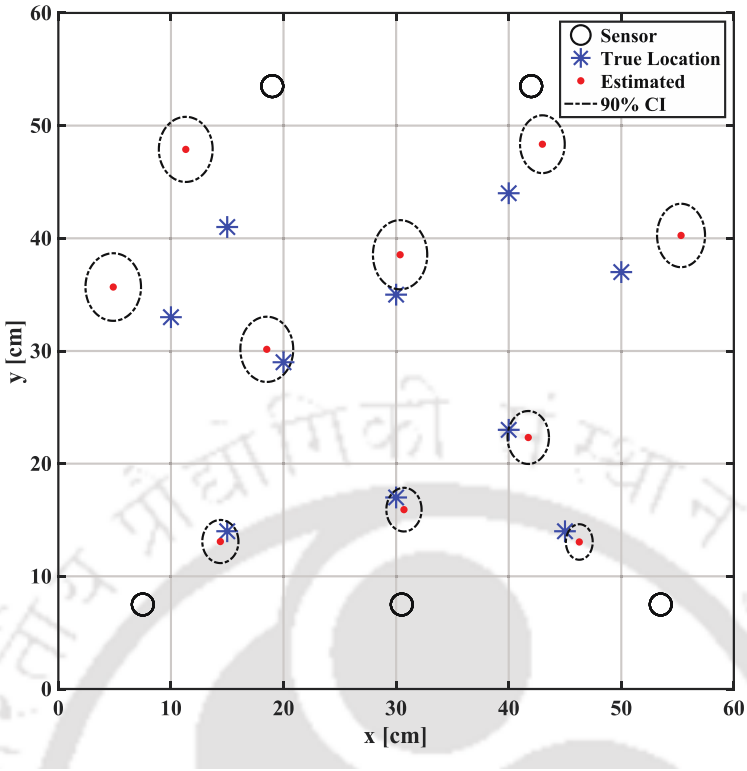

Figure 8.11 Impact location results showing true and estimated locations using low-fidelity PINN.

different number of neurons per layer. A new hidden layer is included to the network if the accuracy is increased with the included new layer.

8.6 Results and Discussion

In this section, three sets of results are presented to illustrate the performance of the proposed framework. The results are presented in the first two sets using data-driven ANN and PINN. The intention of these two sets of results is to illustrate the necessity of a multi-fidelity framework using transfer learning.

A Teflon ball is dropped on 40 different locations of the plate, given the wave velocity profile (Figure 8.3) is known to generate high-fidelity data $\mathcal{D}_H$, as shown in Figure 8.7. These data are randomly divided into two categories. The first category consists of the TDOA and uncertainty of the sensor corresponding to the thirty different locations, as illustrated by the blue star in Figure 8.7 are used to train the neural network model. The red circles in Figure 8.7 depict rest of the data used to evaluate the efficacy of the proposed model.

Table 8.2 Source estimation results using data-driven ANN.

Point	Actual Location		Estimated Location		ε_r (cm)
	x_s (cm)	y_s(cm)	μ_{x_s} (cm)	μ_{x_s} (cm)	
1	15	14	9.8	1.0	14.0
2	30	17	31.5	16.1	1.7
3	40	23	43.8	18.9	5.6
4	10	33	18.5	29.1	9.3
5	20	29	7.0	14.7	19.3
6	40	44	39.9	41.7	2.3
7	15	41	17.2	41.5	2.2
8	50	37	51.4	22.7	14.4
9	45	14	48.9	33.6	**19.9**
10	30	35	31.4	20.7	14.4
				Average (cm):	10.3

8.6.1 Estimation of impact location using high-fidelity data-driven ANN

A data-driven ANN is modelled to solve the problem under consideration. The ANN estimates the location of impact deterministically as in the observed high-fidelity data; the impact location information is deterministic. The network has five inputs and five hidden layers with 50 neurons each. The five inputs are the TDOA information measured from 5 sensors installed on the plate. The network has two outputs corresponding to the x- and y-coordinates of the estimated locations. Hyperbolic tangent (tanh) activation is used for all except the last layer. Linear activation is considered for the last layer. The Adam optimizer is run for 50,000 iterations for training the ANN with available 30 training data. The training loss is converged satisfactorily, as presented in Figure 8.8. However, the network over-fitted the data, as one can observe that the test loss is converged but significant.

The results obtained from data-driven ANN are illustrated in Figure 8.9 in terms of true locations and estimated locations. To evaluate the accuracy of the results, an error function is defined as

$$\varepsilon_r = \sqrt{(\mu_{x_s} - x_s)^2 + (\mu_{y_s} - y_s)^2}. \tag{8.27}$$

where, (x_s, y_s) are the true impact coordinates and (μ_{x_s}, μ_{y_s}) are the NN estimated coordinates. Table 8.2 summarises the impact of localisation results using data-driven ANN. It is observed from Table 8.2 that the performance of the data-driven ANN in the prediction of AE source location is poor, with an average error of 10.3217 cm and a maximum error of 19.9423 cm.

8.6.2 Estimation of impact location using low-fidelity PINN

To solve the problem under consideration, the unknown location and corresponding uncertainty ($\mathbf{u} = \{\mu_{x_s}, \sigma_{x_s}, \mu_{y_s}, \sigma_{y_s}\}^T$) are first represented by using an NN. The network comprises ten inputs, five hidden layers with 50 neurons per layer and four outputs. The ten inputs are TDOA information ($\mu_{\Delta t_{1i}}$) and corresponding uncertainty in the TOF measurement (σ_t) of the installed five sensors. Hyperbolic tangent (tanh) activation is used in all the layers except the last layers. Linear activation is considered for the last layer. The residual for training the network is given as

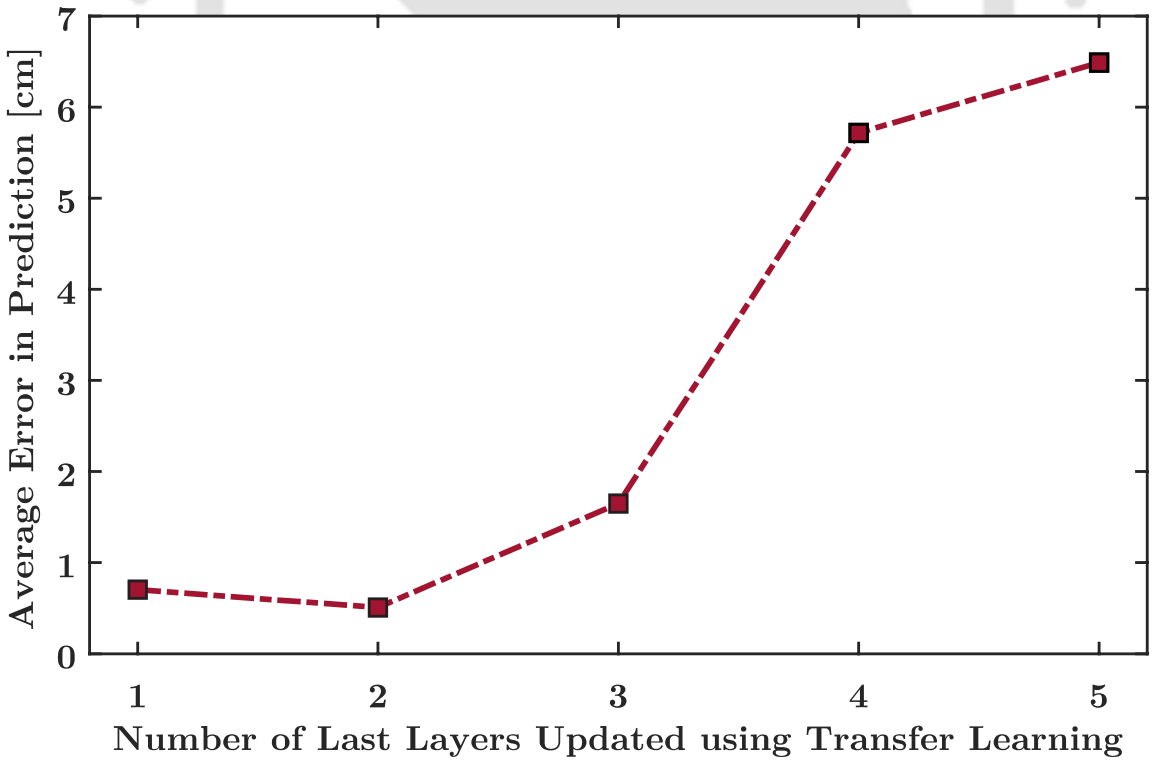

Figure 8.12 The plot of the performance summary of the proposed mfPINN framework in predicting the AE source location while the last various layers are updated using transfer learning.

$$
\begin{aligned}
&R_k \\
&= \sqrt{\frac{(\mu_{x_s}^2)_k + (\sigma_{x_s}^2)_k - 2(\mu_{x_s})_k x_i + x_i^2 + (\mu_{y_s}^2)_k + (\sigma_{y_s}^2)_k - 2(\mu_{y_s})_k y_i + y_i^2}{\{v(\theta_i)\}^2} - \sigma_{t_i}^2} \\
&- \sqrt{\frac{(\mu_{x_s}^2)_k + (\sigma_{x_s}^2)_k - 2(\mu_{x_s})_k x_1 + x_1^2 + (\mu_{y_s}^2)_k + (\sigma_{y_s}^2)_k - 2(\mu_{y_s})_k y_1 + y_1^2}{\{v(\theta_1)\}^2} - \sigma_{t_1}^2} \\
&- \mu_{\Delta t_{1i}}.
\end{aligned}
\tag{8.28}
$$

where, R_k is the residual and $\tilde{\mathbf{u}} = \{\mu_{x_s}, \sigma_{x_s}, \mu_{y_s}, \sigma_{y_s}\}^T$ is obtained from the NN output. 'i' and 'k' in the suffix indicating the ith sensor and kth collocation point. For training the low-fidelity PINN, the collocation points, as shown in Figure 8.10 are generated. The number of collocation points is 961 with an interval of 2 cm in x- and y-directions.

Naively initiating the input in the NN will not ensure that the model is trained within the given plate boundary. Alternatively, one can create the TDOA (Δt_{1i}) information by using Eq. (8.4) corresponding to these collocation points in a deterministic sense. However, this step can be avoided by approximately estimating

Table 8.3 Source estimation results using low-fidelity PINN.

Point	Actual Location		Estimated Location		ε_r (cm)
	x_s (cm)	y_s(cm)	μ_{x_s} (cm)	μ_{x_s} (cm)	
1	15	14	14.2	12.8	1.4
2	30	17	31.0	16.3	1.2
3	40	23	41.6	22.2	1.8
4	10	33	5.9	35.0	4.6
5	20	29	18.4	30.1	2.0
6	40	44	43.1	48.7	5.7
7	15	41	12.1	48.3	**7.9**
8	50	37	55.3	40.3	6.2
9	45	14	46.0	13.1	1.3
10	30	35	30.3	38.4	3.4
				Average (cm):	3.6

the largest possible value of TDOA (Δt_{1i}), then initiate the training by providing the TDOA (Δt_{1i}) as an input within the largest possible value. The unconservative estimation of this value can be done by dividing the distance of a furthest point in the plate from a sensor by the minimum value of velocity profile. One must note that the proposed approach is able to take uncertainty into account. Towards this aim, the uncertainty present in the measurement is assumed to be additive zero-mean Gaussian noise of standard deviation σ_t. In particular, different values of $\sigma_t = \{1,2,3,4,5\}\mu s$ are considered during the training process. The low-fidelity input data $\mathcal{D}_L = \{(\mu_{\Delta t_{1i},k}, \sigma_{t,k})\}_{k=1}^{N_L}$ is generated to train the network.

$$\mathcal{D}_L = \mu_{\Delta t_{1i}} \otimes \sigma_{t_i}, \tag{8.29}$$

where, the operator $\otimes$ indicates the Kronecker product. The Adam optimizer is run for 50,000 epochs. A learning rate of 0.001 is used. The loss function used in training the PINN is

$$\mathcal{L}_R = \sum_{k=1}^{N_L} \|R_k\|. \tag{8.30}$$

Table 8.4 Source estimation results using mfPINN

Point	Actual Location		Estimated Location		ε_r (cm)
	x_s (cm)	y_s(cm)	μ_{x_s} (cm)	μ_{x_s} (cm)	
1	15	14	14.7	14.1	0.3
2	30	17	30.1	17.02	0.1
3	40	23	40.5	22.8	0.5
4	10	33	9.7	32.5	0.6
5	20	29	20.6	29.4	0.7
6	40	44	39.2	44.1	**0.8**
7	15	41	15.1	41.2	0.2
8	50	37	49.6	37.1	0.4
9	45	14	45.4	14.4	0.6
10	30	35	29.2	34.9	**0.8**
				Average (cm):	0.5

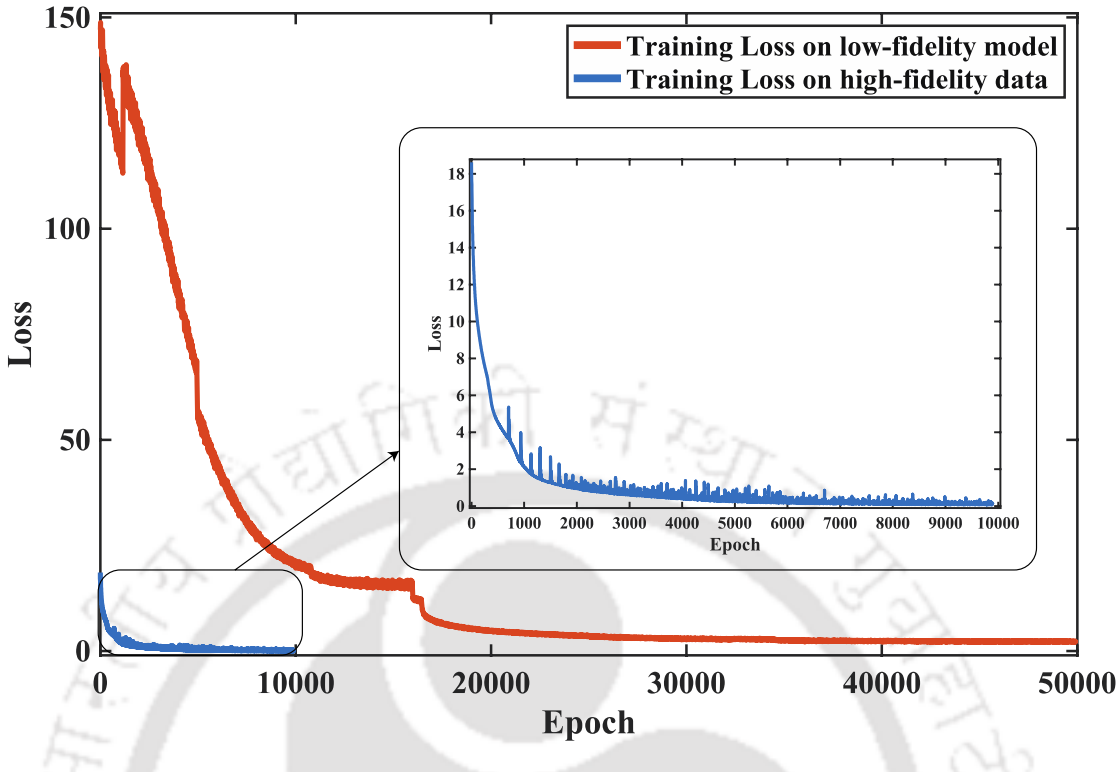

Figure 8.13 The plot of the performance summary of the optimization algorithm during the low-fidelity and high-fidelity training processes.

The variation of training loss of low-fidelity PINN with respect to the number of epochs is illustrated by the red line in Figure 8.13. The results obtained from low-fidelity PINN are presented in Figure 8.11. Table 8.3 summarises the estimated impact location and the average error in the estimation.

The results obtained using only data-driven ANN and low-fidelity PINN are discussed in Sections 8.6.1 and 8.6.2 respectively. Both data-driven ANN and low-fidelity PINN are found to yield erroneous results with an average error of 10.3217 cm and 3.5529 cm respectively and maximum error of 19.9423 cm and 7.8926 cm respectively. Because in the case of high-fidelity ANN, the access to high-fidelity data $\mathcal{D}_H$ is sparse, and the model overfitted the data. On the other hand, the number of data available in the case of PINN is not the issue; instead, the governing physics is an approximate representation of a real scenario. To rescue the problem, we proposed using a multi-fidelity framework that employs both the ANN and PINN. The utility of mfPINN is discussed in the following Section 8.6.3.

8.6.3 Estimation of impact location using multi-fidelity PINN

In mfPINN, the network trained with the low-fidelity model, as discussed in Section 8.6.2 is updated with high-fidelity data by transfer learning. The basic premise here is to store knowledge gained by low-fidelity PINN while training on low-fidelity data to improve the efficiency of the final model after training on a few high-fidelity data. This is achieved by freezing the weights and biases of specific layers in a deep neural network. To retain the knowledge gained from the low-fidelity PINN and avoid overfitting, the network parameters corresponding to the last few layers are updated, and for other layers, the parameters are kept fixed. In the current work, only the last two layers are updated by using transfer learning based on the investigation performed as illustrated in Figure 8.12. Here, the network's performance is monitored by computing the average error in predicting the AE source locations as we increase the number of last layers to be updated. From Figure 8.12, one can observe that when only the last two layers are updated, the average error in predicting AE source location has achieved the minimum value. It should be noted that allowing more than two layers or all the layers to update will lead to possible loss of information gained and will overfit the model while training due to the small size of high-fidelity data. The network architecture of mfPINN considered is the same as before; the only change here is that the Adam optimizer is run for 10,000 epochs with high-fidelity data. Transfer learning is used to update the last two layers of the network. For the Adam optimizer, a learning rate of 0.001 is used. One must note that the training loss with high-fidelity data converged within 10,000 epochs only. On the other hand, it can be observed from Figure 8.13 that 50,000 epochs are required to converge the training loss for the low-fidelity PINN. The results obtained from multi-fidelity PINN are presented in Figure 8.14. Table 8.4 summarises the estimated impact location and the average error in the estimation. The results obtained using the proposed mfPINN are

Table 8.5 Comparison of the performances of data-driven ANN, low-fidelity PINN and mfPINN in the AE source location prediction

Sl. No.	Type of Neural Network	Average Error (cm)	Maximum Error (cm)
1	data-driven ANN	10.3	19.9
2	low-fidelity PINN	3.6	7.9
3	mfPINN	0.5	0.8

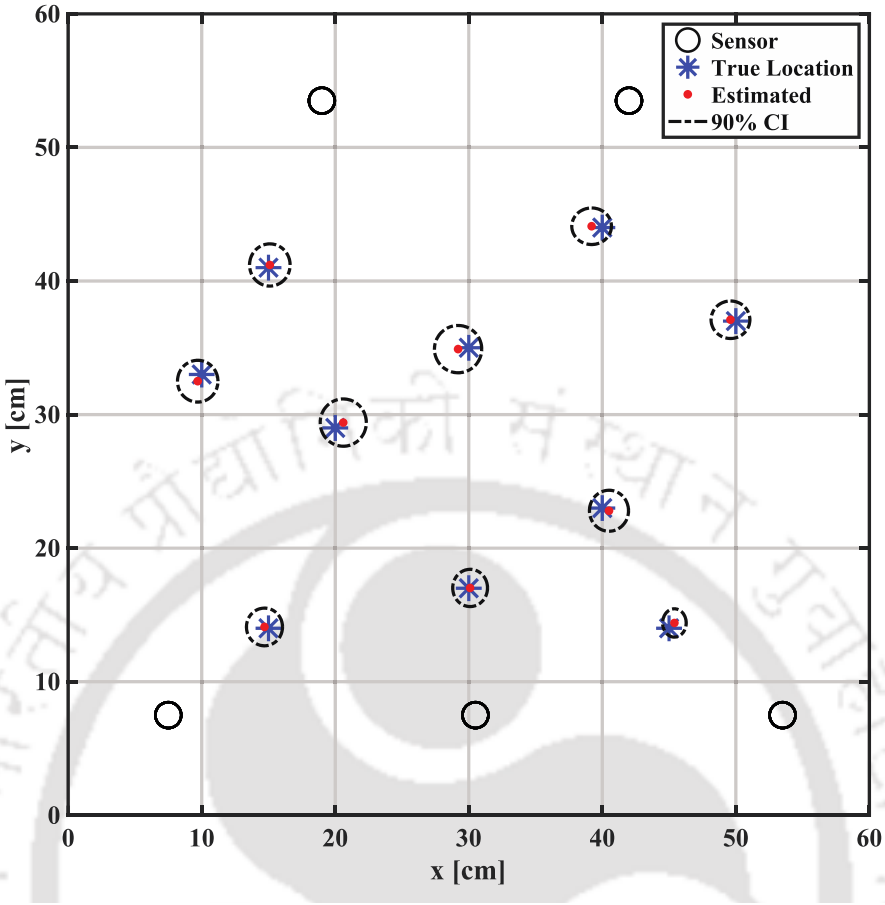

Figure 8.14 Impact location results showing true and estimated locations using mfPINN.

considerably more accurate as compared to data-driven ANN and low-fidelity PINN with an average error of 0.5075 cm and maximum error of 0.8062 cm. Table 8.5 summarises the comparison of the performances of data-driven ANN, low-fidelity PINN and mfPINN in the prediction of AE source location.

8.7 Concluding Remarks

In this study, a probabilistic framework based on mfPINN methods is proposed to estimate the location of AE sources in anisotropic panels. In particular, a deep NN is trained with a low-fidelity model, followed by updating the network with high-fidelity data using transfer learning. These algorithms are applied for the situation where the wave velocity profile is known *a priori*. Experimental tests were carried out on a carbon-fibre reinforced polymer (CFRP) composite panel instrumented with a sparse array of piezoelectric transducers to collect high-fidelity data and evaluate the efficacy of the proposed framework. The AE sources were simulated by dropping a Teflon ball

in order to show that the proposed framework can detect the AE source generated by such a small drop. The results show that the proposed approach can accurately estimate AE source locations with an average error of 0.5075 cm, whereas 10.3217 cm and 3.5529 cm for data-driven ANN and low-fidelity PINN, respectively. However, an advantage of the framework over the other heuristic algorithm is its ability to provide a confidence interval of the estimated AE source location instead of a single point, despite the fact that the training cost of a deep NN is generally higher. However, almost instant estimation can be done once the network has been trained successfully. Another advantage of the proposed method is its ability to consider uncertainty in sensor measurements. The accuracy and computational efficiency of the proposed framework demonstrate its potential application in real-time SHM applications.

Chapter 9
Conclusion and Future Scope

The studies presented in this dissertation focuses on advancing data-driven and ML algorithms for structural health assessments, with a particular emphasis on plate structures, including piezoelectric materials and carbon composite laminates, which present distinct challenges. While existing studies have utilized a range of algorithms to detect damages and system parameters, they often overlook the noise and uncertainties inherent in empirical data. Notably, these algorithms have yet to be rigorously tested on piezoelectric transducers and composite plates. This thesis endeavours to fill this gap by not only identifying and estimating damage in plate structures but also by fine-tuning various algorithms to enhance the assessment of their condition. The key contributions of this research and their potential for future exploration are discussed in subsequent sections.

9.1 Summary and Conclusion

The body of work presented in this doctoral thesis represents a comprehensive endeavour to advance the field of SHM through the lens of data-driven and machine learning methodologies. The culmination of these efforts has yielded a series of novel frameworks and algorithms designed specifically for the nuanced assessment of plate structures, with a pronounced focus on the integrity and functionality of piezoelectric materials and anisotropic composites.

- The development of a data-driven framework based on mrDMD algorithm, which has proven to be a robust technique for the detection of microscale defects in piezoelectric substrates such as PZT. The mrDMD algorithm, enhanced by image registration and KL divergence, has demonstrated an

exceptional ability to extract significant spectral modes, enabling the sensitive and accurate localization of defects. (Refer Chapter 4)

- The thesis further introduced a deep learning-based autoencoder neural network, which marked a significant leap forward in the identification of surface anomalies within PZT sensors. This model harnessed the power of complex waveform big data, utilizing image registration and peak signal-to-noise ratio evaluation to overcome distortion challenges. The approach not only distinguished itself in anomaly detection but also set a precedent for future explorations in big data applications within SHM. (Refer Chapter 5)
- In the domain of probabilistic modelling, the thesis employed the UKF for the stiffness tensor characterization of anisotropic crystals, particularly Lithium Niobate ($LiNbO_3$). This integration of empirical wavefield data with a physics-based model underscored the potential of Bayesian filtering algorithms in delivering optimal parameter estimation by considering the measurement uncertainties. (Refer Chapter 6)
- Moreover, the thesis attempted into the estimation of elastic constants for composite materials, utilizing mulit-output Gaussian Process Regression (moGPR) to associate Lamb wave dispersion curves with experimental observations from SLDV. This methodology provided a compelling non-destructive alternative to traditional destructive testing techniques, particularly for composite laminates. (Refer Chapter 7)
- The final contribution of this thesis was the introduction of a multi-fidelity physics-informed neural network (mfPINN), which ingeniously combined low-fidelity physical models and sparse high-fidelity experimental data. This innovative approach, tailored for acoustic emission source localization within composite panels, not only showcased its precision but also its adaptability to measurement uncertainties. This work accentuated the viability of the methodologies developed in preceding studies and demonstrated their collective strength in a comprehensive, real-world SHM application. Further, this study served as the pivotal that unified and validated the overall research theme. (Refer Chapter 8)

The sum of these contributions encapsulates a significant stride towards a more intelligent, robust, and comprehensive SHM framework. The research has not only bridged the gap between theoretical development and practical implementation but has also set the stage for the continued evolution of SHM systems. Each of the developed methodologies has the potential to be scaled and adapted for broader applications, reaffirming the thesis's impact on the safety, maintenance, and monitoring of critical infrastructures.

In conclusion, the work presented herein has laid down a foundation for future advancements in SHM. By meticulously addressing the challenges of anomaly detection and material characterization, this thesis has carved a pathway towards the realization of more reliable, efficient, and cost-effective monitoring systems that ensure the structural integrity and extend the service life of engineering structures.

9.2 Future Scope

This thesis comprehensively details the theoretical background of various data-driven and ML frameworks, illustrating their application across various engineering scenarios. While the algorithms introduced here have been effectively applied, there is potential for further refinement and enhancement. The studies presented in this thesis opens up numerous avenues for future work:

1. **Integration with IoT Devices**: Future research could explore the integration of the developed algorithms with Internet of Things (IoT) devices for real-time monitoring and assessment, further enhancing the operational efficiency of SHM systems.
2. **Adaptation to Varied Material Geometries**: The adaptation of the proposed methodologies to a broader range of material geometries and compositions would be beneficial, particularly for composite materials with complex architectures.
3. **Adaptation to Varied Noise Condition**: The study assumes that measurement noises are uncorrelated and follow a Gaussian distribution, but in reality, noise can exhibit correlations and non-Gaussian characteristics, and may not always be additive. This highlights the ongoing need for enhancements in Kalman filters, and other ML models to address such complexities in noise behaviour.

4. **Scalability and Field Deployment**: There remains an opportunity to scale these methods for extensive field deployment across various industry sectors, including aerospace, civil infrastructure, and automotive applications.
5. **Advanced Data Acquisition Techniques**: Incorporating more sophisticated data acquisition techniques, such as drone-based imaging or advanced laser scanning, could enrich the datasets used for SHM and provide more comprehensive monitoring capabilities.
6. **Cross-disciplinary Applications**: The potential for cross-disciplinary applications of these frameworks could be explored, such as in biomedical engineering for the health monitoring of biomedical implants.
7. **Enhanced Machine Learning Models**: With the continued advancement in machine learning, future work could include the development of even more sophisticated models that can handle larger datasets, more complex noise patterns, and provide enhanced predictive capabilities.
8. **Robustness to Environmental Variabilities**: Further research is warranted to improve the robustness of SHM systems against environmental variabilities such as temperature fluctuations, humidity, and operational loads.

By building upon the methodologies and findings of this thesis, future researchers can continue to push the boundaries of SHM technology, creating more resilient and intelligent monitoring systems that can predict, adapt, and respond to the ever-changing conditions of the structures they safeguard.

List of Publications

Articles from PhD Thesis

Journal Articles

1. **N. M. M. Kalimullah**, A. Shelke and A. Habib, "A Deep Learning Approach for Anomaly Identification in PZT Sensors using Point Contact Method." ***Smart Materials and Structures*** **(32), 2023. (Impact Factor: 4.1)**
2. **N. M. M. Kalimullah**, A. Shelke and A. Habib, "A Probabilistic Framework for Source Localization in Anisotropic Composite using Transfer Learning based Multi-Fidelity Physics Informed Neural Network (mfPINN)." ***Mechanical Systems and Signal Processing*** **(197), 2023. (Impact Factor: 8.4)**
3. **N. M. M. Kalimullah**, K. Shukla, A. Shelke and A. Habib, "Stiffness Tensor Estimation of Anisotropic Crystal using Point Contact Method and Unscented Kalman Filter." ***Ultrasonics*** **(131), 2023. (Impact Factor: 4.2)**
4. **N. M. M. Kalimullah**, A. Shelke and A. Habib, "Multiresolution Dynamic Mode Decomposition (mrDMD) of Elastic Waves for Damage Localisation in Piezoelectric Ceramic." ***IEEE Access*** **(9), 2021. (Impact Factor: 3.9)**
5. **N. M. M. Kalimullah**, S. Ojha, Maciej Radjieński, A. Shelke and A. Habib, "A Probabilistic Machine Learning Framework for Stiffness Tensor Estimation of Carbon Composite Laminate." ***Mechanical Systems and Signal Processing.*** **(Impact Factor: 8.4)** *(Under Review)*

International Conference Proceedings	1. **N. M. M. Kalimullah**, S. Ojha, A. Shelke, A. Habib, "Acoustic Emission Source Localization in Plates Through Support Vector Machine with Genetic Optimization" in *The Quantitative Nondestructive Evaluation (QNDE)*, 2023. 2. **N. M. M. Kalimullah**, A. Shelke and A. Habib, "Bayesian Filtering for Parameter Estimation of Mechanical Properties of Isotropic Material." in *Proc. Symposium on Electronics (USE)*, 2021. 3. **N. M. M. Kalimullah**, R. D. Kulkarni, A. Shelke and A. Habib, "Point Contact Method for Damage Localisation Using Singular Value Decomposition in Piezoelectric Ceramic Crystal." in *Proc. Asian Conference on Mechanics of Functional Materials and Structures (ACMFMS)*, 2021.

Articles beyond PhD Thesis

Journal Articles	1. S. Ojha, **N. M. M. Kalimullah** and A. Shelke, "Application of Constrained Unscented Kalman Filter (CUKF) for System Identification of Coupled Hysteresis under Bidirectional Excitation." ***Structural Control and Health Monitoring*** **(29), 2022. (Impact Factor: 6.058)** 2. A. Thakur, **N. M. M. Kalimullah**, A. Shelke, B. Hazra and T. Kundu, "NG-DPSM: A Neural Green-Distributed Point Source Method for Ultrasonic Field Emission Near Fluid-Solid Interface using Physics Informed Neural Network." ***Engineering Applications of Artificial Intelligence*** **(131), 2024. (Impact Factor: 8)** 3. A. Thakur, **N. M. M. Kalimullah**, A. Shelke, B. Hazra and T. Kundu, "Ultrasonic Field Estimation for Random P- and S- Wavenumbers in Isotropic Solids using DPSM" ***Wave Motion.*** **(Impact Factor: 2.1)** *(Under Review)* 4. P. Banerjee, S. Ojha, **N. M. M. Kalimullah**, A. Shelke and A. Habib, "Ultrasonic Wave Field Image Augmentation in PZT Sensors using Generative Machine Learning and Coulomb Coupling" ***Measurement Science and Technology.*** **(Impact Factor: 2.4)** *(Under Review)* 5. R. Pal, N. Ghosh, **N. M. M. Kalimullah**, A. Ahmad, F. Melandsø and A. Habib "Subsurface Damage Identification and Localization in PZT Ceramics using Point Contact Excitation and Detection: An Image Processing Framework." ***Ultrasonics.*** **(Impact Factor: 4.2)** *(Under Review)*

International Conference Proceedings	1. P. Banerjee, P. Saxena, **N. M. M. Kalimullah** A. Shelke, A. Habib, "Damage Detection and Localization by Learning Deep Features of Elastic Waves in Piezoelectric Ceramic Using Point Contact Method." ***IEEE CVPR*, 2024.** ***(Accepted)***

Bibliography

[1] S.W. Doebling, C.R. Farrar, M.B. Prime, D.W. Shevitz, Damage identification and health monitoring of structural and mechanical systems from changes in their vibration characteristics: a literature review, LA-13070-MS, Los Alamos, NM: Los Alamos National Laboratory, (1996).

[2] C.R. Farrar, S.W. Doebling, D.A. Nix, Vibration‐based structural damage identification, Philosophical Transactions of the Royal Society of London. Series A: Mathematical, Physical and Engineering Sciences, 359 (2001) 131-149.

[3] H. Sohn, C.R. Farrar, F.M. Hemez, D.D. Shunk, D.W. Stinemates, B.R. Nadler, J.J. Czarnecki, A review of structural health monitoring literature: 1996‐2001, Los Alamos National Laboratory, USA, 1 (2003) 16.

[4] P. Cao, S. Qi, J. Tang, Structural damage identification using piezoelectric impedance measurement with sparse inverse analysis, Smart Materials and Structures, 27 (2018) 035020.

[5] E.Z. Moore, J.M. Nichols, K.D. Murphy, Model-based SHM: Demonstration of identification of a crack in a thin plate using free vibration data, Mechanical Systems and Signal Processing, 29 (2012) 284-295.

[6] R.J. Barthorpe, On model-and data-based approaches to structural health monitoring, (2010).

[7] M.I. Friswell, Damage identification using inverse methods, Philosophical Transactions of the Royal Society A: Mathematical, Physical and Engineering Sciences, 365 (2007) 393-410.

[8] J. Pal, S. Sikdar, S. Banerjee, P. Banerji, A Combined Machine Learning and Model Updating Method for Autonomous Monitoring of Bolted Connections in Steel Frame Structures Using Vibration Data, Applied Sciences, 12 (2022) 11107.

[9] C.R. Farrar, K. Worden, Structural health monitoring: a machine learning perspective, John Wiley & Sons, 2012.

[10] G. Park, H.H. Cudney, D.J. Inman, Impedance-based health monitoring of civil structural components, Journal of infrastructure systems, 6 (2000) 153-160.

[11] M. Azimi, A.D. Eslamlou, G. Pekcan, Data-driven structural health monitoring and damage detection through deep learning: State-of-the-art review, Sensors, 20 (2020) 2778.

[12] F. Luleci, F.N. Catbas, O. Avci, CycleGAN for undamaged-to-damaged domain translation for structural health monitoring and damage detection, Mechanical Systems and Signal Processing, 197 (2023) 110370.

[13] A. Rytter, Vibrational based inspection of civil engineering structures, Dept. of Building Technology and Structural Engineering, PhD (1993).

[14] P. Rizzo, M. Cammarata, D. Dutta, H. Sohn, K. Harries, An unsupervised learning algorithm for fatigue crack detection in waveguides, Smart Materials and Structures, 18 (2009) 025016.

[15] T.T. Tran, E. Ozer, Automated and model-free bridge damage indicators with simultaneous multiparameter modal anomaly detection, Sensors, 20 (2020) 4752.

[16] D.-A. Tibaduiza, M.-A. Torres-Arredondo, L. Mujica, J. Rodellar, C.-P. Fritzen, A study of two unsupervised data driven statistical methodologies for detecting and classifying damages in structural health monitoring, Mechanical Systems and Signal Processing, 41 (2013) 467-484.

[17] C.R. Farrar, K. Worden, An introduction to structural health monitoring, Philosophical Transactions of the Royal Society A: Mathematical, Physical and Engineering Sciences, 365 (2007) 303-315.

[18] H. Sohn, Effects of environmental and operational variability on structural health monitoring, Philosophical Transactions of the Royal Society A: Mathematical, Physical and Engineering Sciences, 365 (2007) 539-560.

[19] Y. Ding, A. Li, T. Liu, Environmental variability study on the measured responses of Runyang Cablestayed Bridge using wavelet packet analysis, Science in China Series E: Technological Sciences, 51 (2008) 517-528.

[20] F. Magalhães, Á. Cunha, E. Caetano, Vibration based structural health monitoring of an arch bridge: From automated OMA to damage detection, Mechanical Systems and signal processing, 28 (2012) 212-228.

[21] E. Figueiredo, I. Moldovan, A. Santos, P. Campos, J.C. Costa, Finite element-based machine-learning approach to detect damage in bridges under operational

and environmental variations, Journal of Bridge Engineering, 24 (2019) 04019061.

[22] E. Figueiredo, G. Park, C.R. Farrar, K. Worden, J. Figueiras, Machine learning algorithms for damage detection under operational and environmental variability, Structural Health Monitoring, 10 (2011) 559-572.

[23] A.B. Noel, A. Abdaoui, T. Elfouly, M.H. Ahmed, A. Badawy, M.S. Shehata, Structural health monitoring using wireless sensor networks: A comprehensive survey, IEEE Communications Surveys & Tutorials, 19 (2017) 1403-1423.

[24] P. Kudela, M. Radzienski, P. Fiborek, T. Wandowski, Elastic constants identification of fibre-reinforced composites by using guided wave dispersion curves and genetic algorithm for improved simulations, Composite Structures, 272 (2021) 114178.

[25] L. Zhang, D. Ozevin, The influence of multi-mode failures in composites on the characteristics of elastic waves, Nondestructive Characterization for Composite Materials, Aerospace Engineering, Civil Infrastructure, and Homeland Security 2013, SPIE, 2013, 869402

[26] O. Putkis, A. Croxford, Stiffness matrix determination of composite materials using Lamb wave group velocity measurements, Nondestructive Characterization for Composite Materials, Aerospace Engineering, Civil Infrastructure, and Homeland Security 2013, SPIE, 2013, 11-22

[27] C.A. Leckey, M.D. Rogge, F.R. Parker, Guided waves in anisotropic and quasi-isotropic aerospace composites: Three-dimensional simulation and experiment, Ultrasonics, 54 (2014) 385-394.

[28] M. Jumani, S. Sapuan, I. RA, Advance composite in aerospace application, Conference: Seminar on Advanced Bio-and Mineral based Natural Fibre Composites (SBMC2021), 2021, 35-39

[29] K. Eltouny, M. Gomaa, X. Liang, Unsupervised learning methods for data-driven vibration-based structural health monitoring: a review, Sensors, 23 (2023) 3290.

[30] Z. Su, C. Yang, N. Pan, L. Ye, L.-M. Zhou, Assessment of delamination in composite beams using shear horizontal (SH) wave mode, Composites Science and Technology, 67 (2007) 244-251.

[31] A.H. Nayfeh, D. Chimenti, Free wave propagation in plates of general anisotropic media, Review of progress in quantitative nondestructive evaluation, Springer, (1989).

[32] A.H. Nayfeh, The general problem of elastic wave propagation in multilayered anisotropic media, The Journal of the Acoustical Society of America, 89 (1991) 1521-1531.

[33] A.H. Nayfeh, Wave propagation in layered anisotropic media: With application to composites, Elsevier, 1995.

[34] B. Hosten, M. Castaings, Transfer matrix of multilayered absorbing and anisotropic media. Measurements and simulations of ultrasonic wave propagation through composite materials, The Journal of the Acoustical Society of America, 94 (1993) 1488-1495.

[35] L. Wang, F. Yuan, Group velocity and characteristic wave curves of Lamb waves in composites: Modeling and experiments, Composites science and technology, 67 (2007) 1370-1384.

[36] M.J. Lowe, Matrix techniques for modeling ultrasonic waves in multilayered media, IEEE transactions on ultrasonics, ferroelectrics, and frequency control, 42 (1995) 525-542.

[37] L. Knopoff, A matrix method for elastic wave problems, Bulletin of the Seismological Society of America, 54 (1964) 431-438.

[38] H. Schmidt, F.B. Jensen, A full wave solution for propagation in multilayered viscoelastic media with application to Gaussian beam reflection at fluid-solid interfaces, The Journal of the Acoustical Society of America, 77 (1985) 813-825.

[39] A. Mal, Wave propagation in layered composite laminates under periodic surface loads, Wave motion, 10 (1988) 257-266.

[40] B. Pavlakovic, M. Lowe, Disperse user manual: a system for generating dispersion curves, Copyright B Pavlakovic, M Lowe, (2003).

[41] D.R. Ramasawmy, B.T. Cox, B.E. Treeby, ElasticMatrix: A MATLAB toolbox for anisotropic elastic wave propagation in layered media, SoftwareX, 11 (2020) 100397.

[42] S. Rokhlin, L. Wang, Stable recursive algorithm for elastic wave propagation in layered anisotropic media: Stiffness matrix method, The Journal of the Acoustical Society of America, 112 (2002) 822-834.

[43] A. Huber, The dispersion calculator: A free software for calculating dispersion curves of guided waves in multilayered composites, 2018, https://www.dlr.de/zlp/en/desktopdefault.aspx/tabid-14332/24874_read-61142/ (accessed 8-May-2023).

[44] I. Bartoli, A. Marzani, F.L. Di Scalea, E. Viola, Modeling wave propagation in damped waveguides of arbitrary cross-section, Journal of sound and vibration, 295 (2006) 685-707.

[45] K. Huang, S. Dong, Propagating waves and edge vibrations in anisotropic composite cylinders, Journal of Sound and Vibration, 96 (1984) 363-379.

[46] G. Liu, K. Dai, X. Han, T. Ohyoshi, Dispersion of waves and characteristic wave surfaces in functionally graded piezoelectric plates, Journal of Sound and Vibration, 268 (2003) 131-147.

[47] B. Masserey, P. Fromme, Surface defect detection in stiffened plate structures using Rayleigh-like waves, NDT&E International, 42 (2009) 564-572.

[48] K. Harri, P. Guillaume, S. Vanlanduit, On-line damage detection on a wing panel using transmission of multisine ultrasonic waves, NDT&E International, 41 (2008) 312-317.

[49] M. Rahman, T. Michelitsch, A note on the formula for the Rayleigh wave speed, Wave Motion, 43 (2006) 272-276.

[50] M. Stavropoulou, G. Exadaktylos, E. Papamichos, I. Larsen, C. Ringstad, Rayleigh wave propagation in intact and damaged geomaterials, International Journal of Rock Mechanics and Mining Sciences, 40 (2003) 377-387.

[51] X. Jian, Y. Fan, R.S. Edwards, S. Dixon, Surface-breaking crack gauging with the use of laser-generated Rayleigh waves, Journal of Applied Physics, 100 (2006).

[52] D. Aggelis, T. Shiotani, Repair evaluation of concrete cracks using surface and through-transmission wave measurements, Cement and Concrete Composites, 29 (2007) 700-711.

[53] M. Castaings, B. Hosten, Lamb and SH waves generated and detected by air-coupled ultrasonic transducers in composite material plates, NDT&E International, 34 (2001) 249-258.

[54] M.V. Golub, A. Boström, Interface damage modeled by spring boundary conditions for in-plane elastic waves, Wave Motion, 48 (2011) 105-115.

[55] M. Castaings, SH ultrasonic guided waves for the evaluation of interfacial adhesion, Ultrasonics, 54 (2014) 1760-1775.

[56] B. Le Crom, M. Castaings, Shear horizontal guided wave modes to infer the shear stiffness of adhesive bond layers, The Journal of the Acoustical Society of America, 127 (2010) 2220-2230.

[57] Z. Fan, M. Castaings, M.J. Lowe, C. Biateau, P. Fromme, Feature-guided waves for monitoring adhesive shear modulus in bonded stiffeners, NDT&E International, 54 (2013) 96-102.

[58] D. Alleyne, P. Cawley, The excitation of Lamb waves in pipes using dry-coupled piezoelectric transducers, Journal of Nondestructive Evaluation, 15 (1996) 11-20.

[59] M. Castaings, B. Hosten, Ultrasonic guided waves for health monitoring of high-pressure composite tanks, NDT&E International, 41 (2008) 648-655.

[60] H.W. Kim, Y.E. Kwon, S.H. Cho, Y.Y. Kim, Shear-horizontal wave-based pipe damage inspection by arrays of segmented magnetostrictive patches, IEEE Transactions on Ultrasonics, Ferroelectrics, and Frequency Control, 58 (2011) 2689-2698.

[61] J.-R. Lee, H. Jeong, C.C. Ciang, D.-J. Yoon, S.-S. Lee, Application of ultrasonic wave propagation imaging method to automatic damage visualization of nuclear power plant pipeline, Nuclear Engineering and Design, 240 (2010) 3513-3520.

[62] R. Ahmad, T. Kundu, Influence of water flow through pipe networks for damage detection using guided waves, Nondestructive Testing of Materials and Structures *RILEM Bookseries*, Springer, 2013, 681-687

[63] L. Satyarnarayan, J. Chandrasekaran, B. Maxfield, K. Balasubramaniam, Circumferential higher order guided wave modes for the detection and sizing of cracks and pinholes in pipe support regions, NDT&E International, 41 (2008) 32-43.

[64] T. Vogt, M. Lowe, P. Cawley, The scattering of guided waves in partly embedded cylindrical structures, The Journal of the Acoustical Society of America, 113 (2003) 1258-1272.

[65] W.-B. Na, T. Kundu, Underwater pipeline inspection using guided waves, Journal of Pressure Vessel Technology, 124 (2002) 196-200.

[66] M. Ebrahimian, M.I. Todorovska, Structural system identification of buildings by a wave method based on a layered Timoshenko beam model, Health Monitoring of Structural and Biological Systems 2014, SPIE, 2014, 385-397

[67] M. Rahmani, M.I. Todorovska, Structural health monitoring of a 54-story steel-frame building using a wave method and earthquake records, Earthquake Spectra, 31 (2015) 501-525.

[68] M.I. Todorovska, M.T. Rahmani, System identification of buildings by wave travel time analysis and layered shear beam models−Spatial resolution and accuracy, Structural Control and Health Monitoring, 20 (2013) 686-702.

[69] J. Quintana, F. Carrión, S. Crespo, Damage detection on a cable stayed bridge using wave propagation analysis, EWSHM-7th European Workshop on Structural Health Monitoring, 2014,

[70] P. Rizzo, A. Marzani, J. Bruck, Ultrasonic guided waves for nondestructive evaluation/structural health monitoring of trusses, Measurement Science and Technology, 21 (2010) 045701.

[71] Y. Wang, X. Zhu, H. Hao, J. Ou, Guided wave propagation and spectral element method for debonding damage assessment in RC structures, Journal of Sound and Vibration, 324 (2009) 751-772.

[72] R. Wang, H. Gu, Y. Mo, G. Song, Proof-of-concept experimental study of damage detection of concrete piles using embedded piezoceramic transducers, Smart Materials and Structures, 22 (2013) 042001.

[73] Y. Lu, J. Li, L. Ye, D. Wang, Guided waves for damage detection in rebar-reinforced concrete beams, Construction and Building Materials, 47 (2013) 370-378.

[74] M. Radzieński, Ł. Doliński, M. Krawczuk, M. Palacz, Damage localisation in a stiffened plate structure using a propagating wave, Mechanical Systems and Signal Processing, 39 (2013) 388-395.

[75] D. Wang, L. Ye, Y. Lu, Z. Su, Probability of the presence of damage estimated from an active sensor network in a composite panel of multiple stiffeners, Composites Science and Technology, 69 (2009) 2054-2063.

[76] C. Haynes, M.D. Todd, E. Flynn, A. Croxford, Statistically-based damage detection in geometrically-complex structures using ultrasonic interrogation, Structural Health Monitoring, 12 (2013) 141-152.

[77] V. Senyurek, Detection of cuts and impact damage at the aircraft wing slat by using Lamb wave method, Measurement, 67 (2015) 10-23.

[78] E. Figueiredo, E. Cross, Linear approaches to modeling nonlinearities in long-term monitoring of bridges, Journal of Civil Structural Health Monitoring, 3 (2013) 187-194.

[79] A. Farhidzadeh, E. Dehghan-Niri, S. Salamone, Gaussian mixture modeling of acoustic emissions for structural health monitoring of reinforced concrete

structures, Sensors and Smart Structures Technologies for Civil, Mechanical, and Aerospace Systems 2013, SPIE, 2013, 72-81

[80] H.-J. Zepernick, A. Finger, Pseudo random signal processing: theory and application, John Wiley & Sons, 2013.

[81] I.K. Fodor, A survey of dimension reduction techniques, Lawrence Livermore National Lab., CA (US), 2002, (accessed

[82] E.J. Candès, X. Li, Y. Ma, J. Wright, Robust principal component analysis?, Journal of the ACM (JACM), 58 (2011) 1-37.

[83] T. Bouwmans, E.H. Zahzah, Robust PCA via principal component pursuit: A review for a comparative evaluation in video surveillance, Computer Vision and Image Understanding, 122 (2014) 22-34.

[84] J. Quiroga, J. Quiroga, L. Mujica, R. Villamizar, M. Ruiz, Temperature robust PCA based stress monitoring approach, Key Engineering Materials, 713 (2016) 288-292.

[85] L.E. Mujica, F. Gharibnezhad, J. Rodellar, M. Todd, Considering temperature effect on robust principal component analysis orthogonal distance as a damage detector, Structural Health Monitoring, 19 (2020) 781-795.

[86] F. Gharibnezhad, L.E. Mujica, J. Rodellar, Applying robust variant of Principal Component Analysis as a damage detector in the presence of outliers, Mechanical Systems and Signal Processing, 50 (2015) 467-479.

[87] F. Gharibnezhad, L.E. Mujica Delgado, J. Rodellar Benedé, Damage detection in the presence of outliers based on robust PCA, Proceedings of the 8th International Conference on Structural Dynamics, EURODYN 2011: Leuven, Belgium, 4-6 July 2011, 2011,

[88] F. Gharibnezhad, L.E. Mujica, J. Rodellar, Comparison of two robust PCA methods for damage detection in presence of outliers, Journal of Physics: Conference Series, IOP Publishing, 2011, 012009

[89] F. Gharibnezhad, L.E. Mujica Delgado, J. Rodellar Benedé, C.-P. Fritzen, Damage detection using robust fuzzy principal component analysis, Proceedings 6th European Workshop on Structural Health Monitoring, 2013, 1-6

[90] X. Li, S. Ding, B. Tan, Accurate defect detection in thin-wall structures with transducer networks via outlier elimination, IEEE Sensors Journal, 18 (2018) 9619-9628.

[91] Y. Zhang, T. Xia, Extracting sparse crack features from correlated background in ground penetrating radar concrete imaging using robust principal component

analysis technique, Nondestructive Characterization and Monitoring of Advanced Materials, Aerospace, and Civil Infrastructure 2016, SPIE, 2016, 980402

[92] S. Bhowmick, S. Nagarajaiah, Automatic detection and damage quantification of multiple cracks on concrete surface from video, International Journal of Sustainable Materials and Structural Systems, 4 (2020) 292-311.

[93] B. Cassels, L.-K. Shark, S.J. Mein, A. Nixon, T. Barber, R. Turner, Robust principal component analysis of ultrasonic sectorial scans for defect detection in weld inspection, Multimodal Sensing: Technologies and Applications, SPIE, 2019, 112-128

[94] Y. Zhang, D. Burns, D. Orfeo, D.R. Huston, T. Xia, Rough ground surface clutter removal in air-coupled ground penetrating radar data using low-rank and sparse representation, Nondestructive Characterization and Monitoring of Advanced Materials, Aerospace, and Civil Infrastructure 2017, SPIE, 2017, 37-43

[95] P. Hehenberger, D. Bradley, Mechatronic futures: Challenges and solutions for mechatronic systems and their designers, Springer, 2016.

[96] J.N. Kutz, S.L. Brunton, B.W. Brunton, J.L. Proctor, Dynamic mode decomposition: data-driven modeling of complex systems, SIAM, 2016.

[97] P.J. Schmid, Dynamic mode decomposition of numerical and experimental data, Journal of Fluid Mechanics, 656 (2010) 5-28.

[98] C.W. Rowley, I. Mezić, S. Bagheri, P. Schlatter, D. Henningson, Spectral analysis of nonlinear flows, Journal of Fluid Mechanics, 641 (2009) 115-127.

[99] J.-N. Juang, R.S. Pappa, An eigensystem realization algorithm for modal parameter identification and model reduction, Journal of Guidance, Control, and Dynamics, 8 (1985) 620-627.

[100] J.H. Tu, C.W. Rowley, D.M. Luchtenburg, S.L. Brunton, J.N. Kutz, On dynamic mode decomposition: Theory and applications, Journal of Computational Dynamics, 1 (2014) 391-421.

[101] J.L. Proctor, S.L. Brunton, B.W. Brunton, J. Kutz, Exploiting sparsity and equation-free architectures in complex systems, The European Physical Journal Special Topics, 223 (2014) 2665-2684.

[102] J.-N. Juang, M. Phan, L.G. Horta, R.W. Longman, Identification of observer/Kalman filter Markov parameters-Theory and experiments, Journal of Guidance, Control, and Dynamics, 16 (1993) 320-329.

[103] M. Phan, J.-N. Juang, R.W. Longman, Identification of linear multivariable systems by identification of observers with assigned real eigenvalues, Journal of the Astronautical Sciences, 40 (1992).

[104] M. Phan, L.G. Horta, J.-N. Juang, R.W. Longman, Linear system identification via an asymptotically stable observer, Journal of Optimization Theory and Applications, 79 (1993) 59-86.

[105] J.-N. Juang, Applied system identification, Prentice-Hall, Inc., 1994.

[106] B.L. Ho, R.E. Kalman, Effective construction of linear state-variable models from input/output data, Proceedings of the 3rd Annual Allerton Conference on Circuit and System Theory, 1965, 449-459

[107] B.O. Koopman, Hamiltonian systems and transformation in Hilbert space, Proceedings of the national academy of sciences of the united states of america, 17 (1931) 315.

[108] I. Mezić, A. Banaszuk, Comparison of systems with complex behavior, Physica D: Nonlinear Phenomena, 197 (2004) 101-133.

[109] I. Mezić, Analysis of fluid flows via spectral properties of the Koopman operator, Annual Review of Fluid Mechanics, 45 (2013) 357-378.

[110] J. Bongard, H. Lipson, Automated reverse engineering of nonlinear dynamical systems, Proceedings of the National Academy of Sciences, 104 (2007) 9943-9948.

[111] M. Schmidt, H. Lipson, Distilling free-form natural laws from experimental data, Science, 324 (2009) 81-85.

[112] S.L. Brunton, J.L. Proctor, J.N. Kutz, Discovering governing equations from data by sparse identification of nonlinear dynamical systems, Proceedings of the National Academy of Sciences, 113 (2016) 3932-3937.

[113] S.L. Brunton, B.W. Brunton, J.L. Proctor, J.N. Kutz, Koopman invariant subspaces and finite linear representations of nonlinear dynamical systems for control, PloS one, 11 (2016) e0150171.

[114] H. Ye, R.J. Beamish, S.M. Glaser, S.C. Grant, C.-h. Hsieh, L.J. Richards, J.T. Schnute, G. Sugihara, Equation-free mechanistic ecosystem forecasting using empirical dynamic modeling, Proceedings of the National Academy of Sciences, 112 (2015) E1569-E1576.

[115] G. Sugihara, R. May, H. Ye, C.-h. Hsieh, E. Deyle, M. Fogarty, S. Munch, Detecting causality in complex ecosystems, Science, 338 (2012) 496-500.

[116] J.N. Kutz, J. Grosek, S.L. Brunton, Dynamic mode decomposition for robust pca with applications to foreground/background subtraction in video streams and multi-resolution analysis, CRC Handbook on Robust Low-Rank and Sparse Matrix Decomposition: Applications in Image and Video Processing, (2016).

[117] M. Bilal, M. Rizwan, S. Saleem, M.M. Khan, M.S. Alkatheir, M. Alqarni, Automatic seizure detection using multi-resolution dynamic mode decomposition, IEEE Access, 7 (2019) 61180-61194.

[118] O. Sikha, K. Soman, Multi-resolution dynamic mode decomposition-based salient region detection in noisy images, Signal, Image and Video Processing, 14 (2020) 167-175.

[119] J.N. Kutz, Data-driven modeling & scientific computation: methods for complex systems & big data, Oxford University Press, 2013.

[120] N.E. Huang, Hilbert-Huang transform and its applications, World Scientific, 2014.

[121] I. Daubechies, Ten lectures on wavelets, SIAM, 1992.

[122] L. Debnath, F.A. Shah, Wavelet transforms and their applications, Springer, 2002.

[123] G. Evensen, Data assimilation: the ensemble Kalman filter, Springer: New York, NY, USA, 2009.

[124] C. Zhang, J.-Z. Huang, G.-Q. Song, L. Chen, Structural damage identification by extended Kalman filter with l1-norm regularization scheme, Structural Control and Health Monitoring, 24 (2017) e1999.

[125] J.Z. Huang, D.S. Li, C. Zhang, H.N. Li, Improved Kalman filter damage detection approach based on lp regularization, Structural Control and Health Monitoring, 26 (2019).

[126] C.-B. Yun, M. Shinozuka, Identification of nonlinear structural dynamic systems, Journal of Structural Mechanics, 8 (1980) 187-203.

[127] M. Hoshiya, E. Saito, Structural identification by extended Kalman filter, Journal of Engineering Mechanics, 110 (1984) 1757-1770.

[128] K. Toki, T. Sato, J. Kiyono, Identification of structural parameters and input ground motion from response time histories, Doboku Gakkai Ronbunshu, 1989 (1989) 243-251.

[129] N. Ott, H. Meder, The Kalman filter as a prediction error filter, Geophysical Prospecting, 20 (1972) 549-560.

[130] Y. Lei, Y. Jiang, Z. Xu, Structural damage detection with limited input and output measurement signals, Mechanical Systems and Signal Processing, 28 (2012) 229-243.

[131] D. Wang, A. Haldar, System identification with limited observations and without input, Journal of Engineering Mechanics, 123 (1997) 504-511.

[132] X. Ling, A. Haldar, Element level system identification with unknown input with Rayleigh damping, Journal of Engineering Mechanics, 130 (2004) 877-885.

[133] H. Katkhuda, A. Haldar, A novel health assessment technique with minimum information, Structural Control and Health Monitoring, 15 (2008) 821-838.

[134] C.-K. Ma, C.-C. Ho, An inverse method for the estimation of input forces acting on non-linear structural systems, Journal of Sound and Vibration, 275 (2004) 953-971.

[135] J.N. Yang, S. Lin, H. Huang, L. Zhou, An adaptive extended Kalman filter for structural damage identification, Structural Control and Health Monitoring, 13 (2006) 849-867.

[136] Y. Lei, F. Chen, H. Zhou, An algorithm based on two-step Kalman filter for intelligent structural damage detection, Structural Control and Health Monitoring, 22 (2015) 694-706.

[137] Y. Lei, Q. Li, F. Chen, Z. Chen, Damage identification of frame structures with joint damage under earthquake excitation, Advances in Structural Engineering, 17 (2014) 1075-1087.

[138] S. Sen, B. Bhattacharya, Online structural damage identification technique using constrained dual extended Kalman filter, Structural Control and Health Monitoring, 24 (2017) e1961.

[139] D.Y. Yun, T. Hong, D.-E. Lee, H.S. Park, Structural damage identification with a tuning-free hybrid extended Kalman filter, Structural Engineering International, 31 (2021) 391-405.

[140] S.J. Julier, J.K. Uhlmann, H.F. Durrant-Whyte, A new approach for filtering nonlinear systems, Proceedings of 1995 American Control Conference-ACC'95, IEEE, 1995, 1628-1632

[141] A. Sitz, U. Schwarz, J. Kurths, H.U. Voss, Estimation of parameters and unobserved components for nonlinear systems from noisy time series, Physical review E, 66 (2002) 016210.

[142] C. Popescu, Y. Wong, The unscented and extended Kalman filter for systems with polynomial restoring forces, 44th AIAA/ASME/ASCE/AHS/ASC Structures, Structural Dynamics, and Materials Conference, 2003, 1410

[143] S. Mariani, A. Ghisi, Unscented Kalman filtering for nonlinear structural dynamics, Nonlinear Dynamics, 49 (2007) 131-150.

[144] R. Astroza, H. Ebrahimian, Y. Li, J.P. Conte, Bayesian nonlinear structural FE model and seismic input identification for damage assessment of civil structures, Mechanical Systems and Signal Processing, 93 (2017) 661-687.

[145] E.N. Chatzi, A.W. Smyth, The unscented Kalman filter and particle filter methods for nonlinear structural system identification with non - collocated heterogeneous sensing, Structural Control and Health Monitoring, 16 (2009) 99-123.

[146] E.N. Chatzi, A.W. Smyth, S.F. Masri, Experimental application of on-line parametric identification for nonlinear hysteretic systems with model uncertainty, Structural Safety, 32 (2010) 326-337.

[147] M. Sheibani, G. Ou, A Bayesian optimized framework for successful application of unscented Kalman filter in parameter identification of MDOF structures, Journal of Low Frequency Noise, Vibration and Active Control, 40 (2021) 1712-1730.

[148] G. Evensen, Sequential data assimilation with a nonlinear quasi - geostrophic model using Monte Carlo methods to forecast error statistics, Journal of Geophysical Research: Oceans, 99 (1994) 10143-10162.

[149] R. Ghanem, G. Ferro, Health monitoring for strongly non - linear systems using the Ensemble Kalman filter, Structural Control and Health Monitoring, 13 (2006) 245-259.

[150] W. Slika, G. Saad, An Ensemble Kalman Filter approach for service life prediction of reinforced concrete structures subject to chloride-induced corrosion, Construction and Building Materials, 115 (2016) 132-142.

[151] H. Nasrellah, C. Manohar, Finite element method based Monte Carlo filters for structural system identification, Probabilistic Engineering Mechanics, 26 (2011) 294-307.

[152] D. Sen, K. Erazo, S. Nagarajaiah, Bayesian estimation of acoustic emissions source in plate structures using particle - based stochastic filtering, Structural Control and Health Monitoring, 24 (2017) e2005.

[153] Z. Wan, T. Wang, S. Li, Z. Zhang, A modified particle filter for parameter identification with unknown inputs, Structural Control and Health Monitoring, 25 (2018) e2268.

[154] M.S. Caywood, D.M. Roberts, J.B. Colombe, H.S. Greenwald, M.Z. Weiland, Gaussian process regression for predictive but interpretable machine learning models: An example of predicting mental workload across tasks, Frontiers in Human Neuroscience, 10 (2017) 647.

[155] C.E. Rasmussen, H. Nickisch, Gaussian processes for machine learning (GPML) toolbox, The Journal of Machine Learning Research, 11 (2010) 3011-3015.

[156] G. Su, B. Yu, Y. Xiao, L. Yan, Gaussian process machine-learning method for structural reliability analysis, Advances in Structural Engineering, 17 (2014) 1257-1270.

[157] L. Muñoz-González, M. Lázaro-Gredilla, A.R. Figueiras-Vidal, Heteroscedastic Gaussian process regression using expectation propagation, 2011 IEEE International Workshop on Machine Learning for Signal Processing, IEEE, 2011, 1-6

[158] P. Goldberg, C. Williams, C. Bishop, Regression with input-dependent noise: A Gaussian process treatment, Advances in Neural Information Processing Systems, 10 (1997).

[159] K. Kersting, C. Plagemann, P. Pfaff, W. Burgard, Most likely heteroscedastic Gaussian process regression, Proceedings of the 24th international conference on Machine learning, 2007, 393-400

[160] I.A. Almosallam, M.J. Jarvis, S.J. Roberts, GPz: Non-stationary sparse Gaussian processes for heteroscedastic uncertainty estimation in photometric redshifts, Monthly Notices of the Royal Astronomical Society, 462 (2016) 726-739.

[161] J. Hensman, R. Mills, S. Pierce, K. Worden, M. Eaton, Locating acoustic emission sources in complex structures using Gaussian processes, Mechanical Systems and Signal Processing, 24 (2010) 211-223.

[162] M. Torres-Arredondo, C.-P. Fritzen, Impact monitoring in smart structures based on Gaussian processes, 4th International Symposium on NDT in Aerospace, 2012,

[163] S. Anderson, P. Aram, B. Bhattacharya, V. Kadirkamanathan, Analysis of composite plate dynamics using spatial maps of frequency-domain features described by Gaussian processes, IFAC Proceedings Volumes, 47 (2014) 949-954.

[164] S. Mohanty, S. Das, A. Chattopadhyay, P. Peralta, Gaussian process time series model for life prognosis of metallic structures, Journal of Intelligent Material Systems and Structures, 20 (2009) 887-896.

[165] Y. Liu, S. Mohanty, A. Chattopadhyay, Condition based structural health monitoring and prognosis of composite structures under uniaxial and biaxial loading, Journal of Nondestructive Evaluation, 29 (2010) 181-188.

[166] S. Mohanty, A. Chattopadhyay, P. Peralta, S. Das, Bayesian Statistic Based Multivariate Gaussian Process Approach for Offline/Online Fatigue Crack Growth Prediction, Experimental Mechanics, 51 (2011) 833-843.

[167] Q. Lu, J. Zhu, W. Zhang, Quantification of fatigue damage for structural details in slender coastal bridges using machine learning-based methods, Journal of Bridge Engineering, 25 (2020) 04020033.

[168] M. Gordan, H.A. Razak, Z. Ismail, K. Ghaedi, Z.X. Tan, H.H. Ghayeb, A hybrid ANN-based imperial competitive algorithm methodology for structural damage identification of slab-on-girder bridge using data mining, Applied Soft Computing, 88 (2020) 106013.

[169] Y. Deng, M. Zhang, D.-M. Feng, A.-Q. Li, Predicting fatigue damage of highway suspension bridge hangers using weigh-in-motion data and machine learning, Structure and Infrastructure Engineering, 17 (2021) 233-248.

[170] M. Kohiyama, K. Oka, T. Yamashita, Detection method of unlearned pattern using support vector machine in damage classification based on deep neural network, Structural Control and Health Monitoring, 27 (2020) e2552.

[171] J.W. Chong, Y. Kim, K.H. Chon, Nonlinear multiclass support vector machine-based health monitoring system for buildings employing magnetorheological dampers, Journal of Intelligent Material Systems and Structures, 25 (2014) 1456-1468.

[172] X. Fang, H. Luo, J. Tang, Structural damage detection using neural network with learning rate improvement, Computers & Structures, 83 (2005) 2150-2161.

[173] S. HekmatiAthar, M. Taheri, J. Secrist, H. Taheri, Neural network for structural health monitoring with combined direct and indirect methods, Journal of Applied Remote Sensing, 14 (2020) 014511-014511.

[174] A. Malekjafarian, F. Golpayegani, C. Moloney, S. Clarke, A machine learning approach to bridge-damage detection using responses measured on a passing vehicle, Sensors, 19 (2019) 4035.

[175] I.H. Witten, E. Frank, Data mining: practical machine learning tools and techniques with Java implementations, Acm Sigmod Record, 31 (2002) 76-77.

[176] D.A. Tibaduiza, L.E. Mujica, J. Rodellar, Damage classification in structural health monitoring using principal component analysis and self - organizing maps, Structural Control and Health Monitoring, 20 (2013) 1303-1316.

[177] O. Avci, O. Abdeljaber, S. Kiranyaz, D. Inman, Structural health monitoring with self-organizing maps and artificial neural networks, Topics in Modal Analysis & Testing, Volume 8: Proceedings of the 37th IMAC, A Conference and Exposition on Structural Dynamics 2019, Springer, 2020, 237-246

[178] D. Feng, M.Q. Feng, Computer vision for SHM of civil infrastructure: From dynamic response measurement to damage detection - A review, Engineering Structures, 156 (2018) 105-117.

[179] X.-W. Ye, C.-Z. Dong, T. Liu, A review of machine vision-based structural health monitoring: Methodologies and applications, Journal of Sensors, 2016 (2016).

[180] S. Khan, T. Yairi, A review on the application of deep learning in system health management, Mechanical Systems and Signal Processing, 107 (2018) 241-265.

[181] X. Ye, T. Jin, C. Yun, A review on deep learning-based structural health monitoring of civil infrastructures, Smart Struct. Syst, 24 (2019) 567-585.

[182] L. Hou, H. Chen, G. Zhang, X. Wang, Deep learning-based applications for safety management in the AEC industry: A review, Applied Sciences, 11 (2021) 821.

[183] R. Hou, Y. Xia, Review on the new development of vibration-based damage identification for civil engineering structures: 2010–2019, Journal of Sound and Vibration, 491 (2021) 115741.

[184] M. Mousavi, A.H. Gandomi, Deep learning for structural health monitoring under environmental and operational variations, Nondestructive Characterization and Monitoring of Advanced Materials, Aerospace, Civil Infrastructure, and Transportation XV, SPIE, 2021, 100-107

[185] M. Mousavi, A.H. Gandomi, Prediction error of Johansen cointegration residuals for structural health monitoring, Mechanical Systems and Signal Processing, 160 (2021) 107847.

[186] R. Zhang, Y. Liu, H. Sun, Physics-guided convolutional neural network (PhyCNN) for data-driven seismic response modeling, Engineering Structures, 215 (2020) 110704.

[187] R. Zhang, Z. Chen, S. Chen, J. Zheng, O. Büyüköztürk, H. Sun, Deep long short-term memory networks for nonlinear structural seismic response prediction, Computers & Structures, 220 (2019) 55-68.

[188] T. Li, Y. Pan, K. Tong, C.E. Ventura, C.W. de Silva, Attention-based sequence-to-sequence learning for online structural response forecasting under seismic excitation, IEEE Transactions on Systems, Man, and Cybernetics: Systems, 52 (2021) 2184-2200.

[189] D.-E. Choe, H.-C. Kim, M.-H. Kim, Sequence-based modeling of deep learning with LSTM and GRU networks for structural damage detection of floating offshore wind turbine blades, Renewable Energy, 174 (2021) 218-235.

[190] Y. Tian, Y. Xu, D. Zhang, H. Li, Relationship modeling between vehicle - induced girder vertical deflection and cable tension by BiLSTM using field monitoring data of a cable - stayed bridge, Structural Control and Health Monitoring, 28 (2021) e2667.

[191] L. Yang, D. Zhang, G.E. Karniadakis, Physics-informed generative adversarial networks for stochastic differential equations, SIAM Journal on Scientific Computing, 42 (2020) A292-A317.

[192] G. Tsialiamanis, E. Chatzi, N. Dervilis, D. Wagg, K. Worden, An application of generative adversarial networks in structural health monitoring, EURODYN 2020: Proceedings of the XI International Conference on Structural Dynamics, European Association for Structural Dynamics (EASD), 2020, 3816-3831

[193] G. Fan, J. Li, H. Hao, Y. Xin, Data driven structural dynamic response reconstruction using segment based generative adversarial networks, Engineering Structures, 234 (2021) 111970.

[194] G.E. Hinton, R.R. Salakhutdinov, Reducing the dimensionality of data with neural networks, Science, 313 (2006) 504-507.

[195] X. Jiang, J. Gao, X. Hong, Z. Cai, Gaussian processes autoencoder for dimensionality reduction, Advances in Knowledge Discovery and Data Mining: 18th Pacific-Asia Conference, PAKDD 2014, Tainan, Taiwan, May 13-16, 2014. Proceedings, Part II 18, Springer, 2014, 62-73

[196] A. Makhzani, B. Frey, K-sparse autoencoders, arXiv preprint arXiv:1312.5663, (2013).

[197] P. Vincent, H. Larochelle, I. Lajoie, Y. Bengio, P.-A. Manzagol, L. Bottou, Stacked denoising autoencoders: Learning useful representations in a deep

network with a local denoising criterion, Journal of Machine Learning Research, 11 (2010).

[198] S. Rifai, P. Vincent, X. Muller, X. Glorot, Y. Bengio, Contractive auto-encoders: Explicit invariance during feature extraction, Proceedings of the 28th International Conference on Machine Learning, 2011, 833-840

[199] C. Doersch, Tutorial on variational autoencoders, arXiv preprint arXiv:1606.05908, (2016).

[200] S. Hawkins, H. He, G. Williams, R. Baxter, Outlier detection using replicator neural networks, International Conference on Data Warehousing and Knowledge Discovery, Springer, 2002, 170-180

[201] J. Chen, S. Sathe, C. Aggarwal, D. Turaga, Outlier detection with autoencoder ensembles, Proceedings of the 2017 SIAM International Conference on Data Mining, SIAM, 2017, 90-98

[202] W. Lu, Y. Cheng, C. Xiao, S. Chang, S. Huang, B. Liang, T. Huang, Unsupervised sequential outlier detection with deep architectures, IEEE transactions on image processing, 26 (2017) 4321-4330.

[203] M. Hasan, J. Choi, J. Neumann, A.K. Roy-Chowdhury, L.S. Davis, Learning temporal regularity in video sequences, Proceedings of the IEEE Conference on Computer Vision and Pattern Recognition, 2016, 733-742

[204] P. Malhotra, A. Ramakrishnan, G. Anand, L. Vig, P. Agarwal, G. Shroff, LSTM-based encoder-decoder for multi-sensor anomaly detection, arXiv preprint arXiv:1607.00148, (2016).

[205] W. Luo, W. Liu, S. Gao, Remembering history with convolutional lstm for anomaly detection, 2017 IEEE International Conference on Multimedia and Expo (ICME), IEEE, 2017, 439-444

[206] K. Ding, J. Li, R. Bhanushali, H. Liu, Deep anomaly detection on attributed networks, Proceedings of the 2019 SIAM International Conference on Data Mining, SIAM, 2019, 594-602

[207] M. Raissi, A. Yazdani, G.E. Karniadakis, Hidden fluid mechanics: Learning velocity and pressure fields from flow visualizations, Science, 367 (2020) 1026-1030.

[208] J. Willard, X. Jia, S. Xu, M. Steinbach, V. Kumar, Integrating scientific knowledge with machine learning for engineering and environmental systems, ACM Computing Surveys, 55 (2022) 1-37.

[209] F.-G. Yuan, S.A. Zargar, Q. Chen, S. Wang, Machine learning for structural health monitoring: challenges and opportunities, Sensors and smart structures technologies for civil, mechanical, and aerospace systems 2020, 11379 (2020) 1137903.

[210] A.J. McHutchon, Nonlinear modelling and control using Gaussian processes, Citeseer, 2015, (accessed

[211] B. Jafrasteh, D. Hernández-Lobato, S.P. Lubián-López, I. Benavente-Fernández, Gaussian processes for missing value imputation, Knowledge-Based Systems, 273 (2023) 110603.

[212] A. McHutchon, C. Rasmussen, Gaussian process training with input noise, Advances in neural information processing systems, 24 (2011).

[213] M.R. Jones, T.J. Rogers, E.J. Cross, Constraining Gaussian processes for physics-informed acoustic emission mapping, Mechanical Systems and Signal Processing, 188 (2023) 109984.

[214] E.J. Cross, T.J. Rogers, T.J. Gibbons, Grey-box modelling for structural health monitoring: physical constraints on machine learning algorithms, Structural Health Monitoring 2019: Enabling Intelligent Life-Cycle Health Management for Industry Internet of Things (IIOT) - Proc. of the 12th Int. Workshop on Structural Health Monitoring, 2019,

[215] L. Yang, X. Meng, G.E. Karniadakis, B-PINNs: Bayesian physics-informed neural networks for forward and inverse PDE problems with noisy data, Journal of Computational Physics, 425 (2021) 109913.

[216] T. Poggio, H. Mhaskar, L. Rosasco, B. Miranda, Q. Liao, Why and when can deep-but not shallow-networks avoid the curse of dimensionality: a review, International Journal of Automation and Computing, 14 (2017) 503-519.

[217] A. Jentzen, D. Salimova, T. Welti, A proof that deep artificial neural networks overcome the curse of dimensionality in the numerical approximation of Kolmogorov partial differential equations with constant diffusion and nonlinear drift coefficients, Communications in Mathematical Science, 19 (2021) 1167-1205.

[218] R. Cooper, A.A. Popov, A. Sandu, Investigation of nonlinear model order reduction of the quasigeostrophic equations through a physics-informed convolutional autoencoder, arXiv preprint arXiv:2108.12344, (2021).

[219] A.D. Jagtap, E. Kharazmi, G.E. Karniadakis, Conservative physics-informed neural networks on discrete domains for conservation laws: Applications to

forward and inverse problems, Computer Methods in Applied Mechanics and Engineering, 365 (2020) 113028.

[220] A.D. Jagtap, G.E. Karniadakis, Extended Physics-Informed Neural Networks (XPINNs): A Generalized Space-Time Domain Decomposition Based Deep Learning Framework for Nonlinear Partial Differential Equations, Communications in Computational Physics, 28 (2020) 2002-2041.

[221] K. Shukla, A.D. Jagtap, G.E. Karniadakis, Parallel physics-informed neural networks via domain decomposition, Journal of Computational Physics, 447 (2021) 110683.

[222] J. Cho, S. Nam, H. Yang, S.-B. Yun, Y. Hong, E. Park, Separable PINN: Mitigating the Curse of Dimensionality in Physics-Informed Neural Networks, arXiv preprint arXiv:2211.08761, (2022).

[223] G.E. Karniadakis, I.G. Kevrekidis, L. Lu, P. Perdikaris, S. Wang, L. Yang, Physics-informed machine learning, Nature Reviews Physics, 3 (2021) 422-440.

[224] H. Jiang, C. Wan, K. Yang, Y. Ding, S. Xue, Continuous missing data imputation with incomplete dataset by generative adversarial networks-based unsupervised learning for long-term bridge health monitoring, Structural Health Monitoring, 21 (2022) 1093-1109.

[225] G. Fan, Z. He, J. Li, Structural dynamic response reconstruction using self-attention enhanced generative adversarial networks, Engineering Structures, 276 (2023) 115334.

[226] L. Yang, S. Treichler, T. Kurth, K. Fischer, D. Barajas-Solano, J. Romero, V. Churavy, A. Tartakovsky, M. Houston, M. Prabhat, Highly-scalable, physics-informed GANs for learning solutions of stochastic PDEs, 2019 IEEE/ACM Third Workshop on Deep Learning on Supercomputers (DLS), IEEE, 2019, 1-11

[227] A. Habib, E. Twerdowski, M. von Buttlar, M. Pluta, M. Schmachtl, R. Wannemacher, W. Grill, Acoustic holography of piezoelectric materials by Coulomb excitation, Health Monitoring and Smart Nondestructive Evaluation of Structural and Biological Systems V, International Society for Optics and Photonics, 2006, 61771A

[228] A. Habib, U. Amjad, M. Pluta, U. Pietsch, W. Grill, Surface acoustic wave generation and detection by Coulomb excitation, Health Monitoring of Structural and Biological Systems 2010, International Society for Optics and Photonics, 2010, 76501T

[229] A. Habib, A. Shelke, M. Pluta, T. Kundu, U. Pietsch, W. Grill, Imaging of acoustic waves in piezoelectric ceramics by coulomb coupling, Japanese Journal of Applied Physics, 51 (2012) 07GB05.

[230] A. Habib, E. Twerdowski, M. von Buttlar, R. Wannemacher, W. Grill, The influence of the radius of the electrodes employed in Coulomb excitation of acoustic waves in piezoelectric materials, Health Monitoring of Structural and Biological Systems 2007, International Society for Optics and Photonics, 2007, 653214

[231] J.N. Kutz, X. Fu, S.L. Brunton, Multiresolution dynamic mode decomposition, SIAM Journal on Applied Dynamical Systems, 15 (2016) 713-735.

[232] S. Kullback, R.A. Leibler, On information and sufficiency, The annals of mathematical statistics, 22 (1951) 79-86.

[233] K.K. Chen, J.H. Tu, C.W. Rowley, Variants of dynamic mode decomposition: boundary condition, Koopman, and Fourier analyses, Journal of nonlinear science, 22 (2012) 887-915.

[234] P.J. Schmid, K.E. Meyer, O. Pust, Dynamic mode decomposition and proper orthogonal decomposition of flow in a lid-driven cylindrical cavity, 8th International Symposium on Particle Image Velocimetry, 2009, 25-28

[235] M. Budišić, R. Mohr, I. Mezić, Applied koopmanism, Chaos: An Interdisciplinary Journal of Nonlinear Science, 22 (2012) 047510.

[236] S.L. Brunton, J.L. Proctor, J.N. Kutz, Compressive sampling and dynamic mode decomposition, arXiv preprint arXiv:1312.5186, (2013).

[237] M.R. Jovanović, P.J. Schmid, J.W. Nichols, Sparsity-promoting dynamic mode decomposition, Physics of Fluids, 26 (2014) 024103.

[238] S.L. Brunton, J.N. Kutz, Data-driven science and engineering: Machine learning, dynamical systems, and control, Cambridge University Press, 2022.

[239] M. Gavish, D.L. Donoho, The optimal hard threshold for singular values is $4/\sqrt{3}$, IEEE Transactions on Information Theory, 60 (2014) 5040-5053.

[240] B. Zitova, J. Flusser, Image registration methods: a survey, Image and Vision Computing, 21 (2003) 977-1000.

[241] L.G. Brown, A survey of image registration techniques, ACM Computing Surveys, 24 (1992) 325-376.

[242] A. Hore, D. Ziou, Image quality metrics: PSNR vs. SSIM, 20th International Conference on Pattern Recognition, IEEE, 2010, 2366-2369

[243] C.R. Gin, D.E. Shea, S.L. Brunton, J.N. Kutz, DeepGreen: Deep learning of Green' s functions for nonlinear boundary value problems, Scientific Reports, 11 (2021) 1-14.

[244] J. Bakarji, K. Champion, J. Nathan Kutz, S.L. Brunton, Discovering governing equations from partial measurements with deep delay autoencoders, Proceedings of the Royal Society A, 479 (2023) 20230422.

[245] E.D. Niri, A. Farhidzadeh, S. Salamone, Nonlinear Kalman Filtering for acoustic emission source localization in anisotropic panels, Ultrasonics, 54 (2014) 486-501.

[246] R. Madankan, P. Singla, T. Singh, P.D. Scott, Polynomial-chaos-based Bayesian approach for state and parameter estimations, Journal of Guidance, Control, and Dynamics, 36 (2013) 1058-1074.

[247] J.L. Crassidis, J.L. Junkins, Optimal estimation of dynamic systems, Chapman & Hall/CRC Applied Mathematics & Non-linear Science, Boca Raton, 2004.

[248] S. Thrun, Probabilistic robotics, Communications of the ACM, 45 (2002) 52-57.

[249] B.A. Auld, Acoustic fields and waves in solids, John Wiley and Sons, New York, 1973.

[250] F.I. Fedorov, Theory of elastic waves in crystals, Springer Science & Business Media, 1968.

[251] S. Särkkä, Bayesian filtering and smoothing, Cambridge university press, 2013.

[252] G. Welch, G. Bishop, An introduction to the Kalman filter, (1995).

[253] E.A. Wan, R. Van Der Merwe, The unscented Kalman filter for nonlinear estimation, Proceedings of the IEEE 2000 Adaptive Systems for Signal Processing, Communications, and Control Symposium (Cat. No. 00EX373), Ieee, 2000, 153-158

[254] A.W. Amer, S. Roy, F. Kopsaftopoulos, Probabilistic SHM under varying loads via the integration of Gaussian Process Regression and physics-based guided-wave propagation models, AIAA Scitech 2021 Forum, 2021, 0434

[255] H. Fekrmandi, Y. Gwon, Reliability of surface response to excitation method for data-driven prognostics using Gaussian process regression, health monitoring of structural and biological systems XII, SPIE, 2018, 630-637

[256] Q.-A. Wang, C. Zhang, Z.-G. Ma, Y.-Q. Ni, Modelling and forecasting of SHM strain measurement for a large-scale suspension bridge during typhoon events

using variational heteroscedastic Gaussian process, Engineering Structures, 251 (2022) 113554.

[257] A. Huber, M.G. Sause, Classification of solutions for guided waves in anisotropic composites with large numbers of layers, The Journal of the Acoustical Society of America, 144 (2018) 3236-3251.

[258] L. Wang, S. Rokhlin, Analysis of ultrasonic wave propagation in multiply composites: homogenization and effective anisotropic media, AIP Conference Proceedings, American Institute of Physics, 2001, 1015-1022

[259] S. Rokhlin, D. Chimenti, P. Nagy, Physical ultrasonics of composites, Oxford University Press, 2011.

[260] A. Martens, K. Van Den Abeele, S. Delrue, M. Kersemans, Visco-elastic material characterisation by means of the Ultrasonic Polar Scan (PhD Thesis), KU Leuven, (2020).

[261] E.L. Tan, Stiffness matrix method with improved efficiency for elastic wave propagation in layered anisotropic media, The Journal of the Acoustical Society of America, 118 (2005) 3400-3403.

[262] C.K. Williams, C.E. Rasmussen, Gaussian processes for machine learning, MIT press, Cambridge, MA, 2006.

[263] C.M. Bishop, Pattern recognition and machine learning, 1 ed., Springer New York, NY, 2006.

[264] M.A. Alvarez, L. Rosasco, N.D. Lawrence, Kernels for vector-valued functions: A review, Foundations and Trends® in Machine Learning, 4 (2012) 195-266.

[265] C.A. Micchelli, M. Pontil, On learning vector-valued functions, Neural computation, 17 (2005) 177-204.

[266] P. Kudela, M. Radzienski, P. Fiborek, T. Wandowski, Elastic constants identification of woven fabric reinforced composites by using guided wave dispersion curves and genetic algorithm, Composite Structures, 249 (2020) 112569.

[267] D. Gsell, G. Feltrin, S. Schubert, R. Steiger, M. Motavalli, Cross-laminated timber plates: Evaluation and verification of homogenized elastic properties, Journal of Structural Engineering, 133 (2007) 132-138.

[268] S. Chakraborty, Transfer learning based multi-fidelity physics informed deep neural network, Journal of Computational Physics, 426 (2021) 109942.

[269] M. Raissi, P. Perdikaris, G.E. Karniadakis, Physics-informed neural networks: A deep learning framework for solving forward and inverse problems involving nonlinear partial differential equations, Journal of Computational Physics, 378 (2019) 686-707.

[270] Y. Zhu, N. Zabaras, P.-S. Koutsourelakis, P. Perdikaris, Physics-constrained deep learning for high-dimensional surrogate modeling and uncertainty quantification without labeled data, Journal of Computational Physics, 394 (2019) 56-81.

[271] T. Kundu, S. Das, K.V. Jata, Point of impact prediction in isotropic and anisotropic plates from the acoustic emission data, The Journal of the Acoustical Society of America, 122 (2007) 2057-2066.

[272] N. Sen, T. Kundu, A new wave front shape-based approach for acoustic source localization in an anisotropic plate without knowing its material properties, Ultrasonics, 87 (2018) 20-32.

[273] W.H. Park, P. Packo, T. Kundu, Acoustic source localization in an anisotropic plate without knowing its material properties-a new approach, Ultrasonics, 79 (2017) 9-17.

[274] N. Sen, M. Gawroński, P. Packo, T. Uhl, T. Kundu, Square-shaped sensor clusters for acoustic source localization in anisotropic plates by wave front shape-based approach, Mechanical Systems and Signal Processing, 153 (2021) 107489.

[275] N. Sen, T. Kundu, A new signal energy-based approach to acoustic source localization in orthotropic plates: A numerical study, Mechanical Systems and Signal Processing, 171 (2022) 108843.

[276] F. Ciampa, M. Meo, A new algorithm for acoustic emission localization and flexural group velocity determination in anisotropic structures, Composites Part A: Applied Science and Manufacturing, 41 (2010) 1777-1786.

[277] E.D. Niri, S. Salamone, A probabilistic framework for acoustic emission source localization in plate-like structures, Smart Materials and Structures, 21 (2012) 035009.

[278] E.D. Niri, A. Farhidzadeh, S. Salamone, Determination of the probability zone for acoustic emission source location in cylindrical shell structures, Mechanical Systems and Signal Processing, 60 (2015) 971-985.

[279] G. Andria, F. Attivissimo, N. Giaquinto, Digital signal processing techniques for accurate ultrasonic sensor measurement, Measurement, 30 (2001) 105-114.

[280] B. Lei, G. Xu, M. Feng, Y. Zou, F. Van der Heijden, D. De Ridder, D.M. Tax, Classification, parameter estimation and state estimation: an engineering approach using MATLAB, John Wiley & Sons, 2017.

[281] M. Parrilla, J. Anaya, C. Fritsch, Digital signal processing techniques for high accuracy ultrasonic range measurements, IEEE Transactions on Instrumentation and Measurement, 40 (1991) 759-763.

[282] Y.C. Wu, J.W. Feng, Development and Application of Artificial Neural Network, Wireless Personal Communications, 102 (2018) 1645-1656.

[283] G. Zhou, Y. Ji, X. Chen, F. Zhang, Artificial neural networks and the mass appraisal of real estate, International Journal of Online Engineering, 14 (2018).

[284] R. Benzer, Population dynamics forecasting using artificial neural networks, Fresenius Environmental Bulletin, 12 (2014) 14-26.

[285] P. Kim, Matlab deep learning with machine learning, neural networks and artificial intelligence, Apress, 2017.

[286] S. Goswami, C. Anitescu, S. Chakraborty, T. Rabczuk, Transfer learning enhanced physics informed neural network for phase-field modeling of fracture, Theoretical and Applied Fracture Mechanics, 106 (2020) 102447.

[287] G.P. Pun, R. Batra, R. Ramprasad, Y. Mishin, Physically informed artificial neural networks for atomistic modeling of materials, Nature Communications, 10 (2019) 2339.

[288] S. De, J. Britton, M. Reynolds, R. Skinner, K. Jansen, A. Doostan, On transfer learning of neural networks using bi-fidelity data for uncertainty propagation, International Journal for Uncertainty Quantification, 10 (2020).

[289] G. Cybenko, Approximation by superpositions of a sigmoidal function, Mathematics of Control, Signals and Systems, 2 (1989) 303-314.

[290] K. Hornik, M. Stinchcombe, H. White, Multilayer feedforward networks are universal approximators, Neural Networks, 2 (1989) 359-366.

[291] K. Hornik, M. Stinchcombe, H. White, Universal approximation of an unknown mapping and its derivatives using multilayer feedforward networks, Neural Networks, 3 (1990) 551-560.

[292] B. Hanin, Universal function approximation by deep neural nets with bounded width and relu activations, Mathematics, 7 (2019) 992.

[293] J. Snoek, H. Larochelle, R.P. Adams, Practical bayesian optimization of machine learning algorithms, Advances in Neural Information Processing Systems, 25 (2012).